ADVANCED NUCLEAR FUEL TECHNOLOGY

EDITED BY: Jinbiao Xiong, Yingwei Wu and Ho Jin Ryu
PUBLISHED IN: Frontiers in Energy Research

frontiers Research Topics

frontiers

ISSN 1664-8714
ISBN 978-2-88974-523-4
DOI 10.3389/978-2-88974-523-4

About Frontiers

Frontiers is more than just an open-access publisher of scholarly articles: it is a pioneering approach to the world of academia, radically improving the way scholarly research is managed. The grand vision of Frontiers is a world where all people have an equal opportunity to seek, share and generate knowledge. Frontiers provides immediate and permanent online open access to all its publications, but this alone is not enough to realize our grand goals.

Frontiers Journal Series

The Frontiers Journal Series is a multi-tier and interdisciplinary set of open-access, online journals, promising a paradigm shift from the current review, selection and dissemination processes in academic publishing. All Frontiers journals are driven by researchers for researchers; therefore, they constitute a service to the scholarly community. At the same time, the Frontiers Journal Series operates on a revolutionary invention, the tiered publishing system, initially addressing specific communities of scholars, and gradually climbing up to broader public understanding, thus serving the interests of the lay society, too.

Dedication to Quality

Each Frontiers article is a landmark of the highest quality, thanks to genuinely collaborative interactions between authors and review editors, who include some of the world's best academicians. Research must be certified by peers before entering a stream of knowledge that may eventually reach the public - and shape society; therefore, Frontiers only applies the most rigorous and unbiased reviews.
Frontiers revolutionizes research publishing by freely delivering the most outstanding research, evaluated with no bias from both the academic and social point of view. By applying the most advanced information technologies, Frontiers is catapulting scholarly publishing into a new generation.

What are Frontiers Research Topics?

Frontiers Research Topics are very popular trademarks of the Frontiers Journals Series: they are collections of at least ten articles, all centered on a particular subject. With their unique mix of varied contributions from Original Research to Review Articles, Frontiers Research Topics unify the most influential researchers, the latest key findings and historical advances in a hot research area! Find out more on how to host your own Frontiers Research Topic or contribute to one as an author by contacting the Frontiers Editorial Office: frontiersin.org/about/contact

ADVANCED NUCLEAR FUEL TECHNOLOGY

Topic Editors:
Jinbiao Xiong, Shanghai Jiao Tong University, China
Yingwei Wu, Xi'an Jiaotong University, China
Ho Jin Ryu, Korea Advanced Institute of Science and Technology, South Korea

Citation: Xiong, J., Wu, Y., Ryu, H. J., eds. (2022). Advanced Nuclear Fuel Technology. Lausanne: Frontiers Media SA. doi: 10.3389/978-2-88974-523-4

Table of Contents

frontiers in Energy Research

ORIGINAL RESEARCH
published: 25 February 2021
doi: 10.3389/fenrg.2021.634964

Study of Flow and Heat Transfer Characteristics of Lead-Based Liquid Metals in a Turbulent Tube Flow and the Impacts of Roughness

*Yaou Shen, Shinian Peng, Mingyu Yan *, Yu Zhang, Jian Deng *, Hongxing Yu, Daishun Huang and Zhongchun Li*

Science and Technology on Reactor System Design Technology Laboratory, Nuclear Power Institute of China, Chengdu, China

OPEN ACCESS

Edited by:
Jinbiao Xiong,
Shanghai Jiao Tong University, China

Reviewed by:
Chenglong Wang,
Xi'an Jiaotong University, China
Luteng Zhang,
Chongqing University, China
Xi Huang,
Shenzhen University, China

****Correspondence:***
Mingyu Yan
megatron-prime@hotmail.com
Jian Deng
dengjian_npic@163.com

Specialty section:
This article was submitted to Nuclear Energy, a section of the journal Frontiers in Energy Research

Received: *29 November 2020*
Accepted: *12 January 2021*
Published: *25 February 2021*

Citation:
Shen Y, Peng S, Yan M, Zhang Y, Deng J, Yu H, Huang D and Li Z (2021) Study of Flow and Heat Transfer Characteristics of Lead-Based Liquid Metals in a Turbulent Tube Flow and the Impacts of Roughness. Front. Energy Res. 9:634964. doi: 10.3389/fenrg.2021.634964

Lead-based liquid metals (LLMs) such as lead–bismuth eutectic (LBE) and lead, are currently the most interesting candidate coolants for fast reactors because of their excellent physical properties, which can improve safety and reduce costs. However, in comparison to other liquid metals, previous research on the flow and heat-transfer characteristics of LLMs has been limited. Therefore, this work carried out flow and heat-transfer experiments in LBE flowing through a circular tube in the Natural Circulation Capability Loop (NCCL) facility. The results show a significantly higher friction factor than that of water flowing in a smooth pipe. Furthermore, the Nusselt numbers were found to be lower than those found in data in the literature for experiments carried out in a smooth tube at low Péclet numbers, while they were higher at high Péclet numbers. Therefore, theoretical analyses were performed for LLMs flowing in both smooth and rough pipes, and the impacts of roughness on the heat transfer of an LLM were examined. The theoretical relations for a smooth pipe and a rough pipe were validated using experimental data from the literature and the results of the NCCL experiments, respectively. The results of the theoretical relation for a smooth pipe fitted the literature data well. The derived theoretical relation for a rough pipe with a relative roughness of 0.004 fitted the NCCL data best. Moreover, it was established from the theoretical analysis that roughness has two competitive impacts on the heat transfer of an LLM: it reduces conductive heat transfer while enhancing convective heat transfer. Because conductive heat transfer is important for liquid metals, even with turbulent flow, a small roughness will lead to heat-transfer deterioration at low Péclet numbers, and it may even deteriorate across the whole typical Péclet-number range. This discovery has important implications for the thermal–hydraulic design of LLM reactors, because corrosion and erosion by an LLM will lead to a rough surface after long operating times.

Keywords: lead-bismuth eutectic, flow and heat transfer, roughness impacts, turbulent flow, lead-based liquid metal

HIGHLIGHTS

1. Experimental research on the flow and heat-transfer characteristics of LBE was carried out using the NCCL facility.
2. Theoretical analyses of an LLM flowing in both smooth and rough pipes were performed, and relevant relations were established.
3. Impacts of roughness on LLM heat transfer were theoretically analyzed and preliminarily verified using NCCL experimental data.
4. Theoretical analysis showed that a certain small roughness will worsen the heat transfer of an LLM across the whole typical Péclet-number range, which should be considered during thermal–hydraulic design.

INTRODUCTION

The idea of using liquid metals as reactor coolants began in the 1950s, and it has received increasing attention in recent years because of the excellent heat transfer characteristics and low moderation ratios of such metals. Among them, lead-based liquid metals (LLMs), such as lead–bismuth eutectic (LBE) and pure lead, have very high boiling temperatures that allow the reactor system to operate at normal pressure, and this eliminates the possibility of coolant boiling. Accidents in pressurized water reactors resulting in deterioration of core heat transfer due to system pressure relief or coolant boiling do not constitute a threat to LLM reactors. Additionally, the chemical inertness of LLMs, in contrast to sodium, eliminates the risk of fire and explosion upon contact with water and air. Therefore, despite problems with corrosion and polonium contamination, LLMs remain one of the most competitive coolant candidates for future reactors.

It is generally believed that the flow characteristics of liquid metals, including LLMs, are similar to those of traditional fluids such as water and air (Isakoff, 1951; Brown et al., 1957; Zheng et al., 2016). However, due to their excellent thermal-conductivity coefficients, the heat-transfer characteristics of these materials under turbulent conditions are significantly different from those of ordinary fluids, and this makes their molecular thermal conductivity important, even under turbulent conditions, and it cannot therefore be neglected (Dwyer, 1976; Reed, 1987).

As a basement geometry, there have been many studies on the heat-transfer characteristics of liquid metals, including LBE, flowing in a circular tube. Various heat-transfer equations have been proposed, and most of these are empirical relations based on fitting of experimental data. Furthermore, all of these empirical relations are built on the structural form of the Lyon–Martinelli semi-empirical relation (Martinelli, 1947; Lyon, 1949). This relation has a structural form comprising the sum of thermal conductive and convective terms, in which the thermal conductive term is a constant and the convective term is related to the Péclet number.

For mercury and alkali metals, a large amount of experimental data is available for developing and validating empirical relations. However, comparatively little experimental data relating to LLMs have been obtained, and few relations exist that have been specifically developed for LLMs (Pacio et al., 2015; Zhang et al., 2020b). Although it has long been believed that the heat-transfer relations of other liquid metals can also be applied to LLM, a recent study (Cheng and Tak, 2006) shows that the turbulent Prandtl numbers of LLMs are significantly higher than those of other liquid metals. Furthermore, LLMs have significant corrosion and erosion effects on stainless-steel structural materials. The surface conditions in actual operation may also be different from those with other metals. However, most studies on the heat-transfer characteristics of LLMs have focused on smooth surfaces.

This study focused on these problems, and heat-transfer experiments with LBE flowing in a circular tube were carried out. Theoretical analysis methods for heat-transfer in LLM tubes were established, theoretically derived relations were obtained, and the influence of roughness on heat transfer in liquid metals was examined. The results have important reference significance for understanding LLM heat-transfer mechanisms and industrial thermal–hydraulic design.

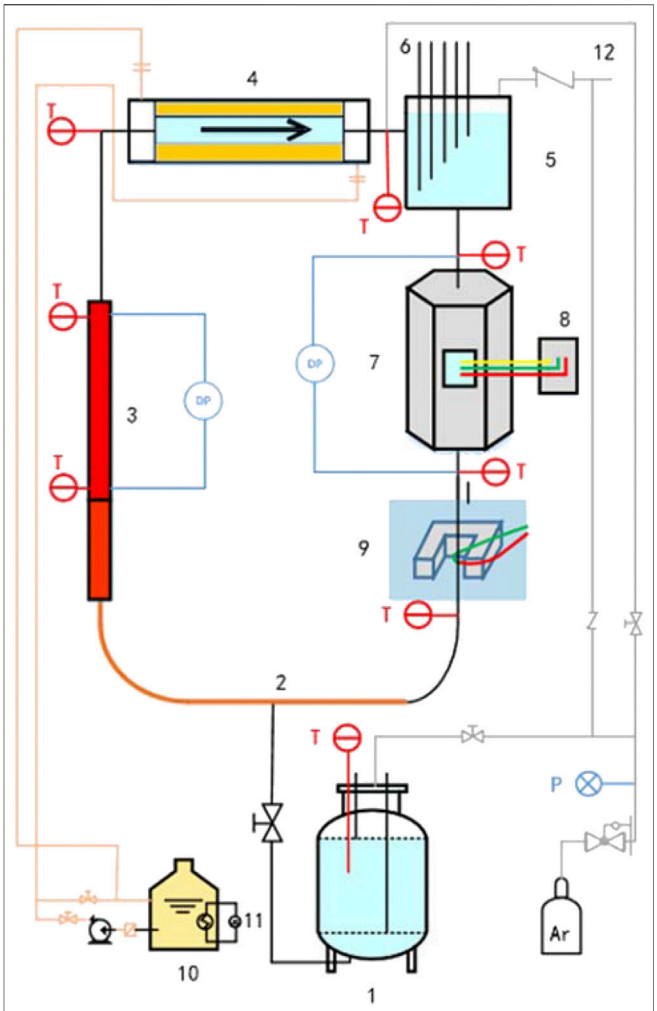

FIGURE 1 | Schematic of the NCCL facility, showing: 1. LBE storage and melting tank; 2. pre-heating section; 3. test section; 4. heat exchanger; 5. EMF calibration tube; 6. liquid-level probes; 7. EMP; 8. EMP control system; 9. EMF; 10. oil storage tank; 11. oil heating system; 12. gas outlet.

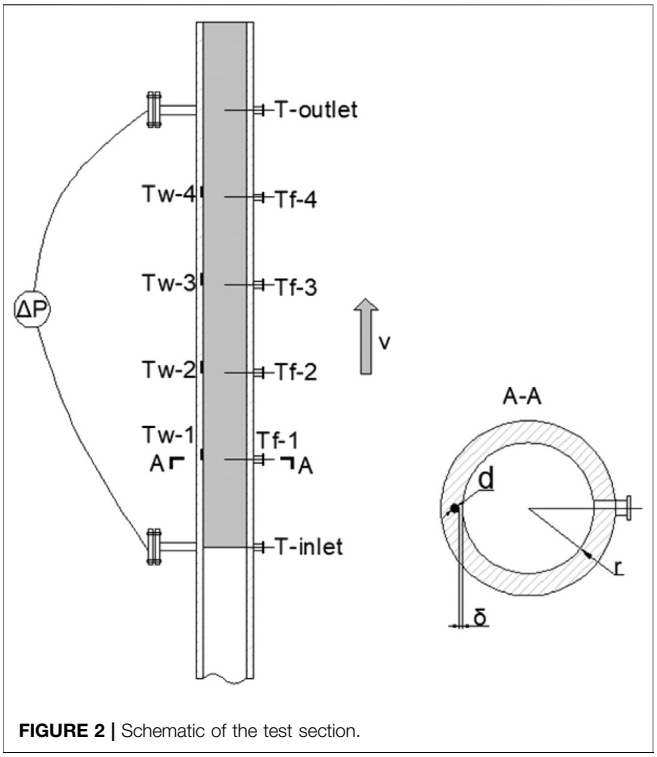

FIGURE 2 | Schematic of the test section.

made from 316 L stainless steel. The general layout of this facility is shown in **Figure 1**.

In these experiments, three circular tubes with different diameters were used as test sections. The internal diameters of the test sections were 20, 35, and 50 mm, and the wall thickness of the test section was 5 mm to ensure a uniform heat flux. The length of the test section was 2 m, and it was divided into two parts, the pre-heating section and the measuring section, each having a length of 1 m. The pre-heating section was designed to ensure that the flow was fully developed before entering the measurement section. The measuring section was equipped with thermocouples and partial-pressure sensors. The heating section was wrapped with 2 mm outer-diameter heating wires with a pitch of 5 mm.

In the experiments, more than 20 thermocouples (TCs), each with an outer diameter of 1.5 mm, were placed at different loop locations to measure the temperature distribution of the LBE. Six thermocouples with an outer diameter of 1.5 mm were used to measure the temperature of the LBE in the measuring section, including two for the inlet and outlet and four for different heights in the measuring section. Four TCs with an outer diameter of 1 mm were embedded in the walls at the same four heights of the test section to measure the wall temperature. A differential pressure sensor was used to measure the pressure drop in the test section. Two pressure sensors were connected to the test section with horizontal tubes to reduce the temperature of the LBE touching the pressure membrane. All the measuring points in the test section are shown in **Figure 2**. More information about the NCCL experimental facility can be found in a previous report (Zhang et al., 2020a).

EXPERIMENTAL METHODS

Experimental Loop

Thermal–hydraulic experiments with LBE flowing in a circular pipe were conducted using the Natural Circulation Capability Loop (NCCL). The NCCL is a high-temperature experimental facility that has three different running modes: pump driving, gas lift, and pure natural circulation. It was designed for performing experimental measurements of the thermal–hydraulic characteristics of LBE to provide support to the design of lead-cooled fast reactors (LFR) and accelerator-driven systems (DAS). The experimental facility is composed of a primary loop containing LBE and a secondary loop with oil for cooling. The LBE loop is rectangular, and it includes a melting tank, riser, pre-heating system, cooling section, electromagnetic pump (EMP), downcomer, electromagnetic flowmeter (EMF), EMF calibration system, electric heating system, and a measuring instrument. The test section is installed in the bottom of the riser. The secondary loop is designed for the cooling of LBE and is connected with the primary loop through a double-tube heat exchanger. The melting tank is used to store and melt the LBE and is heated by heating wires with a heating power of 6 kW. During the experiments, the upper level of LBE is designed to be located in the center of the LBE–oil heat exchanger, leaving enough space to store argon. The EMF is used to measure the flow rate of liquid LBE and is calibrated by the EMF calibration system with five liquid-level sensors at different heights. The entire LBE loop is wrapped with electric heating wires for pre-heating before the LBE enters. The LBE loop is also wrapped with a layer of insulation to reduce heat loss. All pipes and components of this facility in direct contact with LBE are

TABLE 1 | Experimental conditions for each case.

Inner diameter mm	Inlet temp.°C	Heat flux W/m^2	Peclet number/	Test case/
20	300	22,823	508~3,985	Test 1
		32,707	731~3,504	Test 2
		37,876	780~3,648	Test 3
		43,757	731~3,556	Test 4
		56,384	775~2,379	Test 5
	400	22,823	380~3,610	Test 6
		37,876	460~3,764	Test 7
35	300	21,762	677~4,546	Test 8
		30,394	785~4,235	Test 9
		40,466	562~3,961	Test 10
	400	21,762	801~3,106	Test 11
		30,394	617~2,712	Test 12
		40,466	534~1,434	Test 13
50	300	19,131	409~1,769	Test 14
		31,463	926~2,112	Test 15
		41,327	1,096~2,213	Test 16
	340	19,131	438~1,925	Test 17
		31,463	574~2,106	Test 18
		41,327	1,065~1,984	Test 19

Experimental Conditions and Results

The experiments were conducted under stable temperature and pressure conditions. The variables in this experiment included the inner diameter of the test sections, the mass flow rate of the LBE, the

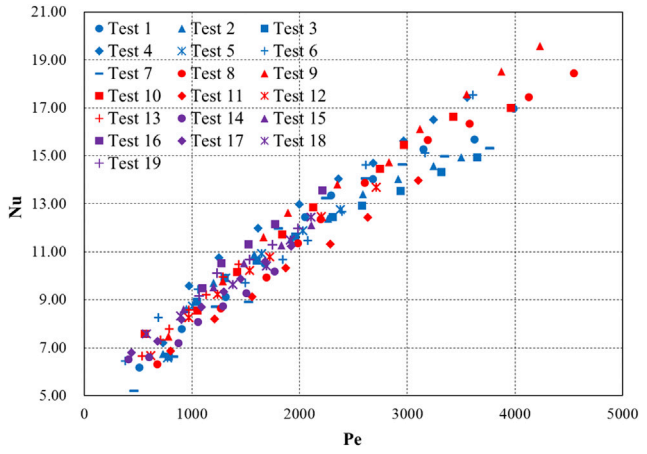

FIGURE 3 | Heat-transfer results from the NCCL experiments.

inlet temperature, and the heat flux added to the test section. Previous work (Zhang et al., 2020a) examined seven cases for a 20-mm-diameter pipe and six cases for a 35-mm-diameter pipe. This study completes six cases for a 50-mm-diameter pipe according to the same experimental methods. The experimental conditions for each case are listed in **Table 1**.

Figure 3 shows the Nusselt-number results under various Péclet numbers for each case. There is a consistent tendency in the experimental data. Significant differences between the cases are not observed in the results, which means that in the range of the parameters considered in these experiments, the inner diameter, inlet temperature, and heat flux at the wall have little impact on the heat-transfer behavior of LBE.

When compared with experimental data in the literature (Johnson et al., 1953; Ibragimov et al., 1960), the Nusselt numbers (Nu) obtained from the NCCL experiments at low Péclet numbers are significantly lower, while the results at high Péclet numbers are higher. The reason for this tendency may be a difference in the wall conditions. The NCCL facility has no oxygen-control system, which may lead to the oxidation of LBE and the corrosion of the inner wall, and thus the condition of a smooth pipe cannot be maintained. **Figure 4** shows the friction-factor results of flow experiments carried out in a 20-mm-diameter pipe. The friction factors are higher than the values corresponding to a smooth pipe and are between the ranges of the results for relative roughness h/d from 0.004 to 0.010. The friction-factor results with relative roughnesses of 0.004 and 0.010 were calculated using an empirical relation based on Moody's curve, which is given later in this report, in **Eq. 25**.

ANALYTICAL STUDY METHODS

Because of a lack of experimental data relating to the flow of LBE or other LLMs, this section describes a theoretical analysis of the impacts of roughness that was carried out based on the methods established for a smooth pipe. These methods are then validated by experimental data from the literature, as detailed in **Section 4.1**. **Section 4.2** then gives the results of these theoretical relations for various relative roughnesses.

Main Assumptions

For liquid metals flowing in a circular tube under fully developed turbulent flow with uniform wall heat flux, Lyon (1949) derived a theoretical heat-transfer integral formula following Martinelli (1947), assumptions:

$$\frac{1}{Nu} = 2\int_0^1 \frac{\left[\left(\int_0^{R_q} VRdR\right)\right]}{R_q\left(1+\frac{\mathrm{Pr}}{\mathrm{Pr}_t}\frac{\varepsilon_M}{\nu}\right)}dR_q, \tag{1}$$

where: V is the dimensionless velocity, which is defined as

$$V = \frac{u}{u_m} = \frac{u^*}{u_m}\frac{u}{u^*} = \sqrt{c_f/2}\ \frac{u}{u^*};$$

u^* is the shear velocity, which is related to mean velocity by $u^* = \sqrt{\tau_w/\rho} = u_m\sqrt{c_f/2}$; and R is the dimensionless radius, which is defined as $R = \frac{r}{r_w}$.

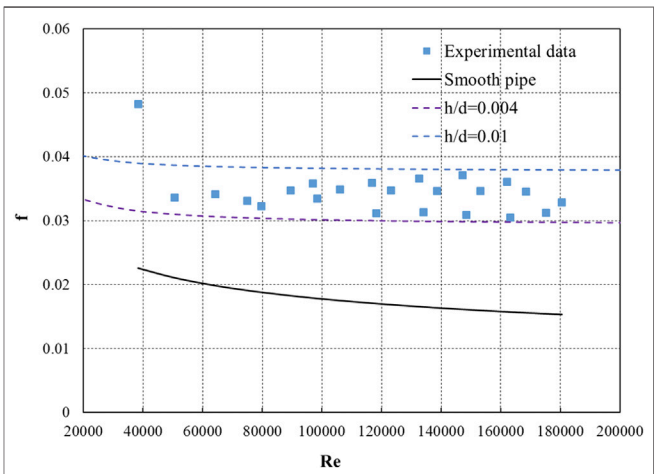

FIGURE 4 | Friction-factor (f) results at different Reynolds numbers (Re) from the NCCL experiments.

The assumptions used by Lyon (1949) to derive the integral formula are as follows. The system is assumed to operate under steady-state conditions with no end effects, and the physical properties of the liquid metal are constant. The total heat flux in the axial direction, including molecular and eddy heat flux, is assumed to be uniform, while the molecular conductivity perpendicular to the flow direction is assumed not to be affected by eddies, velocity, or axial velocity gradients.

To solve the integral formula, because the turbulent Prandtl number (Pr_t) of liquid metals was not known, Lyon assumed $\mathrm{Pr}_t = 1$. Moreover, it was assumed that the flow characteristics of liquid metals were similar to those of ordinary fluids such as water and air. Therefore, experimental data relating to the velocity and eddy diffusivity of momentum distributions of water were used to solve the integral formula. By fitting the numerical integration values of various Péclet numbers (Pe), Lyon's relation for liquid metals was established as

$$\mathrm{Nu} = 7.0 + 0.025Pe^{0.8}. \tag{2}$$

The constant term of **Eq. 2** is called the conductive term, and this represents the contribution of molecular conduction, and the power function of the Péclet number is called the convective term, which expresses the contribution of turbulent convection.

Although the assumption of $\mathrm{Pr}_t = 1$ and the method of fitting of numerical integration results may result in deviations that have been proven to lead to overestimation of the results of experiments performed later, the form of **Eq. 2** is still adopted as the functional form of empirical relations. The deviations can be corrected after fitting using enough experimental data. However, the experimental data available for LLMs are limited. Therefore, a theoretical analysis is needed to discover the heat-transfer characteristics of LLMs.

The theoretical analysis starts from the Lyon–Martinelli integral formula given by **Eq. 1**. To solve this integral formula, the dimensionless velocity and eddy diffusivity of momentum functions, as well as the turbulent Prandtl number, should first be obtained.

Preparation Before Solving the Integral Equation.

The dimensionless velocity of liquid metals can be obtained by substituting the velocity distribution of the turbulent flow of water in a circular tube, which is determined by Nikuradse (1950) relation, into the definition of dimensionless velocity:

$$\begin{aligned} V &= \sqrt{c_f/2}\ \frac{u}{u^*} = \sqrt{c_f/2}\left[5.5 + 2.5\ln 9\,(r_w - r)\frac{u^*}{v}\right)\Big] \\ &= \sqrt{c_f/2}\left[5.5 + 2.5\ln\left[(1-R)\frac{\mathrm{Re}}{2}\sqrt{c_f/2}\right)\right]. \end{aligned} \tag{3}$$

The eddy diffusivity of momentum can be derived by force balance. For a unit-length section of cylindrical fluid, according to force balance:

$$2\pi r\tau = \pi r^2\frac{dP}{dz}. \tag{4}$$

For a fully developed flow, the axial pressure gradient is constant. Therefore, from **Eq. 4**, the shear stress is linear with respect to radius, which means that the shear stress at any radius has a relationship with the shear stress at the wall defined by:

$$\tau = \frac{r}{r_w}\tau_w = \frac{r}{r_w}\,\frac{c_f\rho u_m^2}{2}. \tag{5}$$

However, for a turbulent flow, shear stress is defined as:

$$\begin{aligned} \tau &= \rho(v+\varepsilon_M)\frac{du}{dy} = \rho(v+\varepsilon_M)\frac{d}{dy}\left\{u^*\left[5.5 + 2.5\ln\left(y\frac{u^*}{v}\right)\right]\right\} \\ &= \rho(v+\varepsilon_M)\frac{2.5u^*}{y}. \end{aligned} \tag{6}$$

Combining **Eqs. 5**, **6** derives the eddy diffusivity of momentum function as:

$$\begin{aligned} \frac{\varepsilon_M + v}{v} &= \frac{\tau y}{\rho v 2.5u^*} = \frac{\frac{r}{r_w}\tau_w y}{\rho v 2.5u^*} = \frac{1}{2.5}R\left(y\frac{u^*}{v}\right). \\ &= \frac{1}{2.5}R(1-R)\frac{\mathrm{Re}}{2}\sqrt{c_f/2} \end{aligned} \tag{7}$$

According to the research of Cheng and Tak (2006), the turbulent Prandtl numbers for LLMs are greater than those for other liquid metals. Moreover, Cheng and Tak also found that a constant turbulent Prandtl number is more suitable for the form of Lyon's relation. Therefore, the turbulent Prandtl number used for solving the integral formula of **Eq. 1** for an LLM is 2.5, which is the integral mean value of Cheng and Tak's relations in a typical Péclet-number range.

Solution of the Integral Equation

To solve **Eq. 1**, the dimensionless velocity and diffusivity of momentum functions given in **Eqs. 3**, **7** should first be substituted into it:

$$\frac{1}{Nu} = -\frac{c_f}{64}\int_1^0 \left\{\left[17 + 10\ln\left(\frac{\mathrm{Re}}{2}\sqrt{c_f/\frac{2\big)\big]\mathrm{R_q^2} + 10\big(\mathrm{R_q^2} - 1\big)\ln\big(1-\mathrm{R_q}\big) - 10\mathrm{R_q}\big\}^2}{\mathrm{R_q}\left\{1 + \frac{\mathrm{Pr}}{\mathrm{Pr_t}}\left[\frac{1}{2.5}\mathrm{R_q}\,(1-\mathrm{R_q})\frac{\mathrm{Re}}{2}\sqrt{c_f/2} - 1\right]\right\}}}\right)\right]\right\}\mathrm{dR_q}. \tag{8}$$

The following variables are defined to simplify **Eq. 8**:

$$\begin{aligned} A &= 1.7 + \ln\left(\frac{\mathrm{Re}}{2}\sqrt{c_f/2}\right), \\ B &= 1 - \frac{\mathrm{Pr}}{\mathrm{Pr}_t}, \\ C &= \frac{\mathrm{Pr}}{\mathrm{Pr}_t}\,\frac{\mathrm{Re}}{5}\sqrt{c_f/2}. \end{aligned} \tag{9}$$

Equation 8 can be simplified by substituting **Eq. 9** into it and letting $x = 1 - R_q$:

$$\frac{1}{Nu} = -\frac{100}{64}c_f\int_1^0 \frac{\left[A(1-x)^2 + \left(x^2 - 2x\right)\ln x - (1-x)\right]^2}{(1-x)[B + Cx(1-x)]}dx. \tag{10}$$

Equation 10 is still a complex integral equation, even after simplification. Therefore, integration by parts is needed. Notice that the denominator has a primitive function as:

$$\begin{aligned} &\int_1^0 \frac{1}{(1-x)[B+Cx(1-x)]}dx = \frac{4B + C + \sqrt{C(4B+C)}}{2B(4B+C)}\ln\left[\sqrt{C(4B+C)}\right. \\ &\left. + C(1-2x)\right] + \frac{4B + C - \sqrt{C(4B+C)}}{2B(4B+C)}\ln\left[\sqrt{C(4B+C)} - C(1-2x)\right] + \frac{\ln(1-x)}{B}. \end{aligned} \tag{11}$$

The following variables are defined to simplify **Eq. 11**:

$$\begin{aligned} D_1 &= \frac{4B + C + \sqrt{C(4B+C)}}{2B(4B+C)}, \\ D_2 &= \frac{4B + C - \sqrt{C(4B+C)}}{2B(4B+C)}, \\ E_1 &= \sqrt{C(4B+C)} + C, \\ E_2 &= \sqrt{C(4B+C)} - C. \end{aligned} \tag{12}$$

Substituting these variables into **Eq. 11** produces:

$$\int_1^0 \frac{1}{(1-x)[B+Cx(1-x)]}dx = D_1\ln(E_1-2Cx) + D_2\ln(E_2+2Cx) + \frac{\ln(1-x)}{B}. \tag{13}$$

Expanding **Eq. 10** using integration by parts, the following equation can be obtained:

$$\begin{aligned}\frac{1}{Nu} = &-\frac{100}{64}c_f\{(A-1)^2[D_1\ln(E_1)+D_2\ln(E_2)] \\ &-\int_1^0\left\{\sum_{n=0}^{3}\varphi_{1n}(A)\left[D_1x^n\ln(E_1-2Cx)+D_2x^n\ln(E_2+2Cx)\right.\right. \\ &\left.+\frac{1}{B}x^n\ln(1-x)\right]+\sum_{n=0}^{3}\varphi_{2n}(A)\left[D_1x^n\ln x\ln(E_1-2Cx)\right. \\ &\left.+D_2x^n\ln x\ln(E_2+2Cx)+\frac{1}{B}x^n\ln x\ln(1-x)\right] \\ &+\sum_{n=1}^{3}\varphi_{3n}(A)\left[D_1x^n(\ln x)^2\ln(E_1-2Cx)+D_2x^n(\ln x)^2\right. \\ &\left.\left.\ln(E_2+2Cx)+\frac{1}{B}x^n(\ln x)^2\ln(1-x)\right]\right\}dx\Big\}.\end{aligned} \tag{14}$$

where $\varphi(A)$ is the polynomial of coefficient A given by:

$$\varphi_{1n}(A)=\begin{cases}A(4A+2) & n=3\\ (1-3A)(4A+2) & n=2\\ (3A-2)(4A+2) & n=1\\ (1-A)(4A+2) & n=0\end{cases},$$

$$\varphi_{2n}(A)=\begin{cases}(8A+2) & n=3\\ -(24A+2) & n=2\\ (20A-4) & n=1\\ 4(1-A) & n=0\end{cases},$$

$$\varphi_{3n}(A)=\begin{cases}4 & n=3\\ -12 & n=2\\ 8 & n=1\end{cases}$$

Equation 14 consists of many integrand functions in the form of simple multiple functions, and these can thus be integrated independently. The results of **Eq. 14** are then:

$$Nu=\frac{0.64BF}{c_f\left\{\begin{array}{l}\left[(-3A^2+4A)\left(\frac{B}{C}\right)^2-(A-1)^2\left(\frac{B}{C}\right)\right]\ln\left(\frac{E_2}{E_1}\right)+\left(-\frac{3}{2}A^2+\frac{11}{2}A-\frac{23}{4}\right)\left(\frac{B}{C}\right)F+2.4F\\ +\left[-2\left(\frac{B}{C}\right)+(-6A+4)\left(\frac{B}{C}\right)^2\right]di\log\left(\frac{E_2}{E_1}\right)\\ +\left[-A\left(\frac{E_2}{2C}\right)^5+(-4A+1)\left(\frac{E_2}{2C}\right)^4+(-5A+3)\left(\frac{E_2}{2C}\right)^3+(-2A+2)\left(\frac{E_2}{2C}\right)^2\right]\ln 2\left(\frac{E_2}{E_1}\right)\\ +\left[2\left(\frac{E_1}{2C}\right)^5-8\left(\frac{E_1}{2C}\right)^4+8\left(\frac{E_1}{2C}\right)^3\right]\ln\left(\frac{E_1}{2C}\right)di\log\left(\frac{E_2}{E_1}\right)\\ +\left[2\left(\frac{E_2}{2C}\right)^5+8\left(\frac{E_2}{2C}\right)^4+8\left(\frac{E_2}{2C}\right)^3\right]\ln\left(\frac{E_2}{2C}\right)di\log\left(\frac{E_1}{E_2}\right)\\ +\left[2\left(\frac{E_2}{2C}\right)^5+8\left(\frac{E_2}{2C}\right)^4+8\left(\frac{E_2}{2C}\right)^3\right]\left[\frac{1}{2}\left(\frac{2C}{E_1}\right)^2\ln^2\left(\frac{E_1}{2C}\right)-\frac{1}{2}\ln^2\left(\frac{E_1}{2C}\right)\ln\left(\frac{E_2}{E_1}\right)-\frac{2.404}{2}\right]\end{array}\right\}}, \tag{15}$$

where $F=\sqrt{1+\frac{4B}{C}}$. It should be pointed out that during the solving of $\int_1^0 x^n\ln^2 x\ln(E_2+2Cx)dx \quad n=4,3,2$ and $\int_1^0 x^n\ln^2 x\ln(E_1-2Cx)dx \quad n=4,3,2$ by integrating by parts, two non-integrable terms, $\int_{\frac{2C}{E_2}}^0\frac{1}{t}\ln t\ln(1+t)$ and $\int_{\frac{2C}{E_1}}^0\frac{1}{t}\ln t\ln(1-t)$, respectively, are generated, where t is the variable substitution function defined by $t=\frac{2C}{E}x$. The former can be neglected—although it will bring some deviations in the region of low Péclet numbers—and the latter is approximated by the function:

$$\int_{\frac{2C}{E_1}}^0\frac{1}{t}\ln t\ln(1-t)dt=\frac{1}{2}\left(\frac{2C}{E_1}\right)^2\ln^2\left(\frac{E_1}{2C}\right)-\frac{1}{2}\ln^2\left(\frac{E_1}{2C}\right)\ln\left(1-\frac{2C}{E_1}\right)-1.202. \tag{16}$$

The deviations between **Eq. 16** and $\int_{\frac{2C}{E_1}}^0\frac{1}{t}\ln t\ln(1-t)$ are lower than 0.3% in the very large Péclet-number region from 100 to 100,000.

The deviations between **Eq. 15** and the exact integral value of **Eq. 1** are less than 0.4% for a very large region of Péclet numbers between 500 and 10,000. For Péclet numbers less than 500, deviations increase significantly due to the neglect of the non-integrable term. However, the LLM-cooled reactor systems are unlikely to operate at such low Péclet numbers. Therefore, **Eq. 15** has sufficient accuracy for practical applications.

Equation 15 can be further simplified by neglecting some terms in the denominator that only impact the results in the low Péclet-number region. This will lead to a further increase in deviations in the low Péclet-number region, but it will have little impact in the high Péclet-number region. The deviation after neglecting some terms is lower than 5.4% for Péclet numbers greater than 1,000, which is still acceptable for the actual application.

Moreover, if we multiply the numerator and the denominator by F and divide by B/C after neglecting some terms in the denominator, **Eq. 15** becomes:

$$Nu=\frac{0.64(4B+C)}{c_f\left\{\begin{array}{l}\left[(-3A^2+4A)\left(\frac{B}{C}\right)-(A-1)^2\right]F\ln\left(\frac{E2}{E1}\right)\\ +\left(-\frac{3}{2}A^2+\frac{11}{2}A-\frac{23}{4}\right)\left(1+\frac{4B}{C}\right)\\ +\left[-2+(-6A+4)\left(\frac{B}{C}\right)\right]Fdi\log\left(\frac{E2}{E1}\right)\end{array}\right\}}. \tag{17}$$

According to **Eq. 9**, coefficient B is a function of the Prandtl and turbulent Prandtl numbers, both of which are constant. The coefficient C is a function of the Péclet number. Therefore, the numerator of **Eq. 17** is a sum of a constant term and a function of the Péclet number, which has the same structure as Lyon's equation.

However, the denominator is a multiple function of c_f and a complex multinomial, and the latter has the form of a power function of the Péclet number:

$$\left\{\begin{array}{l}\left[\left(-3A^2+4A\right)\left(\frac{B}{C}\right)-(A-1)^2\right]F\ln\left(\frac{E2}{E1}\right)\\ +\left(-\frac{3}{2}A^2+\frac{11}{2}A-\frac{23}{4}\right)\left(1+\frac{4B}{C}\right)\\ +\left[-2+(-6A+4)\left(\frac{B}{C}\right)\right]Fdi\log\left(\frac{E2}{E1}\right)\end{array}\right\}=\alpha Pe^{\beta}, \quad (18)$$

where α and β are coefficients determined by the turbulent Prandtl number and the molecular Prandtl number, and the friction coefficient of turbulent flow in a circular tube is given by $c_f=\frac{f}{4}=\frac{0.316}{4\mathrm{Re}^{0.25}}$. **Equation 17** has a much simpler form:

$$Nu=\frac{10.24}{0.316\mathrm{Pr}^{0.25}\alpha Pe^{(\beta-0.25)}}+\frac{2.56\sqrt{0.156}}{3.16\mathrm{Pr}^{0.125}\mathrm{Pr}_t\alpha}Pe^{(1.125-\beta)}. \quad (19)$$

For LBE, the typical value of the molecular Prandtl number is 0.0147 (IAEA, 2002; NEA, 2015). The value of the turbulent Prandtl number is the integral mean value of Cheng and Tak's relation, which is 2.5. Thus, the theoretical heat-transfer equation for LBE flowing through a circular tube with a uniform heat-flux boundary is:

$$Nu\,(LBE)=\frac{10.287}{Pe^{0.1175}}+\frac{0.0599}{2.5}Pe^{0.7575}. \quad (20)$$

The structure of **Eq. 20** is similar to Lyon's relation and most of the existing relations, but it has a significant difference in that the first (conductive) term, which has a constant value in Lyon's relation, also has a relationship with the Péclet number. Moreover, the conductive term in **Eq. 20** is inversely proportional to the power function of the Péclet number, which means that this value will decrease as the Péclet number increases. The reason for this is that as the Péclet number increases, the turbulent intensity strengthens, and the heat transfer by eddy disturbances increases, which decreases the temperature gradient and thus leads to a decrease in heat transfer by molecular conduction.

RESULTS AND ANALYSIS OF THE IMPACTS OF ROUGHNESS

In this section, the theoretical heat-transfer relation of LBE is first compared with experimental data from published literature and the NCCL facility, and then the impacts of roughness are analyzed to explain the differences from the NCCL data.

Validation of the Theoretical Relation

Johnson et al. (1953) produced the first published experimental data on heat transfer in LBE flowing in a tube. Ibragimov et al. (1960) reported experimental data from LBE and Pb seven years after Johnson et al.'s publication, and they proposed an empirical relation based on the structure of Lyon's relation:

$$Nu=4.5+0.014Pe^{0.8} \quad \text{for } 250<Pe<9000. \quad (21)$$

NEA (2015) proposed another relation based on the experimental data of Ibragimov et al. This relation is thus similar, and only the difference is the coefficient of convective term:

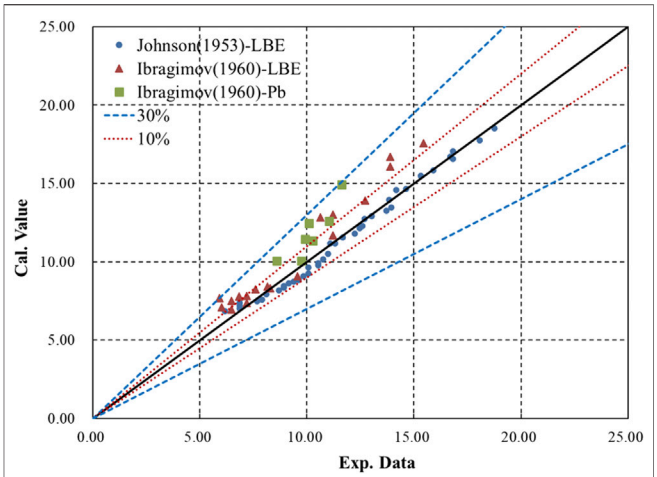

FIGURE 5 | Deviation of **Eq. 20** from experimental LLM data in the literature.

$$Nu=4.5+0.018Pe^{0.8} \quad \text{for } 90<Pe<7000. \quad (22)$$

Stromquist and Boarts (1953) gave a relation similar to Kirillov and Ushakov's, with a difference only in the conductive term:

$$Nu=3.6+0.018Pe^{0.8} \quad \text{for } 88<Pe<4000. \quad (23)$$

Cheng and Tak (2006) evaluated the existing relations mainly based on Johnson et al.'s data and found that Kirillov and Ushakov's relation fitted Johnson et al.'s data well in the low Péclet-number region, while Stromquist and Boarts' relation fitted the data in the high Péclet-number region. Both the relations have the same convective term. Therefore, Cheng and Tak indicated that the conductive term should be a function of the Péclet number for LLM, and they proposed the relation:

$$Nu=M+0.018Pe^{0.8}, \quad (24)$$

$$M=\left\{\begin{array}{ll}4.5 & Pe\le 1000\\ 5.4-9\times10^{-4}Pe & 1000<Pe\le 2000\\ 3.6 & 2000<Pe\end{array}\right. . \quad (24)$$

The theoretical relation given in **Eq. 20** was compared with the literature data as well as the other four relations given in **Eqs. 21–24**. **Figure 5** shows the deviation of **Eq. 20** from the experimental data in the literature for LLMs. It can be seen that **Eq. 20** fits quite well with Johnson et al.'s data. The maximum deviations from all of the literature experimental data (Johnson et al., 1953; Ibragimov et al., 1960) and Johnson et al. (1953) data are 30 and 10.9%, respectively. Moreover, **Eq. 20** shows better conformity with Johnson et al.'s data for high Péclet numbers. The maximum deviation decreases to 5% when the Péclet number is greater than 1,500. The deviation at low Péclet numbers is due to the terms ignored in the derivation of the theoretical relation, as noted above.

Figure 6 shows the deviations of **Eqs. 21–24** from the experimental data in the literature. Ibragimov et al.'s

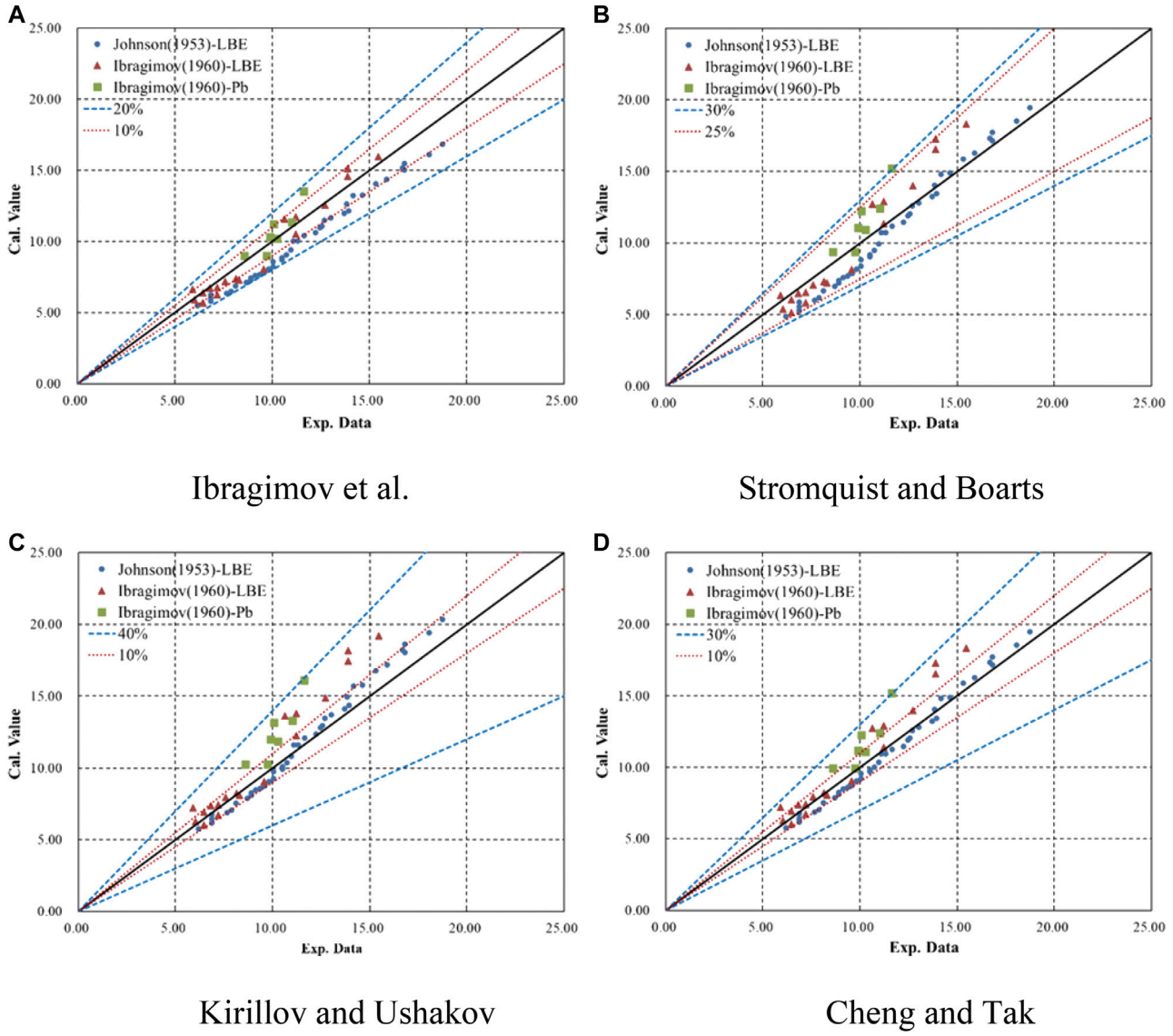

FIGURE 6 | Deviations of other relations from experimental LLM data in the literature.

relation fits his experimental data well, with a maximum deviation of 16.3%, but it underestimates all of Johnson et al.'s data. Stromquist and Boarts' relation fits Johnson et al.'s data very well for high Péclet numbers, while Kirillov and Ushakov's relation fits Johnson et al.'s data for lower Péclet numbers better than Stromquist and Boarts'. As a combination of Stromquist and Boarts' and Kirillov and Ushakov's relations, Cheng and Tak's relation fits Johnson et al.'s data quite well for all Péclet numbers, with a maximum deviation of 10.5%.

Moreover, it can be seen in **Figure 3** that relations that take the conductive term as constant will lead to either an underestimation at low Péclet numbers or an overestimation at high Péclet numbers. If one takes the conductive term as a function decreasing with Péclet number, as with **Eq. 20** and Cheng and Tak's relation, good consistency with experimental data can be obtained across the full range of Péclet numbers.

The relations were then evaluated by the root-mean-square error (RMSE) method using the experimental data form the literature, and the results are shown in **Table 2**. It can be seen that the theoretical relation given in **Eq. 20** has the best consistency with the experimental data.

Figure 7 shows a comparison of **Eq. 20** with the NCCL experimental data and the literature experimental data. In general, the results from **Eq. 20** do not fall far from the range of the NCCL data. However, the NCCL data are overestimated at lower Péclet numbers and underestimated at higher Péclet numbers. The literature experimental data have the same trend as the NCCL data; however, for most data points, the deviations are still lower than 15%.

TABLE 2 | RMSE results of relations based on literature data.

RMSE of	Eq. 20	Ibragimov	Stromquist	Kirillov	Cheng
All data	1.01	1.27	1.35	1.49	1.09
Johnson's data	0.43	1.49	1.13	0.87	0.61

As noted earlier, a possible reason for the above trend is that the pipe wall is not smooth after testing and operation of the NCCL facility, because it lacks an oxygen-control system. The results of the flow experiments in a 20-mm-diameter pipe after heat-transfer experiments show a significantly higher friction factor at the wall than that for a smooth pipe, as shown in **Figure 4**. Therefore, the impacts of roughness on the flow and heat-transfer behavior for LLMs in a circular tube were analyzed, and this is elaborated in the next section.

Analysis of the Impacts of Roughness.

For a turbulent flow, the roughness of the walls mainly impacts the friction factor at the wall and the velocity distribution. The friction factor for turbulent flow in a rough pipe can be given by an empirical relation based on Moody (1944) curve:

$$f = 0.0055\left[1 + \left(20000\frac{h}{d} + \frac{10^6}{\mathrm{Re}}\right)^{1/3}\right], \tag{25}$$

where h is the absolute roughness and $\frac{h}{d}$ is the relative roughness. The velocity distribution function for turbulent flow in a rough pipe is given by Nikuradse as:

$$\frac{u}{u^*} = 5.5 + 2.5\ln\left(y\frac{u^*}{v}\right) + N,$$

$$N = \begin{cases} 0 \quad , \quad 0 \le \log\left(\frac{u_* h}{v}\right) < 0.55 \\ 1.09 - 2.25\log\left(\frac{u_* h}{v}\right) \quad , \quad 0.55 \le \log\left(\frac{u_* h}{v}\right) < 0.85 \\ 4.08 - 5.75\log\left(\frac{u_* h}{v}\right) \quad , \quad 0.85 \le \log\left(\frac{u_* h}{v}\right) < 1.15 \\ 6.0 - 7.37\log\left(\frac{u_* h}{v}\right) \quad , \quad 1.15 \le \log\left(\frac{u_* h}{v}\right) < 1.83 \\ 2.98 - 5.75\log\left(\frac{u_* h}{v}\right) \quad , \quad 1.83 \le \log\left(\frac{u_* h}{v}\right) \end{cases} \tag{26}$$

It is easy to find that the velocity distribution function for a rough pipe is a summation of the velocity distribution functions for a smooth pipe and a function N with absolute roughness. The value of N is independent of radius, which means that the gradient of velocity in the radial direction for turbulent flow in a rough pipe is the same as that in a smooth pipe.

As discussed above, to solve the heat-transfer integral equation (**Eq. 1**), three variables should first be determined: the dimensionless velocity, the eddy diffusivity of momentum, and the turbulent Prandtl number.

Substituting **Eq. 26** into **Eq. 3**, the dimensionless velocity for LLM flow in a rough pipe is:

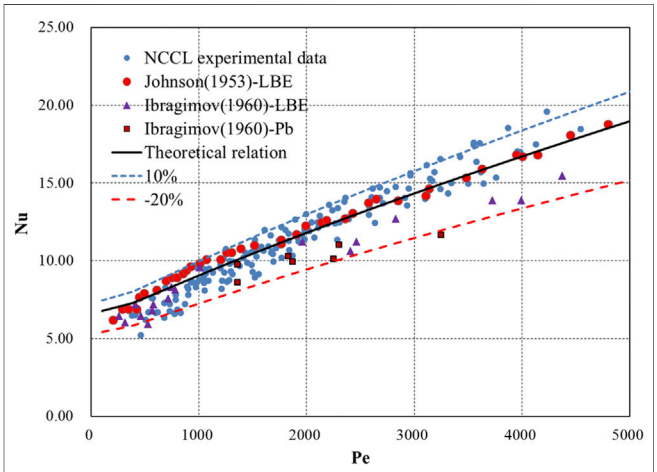

FIGURE 7 | Comparison of **Eq. 20** with NCCL and literature experimental data.

$$V = \sqrt{c_f/2}\,\frac{u}{u^*} = \sqrt{c_f/2}\left\{5.5 + 2.5\ln\left[(r_w - r)\frac{u^*}{v}\right] + N\right\}$$
$$= \sqrt{c_f/2}\left\{5.5 + N + 2.5\ln\left[(1-R)\frac{\mathrm{Re}}{2}\sqrt{c_f/2}\right]\right\}, \tag{27}$$

where the coefficient of friction is related to the friction factor as $c_f = \frac{f}{4}$.

For the eddy diffusivity of momentum, because the gradient of velocity is the same as that in a smooth pipe, **Eq. 7** is also suitable for LLM flow in a rough pipe; roughness only impacts the friction coefficient. Furthermore, the roughness has no impact on the turbulent Prandtl number, according to Cheng and Tak (2006) turbulent-Prandtl-number model. The model indicates that the average turbulent Prandtl number is only dependent on to the Péclet number. Therefore, by substituting **Eqs. 27**, **7** into **Eq. 1**, **Eq. 8** becomes:

$$\frac{1}{Nu} = -\frac{c_f}{64}\int_1^0 \left\{\left[4(5.5+N) - 5 + 10\ln\left(\frac{\mathrm{Re}}{2}\sqrt{c_f/\frac{2)\right]\mathrm{R_q^2} + 10\left(\mathrm{R_q^2} - 1\right)\ln\left(1-\mathrm{R_q}\right) - 10\mathrm{R_q}\right\}^2}{\mathrm{R_q}\left\{1 + \frac{\mathrm{Pr}}{\mathrm{Pr_t}}\left[\frac{1}{2.5}\mathrm{R_q}\left(1-\mathrm{R_q}\right)\frac{\mathrm{Re}}{2}\sqrt{\mathrm{c_f}/2} - 1\right]\right\}}}\right)\mathrm{dR_q}. \tag{28}$$

This only leads to a difference in coefficient A, and the other coefficients are the same as those defined in **Eqs. 9**, **12**, **15**:

$$A = \frac{4(5.5+N) - 5}{10} + \ln\left(\frac{\mathrm{Re}}{2}\sqrt{c_f/2}\right). \tag{29}$$

TABLE 3 | Coefficients of **Eq. 30** for different relative roughnesses.

h/d	a	b	c	d
0.002	12.8773	0.1809	0.0385	0.8115
0.003	13.7931	0.1877	0.0425	0.8069
0.004	14.6453	0.1935	0.0463	0.8023
0.005	15.4683	0.1987	0.0500	0.7978
0.006	16.2025	0.2030	0.0534	0.7940
0.008	17.5103	0.2100	0.0597	0.7877

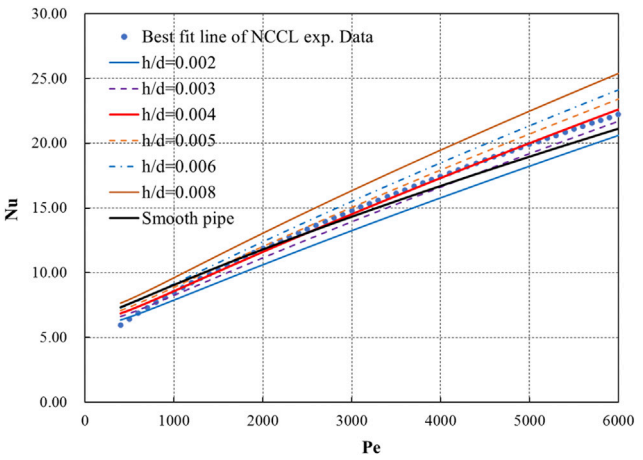

FIGURE 8 | Results of **Eq. 30** for different relative roughnesses.

Therefore, **Eq. 17** is still suitable for predicting heat transfer for an LLM flowing in a rough pipe by changing the coefficient *A* to **Eq. 29** and using the friction coefficient given by **Eq. 25**. The simplified equation used for application then has the same structure as **Eq. 20**:

$$Nu = \frac{a}{Pe^b} + \frac{c}{2.5} Pe^d. \tag{30}$$

The coefficients of **Eq. 30** are determined by the relative roughness, which influences the friction coefficient and the velocity-related coefficient A, and the molecular Prandtl number. **Table 3** gives the coefficients for different relative roughnesses. **Figure 8** shows a comparison of the results of **Eqs. 30**, **20** for a smooth pipe and the best-fit line of the NCCL experimental data.

The results from **Eq. 30** are in general lower than or near the results from **Eq. 20** at low Péclet numbers, but they increase faster than the latter as the Péclet number increases. For turbulent flow, roughness has two opposite effects on heat transfer. First, it can enhance the turbulence intensity, which is beneficial to enhancing convective heat transfer. Second, it destroys the bottom layer of laminar flow, thus weakening the influence of conductive heat transfer, as shown in **Figure 9**. For liquid metals, conduction has a significant effect on heat transfer. Therefore, at low Péclet numbers, due to the low turbulence intensity, the adverse effect caused by the weakening of heat conduction is greater, resulting in the overall deterioration of heat transfer. As the Péclet

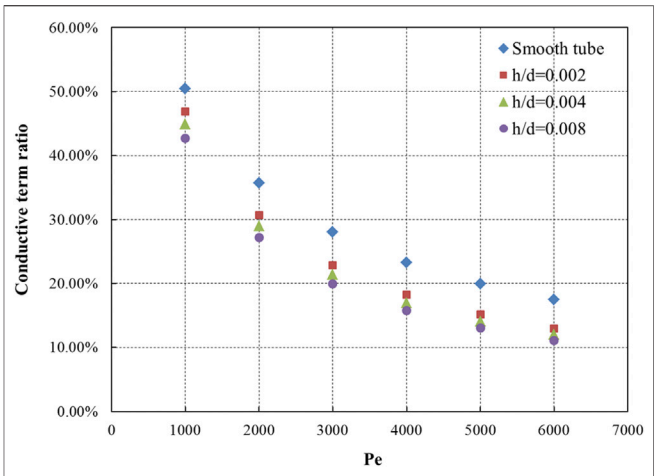

FIGURE 9 | Ratios of the conductive term for different relative roughnesses.

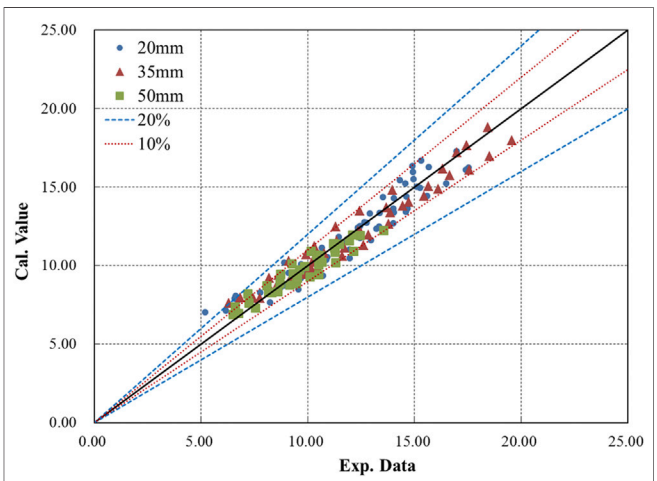

FIGURE 10 | Deviation of **Eq. 30** with a relative roughness of 0.004 from the NCCL experimental data.

number increases, turbulence gradually strengthens, and convective heat transfer intensifies, which leads to the improvement of heat transfer.

Furthermore, lower relative roughnesses have a smaller impact zone, which means that the roughness will mainly impact the bottom layer of laminar flow. Impacts on the turbulence intensity in the area of the turbulent core will only appear when the Reynolds number is large enough. Something else that can be seen in **Figure 8** is that the results of **Eq. 30** for a relative roughness of 0.004 are very close to the best-fit line of the NCCL experimental data. **Figure 10** shows the deviation of **Eq. 30** with a relative roughness of 0.004 from the NCCL experimental data.

The trends in the predicted results for the NCCL experimental data improve significantly when considering the wall roughness. The results for Péclet numbers lower

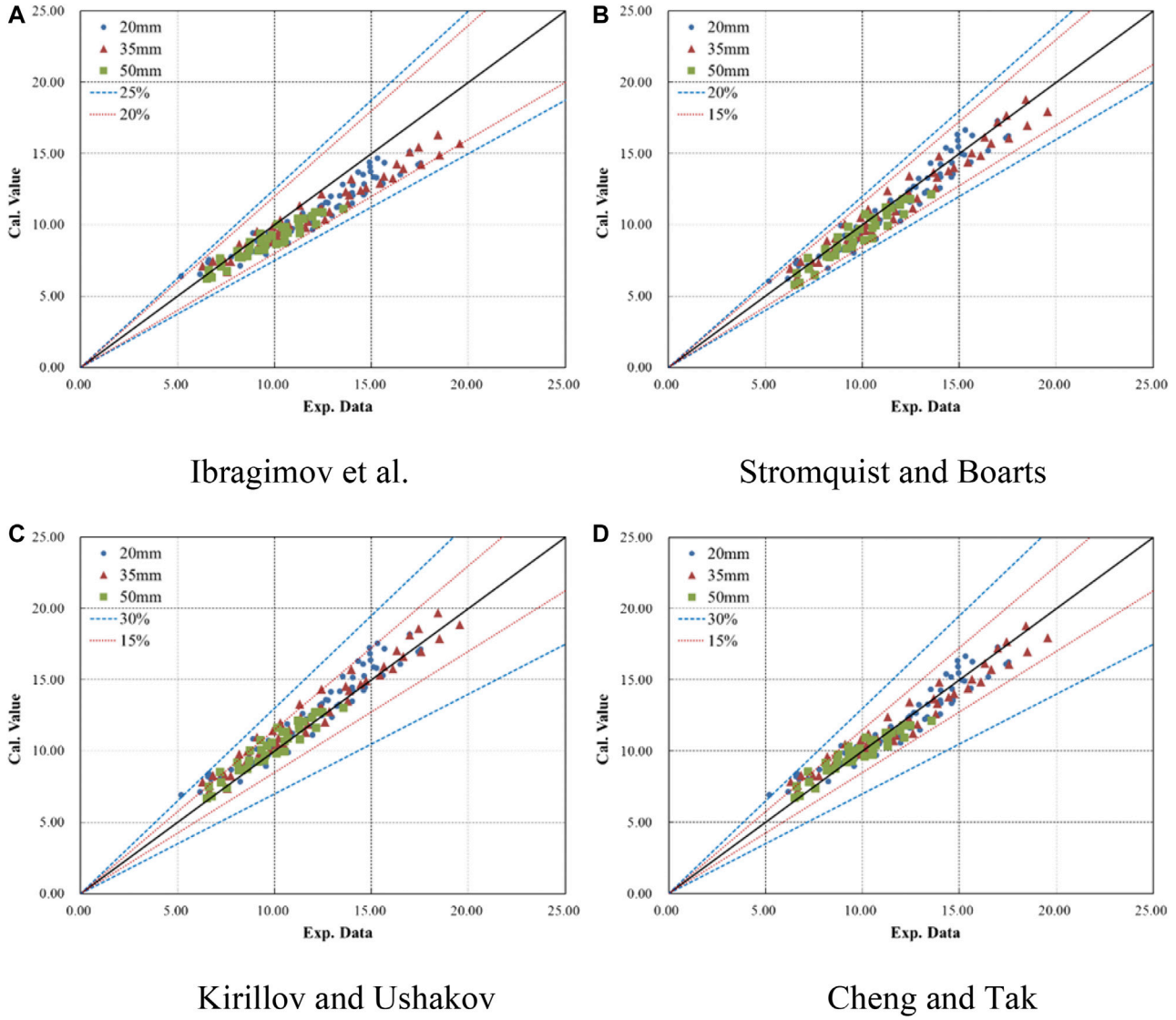

FIGURE 11 | Deviations of other relations from the NCCL experimental data.

than 500 are still slightly overestimated due to the neglect of some terms, as with **Eq. 20**. However, when the Péclet number is greater than 500, the predicted results fit very well with the experimental data, and most results remain within a deviation belt of ±10%. The maximum deviation for Péclet numbers greater than 500 is 21.55%, and this decreases to 14.05% for Péclet numbers greater than 1,000. **Figure 11** shows the deviations of the other relations from the NCCL experimental data, although these relations were not developed for LLM flow in a rough pipe.

Ibragimov et al.'s relation underestimates most experimental data, and the deviation increases as the Péclet number increases, while Kirillov and Ushakov's relation overestimates most data. Stromquist and Boarts' relation fits the NCCL experimental data very well, because it underestimates the literature data at a low Péclet numbers, which seems proper for a rough pipe. Cheng and Tak's relation fits the experimental data well at high Péclet numbers but overestimates at low Péclet numbers, as with Kirillov and Ushakov's relation.

Figure 12 shows the RMSE results for each relation when compared with the NCCL experimental data. **Eq. 30** with a relative roughness of 0.004 has the lowest RMSE result of all the relations for heat transfer of an LLM flowing in a pipe. Stromquist and Boarts' relation also gives good results, but the error increases when the Péclet number is greater than 1,000.

In conclusion, the theoretical relation for heat transfer of an LLM flowing in a rough pipe reveals the impacts of roughness, which can explain the deviation between the NCCL experimental data and experimental data in the literature. The results of **Eq. 30** with a relative roughness of 0.004 show good consistency with the NCCL data.

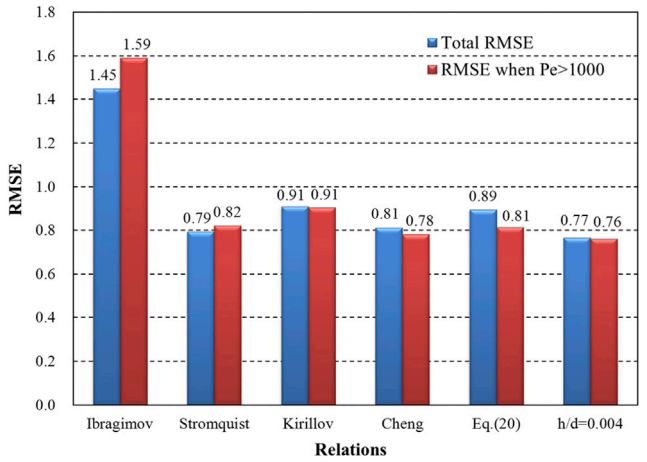

FIGURE 12 | RMSE values for the various relations when compared with the NCCL experimental data.

CONCLUSION

An experimental study of the flow and heat transfer of LBE flowing in a circular tube under uniform heat-flux boundary conditions was carried out at the NCCL facility. A total of 19 cases with different conditions based on three pipes with different inner diameters were tested, and a total of 152 heat-transfer data points, covering a Péclet-number range from 380 to 4,600, were obtained. The heat-transfer results from the NCCL tests showed a different tendency from the experimental data in the literature: at low Péclet numbers the results were smaller, while they were higher at high Péclet numbers. The flow results from the NCCL tests showed a much higher friction factor than expected for a smooth pipe, which reflects the characteristics of a rough pipe. A theoretical study was therefore performed, and the resulting relation was validated using experimental data from the literature. The theoretical relation shows good agreement with the literature data, especially Johnson et al.'s data, and it has the best RMSE result when compared with the other four existing relations that have been developed or considered to be suitable for an LLM. The theoretical relation for an LLM flowing in a rough pipe was then established using the same methods while taking account of the impacts of roughness.

The main conclusions based on these experimental investigations and theoretical analyses are as follows.

1. The heat-transfer results of the NCCL experiments under various conditions indicate that the inner diameter of the pipes, the inlet temperature, the heat flux at the wall, and the physical properties that have strong relations with temperature, have little impact on the Nu–Pe relation of an LLM.
2. The theoretical relation reveals that the heat transfer of an LLM consists of a conductive term and a convective term. The conductive term, which has for a long time generally been considered as a constant, has now been demonstrated to also have a relationship with the Péclet number.
3. Moreover, the value of the conductive term decreases slightly from 4.57 to 3.70 as the Péclet number increases from 1,000 to 6,000, while the ratio of the conductive term to the total heat transfer decreases dramatically from 50.45 to 17.51% due to the rapid increase of the convective term.
4. The roughness has two competing impacts on the heat-transfer behavior of an LLM flowing through a pipe. On the one hand, it reduces conductive heat transfer due to destruction of the laminar sub-layer; on the other hand, it increases convective heat transfer due to the enhancement of turbulent flow. Therefore, heat transfer increases more rapidly as the relative roughness or Péclet number increase. A relative roughness $h/d \geq 0.006$ improves the heat transfer, while $h/d \leq 0.002$ will cause heat transfer to be worse than that in a smooth pipe in the typical Péclet-number range for an LLM. For relative roughness $0.02 < h/d < 0.006$, systems operating at higher Péclet numbers are beneficial for heat transfer.

The theoretical relation for a rough pipe with a relative roughness of 0.004 provides the best fit for the heat-transfer results of the NCCL experiments. However, the relative roughness derived by the relation from the Moody curve, which is used for water, produces friction-factor results from the NCCL experiments that is greater than 0.004. There may be several reasons for this, including the uncertainty of the relevant instruments, differences in the flow characteristics between an LLM and water, and the simplification of the object during theoretical analysis. Therefore, further research on the flow characteristics of LLMs is needed to resolve this question.

DATA AVAILABILITY STATEMENT

The original contributions presented in the study are included in the article/Supplementary Material, further inquiries can be directed to the corresponding author.

AUTHOR CONTRIBUTIONS

YS: Conceptualization, Methodology, Validation, Formal analysis, Investigation SP: Conceptualization, Resources, Supervision MY: Conceptualization, Methodology, Project administration YZ: Conceptualization, Methodology, Resources JD: Methodology, Resources, Supervision HY: Writing-Reviewing and Editing DH: Writing-Reviewing and Editing ZL: Writing-Reviewing and Editing.

FUNDING

The authors of this paper appreciate the financial support from: The National Key Research and Development Program of China (No. 2019YFB1901300) National Natural Science Foundation of China (Series number 11705189)

REFERENCES

Brown, H. E., Amstead, B. H., and Short, B. E. (1957). Temperature and velocity distribution and transfer of heat in a liquid metal. *Trans. Am. Soc. Mech. Eng.* 79, 279–285.

Cheng, X., and Tak, N. (2006). Investigation on turbulent heat transfer to lead–bismuth eutectic flows in circular tubes for nuclear applications. *Nucl. Eng. Des.* 236 (4), 385–393. doi:10.1016/j.nucengdes.2005.09.006

Dwyer, O. E. (1976). Liquid metal heat transfer. *Sodium-NaK Engineering Handbook* 2, 73–191.

IAEA (2002). *Comparative assessment of thermophysical and thermohydraulic characteristics of lead, lead-bismuth and sodium coolants for fast reactors*. Vienna, Austria: IAEA-TECDOC-1289.

Ibragimov, M., Subbotin, V. I., and Ushakov, P. A. (1960). Investigation of heat transfer in the turbulent flow of liquid metals in tubes. *Atomnaya Energiya* 8 (1), 54–56.

Isakoff, S. E. (1951). *Heat and momentum transfer in tuebulent flow of mercury*, Oak Ridge, TN: United States Atomic Energy Commission Technical Information Service.

Johnson, H. A., Hartnett, J. P., and Clabaugh, W. J. (1953). Heat transfer to molten lead–bismuth eutectic in turbulent pipe flow. *J. Heat Transfer* 75, 1191–1198.

Kirillov, P., and Ushakov, P. A. (2001). Heat transfer to liquid metals: specific features, methods of investigation, and main relationships. *Therm. Eng.* 48 (1), 50–59.

Lyon, R. N. (1949). *Forced convection heat transfer theory and experiments with liquid metals*. Oak Ridge, TN: Oak Ridge National Laboratory.

Martinelli, R. C. (1947). Heat transfer to molten metals. *Trans. Am. Soc. Mech. Eng.* 69, 947–959.

Moody, F. F. (1944). Friction factors for pipe flow. *Transaction ASME* 66, 671.

NEA (2015). *Handbook on lead–bismuth eutectic alloy and lead properties, materials compatibility, thermal hydraulics and technologies*. Paris, France: OECD.

Nikuradse, J. (1950). *Laws of flow in rough pipes*. Washington, DC: National Advisory Committee for Aeronautics.

Pacio, J., Morocco, L., and Wetzel, T. (2015). Review of data and correlations for turbulent forced convective heat transfer of liquid metals in pipes. *Heat Mass Tran.* 51 (2), 153–164. doi:10.1007/s00231-014-1392-3

Reed, C. B. (1987). "Convective heat transfer in liquid metals," in *Chapter 9 from handbook of single-phase convective heat transfer*. Editors S. Kakac, R. Shah, and W. Aung (Hoboken, NJ: John Wiley & Sons).

Stromquist, W., and Boarts, R. (1953). *Effect of wetting on heat transfer characteristics of liquid metals*, Oak Ridge, TN: United States Atomic Energy Commission Technical Information Service.

Zhang, Y., Wang, C., Cai, R., Lan, Z., Shen, Y., Zhang, D., et al. (2020a). Experimental investigation on flow and heat transfer characteristics of lead-bismuth eutectic in circular tubes. *Appl. Therm. Eng.* 180, 115820. doi:10.1016/j.applthermaleng.2020.115820

Zhang, Y., Wang, C., Lan, Z., Wei, S., Chen, R., Tian, W., et al. (2020b). Review of thermal-hydraulic issues and studies of lead-based fast reactors. *Renew. Sustain. Energy Rev.* 120, 109625. doi:10.1016/j.rser.2019.109625

Zheng, J., Chen, Z., Zhao, P., and Chen, H. (2016). Study on flow similarity laws between water and liquid lead-bismuth under natural circulation. *Nucl. Power Eng.* 37, 31–33. doi:10.13832/j.jnpe.2016.03.0031

Conflict of Interest: The authors declare that the research was conducted in the absence of any commercial or financial relationships that could be construed as a potential conflict of interest.

NOMENCLATURE

Nu Nusselt number

Pe Péclet number

Pr Prandtl number

$\mathbf{Pr}_t$ turbulent Prandtl number

Re Reynolds number

u velocity

u_m mean velocity

$u^\star$ shear velocity

T temperature

P pressure

f friction factor

c_f friction coefficient

z axial distance

r radius

r_w tube inside radius

y distance from the wall

R radius ratio

R_q variables in successive integrations

V velocity ratio

h absolute roughness

ρ density

υ kinematic viscosity

τ shear stress

τ_w shear stress at the wall

ε_M eddy diffusivity of momentum

frontiers in Energy Research

ORIGINAL RESEARCH
published: 19 March 2021
doi: 10.3389/fenrg.2021.651339

Finite-Element Simulation of Residual Stresses During the Processing of Lumped Burnable Absorber Fuel

*Qusai Mistarihi and Ho Jin Ryu**

Department of Nuclear and Quantum Engineering, KAIST, Daejeon, South Korea

UO_2–Gd_2O_3 fuel is mostly used as a burnable absorber fuel in the form of a homogenous mixture of Gd_2O_3 and UO_2. More effective reactivity control can be achieved by lumping Gd_2O_3 within the UO_2 because this enhances the spatial self-shielding factor of the burnable absorber fuel. The fabrication of lumped burnable absorber fuel containing lumped Gd_2O_3 spherical particles or compacts has been experimentally demonstrated using yttrium-stabilized zirconia (YSZ) as a UO_2 fuel surrogate. Interfacial cracks or gaps forming under the interfacial stress that develops during the fabrication of the fuel can be eliminated by controlling the initial density of the lumped Gd_2O_3. In this study, this interfacial stress during the fabrication process was simulated using finite element methods. The effect of the size, shape, and initial density of the lumped Gd_2O_3 on the distribution and magnitude of the interfacial stress was investigated. The addition of Gd_2O_3 spherical particles resulted in a lower and more uniform interfacial stress distribution than the addition of cylindrical Gd_2O_3 compacts. The interfacial stress was increased with increasing Gd_2O_3 size and initial density. The calculated interfacial stress was compared with experimental results to estimate the threshold stress for crack development in a lumped burnable absorber fuel.

Keywords: finite element analysis, sintering stress, lumped burnable absorber fuel, interfacial cracks, shrinkage mismatch

OPEN ACCESS

Edited by:
Mingjun Wang,
Xi'an Jiaotong University, China

Reviewed by:
Wenzhong Zhou,
Sun Yat-sen University, China
Muhammad Saeed,
East China University of Technology, China
Rulei Sun,
Harbin Engineering University, China

***Correspondence:**
Ho Jin Ryu
hojinryu@kaist.ac.kr

Specialty section:
This article was submitted to Nuclear Energy, a section of the journal Frontiers in Energy Research

Received: *09 January 2021*
Accepted: *02 March 2021*
Published: *19 March 2021*

Citation:
Mistarihi Q and Ryu HJ (2021) Finite-Element Simulation of Residual Stresses During the Processing of Lumped Burnable Absorber Fuel. Front. Energy Res. 9:651339. doi: 10.3389/fenrg.2021.651339

INTRODUCTION

The potential use of Gd as a burnable absorber was recognized many years ago, considering its extremely high thermal neutron absorption cross-section. Gd is usually used in the form of Gd_2O_3 uniformly mixed with UO_2 as a fuel matrix. Owing to the relatively high thermal neutron absorption cross-section, few fuel rods must contain Gd_2O_3. However, the main limitations of Gd_2O_3 are the significant end-of-cycle penalty due to the existence of Gd isotopes with higher thermal neutron absorption cross-sections (i.e., ^{155}Gd and ^{157}Gd) (Grossbeck et al., 2001) and the degradation of the fuel's thermophysical properties (IAEA, 1995; Durazzo et al., 2013; Choe et al., 2016a). One possible way to overcome these limitations is changing the design of the UO_2–Gd_2O_3 mixed fuel.

Several burnable absorber fuel designs have been developed for small modular pressurized water reactors (SMPWRs) in order to eliminate the use of soluble boron and improve the reactor performance in terms of increasing the fuel cycle length while maintainig a flat power distribution.

Choe et al. (2016b) have proposed the use of a thin-layer of Zr-^{167}Er ($\sim$ 0.1–0.2 mm) on the inner side of the cladding as a new burnable absorber fuel design. A low burn-up swing of 548 pcm and cycle length of 26.5 months can be obtained for SMPWRs loaded with this burnable absorber fuel design. Another advanced burnable absorber fuel design integrated four azimuthally B_4C pads, with a thickness up to 90 μm and span up to 70^o, in the guide-thimble ring (Yahya and Kim, 2017a). This burnable absorber fuel design achieved a cycle length of about 53 months and a burnup swing between 634 and 800 pcm. Recently, a new design for burnable absorber fuel, called centrally shielded burnable absorber (CSBA), was developed (Nguyen et al., 2019). The CSBA comprises lumped Gd_2O_3 in the center of a UO_2 fuel pellet. The lumping of Gd_2O_3 results in a slower burn-out rate and longer suppression of the excess of reactivity due to spatial self-shielding effect (Galperin et al., 1986; Yahya and Kim, 2017b). It was found that the spherically lumped burnable absorber has a higher self-shielding factor than other lumped burnable absorber designs like cylindrical or slab due to the its higher volume-to-surface-area ratio (Fleming, 1982). Nguyen et al. (2019) studied the effect of the size and number of spherically lumped Gd_2O_3, and found that a more excess reactivity subression and flat power distribution can be obtained by increasing the Gd_2O_3 sphere radius from 1 mm to 1.3 mm or the number of Gd_2O_3 sphere (radius = 1 mm) from 1 to 3. They found that a low burn-up swing ($\sim$1100 pcm), long cycle length ($\sim$37 months), and higher burnup ($\sim$30 GWd/tU) can be obtained for a small modular reactor loaded with one Gd_2O_3 sphere (radius = 1.69 mm) in the center, two Gd_2O_3 spheres (radius = 1.26 mm) in the intermediate region, three Gd_2O_3 spheres (radius = 0.7 mm) in the outer region (Nguyen et al., 2019). The fabrication of CSBA using yttria-stabilized zirconia (YSZ) as a surrogate for UO_2 and either lumped Gd_2O_3 pellets, spherical particles, or rods was recently demonstrated (Mistarihi et al., 2018).

One of the major challenges in CSBA fuel design is the formation of interfacial cracks that may form under the stress mismatch developed during the sintering or cooling processes. This may arise from mismatches in the densification and thermal expansion coefficients (TECs), as well as phase transformations, of the sintered materials (Sglavo and Bellettati, 2017). The existence of these interfacial cracks can increase the intensity of fuel cracking during reactor operation and eventually limit fuel performance. In our previous study (Mistarihi et al., 2018), we concluded that interfacial cracks were not formed in YSZ pellets containing lumped Gd_2O_3 because of the TEC mismatch or the phase transformation of Gd_2O_3. The TECs of YSZ and Gd_2O_3 are similar and interfacial cracks were absent from Gd_2O_3 mini-pellets pre-sintered at temperatures below the phase transformation temperature. Thus, interfacial cracks could be mainly attributed to the sintering stresses resulting from the shrinkage rate mismatch.

Several factors control the sintering stresses that develop during the processing of composites, including shrinkage rate mismatch, volume fraction, and the shape and size of inclusions (Davidge and Green, 1968). The results of our previous study (Mistarihi et al., 2018) showed that, in YSZ oxide pellets containing lumped Gd_2O_3 mini-pellets, interfacial cracks were formed only when using mini-pellets with high initial densities. However, no interfacial cracks were observed in the case of YSZ oxide pellets containing lumped Gd_2O_3 spherical particles with high initial densities. The fabricated Gd_2O_3 spherical particles and mini-pellets had similar relative densities, but they differed in size and shape. Therefore, the effect of the shape, size, and shrinkage rate of the lumped Gd_2O_3 on the formation of interfacial cracks during the manufacturing of YSZ oxide pellets containing lumped Gd_2O_3 is investigated in this study.

One method to investigate interfacial crack formation during the processing of composites is to determine the stress distribution. By determining the stress distribution, areas of high stress concentration can be located. These areas are important for the integrity of composites because failure, signified by the formation of interfacial cracks, begins in them (Agarwal, 1972). Several analytical studies based on the theory of elasticity have been performed to determine stress distributions in composites using simplified physical models such as spherical particles (Selsing, 1961) or fibers (Delale, 1988) distributed in infinite matrices. However, the behaviors of powder compacts during sintering are not elastic, and the relationship between the stress and deformation during the sintering process is complex. Nonetheless, the finite-element analysis (FEA) method allows the implementation of complex stress–deformation relationships and the analysis of complex geometries.

Because powder compacts exhibit viscoelastic behaviors, several phenomenological models have been developed to describe their behaviors during sintering. Riedel et al. (1993), using a simple 2D hexagonal grain structure with pores at the triple points, developed an isotropic linear viscous constitutive equation to describe sintering-dominated grain boundary diffusion. Olevsky (1998) developed a phenomenological model based on the continuum theory of sintering by determining the sintering parameters from the rheological behaviors of porous materials during sintering. This model was implemented in an FEA code (COMSOL) and used to study the sintering behavior of different powder compacts (Al_2O_3 and YSZ) processed by spark plasma sintering (Olevsky et al., 2012) and microwave sintering (Manière et al., 2017). In these studies (Olevsky et al., 2012; Manière et al., 2017), FEA was mostly used to predict the shrinkage rate and temperature distribution of the powders during sintering. Li et al. (2020) used the finite element software (ABAQUS) to study the stress distribution in the cladding of dispersed plate-type fuel as a function of irradiation time and temperatures by implementing nuclear fuel correlation as a subroutine.

In this study, the Olevsky model for sintering was implemented in the COMSOL Multiphysics code and used to understand the stress distribution formed during the manufacturing of YSZ oxide pellets containing lumped Gd_2O_3. In addition, the applicability of the CSBA to UO_2 was investigated, and the stress distribution in UO_2 containing lumped Gd_2O_3 was determined and compared with that of the YSZ-based pellets. The novelty of this study is to estimate the stress distribution and magnitude in the lumped burnable absorber fuel design during the fabrication process.

MATERIALS AND METHODS

Governing Equations

Thermal, mechanical (linear elastic and sintering), and densification models were coupled by the FEA method (COMOSOL Multiphysics 5.4 code) and used to study the temperature, stress, and density distributions during the manufacturing of YSZ or UO_2 oxide pellets containing either lumped Gd_2O_3 spheres or mini-pellets. The heat-transfer model applied to the entire pellet is expressed by the following equation:

$$\rho C_p \frac{\partial T}{\partial t} + \nabla.\left(-k\nabla T\right) = 0 \quad (1)$$

where ρ is the material density ($g.cm^{-3}$), C_p is the heat capacity ($J.kg^{-1}K^{-1}$), T is the temperature (K), t is the time (s), and k is the thermal conductivity of the material ($W.m^{-1}.K^{-1}$).

The Gd_2O_3 spherical particle or mini-pellet was assumed to exhibit pure elastic behavior, wherein the relationship between the stress and deformation is expressed by Hooke's law:

$$\sigma_{ij} = C\dot{\varepsilon}_{ij} \quad (2)$$

where σ_{ij} is the stress tensor ($N.m^{-2}$), $\dot{\varepsilon}_{ij}$ is the strain tensor (s^{-1}), and **C** is a fourth-order tensor that is a function of the shear modulus (*G*) and Young's modulus (*E*) of the material.

The YSZ and UO_2 powder compact was assumed to exhibit a non-linear viscous behavior expressed by Olevsky (1998) phenomenological model (Eqs 3–6) based on the continuum theory of sintering:

$$\sigma_{ij} = \frac{1}{A(T)}\left(\varphi\dot{\varepsilon}_{ij} + \left(\psi - \frac{1}{3}\varphi\right)\dot{e}\delta_{ij}\right) + S\delta_{ij} \quad (3)$$

$$A(T) = \frac{A}{T}e^{-\frac{Q}{RT}} \quad (4)$$

$$\dot{e} = \dot{\varepsilon}_x + \dot{\varepsilon}_y + \dot{\varepsilon}_z \quad (5)$$

$$\varphi = (1-P)^2, \psi = \frac{2}{3}\frac{(1-P)^3}{P}, S = \frac{3\alpha}{r}(1-P)^2 \quad (6)$$

where A(T) is the creep rate factor having the form of an Arrhenius-type equation, *Q* is the activation energy for deformation, A is a pre-exponential factor, φ is the shear viscosity (Pa.s), Ψ is the bulk viscosity (Pa.s), $\dot{e}$ is the shrinkage rate (s^{-1}), δ_{ij} is the identity tensor, S is the effective sintering stress (Pa), P is the porosity, α is the surface energy ($J.m^{-2}$), Q is the activation energy ($J.mol^{-1}$), R is the gas constant 8.314 ($J.mol^{-1}.K^{-1}$), and *r* is the average particle radius (m).

The densification of YSZ and UO_2 during the manufacturing process is expressed as the evolution of density during the fabrication process. The density can be related to porosity using the following expression:

$$\rho_{eff} = \rho_t(1-P) \quad (7)$$

where ρ_{eff} is the effective density of the material during the sintering process and ρ_t is the theoretical density of the material. Therefore, the densification of YSZ and UO_2 during the fabrication process can be calculated by the evolution of the porosity, which evolves according to the equation of mass conservation:

$$\dot{P} + \dot{e}P = \dot{e} \quad (8)$$

Materials Properties

For Gd_2O_3, the experimentally measured densities of the 1400 °C, 1500 °C, and 1600 °C pre-sintered Gd_2O_3 were obtained from our previous study (Mistarihi et al., 2018) and used in the simulation. These densities were approximately 6.29 ± 0.13, 7.10 ± 0.04, and 7.75 ± 0.0.6 g/cm^3, corresponding to relative densities (RDs) of 75.5 ± 1.5, 85.2 ± 0.5, and 93.4 ± 0.8%, respectively. The RD equals to the experimentally measured density divided by the theoretical density.

The elastic and shear moduli of Gd_2O_3 as functions of temperature for samples with an RD of 96.75% were measured by Dole and Hunter (1976). Haglund and Hunter (1973) measured the elastic properties of polycrystalline Gd_2O_3 with different initial porosities ranging from 2.5% to 36.7% as functions of temperature. The elastic properties were found to decrease linearly with the initial porosity of the sintered samples. The initial porosity of the sintered samples was varied by changing the sintering temperature (Haglund and Hunter, 1973). The reported values of *E* and *G* of Gd_2O_3 as functions of *T* and RD were fitted to first-degree polynomials; the determined parameters of the fitting function are shown in Eqs 9 and 10.

$$E = 0.00428 \times T + 265.30732 \times RD - 0.02349 \times T \times RD - 117.14246 \quad (9)$$

$$G = 0.00158 \times T + 104.39288 \times RD + 0.00584 \times T \times RD - 46.46078 \quad (10)$$

Using the experimentally measured RDs of the 1400 °C, 1500 °C, and 1600 °C pre-sintered Gd_2O_3, *E* and *G* as functions of *T* were calculated using Eqs 9 and 10.

The thermal conductivity of the fully sintered Gd_2O_3 as a function of temperature was experimentally measured using the laser flash method, and the results are shown in **Figure 1**. The thermal conductivity of fully dense Gd_2O_3 at temperatures higher than 800 °C was extrapolated from the experimentally measured data.

The thermal conductivities of the 1400 °C, 1500 °C, and 1600 °C pre-sintered Gd_2O_3 as functions of *T* were calculated from the thermal conductivity of the fully densified Gd_2O_3 using a modified Maxwell–Eucken correlation (Eq. 11):

$$K_p = 1.0789\, K_{100}\left(\frac{1-P}{1+0.5P}\right) \quad (11)$$

where K_{100} and K_p are the thermal conductivities of fully dense and porous Gd_2O_3, respectively.

For YSZ, the thermal conductivity and heat capacity as a function of T and density were provided by Manière et al. (2017) and used in the simulation (Eqs 12-13). The surface energy was provided by Tsoga and Nikolopoulos (1996) as given by Eq. 14. The density was calculated from the determined porosity. The average particle radius of 700 nm (Sigma Aldrich) was used in the simulation. The creep factor (Eq. 15) was determined by fitting the experimentally determined density of YSZ with those predicted by the FEA of YSZ oxide pellets without Gd_2O_3 spheres or mini-pellets. The density of YSZ was determined from the experimentally measured shrinkage of YSZ after correcting its TEC (9.75×10^{-6} K^{-1}) (Song et al., 2011).

$$k = (1.96 - 2.32 \times 10^{-4}T + 6.33 \times 10^{-7}T^2 - 1.91 \times 10^{-10}T^3)(1-1.5P) \quad (12)$$

$$C_p = \begin{cases} (43 + 2.35T - 0.34 \times 10^{-3}T^2 + 4.25 \times 10^{-6}T^3 - \\ 2.09 \times 10^{-9}T^4 + 4.06 \times 10^{-13}T^5)(1 - 1.5P), \\ \quad 273 < T(K) < 1473 \\ 638(1 - 1.5P), 1473 < T(K) < 2200 \end{cases} \quad (13)$$

$$\alpha = 1.927 - 0.428 \times 10^{-3}T \quad (14)$$

$$A(T) = \begin{cases} \frac{0.12}{T} e^{-\frac{200000}{RT}}, 273 < T(K) < 1300 \\ 23 \times 10^{-10}\left(1 - \frac{1}{1 + e^{\frac{T-1895.58}{63}}}\right), \\ \quad 1300 < T(K) < 1800 \end{cases} \quad (15)$$

For UO_2, the surface energy as a function of T from 273 to 3120 K was provided by Hall and Mortimer (1986). Fink (2000) summarized this reported data and provided a correlation for the mean value of the surface energy of UO_2 as a function of T (Eq. 16):

$$\alpha = 0.85 - 1.4 \times 10^{-4}(T - 273.15) \quad (16)$$

The heat capacity of the stoichiometric UO_2 was measured by Kerrisk and Clifton (1972) over the temperature range 483–3107 K. These data were summarized and fitted to Eq. 17 in MATPRO (Siefken et al., 2001):

$$C_p = \frac{K_1 M^2 e^{\frac{\theta}{T}}}{T^2\left[e^{\frac{M}{T}} - 1\right]^2} + K_2 T + \frac{YK_3 E_D}{2RT^2} e^{\frac{-E_D}{RT}} \quad (17)$$

where Y is the oxygen-to-metal ratio (equal to 2), R is the universal gas constant (8.3143 J/mol·K), and M is the Einstein constant (535.285). The constants K_1, K_2, K_3, and E_D are equal to 296.7, 2.43×10^{-2}, 8.745×10^{7}, and 1.577×10^{5}.

Lucuta et al. (1996) summarized the thermal conductivity of non-irradiated and fully dense UO_2 and fitted the data to a function comprising a hyperbolic term for the lattice contribution through phonon–defect and phonon–phonon scattering processes and an exponential term for polaron contributions. The exponential term becomes dominant for high temperatures $T > 1900$ K.

$$k_o = \frac{1}{0.0375 + 2.165 \times 10^{-4}T} + \frac{4.715 \times 10^{9}}{T^2} e^{\frac{-16361}{T}} \quad (18)$$

The creep factor of UO_2 was generated in a similar way to that of YSZ and is expressed by Eq. 19.

$$A(T) = \begin{cases} \frac{0.12}{T} e^{-\frac{200000}{RT}}, 273 < T(K) < 1300 \\ 30 \times 10^{-10}\left(1 - \frac{1}{1 + e^{\frac{T-1795.58}{100}}}\right), \\ \quad 1300 < T(K) < 1800 \end{cases} \quad (19)$$

An average particle radius of 2400 nm was used for the simulation of UO_2 (Yeo et al., 2013).

The shrinkage rates of the green YSZ, UO_2, and Gd_2O_3 compacts and the 1400 °C, 1500 °C, and 1600 °C pre-sintered pellets were measured by a dilatometer (DIL 402C) up to 1600 °C in an air atmosphere with a heating rate of 10 °C/min and a holding time of 3 h. The results are shown in **Figure 2**.

Geometric Models

2-D axisymmetric simulation models were developed to study the sintering stress distributions during the fabrication process of YSZ pellets containing lumped Gd_2O_3 mini-pellets or spherical particles. The geometrical models used in the FEA simulations are shown in **Figure 3**.

In order to determine the critical sintering stress for cracking, simulation models of YSZ oxide pellets with a Gd_2O_3 mini-pellet pre-sintered at 1400 °C, 1500 °C, or 1600 °C having the average measured dimensions of the pre-sintered pellets (see **Table 1**) and the measured shrinkage rates of the pellets sintered at 1400, 1500, and 1600 °C (see **Figure 2**) were developed. Simulation models of YSZ oxide pellets containing either lumped Gd_2O_3 spherical particles or mini-pellets of the same size and the shrinkage rate of the 1400 °C pre-sintered pellets were also developed to understand the effect of the lumped Gd_2O_3 shape on the formation of interfacial cracks. In addition, simulation models of YSZ oxide pellets with lumped Gd_2O_3 spherical particles of 1.5, 2, or 3 mm in diameter and the shrinkage rate of the pellets pre-sintered at 1400 °C were developed to determine the critical size of the lumped Gd_2O_3 spherical particles. Finally, simulation models of YSZ oxide pellets with a Gd_2O_3 spherical particle having the shrinkage rate of the pellet at 1400 °C, 1500 °C, or 1600 °C and the size of 1.5 mm were developed to understand the effect of the shrinkage rate on the formation of interfacial cracks.

Initial and Boundary Conditions

The simulation models were assumed to have an initial temperature of 25 °C. The outer surfaces of the simulation

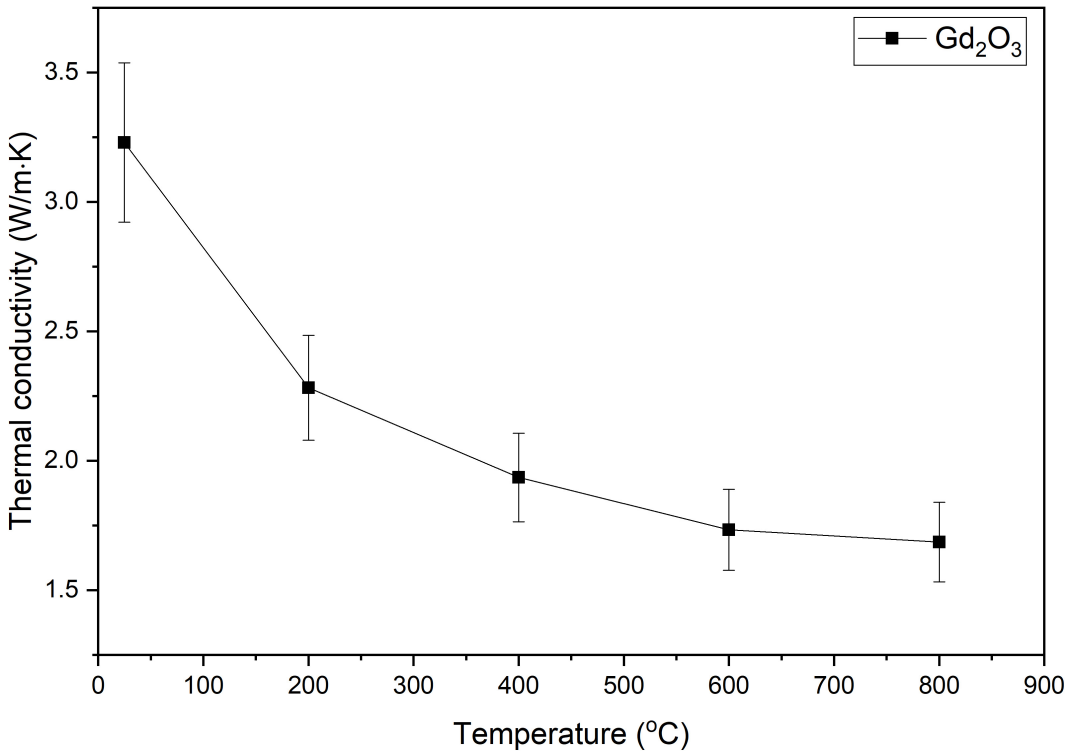

FIGURE 1 | Thermal conductivity of fully dense Gd_2O_3 with increases in sintering temperature from 25 °C to 800 °C.

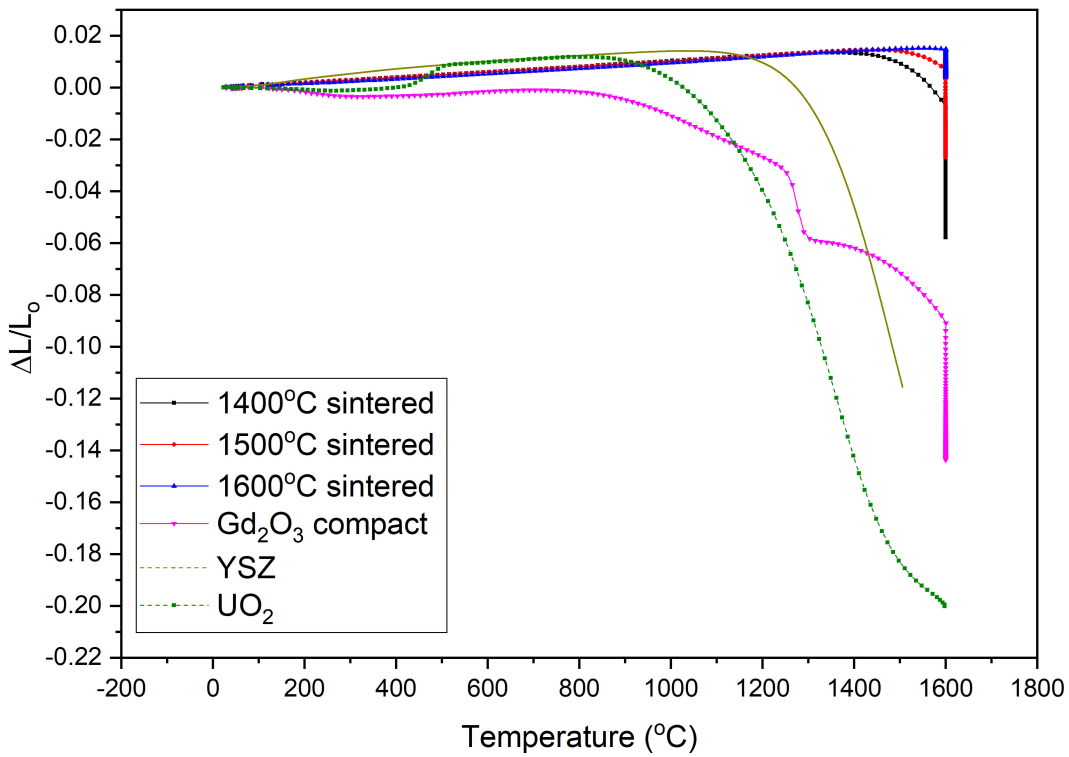

FIGURE 2 | Shrinkage behaviors of Gd_2O_3 compact, sintered Gd_2O_3 pellet, YSZ compact, and UO_2 compact.

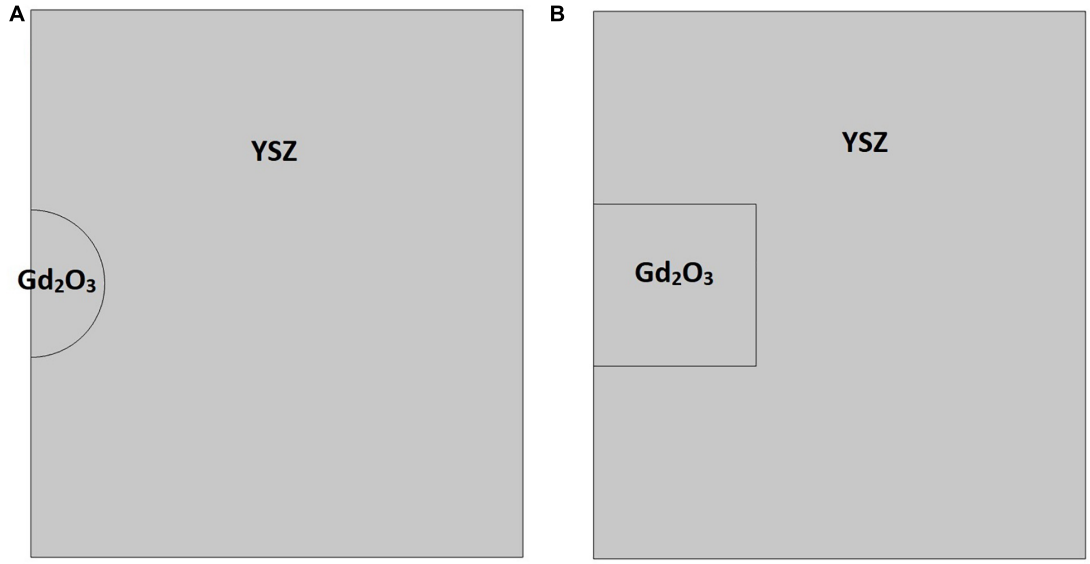

FIGURE 3 | Geometrical models of YSZ oxide pellet containing **(A)** lumped Gd_2O_3 spherical particle and **(B)** mini-pellet.

models of the YSZ oxide pellets containing a lumped Gd_2O_3 sphere or mini-pellet were heated from 25 °C to 1500 °C or 1600 °C for the case of YSZ or UO_2 with a heating rate of 10 °C/min, in accordance with the experimental procedures.

RESULTS AND DISCUSSION

YSZ pellet

Figure 4 shows the FEA simulation results for the maximum sintering stress in YSZ oxide pellets containing a lumped Gd_2O_3 mini-pellet pre-sintered at 1400 °C, 1500 °C, or 1600 °C during heating from 25 °C to 1500 °C.

As shown in **Figure 4**, the maximum sintering stress in the YSZ oxide pellets containing a lumped Gd_2O_3 mini-pellet was almost constant in the temperature range 25–1100 °C and began increasing almost exponentially at approximately 1150 °C, corresponding to the temperature at which the YSZ pellet started to shrink (see **Figure 2**). As the pre-sintering temperature increased from 1400 °C to 1600 °C, the maximum sintering stress increased, which could be attributed to the increase in the shrinkage rate mismatch (see **Figure 2**). Previous experimental observations (Mistarihi et al., 2018) showed no interfacial cracks in YSZ pellets containing lumped Gd_2O_3 mini-pellets pre-sintered at 1400 °C, while cracks appeared in the YSZ oxide pellets containing lumped Gd_2O_3 mini-pellets pre-sintered at 1500 °C or higher. The maximum sintering stress in the YSZ oxide pellet containing a lumped Gd_2O_3 mini-pellet pre-sintered at 1400 °C during the fabrication process was calculated by FEA as approximately 120 MPa; that with the mini-pellets pre-sintered at 1500 °C was approximately 150 MPa. This indicates that sintering stresses in the range 120–150 MPa would result in the formation of interfacial cracks in the YSZ oxide pellet containing lumped Gd_2O_3. The flexural strength of the fully dense YSZ at room temperature is approximately 1000 MPa (Masaki, 1986) and it decreases almost linearly with increasing porosity to 170 MPa for YSZ with an RD of 40% (Gain et al., 2006). However, simulation studies of the residual stresses during the fabrication of ceramic composites have shown that residual stresses as low as 25 kPa (Schoenberg et al., 2006) or 90 MPa (DeHoff et al., 2008) can cause the formation of interfacial cracks in ceramic composites.

TABLE 1 | Dimensions of Gd_2O_3 mini-pellets after pre-sintering at different temperatures.

	Initial sintering temperature (°C)		
	1400	**1500**	**1600**
Height (mm)	1.67 ± 0.01	1.6 ± 0.05	1.54 ± 0.01
Diameter (mm)	2.76 ± 0.03	2.66 ± 0.04	2.57 ± 0.03

Figure 5 shows the stress distribution in the YSZ oxide pellet containing either a lumped Gd_2O_3 sphere ($r = 0.75$ mm) or mini-pellet ($r = h = 0.83$ mm) with the same volume of approximately 1.77 mm^3 and the shrinkage rate of the 1400 °C pre-sintered Gd_2O_3 at a sintering temperature of 1300 °C.

As shown in **Figure 5**, the addition of Gd_2O_3 spheres resulted in the formation of symmetric stresses around the interface. Meanwhile, the Gd_2O_3 mini-pellet caused the formation of localized stresses at the edges of the mini-pellet. The formation of these localized stresses indicates that cracks would form in these areas, which is in good agreement with the experimental observation presented in our previous study (Mistarihi et al., 2018), where interfacial cracks in YSZ pellets containing lumped Gd_2O_3 mini-pellets were observed at the mini-pellet edges.

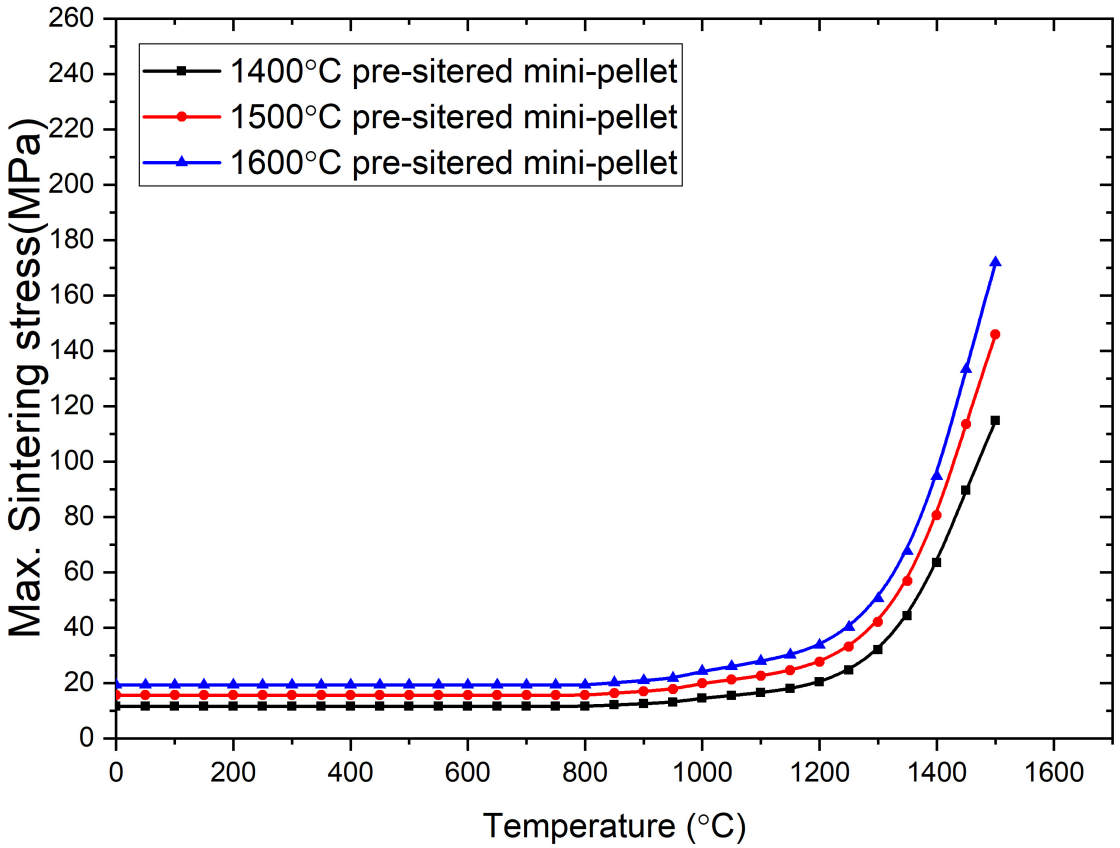

FIGURE 4 | FEA-predicted maximum sintering stresses in YSZ oxide pellet containing a lumped Gd_2O_3 mini-pellet pre-sintered at 1400 °C, 1500 °C, or 1600 °C.

The FEA-calculated maximum sintering stresses in YSZ oxide pellets containing either a lumped Gd_2O_3 sphere (r = 0.75 mm) or mini-pellet ($r = h$ = 0.83 mm) with equal volume and shrinkage rates during the sintering process are shown in **Figure 6**. In order to investigate the effect of the dimensions of the Gd_2O_3 mini-pellets on the sintering stresses developed during the manufacturing of YSZ oxide pellets containing lumped Gd_2O_3 mini-pellets, simulation models were also developed with Gd_2O_3 mini-pellets of equal volume to the spheres but the reduced r/h ratio of 0.5. The maximum sintering stresses developed during the manufacturing of the YSZ oxide pellet containing a lumped Gd_2O_3 mini-pellet ($r = 1/2h$ = 0.65 mm) as calculated by FEA are also shown in **Figure 6**.

The addition of mini-pellets yielded higher sintering stress over the entire temperature range, which can be attributed to the localized stresses at the edges of the mini-pellets. These higher localized sintering stresses are mainly caused by the outward bending of the Gd_2O_3 mini-pellet due to the shrinkage of the YSZ. The temperature gradient caused uniform shrinkage of the Gd_2O_3 spheres, yielding lower and symmetric sintering stresses in the YSZ oxide pellet containing a lumped Gd_2O_3 sphere. DeHoff et al. (2008) studied the stress distributions of bilayer open-ended cylindrical ceramics and spherical-core ceramics and found that the open-ended cylinder ceramics showed localized stresses at the upper edges of the cylinders, whereas the spherical-core ceramics had symmetric stress distributions around the core–shell interface. This indicates that the use of spherical Gd_2O_3 is better than that of mini-pellets to maintain the integrity of the CSBA fuel during fabrication. The localized stresses developed in the YSZ pellet containing a lumped Gd_2O_3 mini-pellet can be reduced by decreasing the aspect ratio of the mini-pellet because this diminishes the outward bending caused by the temperature gradient.

Figure 7 shows the FEA-calculated maximum sintering stress in YSZ oxide pellets containing lumped Gd_2O_3 spheres of equal size (r = 0.75 mm) but the shrinkage rates of Gd_2O_3 sintered at 1400 °C, 1500 °C, and 1600 °C. As shown in **Figure 7**, the maximum sintering stress during fabrication was increased with increases in the pre-sintering temperature of the lumped Gd_2O_3, which could be attributed to the increases in the shrinkage rate mismatch.

According to the experimental observation in our previous study (Mistarihi et al., 2018), interfacial cracks were observed in YSZ oxide pellets containing lumped Gd_2O_3 mini-pellets pre-sintered at 1500 °C or higher, but not in YSZ containing lumped Gd_2O_3 spherical particles pre-sintered at 1600 °C. As can be seen from **Figure 7**, the calculated maximum sintering stress in the YSZ pellet containing a 0.75-mm-radius lumped Gd_2O_3 sphere pre-sintered at 1600 °C is approximately 105 MPa. The maximum calculated sintering stress in the YSZ pellet containing

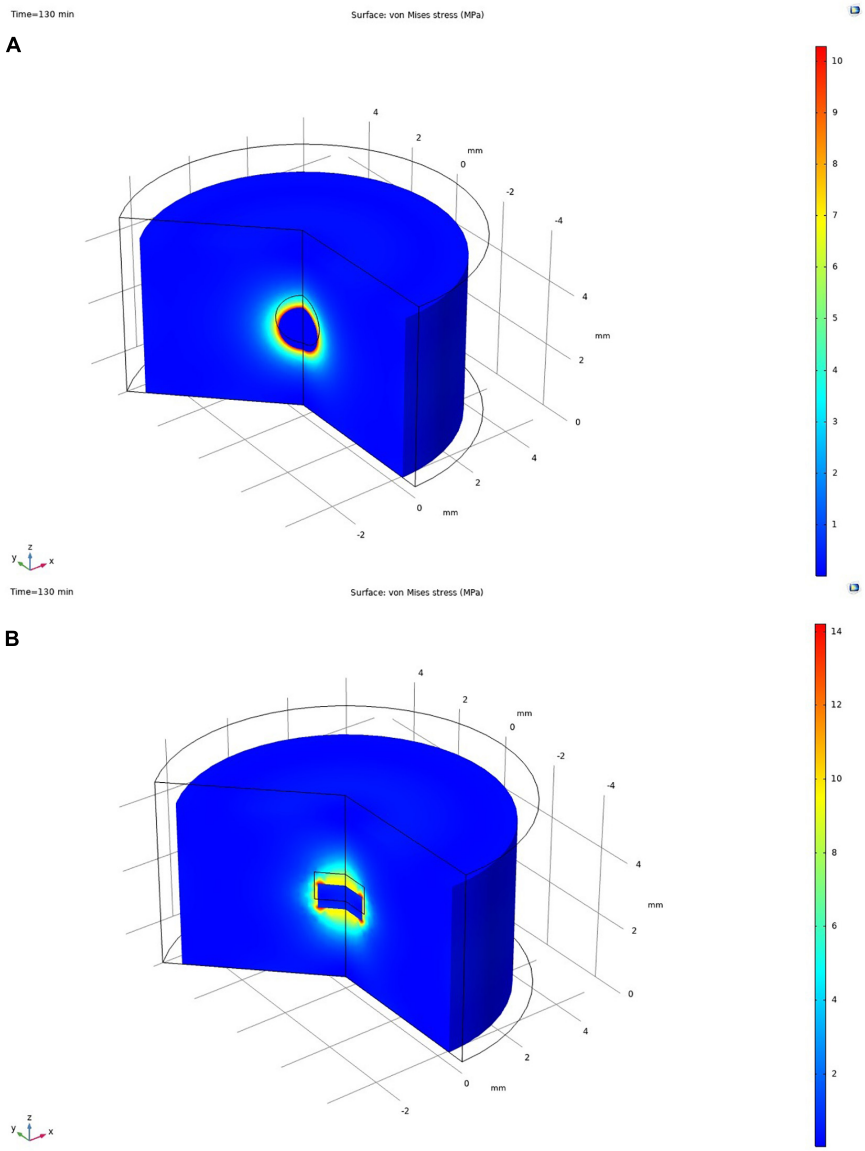

FIGURE 5 | Stress distributions in YSZ oxide pellets containing lumped Gd_2O_3 **(A)** sphere (r = 0.75 mm) or **(B)** mini-pellet ($r = h$ = 0.83 mm). (r is the radius of the sphere or mini-pellet and h is the height of the mini-pellet).

the 1500 °C pre-sintered mini-pellet was approximately 150 MPa (**Figure 4**). Therefore, the absence of interfacial cracks in the case of the YSZ pellet containing Gd_2O_3 spherical particles pre-sintered at 1600 °C could be attributed to the reduced symmetric sintering stress relating to their smaller sizes and spherical shapes, compared to those of the 1500 °C pre-sintered mini-pellet.

The effect of the Gd_2O_3 sphere size on the maximum sintering stress in YSZ oxide pellets containing lumped Gd_2O_3 spheres with the shrinkage rate of the 1400 °C sintered Gd_2O_3 during sintering is shown in **Figure 8**. As shown, the maximum sintering stress was increased with increases in the size of the Gd_2O_3 spheres. However, the increase was much smaller than that observed with increases in the Gd_2O_3 shrinkage rates. This indicates that the sintering stresses developed in the YSZ oxide pellets containing lumped Gd_2O_3 spheres are mostly controlled by the Gd_2O_3 shrinkage rate.

UO_2 Fuel Pellet

Experimental studies using UO_2 are expensive and present high levels of radiotoxicity. In an experimental demonstration (Mistarihi et al., 2018) of the fabrication of oxide pellets containing lumped Gd_2O_3 spherical particles, mini-pellets, or rods, YSZ was used as a surrogate for UO_2 because it has a similar crystal structure, high melting temperature, and sintering kinetics. However, for fabrication studies, the shrinkage rate and

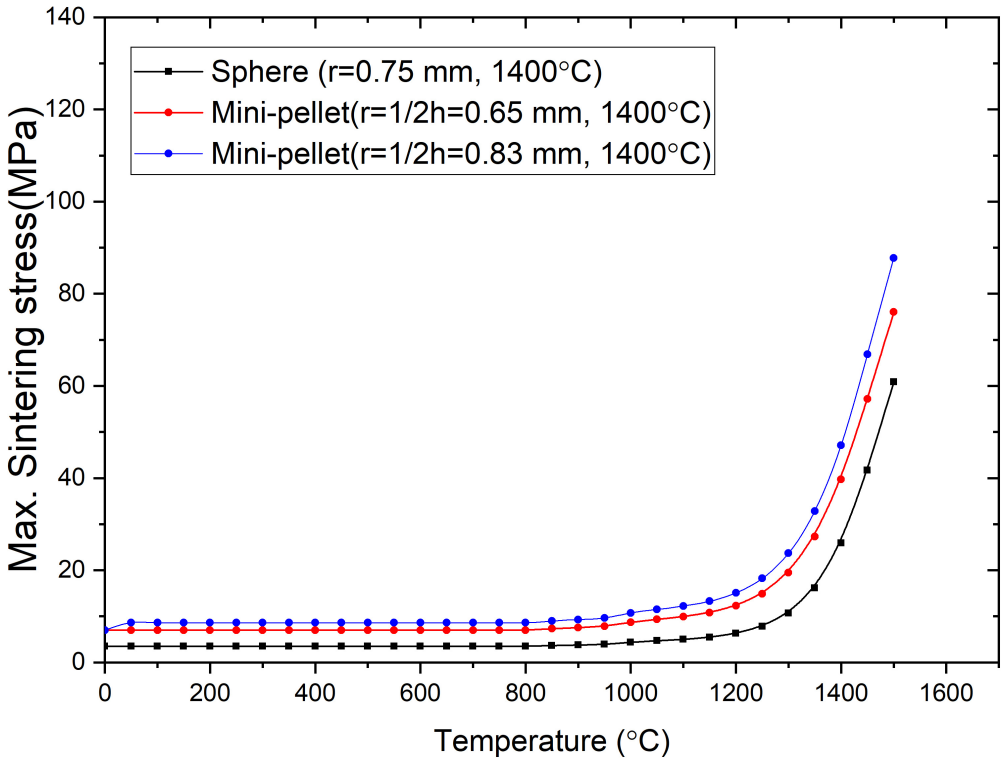

FIGURE 6 | FEA-calculated maximum sintering stress in YSZ oxide pellets containing lumped Gd_2O_3 spheres and mini-pellets of the same volume and shrinkage rate.

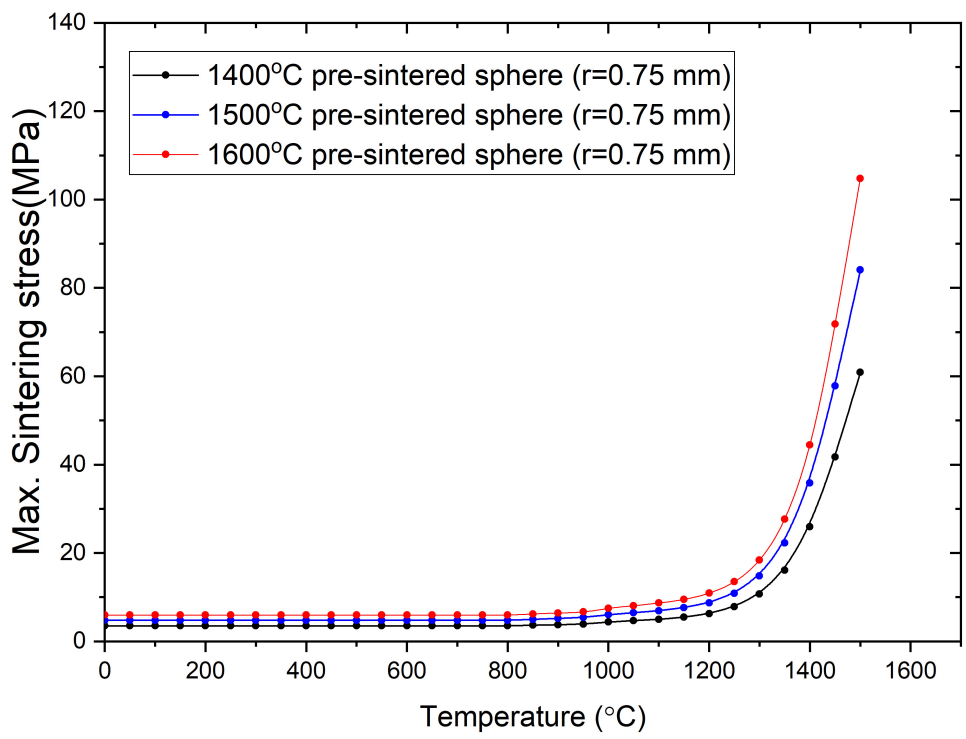

FIGURE 7 | FEA-calculated maximum sintering stress in YSZ oxide pellets containing lumped Gd_2O_3 spheres of equal size (r = 0.75 mm) but different shrinkage rates.

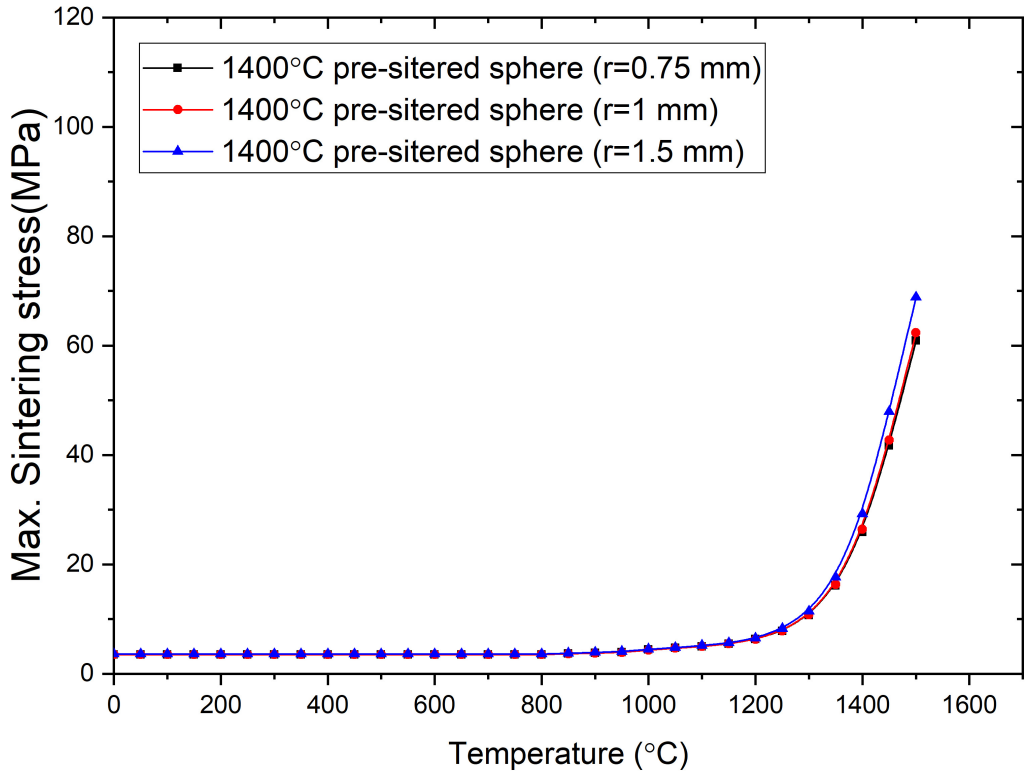

FIGURE 8 | FEA-calculated maximum sintering stress in YSZ oxide pellets containing lumped Gd_2O_3 spheres of different sizes but equal shrinkage rates.

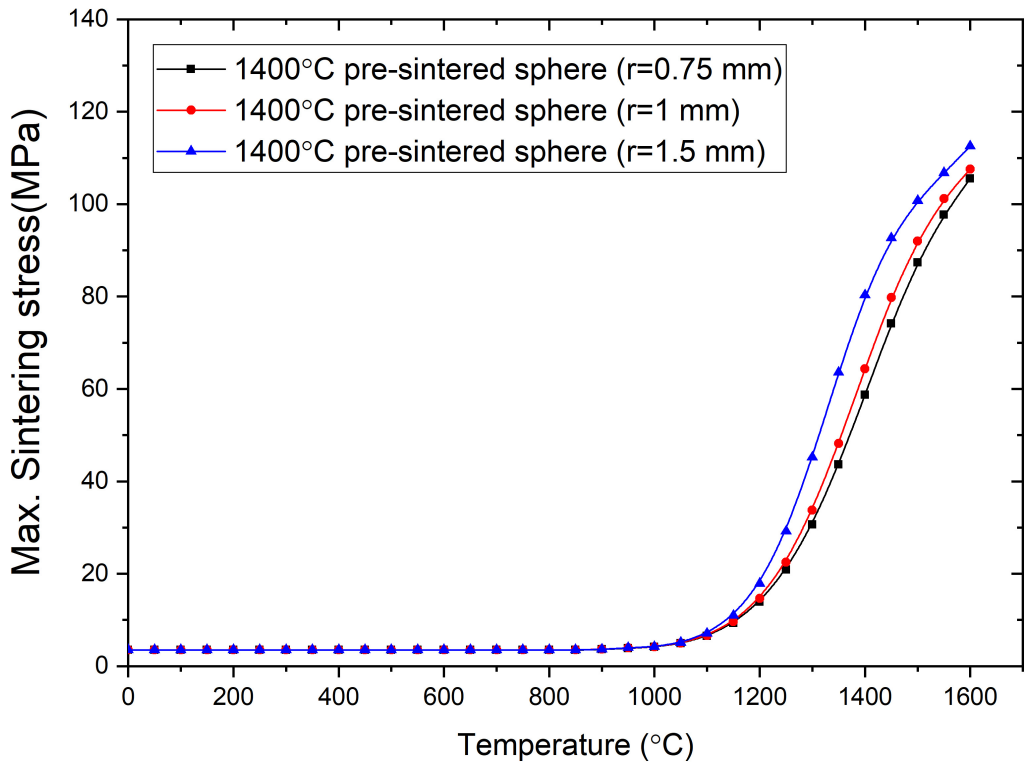

FIGURE 9 | FEA-calculated maximum sintering stress in UO_2 pellets containing lumped Gd_2O_3 spheres of different sizes but equal shrinkage rates.

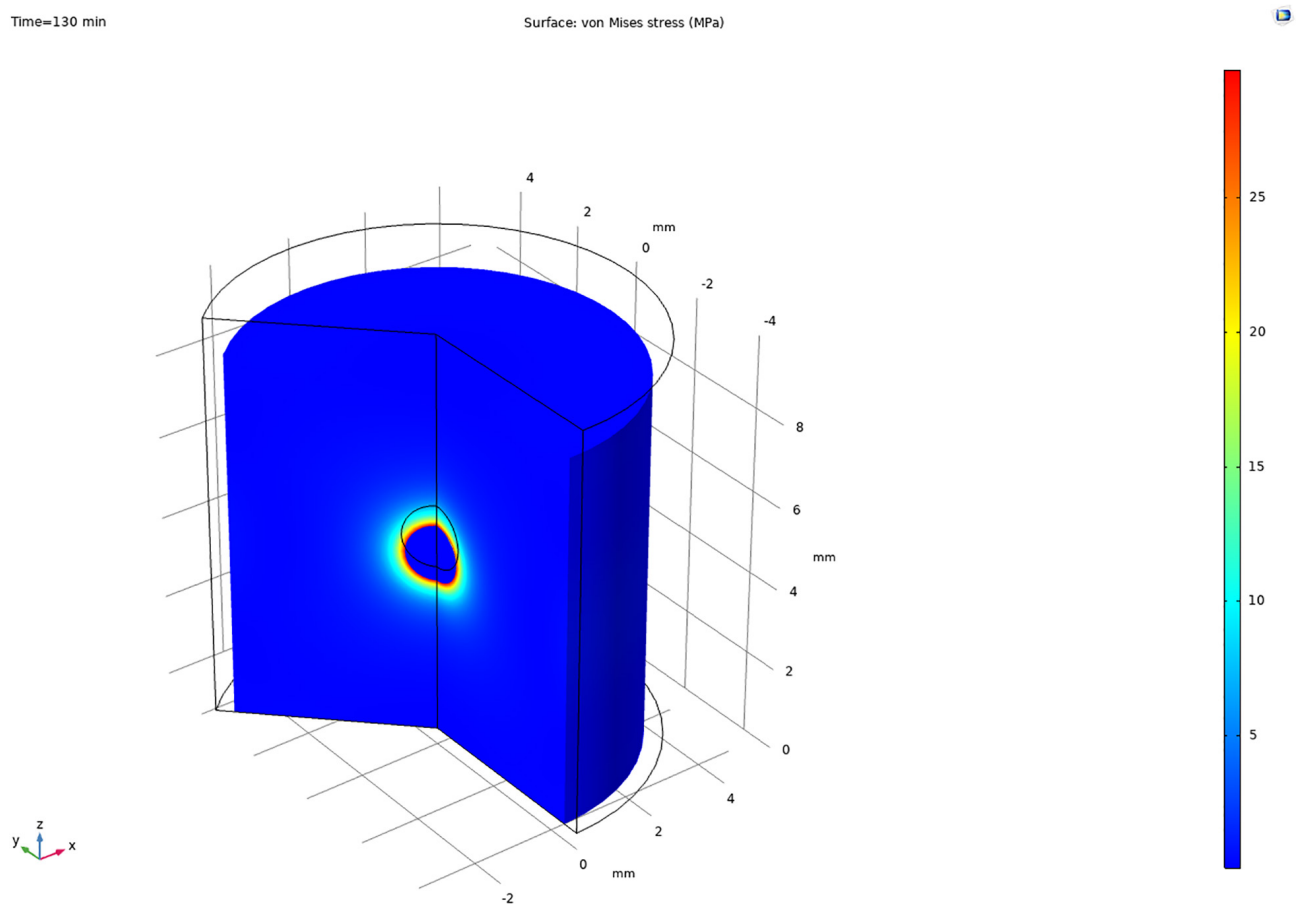

FIGURE 10 | Stress distribution in UO_2 pellet containing a lumped Gd_2O_3 sphere (r = 0.75 mm).

TEC of YSZ and UO_2 must be similar, as well as the diffusivity of Gd^{3+} in the YSZ and UO_2 matrices.

Figure 9 shows the FEA-calculated maximum sintering stress in UO_2 pellets containing a lumped Gd_2O_3 sphere with a shrinkage rate of 1400 °C pre-sintered Gd_2O_3 but different sizes (r = 0.75, 1, 1.5 mm). As shown in **Figure 9**, the maximum sintering stress during the fabrication process was increased with increases in the size of the lumped Gd_2O_3. However, the calculated maximum sintering stresses in the UO_2 fuel pellets were higher than those reported for YSZ pellets. The maximum sintering stresses in UO_2 containing lumped Gd_2O_3 sphere with a radius of 1.5 mm at 1300 °C, 1400 °C, and 1500 °C were about 45.2, 80.3, and 101 MPa, respectively, whereas the maximum sintering stresses determined in YSZ pellet containing the same Gd_2O_3 sphere and at the same sintering temperatures were about 11.4, 29.2, and 68.8 MPa, respectively (see **Figure 8**). This could be attributed to the greater mismatch in the shrinkage rates of UO_2 and Gd_2O_3 relative to that of YSZ and Gd_2O_3 (see **Figure 2**).

The stress distribution in the UO_2 pellet containing a lumped Gd_2O_3 sphere (r = 0.75 mm) with the shrinkage rate of 1400 °C pre-sintered Gd_2O_3 at the sintering temperature of 1300 °C is shown in **Figure 10**. The stress distribution was symmetric, similar to that in the YSZ pellet with the same conditions; however, the stress values were higher than those reported in YSZ, which can again be attributed to the higher shrinkage rate mismatch between UO_2 and Gd_2O_3 relative to that between YSZ and Gd_2O_3 (see **Figure 2**).

Owing to the absence of sufficient experimental data for CSBA fuel using UO_2, it is difficult to set threshold stress values for the formation of interfacial cracks in UO_2-based CSBA. However, the fabrication of UO_2 oxide pellets containing lumped Gd_2O_3 spherical particles pre-sintered at 1400 °C was reported by Oh et al. (2017) using the conventional fabrication conditions for UO_2 of pressing under 3 ton/cm^2 followed by sintering at 1700 °C for 4 h in an H_2 atmosphere at approximately 5 °C/min. Similar results were observed regarding the absence of interfacial cracks and the formation of the gadolinium urinate phase at the interface between UO_2 and Gd_2O_3.

CONCLUSION

The sintering stresses developed in the YSZ oxide pellets containing either lumped Gd_2O_3 spheres or mini-pellets during fabrication from 25 °C to 1500 °C were simulated using the FEA method. Thermal and linear elastic models were used to simulate the sintering stresses in lumped Gd_2O_3, while thermal and sintering models based on the continuum theory of sintering

were used to simulate those in the YSZ powder compact. These models were coupled and implemented using COMSOL Multiphysics code.

The critical sintering stresses for the formation of interfacial cracks in YSZ oxide pellets containing lumped Gd_2O_3 were determined by comparing the FEA-calculated stresses in YSZ oxide pellets containing lumped Gd_2O_3 mini-pellets with the shrinkage rates of 1400 °C, 1500 °C, and 1600 °C sintered Gd_2O_3 with experimental observations. It was found that sintering stresses in the range of 120–150 MPa could cause the formation of interfacial cracks in these pellets.

The effects of the shape, shrinkage rate, and size of lumped Gd_2O_3 on the formation of cracks during fabrication were studied. It was found that the addition of cylindrical Gd_2O_3 mini-pellets resulted in localized and higher stresses at the mini-pellet edges. In contrast, the addition of Gd_2O_3 spherical particles yielded symmetric and lower stresses at the interface between the Gd_2O_3 and YSZ. Increases in the shrinkage rate and size of Gd_2O_3 resulted in higher sintering stresses in the YSZ oxide pellets containing lumped Gd_2O_3.

The sintering stresses developed during the fabrication of UO_2 containing lumped Gd_2O_3 spheres were also estimated. Similar behaviors to those of YSZ were observed. However, the magnitude of the sintering stress was higher because of the higher shrinkage rate mismatch between UO_2 and Gd_2O_3 relative to that between YSZ and Gd_2O_3.

DATA AVAILABILITY STATEMENT

The original contributions presented in the study are included in the article/supplementary material, further inquiries can be directed to the corresponding author.

AUTHOR CONTRIBUTIONS

QM did the finite element simulation and wrote the article. HR supervised and reviewed the written article. Both authors contributed to the article and approved the submitted version.

FUNDING

This study was supported by the KAI-NEET Institute of KAIST and the National Research Foundation (NRF) of Korea grant funded by the Korean Government (Ministry of Science, ICT and Future Planning) (NRF-2016R1A5A1013919, NRF-2018M2A8A1083889, and NRF-2019M2D1A1067210).

REFERENCES

Agarwal, B. D. (1972). *Micromechanics Analysis of Composite Materials Using Finite Element Methods*. Ph.D. thesis, Illinois Institute of Technology, Chicago.

Choe, J., Shin, H. C., and Lee, D. (2016a). New burnable absorber for long-cycle low boron operation of PWRs. *Ann. Nucl. Energy* 88, 272–279. doi: 10.1016/j.anucene.2015.11.011

Choe, J., Zheng, Y., Lee, D., and Shin, H. C. (2016b). Boron-free small modular pressurized water reactor design with new burnable absorber. *Int. J. Energy Res.* 40, 2128–2135. doi: 10.1002/er

Davidge, R. W., and Green, T. J. (1968). The strength of two-phase ceramic glass materials. *J. Mater. Sci.* 3, 629–634. doi: 10.1007/BF00757910

DeHoff, P. H., Barrett, A. A., Lee, R. B., and Anusavice, K. J. (2008). Thermal compatibility of dental ceramic systems using cylindrical and spherical geometries. *Dent. Mater.* 24, 744–752. doi: 10.1016/j.dental.2007.08.008

Delale, F. (1988). Critical fiber size for microcrack suppression in ceramic-fiber ceramic-matrix compoistes. *Eng. Fract. Mech.* 31, 145–155.

Dole, S. L., and Hunter, O. (1976). Elastic properties of some Gd_2O_3-HfO_2 compositions. *J. Nucl. Mater.* 59, 207–214.

Durazzo, M., Saliba-Silva, A. M., Urano De Carvalho, E. F., and Riella, H. G. (2013). Sintering behavior of UO_2-Gd_2O_3 fuel: pore formation mechanism. *J. Nucl. Mater.* 433, 334–340. doi: 10.1016/j.jnucmat.2012.09.033

Fink, J. (2000). Thermophysical properties of uranium dioxide. *J. Nucl. Mater.* 279, 1–18. doi: 10.1016/S0022-3115(99)00273-1

Fleming, R. F. (1982). Neutron self-shielding factors for simple geometrics. *Int. J. Appl. Radiat. Isot.* 33, 1263–1268. doi: 10.1016/0020-708X(82)90247-2

Gain, A. K., Song, H. Y., and Lee, B. T. (2006). Microstructure and mechanical properties of porous yttria stabilized zirconia ceramic using poly methyl methacrylate powder. *Scr. Mater.* 54, 2081–2085. doi: 10.1016/j.scriptamat.2006.03.009

Galperin, A., Segev, M., and Radkowsky, A. (1986). Substitution of the Soluble boron reactivity control system of a pressurized water reactor by gadolium burnable poisons. *Nucl. Technol.* 75, 127–133. doi: 10.13182/NT86-A33855

Grossbeck, M. L., Renier, J.-P. A., and Grossbeck, M. L. (2001). *Development of improved Burnable Poisons for Commercial Nuclear Power Reactors*. Oak Ridge, TN: Oak Ridge National Laboratory.

Haglund, J. A., and Hunter, O. (1973). Elastic properties of polycrystalline monoclinic Gd_2O_3. *J. Am. Ceram. Soc.* 56, 327–330. doi: 10.1111/j.1151-2916.1973.tb12506.x

Hall, R. O. A., and Mortimer, M. J. (1986). A critical review of the surface energy of UO_2. *J. Less Common Met.* 121, 341–345. doi: 10.1097/00152193-198306000-00031

IAEA (1995). *Characteristics and Use of Urania-Gadolinia Fuels*. Vienna: IAEA.

Kerrisk, J. F., and Clifton, D. G. (1972). Smoothed values of the enthalpy and heat capacity of UO_2. *Nucl. Tech.* 16, 531–535. doi: 10.13182/NT72-6

Li, C., Wu, Y., Wang, Y., Wang, K., Wang, M., Tian, W., et al. (2020). Analysis on the behavior of dispersed plate-type fuel based on fluid-solid coupling method. *Prog. Nucl. Energy* 126:103398. doi: 10.1016/j.pnucene.2020.103398

Lucuta, P. G., Matzke, H., and Hastings, I. J. (1996). A pragmatic approach to modelling thermal conductivity of irradiated UO_2 fuel: review and recommendations. *J. Nucl. Mater.* 232, 166–180. doi: 10.1016/S0022-3115(96)00404-7

Manière, C., Zahrah, T., and Olevsky, E. A. (2017). Fully coupled electromagnetic-thermal-mechanical comparative simulation of direct vs hybrid microwave sintering of 3Y-ZrO_2. *J. Am. Ceram. Soc.* 100, 2439–2450. doi: 10.1111/jace.14762

Masaki, T. (1986). Mechanical properties of toughened ZrO_2-Y_2O_3 ceramics. *J. Am. Ceram. Soc.* 69, 638–640. doi: 10.1111/j.1151-2916.1986.tb04823.x

Mistarihi, Q. M., Park, W., Nam, K., Yahya, M.-S., Kim, Y., and Ryu, H. J. (2018). Fabrication of oxide pellets containing lumped Gd_2O_3 using Y_2O_3-stabilized ZrO_2 for burnable absorber fuel applications. *Int. J. Energy Res* 42, 2141–2151. doi10.1002/er.3995

Nguyen, X. H., Kim, C. H., and Kim, Y. (2019). An advanced core design for a soluble-boron-free small modular reactor ATOM with centrally-shielded burnable absorber. *Nucl. Eng. Technol.* 51, 369–376. doi: 10.1016/j.net.2018.10.016

Oh, J. S., Mistarihi, Q., Ryu, H. J., and Kim, D.-J. (2017). "Fabrication of Gadolinia-containing UO_2 fuel pellet," in *Proceedings of the 42nd International*

Conference and Expo on Advanced Ceramics and Composites, Daytona Beach, FL.

Olevsky, E. A. (1998). Theory of sintering: from discrete to continuum. *Mater. Sci. Eng. R Rep.* 23, 41–100. doi: 10.1016/S0927-796X(98)00009-6

Olevsky, E. A., Garcia-Cardona, C., Bradbury, W. L., Haines, C. D., Martin, D. G., and Kapoor, D. (2012). Fundamental aspects of spark plasma sintering: II. Finite element analysis of scalability. *J. Am. Ceram. Soc.* 95, 2414–2422. doi: 10.1111/j.\hbox{1551-2916}.2012.05096.x

Riedel, H., Meyer, D., Svoboda, J., and Zipse, H. (1993). Numerical simulation of die pressing and sintering — development of constitutive equations. *Int. J. Refract. Met. Hard Mater.* 12, 55–60. doi: 10.1016/0263-4368(93)90016-9

Schoenberg, S. E., Green, D. J., Segall, A. E., Messing, G. L., Grader, A. S., and Halleck, P. M. (2006). Stresses and distortion due to green density gradients during densification. *J. Am. Ceram. Soc.* 89, 3027–3033. doi: 10.1111/j.1551-2916.2006.01182.x

Selsing, J. (1961). Internal stresses in ceramics. *J. Am. Ceram. Soc.* 44, 419–419. doi: 10.1111/j.1151-2916.1961.tb15475.x

Sglavo, V. M., and Bellettati, N. (2017). Ceramic laminates with improved mechanical reliability by tailoring the porosity of the constituting layers. *J. Eur. Ceram. Soc.* 37, 1643–1650. doi: 10.1016/j.jeurceramsoc.2016.11.022

Siefken, L. J., Coryell, E. W., Harvego, E. A., and Hohorst, J. K. (2001). *MATPRO-A Library of Materials Properties for Light-Water-Reactor Accident Analysis*. Idaho Falls, ID: Idaho National Engineering and Environmental Laboratory.

Song, X., Lu, J., Zhang, T., and Ma, J. (2011). Two-stage master sintering curve approach to sintering kinetics of undoped and Al_2O_3-doped 8 Mol% yttria-stabilized cubic zirconia. *J. Am. Ceram. Soc.* 94, 1053–1059. doi: 10.1111/j.1551-2916.2010.04199.x

Tsoga, A., and Nikolopoulos, P. (1996). Surface and grain-boundary energies in yttria-stabilized zirconia (YSZ-8 mol%). *J. Mater. Sci.* 31, 5409–5413. doi: 10.1007/BF01159310

Yahya, M.-S., and Kim, Y. (2017a). An innovative core design for a soluble-boron-free small pressurized water reactor. *Int. J. Energy Res.* 41, 1–9. doi: 10.1002/er.3792

Yahya, M.-S., and Kim, Y. (2017b). "Centrally-shielded burnable absorber for LWR fuel," in *Proceedings of the International Congress on Advances in Nuclear Power Plants* (Fukui and Kyoto: American nuclear society).

Yeo, S., McKenna, E., Baney, R., Subhash, G., and Tulenko, J. (2013). Enhanced thermal conductivity of uranium dioxide-silicon carbide composite fuel pellets prepared by Spark Plasma Sintering (SPS). *J. Nucl. Mater.* 433, 66–73. doi: 10.1016/j.jnucmat.2012.09.015

Conflict of Interest: The authors declare that the research was conducted in the absence of any commercial or financial relationships that could be construed as a potential conflict of interest.

frontiers in Energy Research

ORIGINAL RESEARCH
published: 11 May 2021
doi: 10.3389/fenrg.2021.664345

Numerical Simulation Research on the Irradiation-Thermal-Mechanical Performance Evolution of FCM Fuel

Tang Changbing, Li Yuanming, Jiao Yongjun, Zhang Kun and Wang Peng*

Science and Technology on Reactor System Design Technology Laboratory, Nuclear Power Institute of China, Chengdu, China

FCM fuel which microencapsulated TRISO particles in SiC matrix is a promising ATF (accident tolerant fuel) candidate fuel designed to replace the traditional pellet-cladding fuel rod. In order to predict the in-pile behavior of FCM fuel accurately and to optimize the design of FCM fuel, it is necessary to establish a numerical simulation method of irradiation-thermal -mechanical coupling behavior of FCM fuel. In this study, the related thermal effects and irradiation effects of FCM fuel and the effect of gap heat transfer are considered. User defined subroutines are compiled respectively, and the above-mentioned correlation effects are introduced into ABAQUS software to establish a numerical simulation method for the irradiation-thermal -mechanical coupling behavior of FCM fuel. Based on the established numerical simulation method, the performance evolution of FCM fuel in the reactor is simulated, and the possible failure modes of FCM fuel in the reactor are analyzed. The research results can provide guidance for the optimization design and performance prediction of FCM fuel.

Keywords: ATF, irradiation-thermal-mechanical coupling, numerical simulation, FCM fuel, 3D simulation

OPEN ACCESS

Edited by:
Yingwei Wu,
Xi'an Jiaotong University, China

Reviewed by:
Liangzhi Cao,
Xi'an Jiaotong University, China
Deqi Chen,
Chongqing University, China
Rong Liu,
South China University of Technology, China

****Correspondence:***
Jiao Yongjun
smilesun001@126.com

Specialty section:
This article was submitted to Nuclear Energy, a section of the journal Frontiers in Energy Research

Received: *05 February 2021*
Accepted: *27 April 2021*
Published: *11 May 2021*

Citation:
Changbing T, Yuanming L, Yongjun J, Kun Z and Peng W (2021) Numerical Simulation Research on the Irradiation-Thermal-Mechanical Performance Evolution of FCM Fuel. Front. Energy Res. 9:664345. doi: 10.3389/fenrg.2021.664345

INTRODUCTION

Fully Ceramic Microencapsulated (FCM) fuel is a new concept proposed by the Oak Ridge National Laboratory (ORNL) as a fuel with enhanced accident tolerance (Terrani et al., 2012). FCM fuel which microencapsulated TRISO particles in silicon carbide (SiC) matrix is an integrated fuel designed to replace the traditional pellet-cladding fuel rod. The fuel design can effectively solve the problems of LWR fuel, such as water side corrosion, abrasion, stress corrosion cracking (Olander, 2009). Moreover, FCM fuel design has the advantages of high thermal conductivity (Powers and Wirth, 2010; Terrani et al., 2012), lower swelling and high fission products capability (Boer et al., 2011; Fernández, 2011; Chun et al., 2015; Lee and Cho, 2015), which is one of the most promising ATF fuels candidate (Olander, 2009). FCM can be used in different kinds of reactors such as LWR, SMR (Olander, 2009).

TRISO particle possessed complex multi-layered coating structure, including uranium dioxide kernel, porous pyrolytic carbon layer (Buffer), inner pyrolytic carbon layer (IPyC), silicon carbide layer (SiC) and outer pyrolytic carbon layer (OPyC). The function of the coated layers was designed: buffer layer is mainly designed to absorb fission fragments, reduce radiation damage to outer layers, offered space for accommodating irradiation swelling of uranium dioxide kernel and fission gas. IPyC layer is mainly used to prevent the contact of fission products with SiC, which results in the corrosion of SiC layer caused by fission products. The SiC layer mainly acts as a pressure bearing layer, providing enough mechanical strength for TRISO particles. OPyC layer protects SiC layer from damage (Powers and Wirth, 2010; Williamson et al., 2012; Collin, 2014).

Because of the multiple coating structure of TRISO particles, irradiation-thermal-mechanical phases in application environment, and complex non-line contacting and deformation between TRISO particle and SiC matrix, FCM fuel exhibits complex in-pile behavior (Terrani et al., 2012). A number of efforts have been devoted to studying the FCM fuel performance with focuses on neutronics (Fernández, 2011), thermal-neutronics coupling (Lee and Cho, 2015) accident safety (Boer et al., 2011; Chun et al., 2015). The heterogeneous composition of this fuel design leads to difficulty with thermal and mechanical analyses. Some HTR fuel performance code was used in particle level analyses and provided 1D results of material performance (Collin, 2014; Chun et al., 2015). Chen et al., (2019) (Williamson et al., 2012) investigates the mechanical behavior of SiC layer and SiC matrix, with using 2D homogeneous model and introducing the interaction between TRISO and matrix. Zhou et al. (2020) discuss the effect of spacing of TRISO and size of no-fuel area on integrality of FCM. The result shows that the stress in SiC layer would release by reducing the spacing of TRISO.

Accurate and reliable fuel behavior prediction is not only necessary for reactor safety calculation, fuel design requirements, but also for fuel performance evaluation. In this research, the irradiation-thermal-mechanical coupling behavior of FCM fuel was simulated based on the ABAQUS software. 1/4RVE (representative volume model) was established to calculate the deformation and mechanical behavior of FCM fuel. Properties variation of the related materials was considered.

MATERIAL PROPERTY

Gas and solid swelling of UO_2 kernel is a function ofburnup (MacDonald and Thompson, 1976), Fuel densification occurs in the early stage of irradiation, the densification of UO_2 is also a function ofburnup (MacDonald and Thompson, 1976), Thermal expansion of $UO_2$is a function of temperature (MacDonald and Thompson, 1976)Lucuta modified model which suitable for both low and high burnup stage is adopted as the thermal conductivity model of UO_2kernel, The model takes into account the effects of temperature, fuel densification, fission products and porosity on thermal conductivity (Lucuta et al., 1996). Young's modulus of UO_2 fuel is taken as a constant 219,000 MPa, Poisson's ratio is 0.345 (Hales et al., 2013), density is 10.96 g/cm^3.

Young's modulus, Poisson's ratio, density, specific heat and thermal conductivity of porous pyrolytic carbon materials are 20,000 MPa, 0.23, 1.0 g/cm^3, 720 J/kg K, and 0.5 W/m K (MacDonald and Thompson, 1976) respectively. Irradiation swelling of porous pyrolytic carbon materials is isotropic, which is different with dense pyrolytic carbon materials. The radial and hoop swelling strain are the same in spherical coordinates (Hales et al., 2013):

$$\dot{\varepsilon}_r = \dot{\varepsilon}_t = -0.176e^{(-1.75\Phi)} \tag{1}$$

Φ is thefast neutron fluence, (in 10^{25} n/m^2).

Creep rate of porous pyrolytic carbon materials is (Hales et al., 2013):

$$\dot{\varepsilon}_{cr} = K[\sigma_1 + \nu_c(\sigma_2 + \sigma_3)]\dot{\Phi} \tag{2}$$

ν_c is the Poisson's ratio of creep, $\nu_c = 0.5$, $\dot{\Phi}$ indicates fast neutron flux, (in 10^{25} n/(m^2 s)), σ_1, σ_2, σ_3 are the principal stresses in three directions.

$$K = K_0\left[1 + 2.38\left(1.9 - \rho\right)\right]M_{irr,crep} \tag{3}$$

$$K_0 = 1.996 \times 10^{-29} - 4.415 \times 10^{-32}T + 3.6544 \times 10^{-35}T^2) \tag{4}$$

$M_{irr,crep} = 2$, ρ is density of porous pyrolytic carbon, 1.0 g/cm^3; T is temperature, (in Celsius).

Young's modulus, Poisson's ratio, density, specific heat and thermal conductivity for SiC are 340 GPa, 0.13, 3.18 g/cm^3, 620 J/kg K, and 13.9 W/m K (Snead et al., 2007) respectively. Thermal expansion coefficient of SiC is a function of temperature (Snead et al., 2007), Radiation creep of SiC is expressed by the following empirical correlation (Snead et al., 2007):

$$\dot{\varepsilon}_{creep} = K_1\dot{\Phi}\sigma_e \tag{5}$$

K_1 is set as a constant 0.4×10^{-31}n/m^2/MPa, $\dot{\Phi}$ indicates fast neutron flux, [in n/(m^2·s)], σ_e is effective stress.

Young's modulus, Poisson's ratio, density, specific heat and thermal conductivity for dense pyrolytic carbon materials are 470,000 MPa, 0.23, 1.9 g/cm^3, 720 J/kg K and 4 W/m K (Hales et al., 2013) respectively, the yield strength is set as 137 MPa.Radiation swelling of dense pyrolytic carbon is anisotropic, and the radial and hoop radiation swelling are different in spherical coordinates as follows (Hales et al., 2013):

$$\dot{\varepsilon}_r = -0.077e^{(-\Phi)} + 0.031 \tag{6}$$

$$\dot{\varepsilon}_t = -0.036e^{(-2.1\Phi)} - 0.01 \tag{7}$$

Strain unit is 1/(10^{25} n/m^2), Φ indicates fast neutron fluence, (in 10^{25} n/m^2).

Creep rate of dense pyrolytic carbon materials is (Hales et al., 2013):

$$\dot{\varepsilon}_{cr} = K[\sigma_1 + \nu_c(\sigma_2 + \sigma_3)]\dot{\Phi} \tag{8}$$

ν_c indicates Poisson's ratio, $\nu_c = 0.5$, $\dot{\Phi}$ indicates fast neutron flux, (in 10^{25} n/m^2), σ_1, σ_2, σ_3 are the principal stresses in three directions.

$$K = K_0\left[1 + 2.38\left(1.9 - \rho\right)\right]M_{irr,crep} \tag{9}$$

$$K_0 = 1.996 \times 10^{-29} - 4.415 \times 10^{-32}T + 3.6544 \times 10^{-35}T^2) \tag{10}$$

$M_{irr,\ cerrep} = 2$; ρ is density of dense pyrolytic carbon materials, 1.9 g/cm^3; T is temperature, (in Celsius).

During the irradiation process, gap will be formed between Buffer and IPyC layer and filled with fission gas. The gap thermal transfer coefficient is expressed as follows (Hales et al., 2013):

$$h_{gap} = h_g + h_r \tag{11}$$

where, h_{gap} is gap thermal transfer coefficient, (in W/m^2 K), h_g indicates thermal transfer coefficient of fission gas, (in W/m^2 K), h_r indicates the radiation thermal transfer coefficient, (in W/m^2 K), detailed input parameters can be found in the reference (MacDonald and Thompson, 1976).

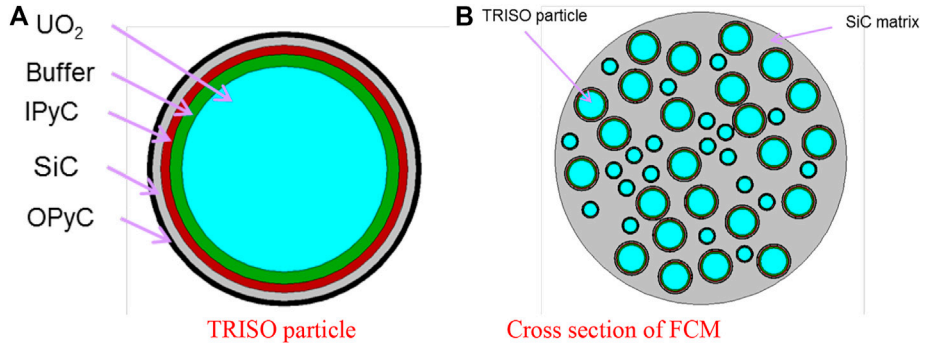

FIGURE 1 | Schematic of FCM structure. **(A)** TRISO particle **(B)** Cross section of FCM.

During the irradiation process, fission gas will generate in the UO_2 kernel and release into the Buffer layer. Because of the low temperature of M3 fuel, the fission gas released mainly as non-thermal way. In the simulation, it is assumed that the fission gas release rate is 10%, regardless of the fuel depletion effect. The Ideal Gas law is used to calculate the gas pressure in the Buffer layer. CO is mainly generated by the combination of carbon atoms and oxygen atoms that diffuse from UO_2 kernel to the Buffer layer. Generation rate is calculated by Proksch model (Hales et al., 2013):

$$\frac{O}{F} = \frac{t^2}{(1.211 \times 10^{10})10^{8500/T}} \tag{12}$$

where, O/F is the average number of oxygen atoms released per fission, neglecting the generation of CO_2.

The Ideal Gas law equation is:

$$P = \frac{nRT}{V} \tag{13}$$

where, P is gas pressure, n is the number of moles of gas, R is the gas constant, T is temperature, V represents the free space volume between Buffer layer and IPyC (Including gap volume and porosity volume in Buffer layer, the porosity of Buffer layer is considered as 56%).

NUMERICAL MODEL

FCM consists of TRISO particles and matrix. TRISO particles owns a complex multi-layered coating structure, including UO_2 kernel, buffer layer, IPyC layer, SiC layer and OPyC layer from inside to outside. Numerous TRISO particles are contained in SiC matrix. **Figure 1** shows a typical structure of FCM.

The UO_2 kernel radius and thickness of buffer layer, IPyC layer, SiC layer and OPyC layer are 420.0, 50, 35, 35, 20 μm respectively. Volume fraction of TRISO particles is 45% in FCM pellet (the UO_2 volume fraction is 18.98%). Considering that FCM fuel is a dispersion fuel with complex structure, it is difficult to model and simulation the whole fuel. In order to analyze the radiation-thermal-mechanical coupling performance of FCM

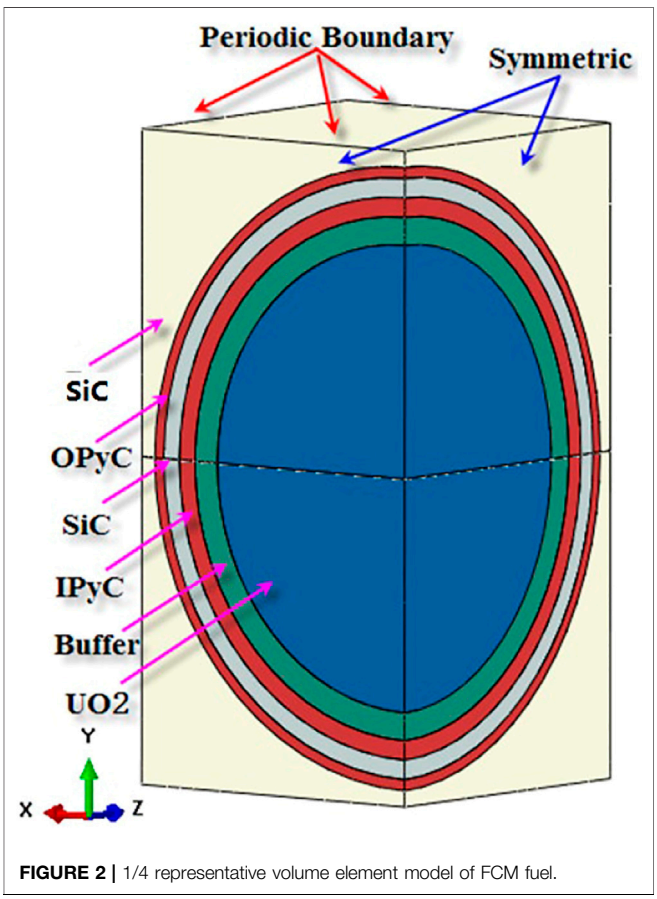

FIGURE 2 | 1/4 representative volume element model of FCM fuel.

fuel, it is necessary to extract representative volume element (RVE) from FCM fuel for simulation analysis. Assuming that the minimum FCM fuel representative volume element (RVE) edge length is L (μm), the TRISO volume is Vf and the TRISO particle radius is R (μm), when TRISO particles are uniformly distributed in the SiC matrix, the relationships among them are as follows:

$$Vf = \frac{(4/3)\pi R^3}{L^3} \tag{14}$$

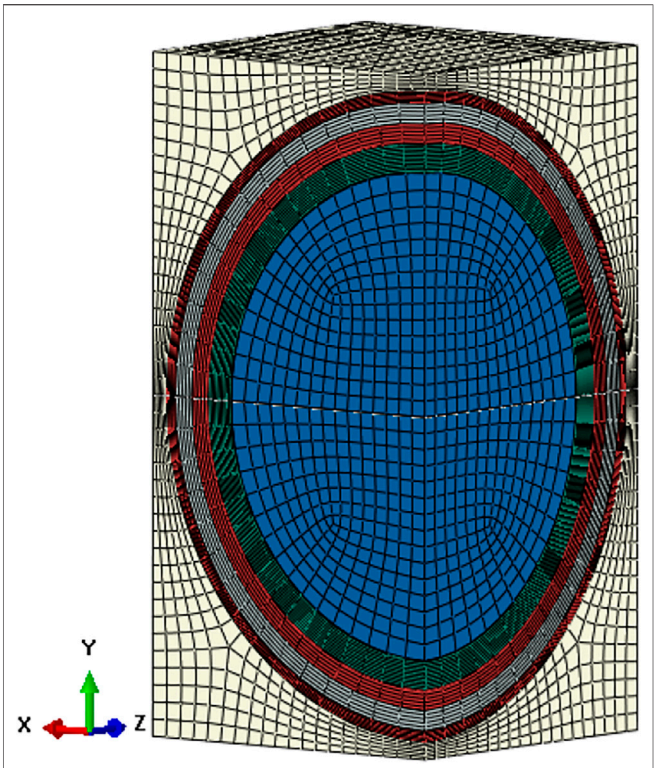

FIGURE 3 | Mesh model of 1/4 RVE of FCM fuel.

According to the above equation, the minimum RVE edge length L is 900 μm. Based on the symmetry of RVE, a 1/4 RVE model is established as shown in **Figure 2**. The two sections are defined as symmetrical boundary conditions in Cartesian coordinate system (three-dimensional rectangular coordinate system in global space). Considering the high thermal conductivity of FCM fuel, for simplification, the external surface of RVE is set a fixed temperature boundary condition (698 K, 100 K higher than the coolant temperature). The IPyC layer and Buffer layer are closely connected, and the boundary condition between the two layers is isothermal. Initial zero stress temperature of the whole FCM fuel RVE is 300 K. The linear power of FCM fuel is 200 W/cm, fuel diameter is 9 mm. Two situation cases are simulated in this research work. In first case, the steady operation lasts for 1,100 days, and then followed by a power transient for 9 s, with the power jumping from 100%FP to 150%FP. In the another case, the steady operation lasted for 1,100 days, and then followed by a water loss accident for 200 s, the power decreased from 100 to 10% FP, and the coolant temperature increased from 698 to 1473 K. Assuming that the fast neutron fluence in the end of steady operation reaches at 9.5×10^{21} n/cm^2.

Due to the complexity of FCM fuel material models such as irradiation swelling, irradiation creep and thermal conductivity, it is difficult to input them in a simple interface. In this simulation, the complex material model is introduced into the finite element simulation calculation by compiling corresponding user-defined subroutines UMAT (customized material constitutive relation subroutine), GAPCON (gap thermal conduction subroutine), DLOAD (gap pressure subroutine) and so on. The analysis step type is transient complete temperature displacement coupling analysis step. The element type is implicit first-order temperature displacement coupling element.

Three types of mesh number, including 6,240, 12,023 and 24,960, have been adapted to investigate the mesh independence. The results show that the data deviation of temperature, stress and strain caused by different mesh number is less than 2%. Considering the precision and effectiveness of computation, the mesh number of whole model is set to 12,023 and the number of nodes is 15,180 as **Figure 3** shows.

VERIFICATION

The verification for FCM fuel is difficult for lacking of experiment data. Therefore a code to code verification is chosen to verify this simulation. According to the open literature, BISON is an advanced three dimension fuel performance code, and the BISON has been used to simulate the irradiation-thermal-mechanical performance of TRISO fuel in published literature. Based on the numerical simulation method established in this study, if the effect of matrix is not considered, it can be directly used to simulate the performance of TRISO fuel. According to the simulation results, the results obtained by the numerical simulation method established in this study are consistent with those obtained by BISON, The specific comparison results can be seen in the previous published articles (Changbing et al., 2019). The validity of this numerical simulation method has been verified and can be used for this study.

RESULTS AND DISCUSSION

Temperature Result

Figure 4 shows the temperature distribution contour of FCM fuel RVE model at the beginning, end of irradiation, power transient and LOCA conditions. According to the temperature distribution contour, the maximum temperature of the fuel is always maintained at the center of the RVE model. Under the steady operation condition, the temperature difference between the center of the RVE model and the outer surface is about 70 K. The difference of the maximum temperature at the beginning and the end of irradiation is about 20 K, and the temperature at the end of irradiation is higher. The maximum temperature increases about 55 K under power transient condition, and the whole temperature increases significantly under LOCA condition. The reason for the above phenomenon is that center UO_2 particle produces heat, so the highest temperature appears in the center. The thermal conductivity of fuel decreases with the increase of burnup, so the maximum temperature at the end of irradiation increases. In the power transient, the temperature rises due to the increase of heat generation, and the whole temperature rises due to the loss of external coolant in the LOCA condition.

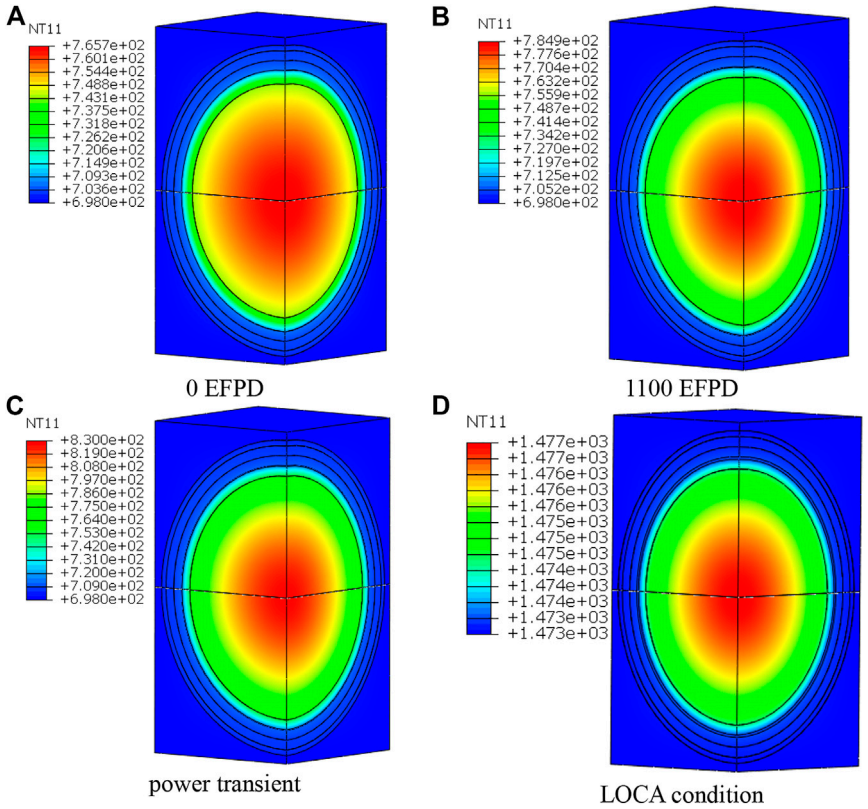

FIGURE 4 | Temperature distribution contour of FCM fuel RVE model under different conditions (EFPD, Effective Full Power Day). **(A)** 0 EFPD. **(B)** 1100 EFPD. **(C)** power transient. **(D)** LOCA condition.

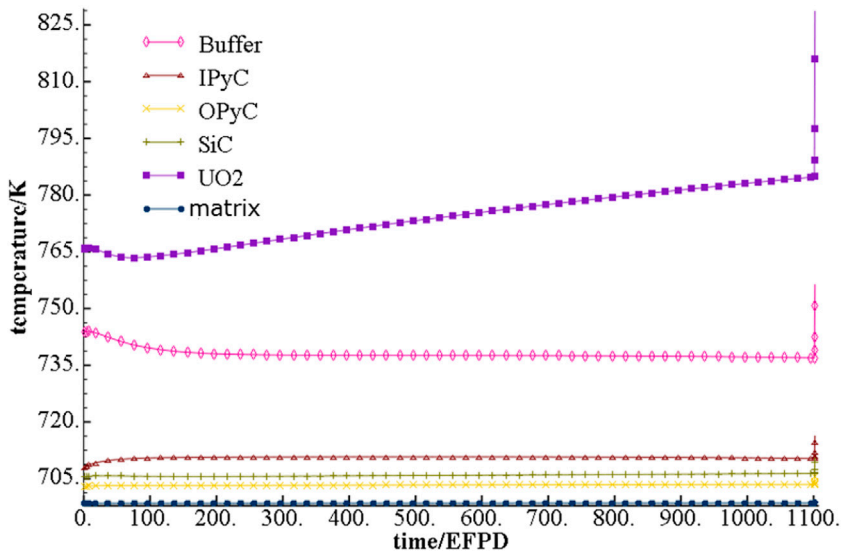

FIGURE 5 | Maximum temperature of each layer of material variation under steady operation condition and power transient condition.

The variation of the maximum temperature of each layer under steady operation and power transient conditions as shown in **Figure 5**. According to the variation results, it can be seen that the temperature change of UO_2 fuel and buffer layer is more obvious for the power transient, while the temperature change of other layers is not obvious. The results are related to

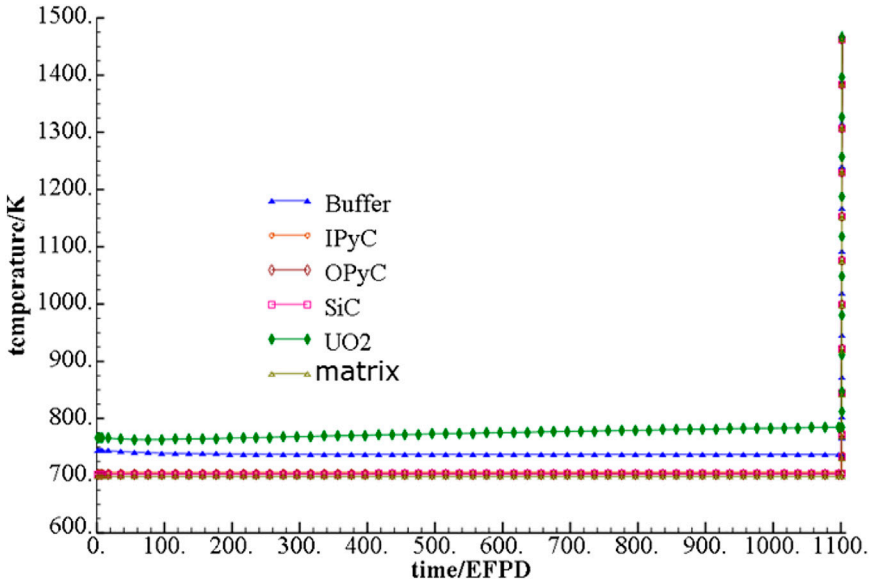

FIGURE 6 | Max temperature of each layer of material variation under steady operation condition and LOCA condition.

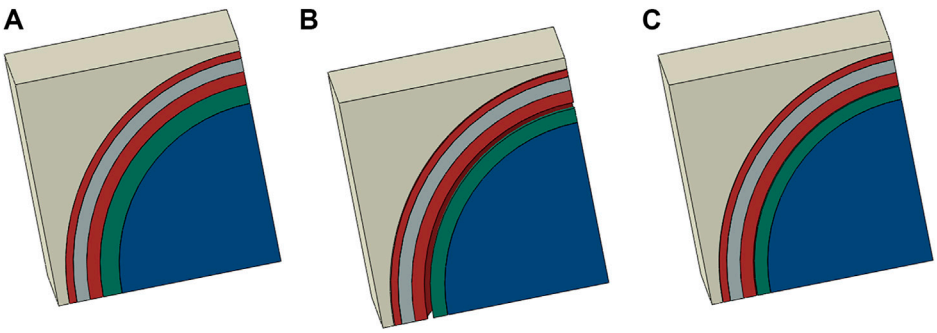

FIGURE 7 | Structural changes of FCM fuel RVE model at different irradiationtime. **(A)** 0 EFPD. **(B)** 200 EFPD. **(C)** 1,100 EFPD.

two factors. On the one hand, the higher the thermal conductivity of the material, the less obvious the transient change of fuel power. Because the thermal conductivity of UO_2 and buffer is relatively low, they are more sensitive to the change of temperature. On the other hand, the gap heat transfer ability is poor, so the UO_2 and buffer inside the gap are more sensitive to the change of temperature.

The max temperature of each layer of material variation under steady operation condition and LOCA condition is shown in **Figure 6**. According to the variation results, it can be seen that the temperature of each layer will rise significantlyunder LOCA conditions. The reason for this phenomenon is that under LOCA conditions, the heat production of fuel particle decreases, and the fuel pellet temperature will rise rapidly due to the loss of coolant.

Geometry Change Result

The simulation results show that the corresponding structural changes of FCM fuel RVE model at the 0 EFPD, 200 EFPD and 1,100 EFPD are shown as **Figure 7**. According to the deformation results of the structure, it can be seen that the layers of the structure keep close bonding at the initial stage of irradiation. With the increase of irradiation time, there is a gap occurs between the buffer and ipyc layer, which still exists at the end of irradiation time. The reason for this phenomenon is that the buffer layer and ipyc layer will shrink under irradiation, so the gap will appear at the interface due to the irradiation shrinkage.

The change curves of buffer outer diameter and IPyC inner diameter in steady operation stage are shown in the **Figure 8**. According to **Figure 8**, it can be seen that the outer diameter of Buffer layer first decreases and then gradually increases with the increase of irradiation time, while the inner diameter of the IPyC layer is opposite to the change trend of the outer diameter of the Buffer layer, which first increases and then gradually decreases with the increase of irradiation time. The outer diameter change trend of Buffer layer is caused by radiation shrinkage of buffer

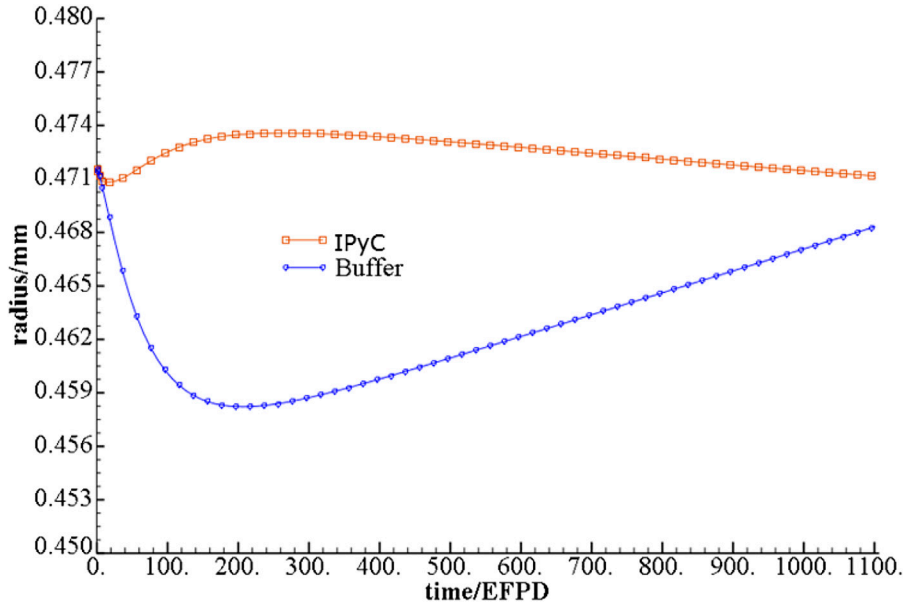

FIGURE 8 | Buffer outer diameter and IPyC layer inner diameter variation with EFPD.

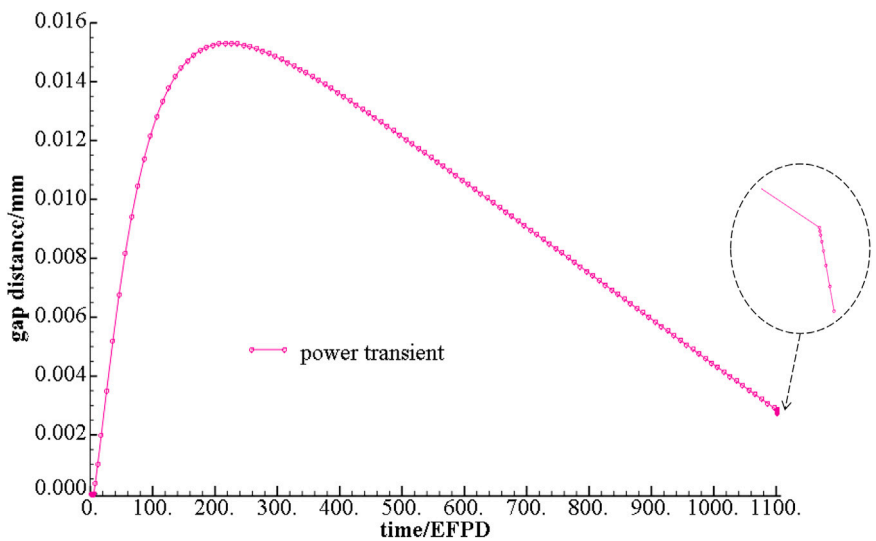

FIGURE 9 | Variation of gap distance with EFPD under power transient condition.

and radiation swelling of UO_2, and the inner diameter change trend of IPyClayer is mainly caused by radiation shrinkage at initial stage of irradiation and radiation swelling at middle and late stage of irradiation.

The difference between the inner diameter of IPyC layer and the outer diameter of Buffer layer is the gap distance. The variation of gap distance during steady operation and power transient condition is shown in **Figure 9**. The results show that the gap distance increases first and then decreases gradually with the increase of operation time at steady operation condtion. In the power transient condition, due to the larger thermal expansion of UO_2, the gap will decrease slightly.

Stress Change Result

The hoop stress contour of FCM fuel RVE model at the initial stage of irradiation time, the end of irradiation time, power transient condition and LOCA condition are shown in **Figure 10**. According to the hoop stress distribution contour, it can be seen that the hoop stress distribution of each layer is obviously different. For stress analysis of FCM fuel, it is usually

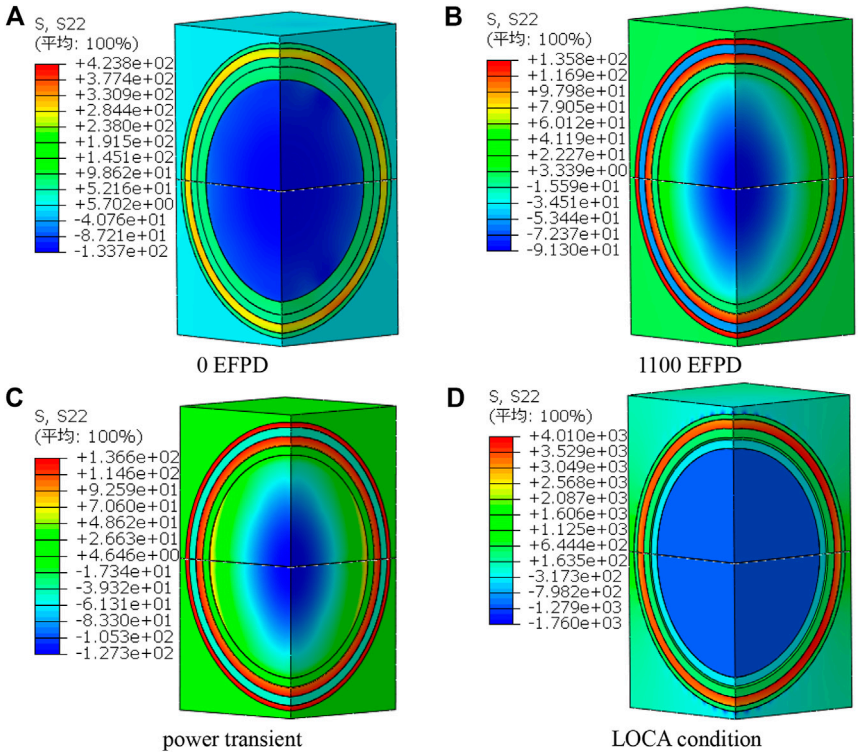

FIGURE 10 | hoop stress distribution contour of RVE model under different conditions. **(A)** 0 EFPD. **(B)** 1,100 EFPD. **(C)** Power transient. **(D)** LOCA condition.

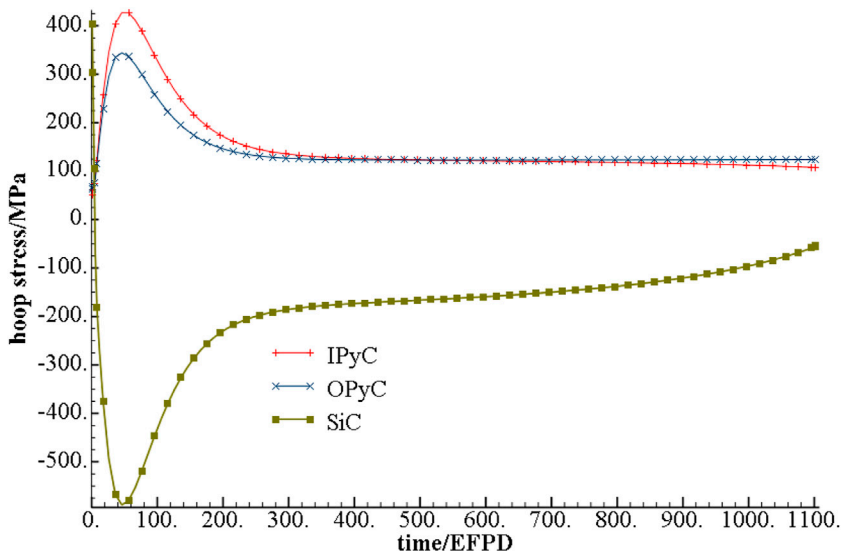

FIGURE 11 | Hoop stress of the PyC layer and SiC layer variation with EFPD under power transient condition.

more concerned about the hoop stress on PyC layer and SiC layer, which directly affects the corresponding structural integrity.

Hoop stress of PyC layer and SiC layer variation with EFPD under steady operation condition and power transient condition as shown in **Figure 11**. According to **Figure 11**, it can be seen that in the steady operation period, the hoop stress of PyC layer first increases, then decreases, and finally tends to be stable with the increase of irradiation time. However, the hoop stress of SiC layer is just opposite to that of PyC layer, with the increase of operation time, the hoop stress first decreases, then increases, and finally

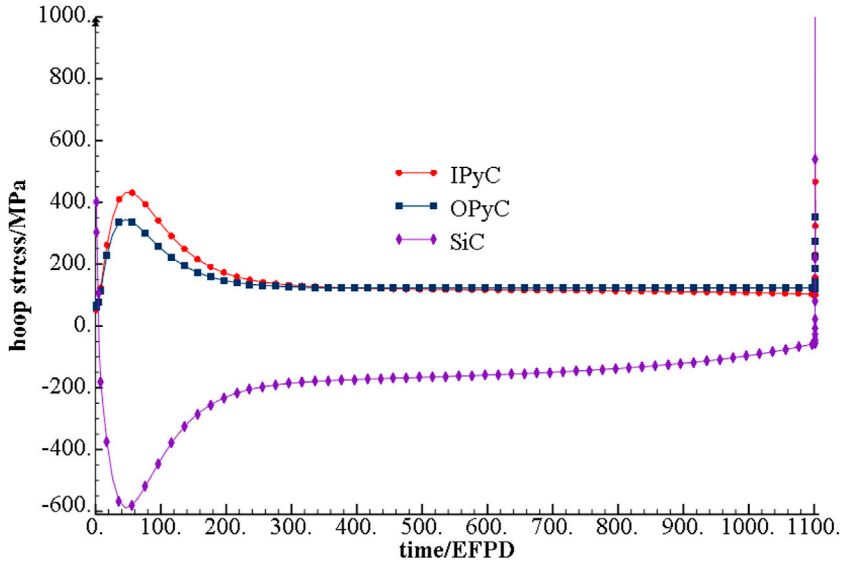

FIGURE 12 | Hoop stress of the PyC layer and SiC layervariation with EFPD under LOCA condition.

tends to be stable. At the beginning, the internal stress value of each layer is mainly caused by the difference of thermodynamic properties and irradiation properties of each layer, and then the stress value tends to be stable, mainly due to the creep effect of each layer. The hoop stress of the PyC layer and SiC layer is not sensitive to the power transient, and the stress change is very small under the power transient.

Hoop stress of PyC layer and SiC layer variation with EFPD under steady operation condition and LOCA condition as shown in **Figure 12**. According to **Figure 12**, it can be seen that the hoop stress of PyC layer and SiC layer is sensitive to LOCA condition. Under LOCA condition, the hoop stress changes greatly, resulting in large tensile stress and structural damage. Under LOCA condition, the overall temperature of FCM fuel rises rapidly. Due to the difference of thermodynamic properties of each materials, large stress will be produced in it. When the stress reaches a certain value, it may lead to the structural failure of FCM fuel.

The gas produced by UO_2 fission would be released into the gap, which will lead to obvious gap pressure. Gap pressure variation with EFPD under steady operation condition as shown in **Figure 13**. According to **Figure 13**, it can be seen

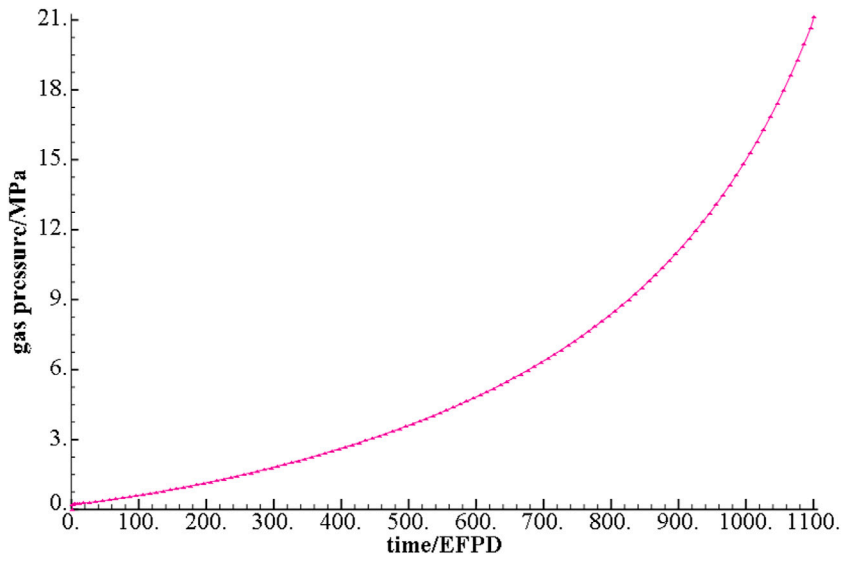

FIGURE 13 | Gap pressure variation with EFPD under steady operation condition.

that with the increase of irradiation time, the gap pressure increases gradually. The maximum gap pressure appears at the end of irradiation time, and the corresponding value is about 21 MPa. According to the operation experience of high temperature gas cooled reactor, TRISO particles can still maintain its structural integrity when the internal gap pressure reaches about 50 MPa. Therefore, it can be inferred that the gap pressure will not lead to the structural failure of TRISO particles, which is consistent with the previous stress analysis results.

CONCLUSION

In this research, three-dimensional model was established to simulate the irradiation-thermal-mechanical coupling behavior of FCM fuel by using ABAQUS software. The results indicated that:

(1) The temperature difference in FCM is small under steady operation and power transient, except for temperature change of UO_2 fuel and buffer layer due to power transient. The temperature of whole fuel will rise significantly under LOCA conditions.
(2) In the steady operation period, the hoop stress of PyC layer first increases, then decreases, and finally tends to be stable with the increase of irradiation time. However, the hoop stress of SiC layer is just opposite to that of PyC layer, with the increase of operation time, the hoop stress first decreases, then increases, and finally tends to be stable. The hoop stress of the PyC layer and SiC layer is not sensitive to the power transient, but sensitive to the LOCA condition.
(3) The pressure of gap would rise under steady operation and achieve about 21 MPa at the EOL, which could not result in structure failure of TRISO particles. Meanwhile, the gap increases initially and then decreases under steady operation. For power transient, the gap will decrease slightlydue to the larger thermal expansion of UO_2.

The establishment of this numerical simulation method could provide guidance for the optimization design and performance prediction of FCM fuel. In the following study, the SiC fracture and its influence on Csdiffusivitywill also be introduced into numerical simulation to simulate more accurate radiation-thermal-mechanical coupling performance of FCM fuel.

DATA AVAILABILITY STATEMENT

The raw data supporting the conclusion of this article will be made available by the authors, without undue reservation.

AUTHOR CONTRIBUTIONS

TC is responsible for numerical simulation modeling and calculation of FCM fuel, data processing, part of the article writing. JY is responsible for the guidance of the whole simulation technology. The rest of the authors are responsible for the preparation and modification of the whole article and the drawing of related pictures.

FUNDING

This research was supported by the National Natural Science Foundation of China (U20B2013), National Key R&D Program of China (2018YFE0116100) and Science and Technology on Reactor System Design Technology Laboratory.

REFERENCES

Boer, B., Sen, R. S., Pope, M. A., and Ougouag, A. M. (2011). *Material Performance of Fully-Ceramic Micro-Encapsulated Fuel Under Selected LWR Design Basis Scenarios[R]*. Idaho Falls, ID: Idaho National Laboratory (INL).

Changbing, T., Yongjun, J., Yuanming, L., Yi, Z., and Hua, P. (2019). Preliminary Research on the Irradiation-Thermal-Mechanical Coupling Behavior Simulation Method of FCM Fuel. *Int. J. Adv. Nucl. Reactor Des. Tech.* 1, 51–56. doi:10.1016/j.jandt.2019.10.002

Chen, P., Qiu, S., Liu, S., and Zhou, Y. (2019). Preliminary Analysis of a Fully Ceramic Microencapsulated Fuel Thermal–Mechanical Performance[J]. *Computation* 8, 448–461. doi:10.3390/computation8010013

Chun, J.-H., Lim, S.-W., Chung, B.-D., and Lee, W.-J. (2015). Safety Evaluation of Accident-Tolerant FCM Fueled Core with SiC-Coated Zircalloy Cladding for Design-Basis-Accidents and beyond DBAs. *Nucl. Eng. Des.* 289, 287–295. doi:10.1016/j.nucengdes.2015.04.021

Collin, B. P. (2014). Modeling and Analysis of UN TRISO Fuel for LWR Application Using the PARFUME Code[J]. *J. Nucl. Mater.* 451 (1–3), 65–77. doi:10.1016/j.jnucmat.2014.03.032

Fernández, G. D. (2011). "Safety Aspects of Ceramic Fully Encapsulated Fuel for Light Water Reactors[D]," in *Universitat Politècnica de Catalunya. Escola Tècnica Superior d'Enginyeria Industrial de Barcelona* (Barcelona, Spain: Enginyeria Industrial).

Hales, J. D., Williamson, R. L., Novascone, S. R., Perez, D. M., Spencer, B. W., and Pastore, G. (2013). Multidimensional Multiphysics Simulation of TRISO Particle Fuel. *J. Nucl. Mater.* 443 (1), 531–543. doi:10.1016/j.jnucmat.2013.07.070

Lee, Y., and Cho, N. Z. (2015). Steady- and Transient-State Analyses of Fully Ceramic Microencapsulated Fuel Loaded Reactor Core via Two-Temperature Homogenized Thermal-Conductivity Model. *Ann. Nucl. Energ.* 76, 283–296. doi:10.1016/j.anucene.2014.09.027

Lucuta, P. G., Matzke, H., and Hastings, I. J. (1996). A Pragmatic Approach to Modelling Thermal Conductivity of Irradiated UO2 Fuel: Review and Recommendations. *J. Nucl. Mater.* 232 (2), 166–180. doi:10.1016/s0022-3115(96)00404-7

MacDonald, P. E., and Thompson, L. B. (1976). *MATPRO: A Handbook of Materials Properties for Use in the Analysis of Light Water Reactor Fuel Rod Behavior[R]*. Idaho Falls, ID: Idaho National Laboratory(INL).

Olander, D. (2009). Nuclear Fuels - Present and Future. *J. Nucl. Mater.* 389 (1), 1–22. doi:10.1016/j.jnucmat.2009.01.297

Powers, J. J., and Wirth, B. D. (2010). A Review of TRISO Fuel Performance Models. *J. Nucl. Mater.* 405 (1), 74–82. doi:10.1016/j.jnucmat.2010.07.030

Snead, L. L., Nozawa, T., Katoh, Y., Byun, T.-S., Kondo, S., and Petti, D. A. (2007). Handbook of SiC Properties for Fuel Performance Modeling. *J. Nucl. Mater.* 371 (1), 329–377. doi:10.1016/j.jnucmat.2007.05.016

Terrani, K. A., Snead, L. L., and Gehin, J. C. (2012). Microencapsulated Fuel Technology for Commercial Light Water and Advanced Reactor Application [J]. *J. Nucl. Mater.* 427 (1–3), 209–224. doi:10.1016/j.jnucmat.2012.05.021

Williamson, R. L., Hales, J. D., Novascone, S. R., Tonks, M. R., Gaston, D. R., Permann, C. J., et al. (2012). Multidimensional Multiphysics Simulation of Nuclear Fuel Behavior. *J. Nucl. Mater.* 423 (1), 149–163. doi:10.1016/j.jnucmat.2012.01.012

Zhou, Y., Xiao, Z., Liu, S., Chen, P., Pang, H., Xin, Y., et al. (2020). Effect of Structure on the Thermal-Mechanical Performance of Fully Ceramic Microencapsulated Fuel. *Computation* 8, 13–28. doi:10.3390/computation8010013

Conflict of Interest: CT, YL, YJ, KZ, PW were employed by Nuclear Power Institute of China.

frontiers in Energy Research

ORIGINAL RESEARCH
published: 13 May 2021
doi: 10.3389/fenrg.2021.620970

Investigation on Rod Bundle CHF Mechanistic Model for DNB and DO Prediction Under Wide Parameter Range

Wei Liu, Shinian Peng, Guangming Jiang and Yu Liu*

State Key Laboratory of Reactor System Design Technology, Nuclear Power Institute of China, Chengdu, China

For a water cooled reactor, the key thermal-hydraulic parameters span a wide range corresponding to different CHF regimes. Under accident conditions, due to the flow regime transition and interchannel mixing effect, the corresponding CHF can transition from the DO to DNB regime. In order to continuously and accurately predict DNB and DO regime CHF under wide parameter range for rod bundle channel, a comprehensive CHF mechanistic model covering the DNB and DO regime CHF prediction is established based on the rod bundle CHF-regime criterion. The DNB regime CHF mechanistic model of superheated liquid layer depletion under turbulence fluctuation bubbles and the mature DO regime CHF mechanistic model are combined to form the comprehensive CHF model. Furthermore, the comprehensive CHF model is assessed by 5 × 5 rod bundle CHF experimental data independently obtained by the Nuclear Power Institute of China (NPIC). The statistical evaluation and parametric trend analysis show that the maximum mean error of P/M is within ±22%, and the local pressure, mass flux, and quality do not have any effects on the average deviations of the predicted flux P from the measured flux M. This indicates that the comprehensive CHF mechanistic model can accurately and continuously predict the DNB and DO regime CHF in the rod bundle channel.

Keywords: departure from nucleate boiling, dryout, rod bundle channel, critical heat flux, mechanistic model

OPEN ACCESS

Edited by:
Jinbiao Xiong,
Shanghai Jiao Tong University, China

Reviewed by:
Liangming Pan,
Chongqing University, China
Ivo Kljenak,
Institut Jožef Stefan (IJS), Slovenia

****Correspondence:***
Wei Liu
liuwei0958@126.com

Specialty section:
This article was submitted to Nuclear Energy, a section of the journal Frontiers in Energy Research

Received: *24 October 2020*
Accepted: *23 April 2021*
Published: *13 May 2021*

Citation:
Liu W, Peng S, Jiang G and Liu Y (2021) Investigation on Rod Bundle CHF Mechanistic Model for DNB and DO Prediction Under Wide Parameter Range. Front. Energy Res. 9:620970. doi: 10.3389/fenrg.2021.620970

INTRODUCTION

Critical heat flux (CHF) is an important thermal safety limit in the research and development of nuclear fuel assemblies and reactor thermal-hydraulic design and safety analysis. According to the different flow regimes and heat transfer characteristics corresponding to CHF, the flow boiling crisis in rod bundle channel can be divided into DNB regime and dryout (DO) regime (Tong, 1967).

For the pressurized water reactor (PWR), subcooled nucleate boiling occurs at the hot channel exit under normal operation conditions. Thus, the DNB regime CHF is the most likely to occur due to the low vapor quality in the channel. Under accident conditions, there are several kinds of flow regimes existing in the rod bundle channel. Moreover, due to the interchannel mixing mechanisms (Xiong et al., 2020) and the cross flow caused by the mixing vanes between adjacent open channels (Qu et al., 2019), the flow regime

Abbreviations: CHF, critical heat flux; DNB, departure from nucleate boiling; DO, dryout; HP, high pressure; NPIC, Nuclear Power Institute of China; PWR, pressurized water reactor.

could transition from annular flow to bubble flow or slug flow. Accordingly, the corresponding CHF will also transition from the DO to DNB regime (Yang et al., 2019), as shown in **Figure 1**.

In addition, under the normal operation and accident conditions of PWR, the key thermal-hydraulic parameters span a wide range. For example, the pressure ranges from 2 to 17 MPa, the mass flux ranges from several hundred to nearly 5,000 kg/m^{2}s, and the corresponding equilibrium quality ranges from −0.2 to 0.5. Obviously, such a wide range of thermal-hydraulic parameters may cover different CHF regimes (Groeneveld et al., 2018).

At present, due to the complex nature of two-phase flow with heat transfer in the rod bundle channel, the method for rod bundle CHF prediction is mainly CHF empirical correlation. In the development of CHF correlation, there is no classification for DNB and DO regime CHF conditions while all the CHF experimental data are put together to develop the CHF correlation (Chai et al., 2003). Moreover, once the application scope and original object of CHF empirical correlation are exceeded, the prediction accuracy will be significantly reduced. In addition, since the CHF empirical correlation usually depends on the specific correction factors, it has great uncertainty when it is extended to the condition lacking of CHF experimental data (Weisman and Pei, 1983).

Although extensive research has been carried out on CHF mechanisms and obtained several representative CHF mechanistic models with relatively high prediction accuracy (Zhang and Hewitt, 2016; Liu et al., 2020b), these CHF mechanistic models are all developed for a specific flow regime and often only applicable to DNB or DO regime CHF prediction. Obviously, the CHF prediction ability is limited to the flow or CHF regime. As Zeigarnik (Zeigarnik, 1996) pointed out, there is no universal flow boiling CHF mechanistic model that can predict CHF in the regimes of high subcooled, low subcooled, and saturated. Because there are different flow regimes and heat transfer modes in such a wide span range, only the main process can be modeled.

At present, different comprehensive CHF mechanistic models have been developed for prediction of DNB and DO regime CHF in round tubes (Kataoka et al., 1997; Kodama and Kataoka, 2002; Liu et al., 2019). However, the void fraction or quality is often used as the classification criterion for different CHF regimes in most of these comprehensive CHF mechanistic models. The accuracy and reliability of the CHF classification criterion still need further study.

Due to the complex nature of CHF phenomenon, the challenges of experimental measurement technology, and the characteristics of wide parameter range across different CHF regimes, the coexistence of various CHF mechanistic models at this stage seems reasonable and unchangeable.

In order to accurately and continuously predict the DNB and DO regime CHF in rod bundle channel under the wide parameter range, a feasible method is to classify the CHF conditions into different regimes and then establish the corresponding CHF mechanistic model based on the specific CHF-regime visualization phenomenon and mechanism hypothesis. Finally, different regimes of the CHF mechanistic model are combined to form the comprehensive CHF mechanistic model throughout the CHF-regime criterion.

In previous studies, the author has obtained the classification criterion for CHF conditions in the rod bundle channel with the dimensional analysis method (Liu et al., 2021a) and developed the DNB regime CHF mechanistic model of superheated liquid layer depletion under turbulence fluctuation bubbles (Liu et al., 2021b). In this study, a comprehensive CHF mechanistic model covering different regimes of CHF prediction will be established by using the existing research results and the mature DO regime CHF mechanistic model. The comprehensive CHF mechanistic model will be assessed by the 5 × 5 full-length rod bundle CHF experimental data independently obtained by the Nuclear Power Institute of China (NPIC), and the statistical evaluation and parametric trend analysis will be carried out by using statistical methods.

EXISTING ROD BUNDLE CHF RESEARCH RESULTS

Rod Bundle CHF-Regime Criterion

In order to correctly distinguish the rod bundle CHF regimes, a general dimensionless rod bundle CHF correlation is obtained based on the dimensional analysis method (Liu et al., 2021a). The real vapor quality, Katto number, and boiling length are introduced to establish the basic form of the dimensionless CHF correlation. According to the deep analysis of the distribution trend of typical CHF experimental data and the CHF characteristics of different CHF regimes, the CHF in rod bundle are separated into DO, DNB, and HP-DNB regimes. The dimensionless equations between the boundaries of each regime are established, and a clearly defined map of characteristic regimes of CHF in rod bundle is determined.

The equation of the dividing line between DO and DNB regimes is,

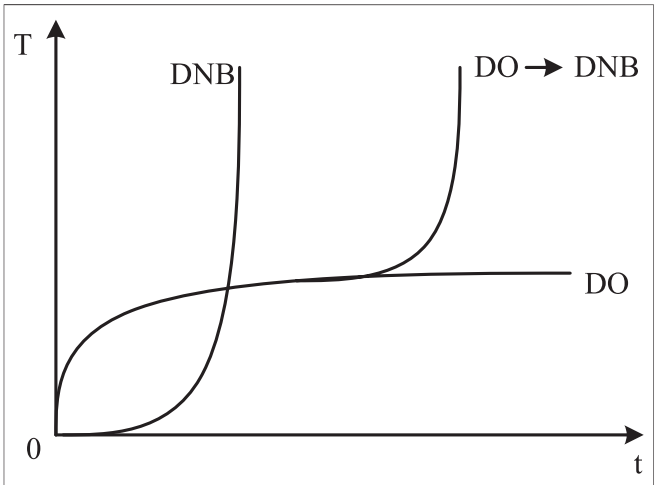

FIGURE 1 | Transition from DO to DNB regime CHF.

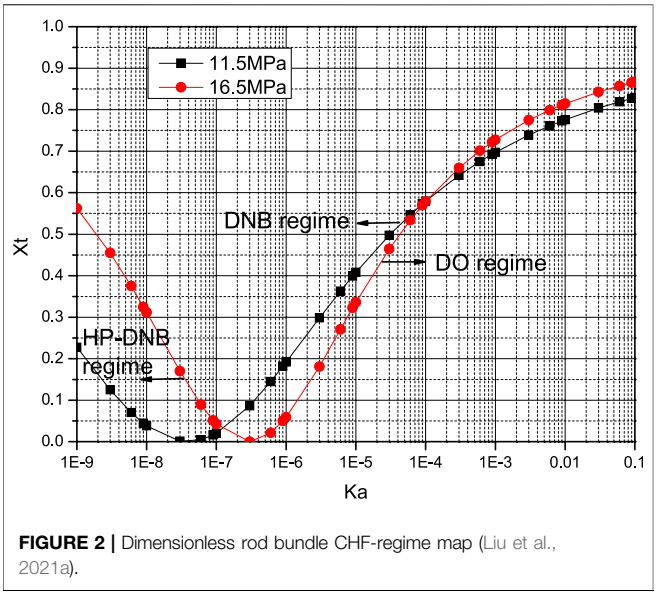

FIGURE 2 | Dimensionless rod bundle CHF-regime map (Liu et al., 2021a).

$$x_t = \left(\left(1.536\ln\left(\frac{0.1}{(\rho_v/\rho_l)^{0.516}Ka^{0.055}}\right)\right)^2\Big/ \times\left(\left(1.536\ln\left(\frac{0.1}{(\rho_v/\rho_l)^{0.516}Ka^{0.055}}\right)\right)^2+1\right)\right),$$

where $Ka = \sigma\rho_l/G^2 l$.

The equation of the dividing line between DNB and HP-DNB regimes is,

$$x_t = \frac{\left(\ln\left(\frac{1.863Ka^{0.06}}{(\rho_v/\rho_l)^{0.175}}\right)\Big/\left(0.651 - 0.786*(\rho_v/\rho_l)^{0.5}\right)\right)^2}{\left(\ln\left(\frac{1.863Ka^{0.06}}{(\rho_v/\rho_l)^{0.175}}\right)\Big/\left(0.651 - 0.786*(\rho_v/\rho_l)^{0.5}\right)\right)^2+1}.$$

Figure 2 shows the dimensionless rod bundle CHF-regime map for ρ_v/ρ_l of 0.1 (about 11.5 MPa) and 0.2 (about 16.5 MPa), respectively.

It can be seen from **Figure 2** that when the Katto number is large and real vapor quality is high, the CHF is corresponding to the DO regime. When the Katto number is small and real vapor quality is low, the CHF is corresponding to the DNB regime. The Katto number of the boundary point between DO and DNB regimes is about 10^{-7}. With the increase of pressure, the boundary point moves right, and the boundary line between DNB and HP-DNB regimes moves up. Consequently, the HP-DNB regime is expanded.

The above research results provide a theoretical basis for the classification of rod bundle CHF conditions.

DNB Regime CHF Mechanistic Model

Under subcooled and low quality flow boiling conditions, a general CHF mechanistic model is essential to the thermal-hydraulic design and safety analysis. Based on the mechanism of superheated liquid layer depletion (Chun et al., 2000; Liu et al., 2021c), the net mass transfer from the bulk liquid to the superheated liquid layer caused by turbulent velocity fluctuations of flowing bubbles is determined, and a new calculation method of superheated liquid layer thickness is developed (Liu et al., 2021b). After matching with other constitutive equations, a novel CHF mechanistic model for subcooled and low quality flow boiling conditions has been developed, as shown in **Figure 3**.

For a fixed axial control volume Δz in the superheated liquid layer, the mass conservation equation is:

$$m - (m + \Delta m) - \Delta m_{\text{evap}} + m_{\text{turb}} = 0,$$

where Δm_{evap} is the mass flow rate of evaporation and m_{turb} is the turbulent mass flow rate transported from bulk flow to the superheated liquid layer.

After simplification,

$$\Delta m = v^*\rho\pi D\Delta z - \frac{(q - q_{\text{conv}})\pi D\Delta z}{h_{fg}}.$$

The radial net two-phase mass exchange rate from the bulk flow to the superheated liquid layer caused by turbulent velocity fluctuations (Liu et al., 2021b) is determined as

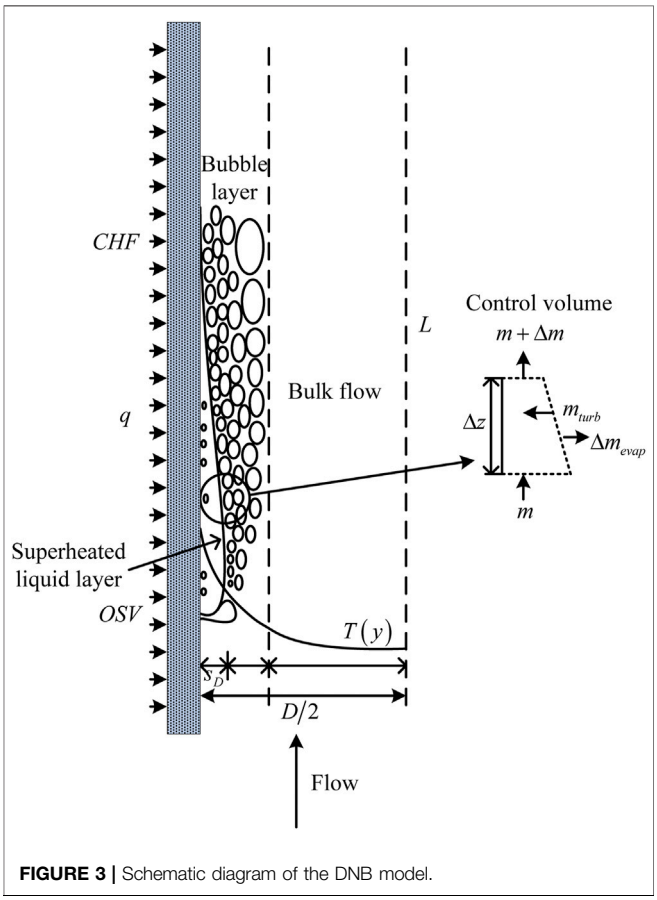

FIGURE 3 | Schematic diagram of the DNB model.

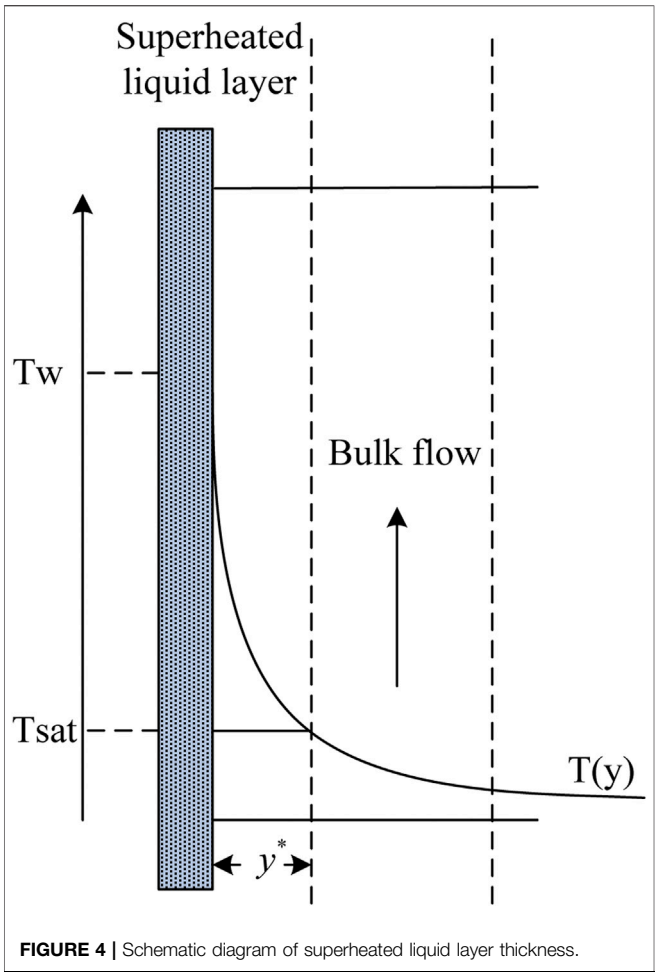

FIGURE 4 | Schematic diagram of superheated liquid layer thickness.

$$v^* = \sigma_{v'}\left(\frac{1}{\sqrt{2\pi}}e^{-\frac{1}{2}\left(\frac{V_{11}}{\sigma_{v'}}\right)^2} - \frac{1}{2}\left(\frac{V_{11}}{\sigma_{v'}}\right)erfc\left(\frac{1}{\sqrt{2}}\frac{V_{11}}{\sigma_{v'}}\right)\right),$$

where $\sigma_{v'}$ is the standard deviation of velocity fluctuations.

Then,

$$m_{\text{turb}} = v^*\rho\pi D\Delta z.$$

The calculation method of the superheated liquid layer thickness on the heating surface is proposed, as shown in **Figure 4**.

The superheated liquid layer thickness y* is obtained directly through thermal equilibrium temperature distribution in the rod bundle channel.

$$T(y^+) = T_w - QPry^+ \quad 0 \le y^+ < 5,$$

$$T(y^+) = T_w - 5Q\left\{Pr + 0.25\ln\left[1 + Pr\left(\frac{y^+}{5} - 1\right)\right]\right\} \quad 5 \le y^+ < 30,$$

$$T(y^+) = T_w - 5Q\left[Pr + 0.25\ln(1 + 5Pr) + \frac{1}{3}\ln\left(\frac{y^+}{30}\right)\right] \quad y^+ \ge 30,$$

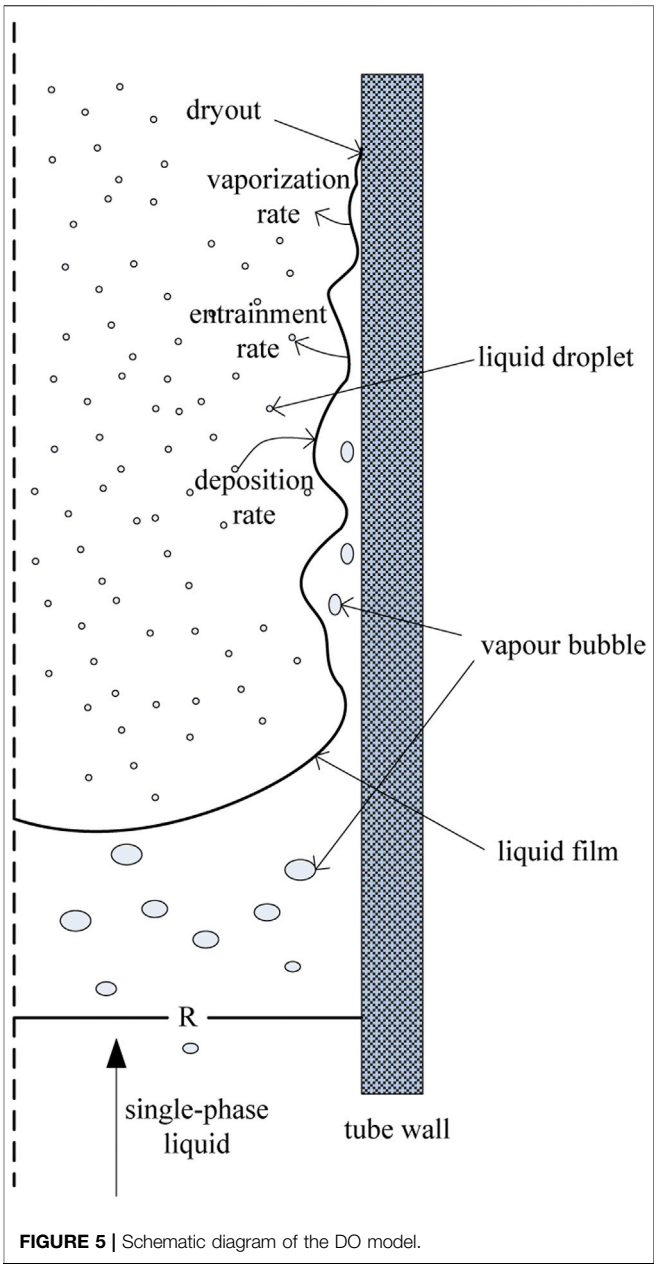

FIGURE 5 | Schematic diagram of the DO model.

where T_w is the wall temperature, Pr is the Prandtl number of the liquid, and Q is a function of the local heat flux, liquid density, specific heat capacity, and friction velocity.

This DNB model is suitable for rod bundle CHF prediction under subcooled and low quality flow boiling conditions.

DO Regime CHF Mechanistic Model

In annular flow, the dryout of liquid film is determined by a balance between the liquid film evaporation, liquid droplet entrainment, and deposition from the entrained core (Groeneveld, 2013), as shown in **Figure 5**.

In the steady state, the mass conservation equation for the liquid film is:

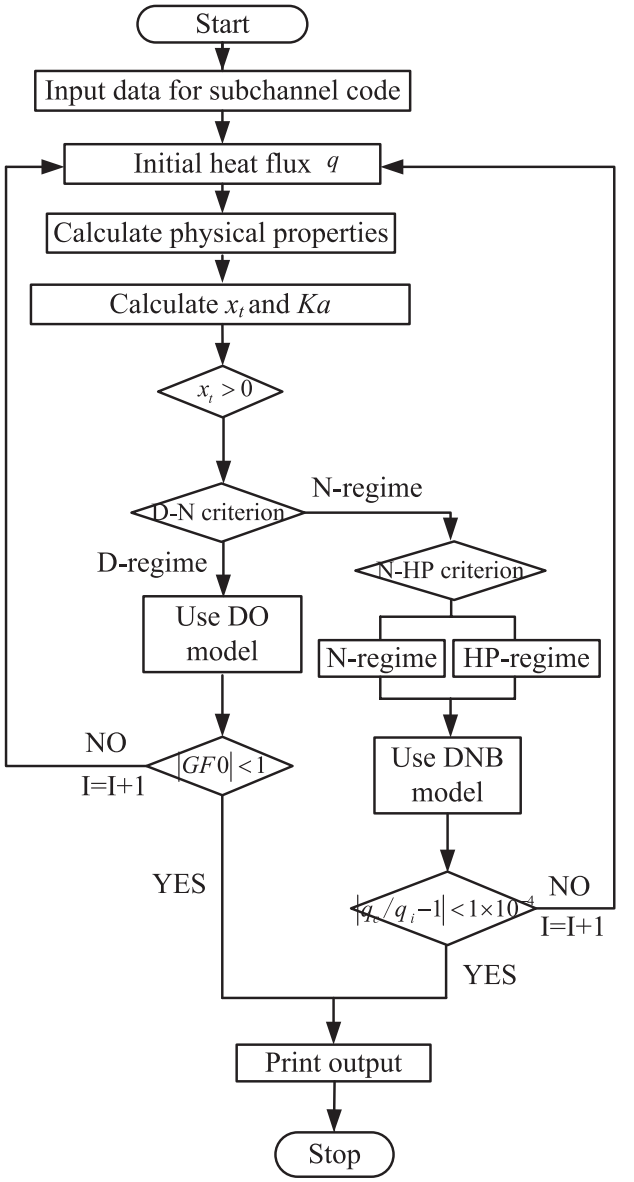

FIGURE 6 | Flowchart of the comprehensive CHF mechanistic model.

$$\frac{D_e}{4}\frac{dG_f}{dz} = D - E - \frac{q}{h_{fg}}.$$

Several models have been proposed for solution of the mass conservation equation. The models differ in the constitutive correlations representing the mechanisms of entrainment and deposition.

In this study, the DO regime CHF mechanistic model for BWR fuel assembly developed by Lim and Weisman (Lim and Weisman, 1988) is used (see reference Lim and Weisman (1988) for the subchannel division and solution steps of this model).

DEVELOPMENT OF COMPREHENSIVE CHF MECHANISTIC MODEL

In this section, the rod bundle CHF-regime criterion for DNB and DO regime CHF determined in *Rod Bundle CHF-Regime Criterion* is used to classify the CHF conditions. Then, the DNB regime CHF mechanistic model of superheated liquid layer depletion under turbulence fluctuation bubbles developed by the author is combined with the DO regime CHF mechanistic model of Lim and Weisman to form a comprehensive CHF mechanistic model covering the DNB and DO regime CHF prediction.

The detailed calculation process of the comprehensive CHF mechanistic model is shown in **Figure 6**.

First of all, input parameters such as pressure, mass flux, subcooling, and equivalent hydraulic diameter for subchannel code are needed to calculate local parameters in the current node. The initial heat flux is q and the corresponding physical properties x_t and Katto number are calculated.

For $x_t > 0$, the D-N criterion is used for judgment. If the current calculation condition belongs to DO regime, then the DO regime CHF model is used to calculate the liquid film flow rate. When the calculated liquid film flow rate is greater than the set value of 1 kg/m^{2}s, it means that CHF has not occurred in the current node, then the next node I + 1 is calculated. If the liquid film flow rate of the last node is still greater than the set value, it means that CHF will not occur in the whole subchannel, then the corresponding heat flux is evaluated.

If the current calculation condition belongs to the DNB regime, the N-HP criterion is used for judgment, and the DNB regime CHF model is used to calculate CHF. When the calculated CHF q_c does not meet the tolerance $|q_c/q_i - 1| < 1 \times 10^{-4}$, the next node I + 1 is calculated. If the last node still does not meet the tolerance, it means that CHF will not occur in the whole subchannel, then the corresponding heat flux is evaluated.

It should be noted that the comprehensive CHF mechanistic model established in this study can automatically and accurately judge and classify the current calculation conditions. Then, the appropriate CHF model is called to calculate and the corresponding CHF is printed. This comprehensive CHF model can accurately and continuously predict the DNB and DO regime CHF in rod bundle channel under the wide parameter range.

ASSESSMENT AND STATISTICAL EVALUATION

CHF Experimental Data

Aiming at the development of advanced Chinese fuel assemblies, NPIC has independently carried out the CHF experiment of 5 × 5 rod bundle with axial uniform and nonuniform heating, taking into account the geometry structure of rod bundle and flow subchannel, heating length, different grid arrangements, rod radial peaking factors, and the guide tube effects (Qin et al.,

TABLE 1 | CHF database and characteristics of each test.

Test series	Element geometry	Axial flux shape	Grid arrangement
TEST 1	Typical	Uniform	Half span
TEST 2	Typical	Uniform	Half span
TEST 5	Typical	Uniform	Half span
TEST 7	Guide tube	Uniform	Full span
TEST 8	Typical	Uniform	Full span
TEST 9	Typical	Cosine1.55	Full span

TABLE 2 | Parameter range of CHF experimental data.

Parameter	Range
Outlet pressure/MPa	2.1–16.7
Inlet mass flux/kg/m^{2}s	960–4760
Inlet temperature/°C	113–330
Local heat flux/kW/m^2	760–2611

2016). In this study, six CHF test series data are selected, and the database and its characteristics are shown in **Table 1**.

Table 2 shows the parameter range of CHF experimental data to assess the comprehensive CHF mechanistic model.

Calculation Method

The local thermal-hydraulic parameters in the 5 × 5 rod bundle of each CHF test series are calculated with the subchannel code CORTH (Liu et al., 2017), which was developed in NPIC for thermal-hydraulic analysis of reactor cores and experimental facilities with heating rod bundles. The rod bundle specific effects such as heating length, mixing strength, cold wall, and axial nonuniform heating are considered to account properly for the calculation of rod bundle local parameters (Dong et al., 2018; Liu et al., 2020a).

Figure 7 shows the subchannel numbering in a 5 × 5 rod bundle.

Assessment Results

Effect of Heating Length

First of all, the effects of heating length on CHF are validated by using the TEST 1, TEST 2, and TEST 5 experimental data. The distribution of P/M in these three series is shown in **Figure 8**.

It can be seen that the comprehensive CHF mechanistic model developed in this study can accurately and continuously predict the DNB and DO regime CHF in the rod bundle channel. All the P/M predicted by the comprehensive CHF mechanistic model are uniformly distributed in the vicinity of one within the mean error of ±22%.

Effect of Mixing Strength

The TEST 8 experimental data are used to validate the effect of spacer span (with intermediate mixing spacer grids to enhance the mixing strength) on CHF prediction. The distribution of P/M in this series is shown in **Figure 9**.

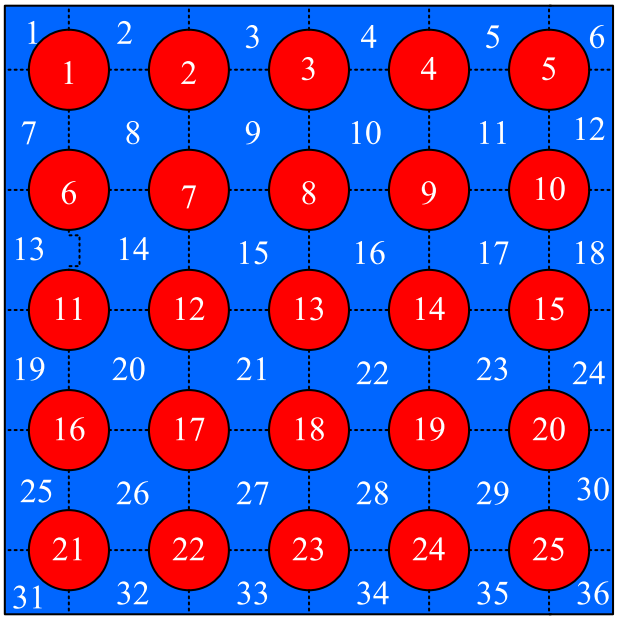

FIGURE 7 | Subchannel numbering in a 5 × 5 rod bundle.

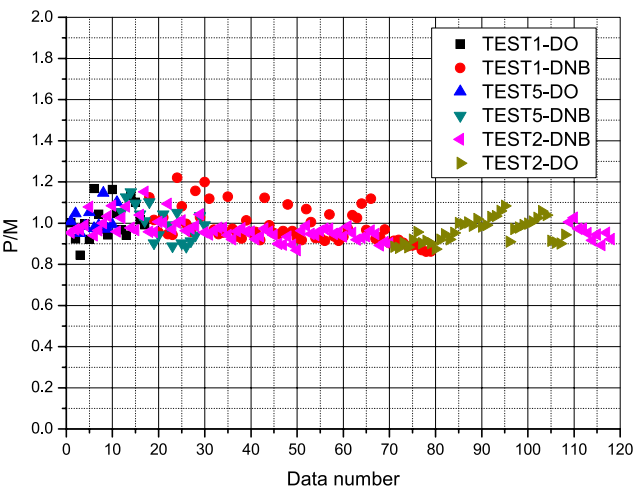

FIGURE 8 | Distribution of P/M in TEST 1, TEST 2, and TEST 5.

Similarly, all the P/M predicted by the comprehensive CHF mechanistic model are uniformly distributed near one within the mean error of ±12%.

Effect of Cold Wall

The effect of cold wall is validated by TEST 7 experimental data. The distribution of P/M in this series is shown in **Figure 10**.

It can be seen that all the P/M predicted by the comprehensive CHF mechanistic model are uniformly distributed near one within the mean error of ±18%.

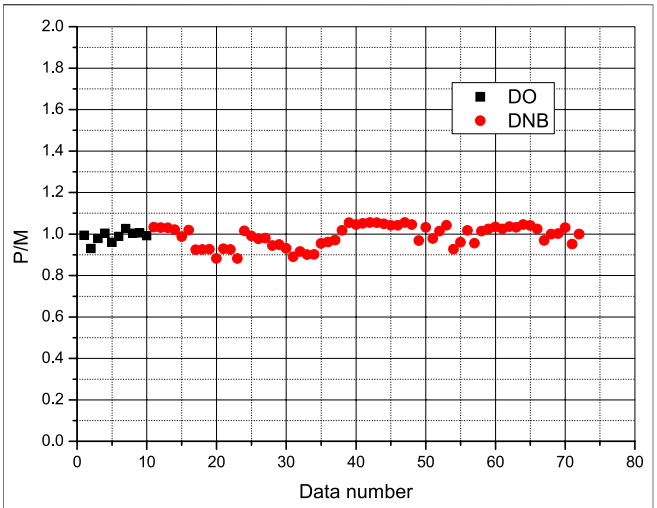

FIGURE 9 | Distribution of P/M in TEST 8.

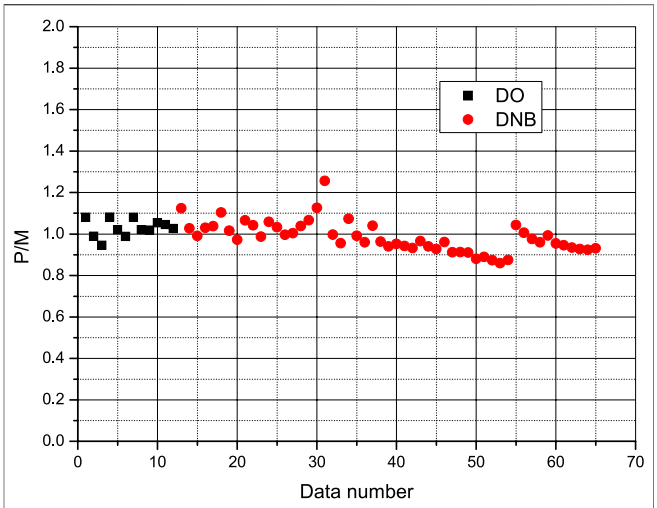

FIGURE 11 | Distribution of P/M in TEST 9.

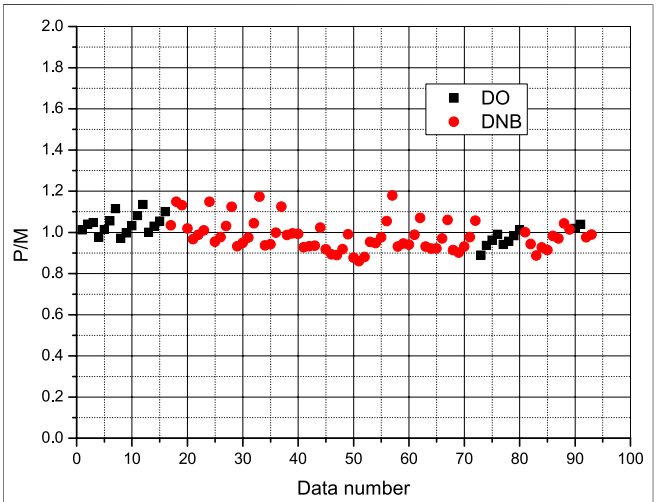

FIGURE 10 | Distribution of P/M in TEST 7.

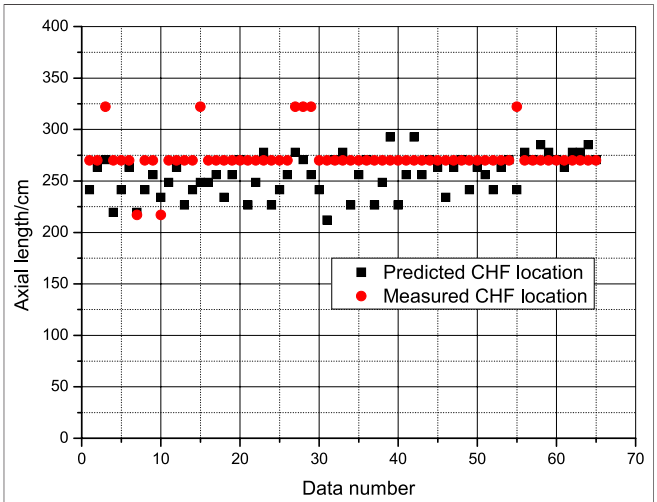

FIGURE 12 | Predicted and measured CHF locations in TEST 9.

Effect of Axial Nonuniform Heating

The TEST 9 experimental data are used to validate the effect of axial nonuniform heating. The distribution of P/M in this series is shown in **Figure 11**.

It can be seen that for the axial nonuniform heating CHF prediction, only one prediction comes up with mean error larger than 20%, and rest of the P/M are uniformly distributed near one within the mean error of ±13%.

For the axial nonuniform heating of TEST 9, the CHF may not occur at the channel exit. **Figure 12** shows the comparison of the CHF mechanistic model–predicted locations with experimentally measured locations. It can be seen that the predicted CHF location is in good agreement with the experimentally measured location, and the deviation of some data points is only within one spacer span. This indicates that the comprehensive CHF mechanistic model can be used to predict the CHF location for the axial nonuniform heating condition.

Statistical Evaluation

Table 3 shows the mean and standard deviation of M/P predicted by the CHF mechanistic model and CF-DRW correlation (Liu W. et al., 2020) based on the CHF experimental data shown in *CHF Experimental Data*. It can be seen that the mean and standard deviation of M/P with these two prediction methods are quite identical.

Figures 13–15 show the distributions of M/P as a function of independent variables such as local pressure, mass flux, and quality, respectively. It can be seen that the distribution of M/P with local pressure, mass flux, and quality have no obvious systematic bias.

Figure 16 shows the flux predicted by the CHF mechanistic model, P, as a function of experimental measured flux M. It can be seen that the distribution of heat fluxes calculated with the comprehensive CHF mechanistic model is well distributed along the 45 line

TABLE 3 | Statistical results of the CHF mechanistic model and CF-DRW correlation.

Test series	M/P	CF-DRW correlation	CHF mechanistic model
TEST 1	Mean	0.949	1.019
	Standard deviation	0.068	0.083
TEST 2	Mean	1.033	1.038
	Standard deviation	0.073	0.054
TEST 5	Mean	0.996	0.996
	Standard deviation	0.048	0.075
TEST 7	Mean	0.994	1.013
	Standard deviation	0.058	0.070
TEST 8	Mean	0.983	1.012
	Standard deviation	0.090	0.051
TEST 9	Mean	1.002	1.011
	Standard deviation	0.051	0.070
All	Mean	0.999	1.019
	Standard deviation	0.064	0.067

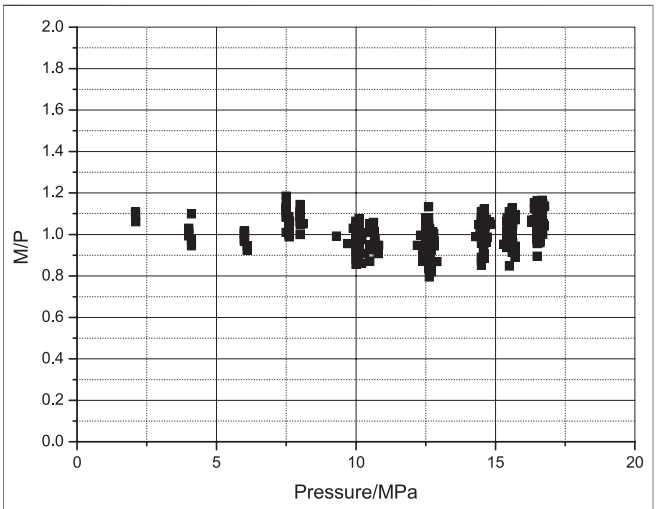

FIGURE 13 | M/P as a function of pressure.

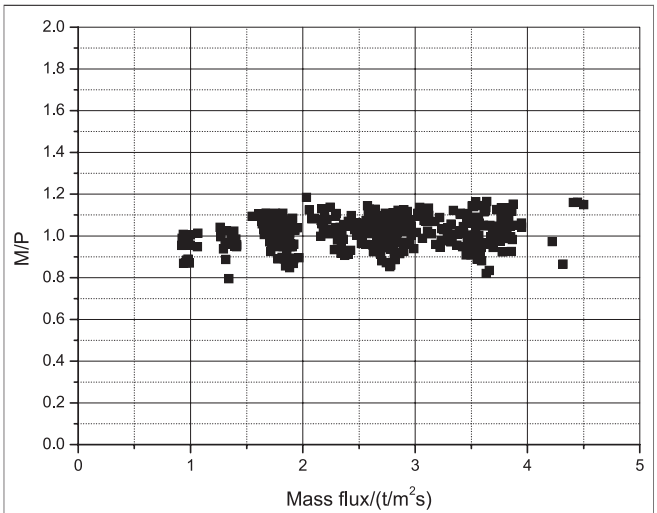

FIGURE 14 | M/P as a function of mass flux.

with measured CHF, and more than 95% experimental data are within the mean error of ±15%.

According to the statistical evaluation results, the comprehensive CHF mechanistic model is a promising candidate for rod bundle CHF prediction under the wide parameter range.

CONCLUSION

In this study, a comprehensive CHF mechanistic model covering DNB and DO regime CHF in a wide parameter range for the rod bundle channel is developed. This model is validated and statistically evaluated as a general CHF prediction method using the 5 × 5 rod bundle CHF experimental data. The important conclusions are as follows:

(1) The comprehensive CHF mechanistic model developed in this study covers the parameter range of PWR under

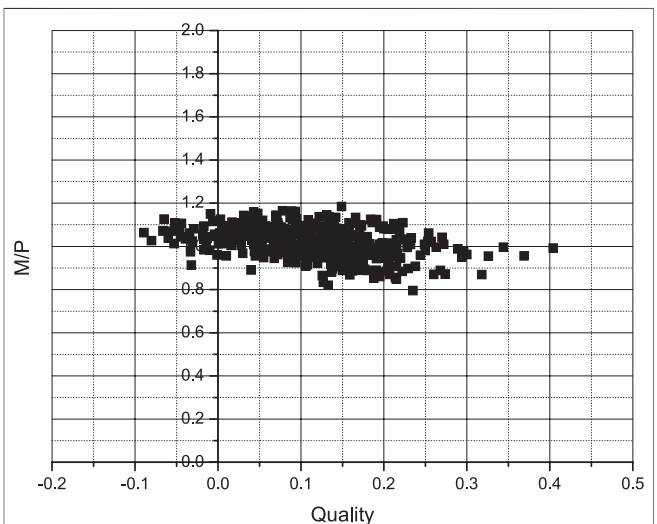

FIGURE 15 | M/P as a function of local quality.

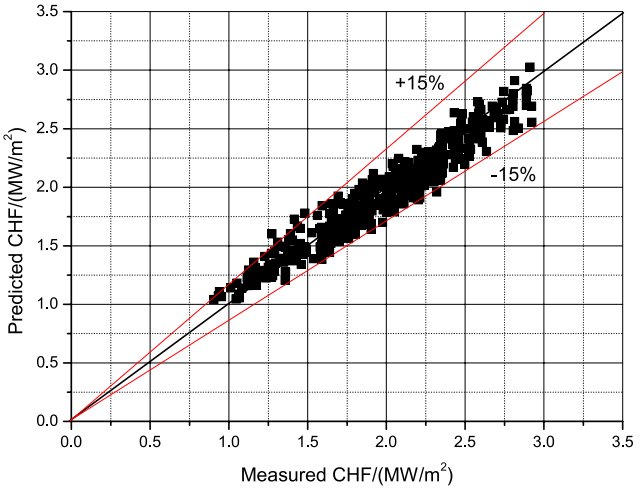

FIGURE 16 | Predicted CHF as a function of measured CHF.

normal operation and accident conditions and can accurately and continuously predict the DNB and DO regime CHF in the rod bundle channel.

(2) The mean and standard deviation of all M/P are 1.019 and 0.067, which are identical to the prediction accuracy of CF-DRW correlation. No specific correction factors such as heating length, cold wall, and axial nonuniform heating effect are needed anymore.

(3) The local pressure, mass flux, and quality do not have any effects on the average deviations of the predicted flux P from the measured flux M. This shows that the comprehensive CHF mechanistic model is a promising candidate for rod bundle CHF prediction under the wide parameter range.

DATA AVAILABILITY STATEMENT

The original contributions presented in the study are included in the article/Supplementary Material; further inquiries can be directed to the corresponding author.

AUTHOR CONTRIBUTIONS

WL: Conceptualization, methodology, and writing—original draft preparation. SP: Supervision. GJ: Data curation and validation. YL: Software and writing—reviewing and editing. All authors read and contributed to the manuscript.

FUNDING

The authors express their appreciation to the Nuclear Power Institute of China for their financial support.

REFERENCES

Chai, G. H., Wang, X. H., Chen, Z. L., and Tao, S. S. (2003). Review of Correlation FC-2000 for Critical Heat Flux Calculation. *Nucl. Power Eng.* S2 (6), 84–87.

Chun, T. H., Baek, W. P., and Chang, S. H. (2000). An Integral Equation Model for Critical Heat Flux at Subcooled and Low Quality Flow Boiling. *Nucl. Eng. Des.* 199, 13–29. doi:10.1016/s0029-5493(00)00224-7

Dong, S., Liu, W., Liu, Y., et al. (2018). Application of the Improved Spacer Grid Model in Subchannel Analysis Code. *Nucl. Technol.* 205 (1-2), 352–363. doi:10.1080/00295450.2018.1491182

Groeneveld, D. (2013). "The Critical Heat Flux Story," in The 15th International Topical Meeting on Nuclear Reactor Thermal Hydraulics, Pisa, Italy, May 12-17.

Groeneveld, D. C., Ireland, A., Kaizer, J., and Vasic, A. (2018). An Overview of Measurements, Data Compilations and Prediction Methods for the Critical Heat Flux in Water-Cooled Tubes. *Nucl. Eng. Des.* 331, 211–221. doi:10.1016/j.nucengdes.2018.02.031

Kataoka, I., Kodama, S., Tomiyama, A., and Serizawa, A. (1997). Study on Analytical Prediction of Forced Convective CHF Based on Multi-Fluid Model. *Nucl. Eng. Des.* 175, 107–117. doi:10.1016/s0029-5493(97)00167-2

Kodama, S., and Kataoka, I. (2002). "Study on Analytical Prediction of Forced Convective chf in the Wide Range of Quality," in 10TH International Conference on Nuclear Engineering, Arlington, VA, USA, April 14-18. .

Lim, J. C., and Weisman, J. (1988). A Phenomenologically Based Prediction of Rod-Bundle Dryout. *Nucl. Eng. Des.* 105 (3), 363–371. doi:10.1016/0029-5493(88)90256-7

Liu, W., Peng, S., Jiang, G., and Liu, Y. (2021a). Analytical Investigation on Rod Bundle CHF-Regime Criterion Based on Dimensionless Groups. *Int. J. Therm. Sci.* 159, 106571. doi:10.1016/j.ijthermalsci.2020.106571

Liu, W., Peng, S., Jiang, G., and Liu, Y. (2021b). Development and Assessment of a New CHF Mechanistic Model for Subcooled and Low Quality Flow Boiling. *Int. J. Heat Mass Transfer* 165, 120641. doi:10.1016/j.ijheatmasstransfer.2020.120641

Liu, W., Peng, S., Jiang, G., Liu, Y., Du, S., Zhang, Y., et al. (2020). Development and Assessment of a New Rod-Bundle CHF Correlation for China Fuel Assemblies. *Ann. Nucl. Energ.* 138, 107175. doi:10.1016/j.anucene.2019.107175

Liu, W., Peng, S., Shan, J., Jiang, G., Liu, Y., Deng, J., et al. (2021c). Applicability Research of Round Tube CHF Mechanistic Model in Rod Bundle Channel. *Nucl. Eng. Technol.* 53, 439–445. doi:10.1016/j.net.2020.07.023

Liu, W., Shan, J., Peng, S., Jiang, G., and Liu, Y. (2019). The Study of Critical Heat Flux in Upflow Boiling Vertical Round Tube under High Pressure. *Sci. Technol. Nucl. Installations* 2019, 1–14. doi:10.1155/2019/3695685

Liu, Y., Dong, S., Shan, J., Zhang, B., Jiang, L., Liu, W., et al. (2020a). A Phenomenological CHF Model for Mixing-Vane Spacers in a Subchannel of a Rod Bundle. *Ann. Nucl. Energ.* 142, 107445. doi:10.1016/j.anucene.2020.107445

Liu, Y., Liu, W., Shan, J., Zhang, B., and Leung, L. K. H. (2020b). A Mechanistic Bubble Crowding Model for Predicting Critical Heat Flux in Subchannels of a Bundle. *Ann. Nucl. Energ.* 137, 107085. doi:10.1016/j.anucene.2019.107085

Liu, Y., Tan, C., Pan, J., et al. (2017). Development of Self-Reliant Subchannel Analysis Code CORTH. *Nucl. Power Eng.* 38 (6), 158–162.

Qin, S., Lang, X., Xie, S., Li, P., Zhuo, W., Liu, W., et al. (2016). Experimental Investigation on Repeatability of CHF in Rod Bundle with Non-uniform Axial Heat Flux Distribution. *Prog. Nucl. Energ.* 90, 151–154. doi:10.1016/j.pnucene.2016.03.015

Qu, W., Xiong, J., Chen, S., and Cheng, X. (2019). High-fidelity PIV Measurement of Cross Flow in 5 × 5 Rod Bundle with Mixing Vane Grids. *Nucl. Eng. Des.* 344, 131–143. doi:10.1016/j.nucengdes.2019.01.021

Tong, L. S. (1967). Heat Transfer in Water-Cooled Nuclear Reactors. *Nucl. Eng. Des.* 6 (4), 301–324. doi:10.1016/0029-5493(67)90111-2

Weisman, J., and Pei, B. S. (1983). Prediction of Critical Heat Flux in Flow Boiling at Low Qualities. *Int. J. Heat Mass Transfer* 26 (10), 1463–1477. doi:10.1016/s0017-9310(83)80047-7

Xiong, J., Qu, W., Zhang, T., Chai, X., Liu, X., and Yang, Y. (2020). Experimental Investigation on Split-Mixing-Vane Forced Mixing in Pressurized Water Reactor Fuel Assembly. *Ann. Nucl. Energ.* 143, 107450. doi:10.1016/j.anucene.2020.107450

Yang, B.-W., Han, B., Liu, A., and Wang, S. (2019). Recent Challenges in Subchannel Thermal-Hydraulics-CFD Modeling, Subchannel Analysis, CHF Experiments, and CHF Prediction. *Nucl. Eng. Des.* 354, 110236. doi:10.1016/j.nucengdes.2019.110236

Zeigarnik, Y. A. (1996). Universal Model of Critical Heat Flux of Subcooled Liquid Boiling in Channels. *High temperature* 34 (1), 48–52.

Zhang, H., and Hewitt, G. F. (2016). New Models of Droplet Deposition and Entrainment for Prediction of CHF in Cylindrical Rod Bundles. *Nucl. Eng. Des.* 305, 73–80. doi:10.1016/j.nucengdes.2016.04.044

Conflict of Interest: The authors declare that the research was conducted in the absence of any commercial or financial relationships that could be construed as a potential conflict of interest.

NOMENCLATURE

D channel diameter (m)/droplet deposition rate (kg/m^{2}s)
De equivalent diameter (m)
E entrainment rate (kg/m^{2}s)
G mass flux (kg/m^{2}s)
h_{fg} latent heat of vaporization (kJ/kg)
Ka Katto number
m mass flow rate (kg/s)
M measured CHF (MW/m^2)
p pressure (MPa)
P predicted CHF (MW/m^2)
Pr Prandtl number
q heat flux (MW/m^2)
q_c critical heat flux (MW/m^2)
T temperature (°C)
v' radial velocity (m/s)
v^* net mass exchange rate (m/s)
V_{11} vapor generation rate (m/s)
x equilibrium quality
x_t real vapor quality
y^* distance from the wall (m)
z axial coordinate (m)
ρ density (kg/m^3)

SUBSCRIPTS

conv forced convection
evap evaporation
l liquid
turb turbulence fluctuations
v vapor
w wall
sat saturation condition

frontiers in Energy Research

ORIGINAL RESEARCH
published: 09 June 2021
doi: 10.3389/fenrg.2021.675494

Experimental Study of Pressure Loss in a 5 × 5–Rod Bundle With the Mixing Vane Spacer Grid

Wenhai Qu[1], Weiyi Yao[1], Jinbiao Xiong[1] and Xu Cheng[2]*

[1]School of Nuclear Science and Engineering, Shanghai Jiao Tong University, Shanghai, China, [2]Institute of Fusion and Reactor Technology, Karlsruhe Institute of Technology, Karlsruhe, Germany

Axial and lateral pressure loss in a 5 × 5 rod–bundle with a split-type mixing vane spacer grid was experimentally measured using differential pressure transmitters at different sub-channel Reynolds numbers (Re) and orienting angles. The geometrical parameters of the 5 × 5–rod bundle are as follows: they have the same diameter (D = 9.5 mm) and pitch (*p* = 12.6 mm) as those of real fuel rods of a typical pressurized water reactor (PWR), with a sub-channel hydraulic diameter (D_h) of 11.78 mm. The characteristics and resistance models of pressure loss are discussed. The main axial pressure loss is caused by the spacer grid, and the spacer grid generates additional wall friction pressure loss downstream of the spacer grid. The lateral pressure loss shows strong correlations with orienting angles and distance from the spacer grid. The lateral pressure loss shows a sudden burst in the mixing vanes region and a slight augmentation at $z = 3D_h$. After $3D_h$, the lateral pressure loss decays in an exponential way with distance from the spacer grid, and it becomes constant quickly at $z = 20D_h$.

Keywords: pressure loss, resistance model development, rod bundle assembly, spacer grid, sliding pressure loss measurement

OPEN ACCESS

Edited by:
Hitesh Bindra, Kansas State University, Manhattan, United States

Reviewed by:
Juliana P. Duarte, Virginia Tech, Blacksburg, United States
Wang Kee In, Korea Atomic Energy Research Institute (KAERI), South Korea

****Correspondence:***
Jinbiao Xiong
xiongjinbiao@sjtu.edu.cn

Specialty section:
This article was submitted to Nuclear Energy, a section of the journal Frontiers in Energy Research

Received: *03 March 2021*
Accepted: *10 May 2021*
Published: *09 June 2021*

Citation:
Qu W, Yao W, Xiong J and Cheng X (2021) Experimental Study of Pressure Loss in a 5 × 5–Rod Bundle With the Mixing Vane Spacer Grid. Front. Energy Res. 9:675494. doi: 10.3389/fenrg.2021.675494

INTRODUCTION

The mixing vane spacer grids in the fuel assembly of a pressurized water reactor (PWR) highly enhance cross-flow, turbulent mixing, and heat transfer in fuel assembly, improving the departure from nucleate boiling (DNB) conditions in PWRs. However, it costs pressure loss in the reactor core due to the relatively large resistance of the spacer grid, and the axial and lateral resistance of the fuel assembly are important parameters, which should be investigated and modeled into a sub-channel analysis code in the design phase and operation phase. In the axial momentum conservation equation, wall friction resistance and spacer grid resistance models are employed to predict the axial pressure loss performance of the fuel assembly, while the lateral resistance model is used for predicting lateral pressure loss (Li et al., 2019).

The classical wall friction factor models for circular pipes are a power function of the Reynolds number (Re), including the Nikuradse equation, the Moody diagram, the Blasius equation, and the McAdams equation (Fang et al., 2011). The Colebrook equation (Colebrook, 1939) considers the wall roughness and Re, but the implicit equation is inconvenient for engineering application. Many explicit correlations were approximated to the Colebrook equation (Churchill, 1973, 1977; Chen, 1979; Haaland, 1983; Manadilli, 1997; Sonnad and Goudar, 2006). These correlations are evaluated precisely enough for predicting the wall friction in pipes (Brkić, 2011; Yıldırım, 2009). However, the geometrical details of the rod bundle reshape the wall friction. The wall friction factor is a function of

Re and P/D (pitch-to-rod diameter) in triangular and square arrangements of rod bundles (Cheng and Todreas, 1986; Lee et al., 2012). The wall friction models should be developed and assessed before applying them in a special design of the rod bundle (Toptan et al., 2018).

The resistance of a spacer grid is mainly decided by the blockage of the flow area and wall friction of the straps (Chun and Oh, 1998; Idelchik, 1986). The resistance of a spacer grid is different for each special design and geometry of rod bundles. The classical resistance models for different spacer grids (Rehme, 1970, 1973) were a function of the ratio of the projected area of the spacer grid to the flow area of the bared rod bundle and the modified spacer grid resistance. A series of similar models of spacer grid resistance were found in the studies by Vog et al. (1971), Savatteri et al. (1986), Cigarini and Donne (1988), Cevolani (1995), Epiney et al. (2010), Pacio et al. (2014), and Schikorr et al. (2010). These resistance models of spacer grids were evaluated (Chenu et al., 2011; Maskal and Aydogan, 2017), and each correlation can only be applied for the special design of the spacer grid. It is essential to develop new correlations of spacer grid resistance for special designs of spacer grids and rod bundles. A sliding pressure–sensing rod in the rod bundle was employed to measure the locally axial pressure loss facing different angles in sub-channels (Caraghiaur et al., 2009). The axial pressure distribution upstream and downstream of the spacer grid facing different orienting angles is almost the same, but it is very different in the spacer grid caused by the complex geometry. Both the local geometry details and the influence of the neighboring sub-channels play an important role in the pressure distribution. Many researchers predicted the axial pressure loss in the rod bundle with the spacer grid using CFD simulations (Chen et al., 2017; Cheng et al., 2017; Wu et al., 2017; Han et al., 2018; In et al., 2015; Xiong et al., 2018; Sibel Tas-Koehler et al., 2020; Wang et al., 2020). The axial pressure upstream of the spacer grid gradually decreases due to the wall friction of the rod bundle. But the axial pressure suddenly jumps down just before the spacer grid, and in the region of the spacer grid, the axial pressure decreases sharply (Wang et al., 2020). Downstream of the spacer grid, the axial pressure increases slightly just near the spacer grid, and then it decreases slowly.

Several studies have investigated the lateral pressure loss in rod bundles. The cross-flow resistance coefficient between sub-channels (Tapucu, 1977) is defined as the ratio of the lateral pressure loss to the laterally kinetic energy, calculated by the cross-flow velocity and fluid density. The cross-flow resistance in a bared rod bundle is a power correlation of the P/D ratio and Re (Liu and Todreas, 1979). In the MATiS-H benchmark exercise (Agbodemegbe et al., 2015; Chang and Tavoularis, 2015), the pressure distribution on the surface of mixing vanes was the mechanism of the cross-flow pattern, and the cross-flow resistance was investigated using the CFD simulation. In the studies by Qu et al. (2019a) and Xiong et al. (2020), a new sliding pressure loss measurement system was designed to measure the lateral pressure loss between sub-channels. The lateral pressure loss decays as an exponential function of the distance from the spacer grid, and the cross-flow resistance was fitted into a correlation of distance from the spacer grid.

In most studies, the impulse pipes are fixed on the channel wall of the rod bundle, which is not the locally axial pressure loss in sub-channels. It is reasonable that the spacer grid generates additional wall friction downstream of the spacer grid. The pressure distribution in the sub-channels is determined by the local flow conditions, but few studies investigate the pressure loss in sub-channels along the axial distance and facing different angles experimentally.

The axial and lateral pressure loss facing different angles along the axial distance upstream and downstream of the spacer grid were measured using the sliding pressure loss measurement system, and corresponding resistance models are proposed and discussed. The experimental data help to understanding the hydraulic performance of the mixing vane spacer grid, and benefit the development of the spacer grid and CFD validation.

EXPERIMENTAL APPARATUS

Experimental Facility and Test Section

The MEdium Scale Hydraulic (MESH) test facility is utilized for the experiment (Qu et al., 2019a) in the Shanghai Jiao Tong University. In the primary loop, the deionized water is vertically driven by the pump from the fluid reservoir to the test section *via* the heat exchanger, cooling pump, and cooling tower. The temperature in the test section is monitored using calibrated thermal couples with an accuracy of 0.1°C at the inlet and the outlet of the test section. The flow rate through the test section is measured using a turbine flow meter with an error of 0.5% in range of 4–50 m^3/h.

The spacer grid with 11 mm long mixing vanes and an inclination angle of 30° is shown in **Figure 1A**. The spacer grid with a height of 40 mm from the bottom plate of 3 mm thickness to the top of the straps with a height of 37 mm is installed in the rod bundle. The top and front views of the mixing vane spacer grid are shown in **Figures 1B,C**. The details of the mixing vanes are shown in **Figure 1D**. The vertical test section is shown in **Figure 2A**, including the inlet section, the measuring section, and the outlet tank. The housing of the test section includes the aluminum frame and four PMMA windows of 1011.5 mm length. A flow straightener at the inlet of the inlet section minimizes disturbance upstream of the test section. In **Figure 2B**, the rod bundle of 1100 mm length is made of aluminum oxidized by chromate and dyed to be black using a colorant. The rod diameter (D) is 9.5 mm with a pitch (P) of 12.6°mm, resulting in the sub-channel hydraulic diameter (D_h) of 11.78 mm. The 517-mm-long rods are fixed on the bottom plate of the spacer grid upstream, and the 580-mm-long rods are fixed downstream of the spacer grid. The rod bundle is fixed on the bottom and top flanges of the measuring section. The laboratory coordinate system is defined as shown in **Figures 2B,C**. The origin (x = 0, y = 0, z = 0) is defined at the center of the central rod on the plane of the upper edge of the straps. The sixteen sub-channels are named in **Figure 2D**.

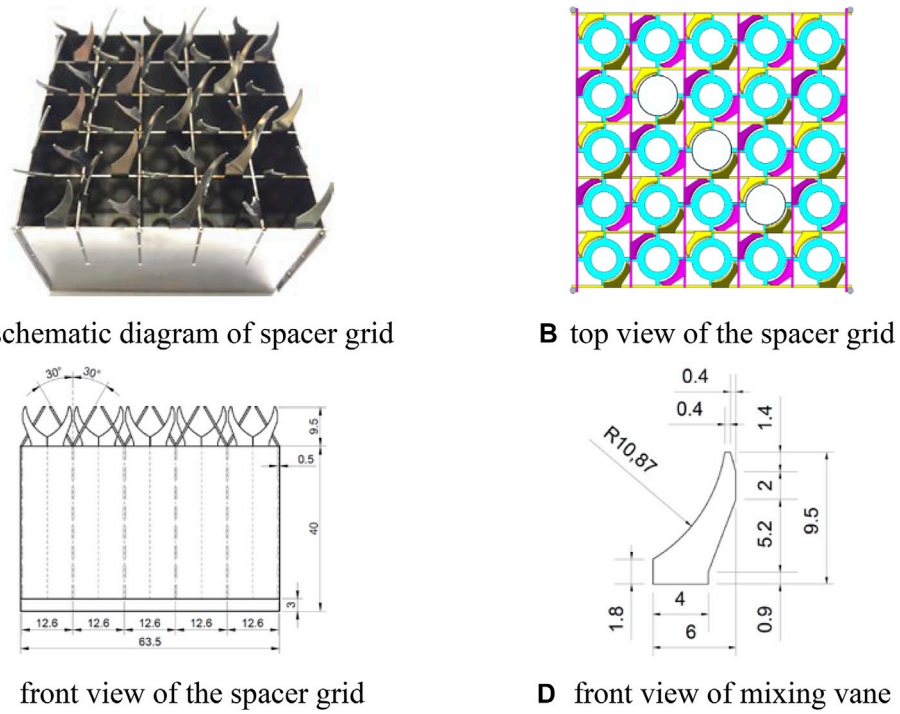

FIGURE 1 | Spacer grid.

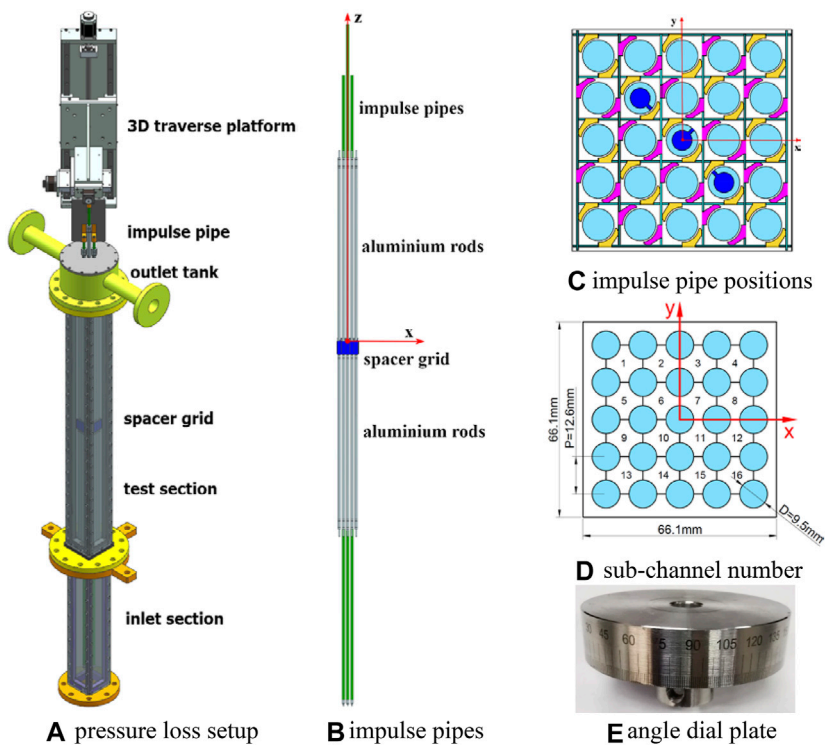

FIGURE 2 | Pressure loss measurement system.

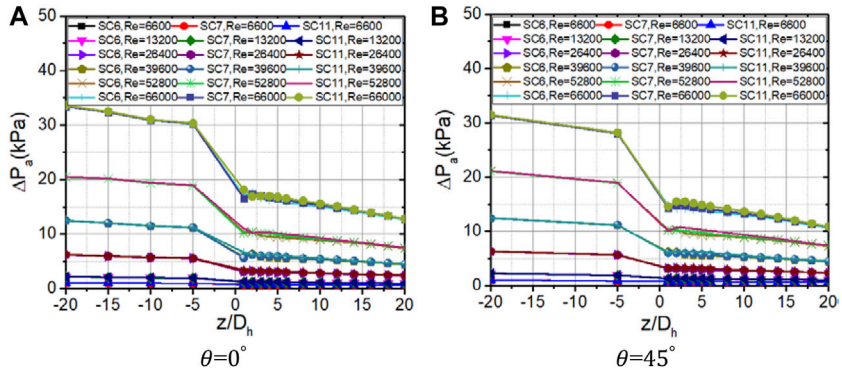

FIGURE 3 | Axial pressure loss of three impulse pipes.

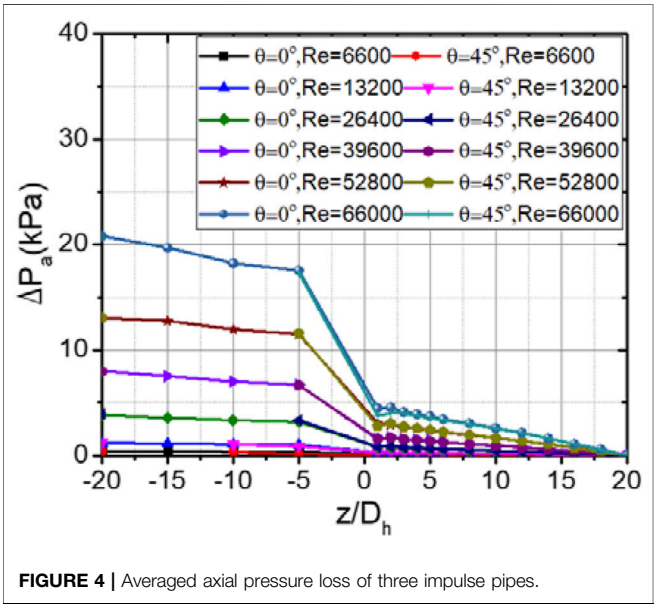

FIGURE 4 | Averaged axial pressure loss of three impulse pipes.

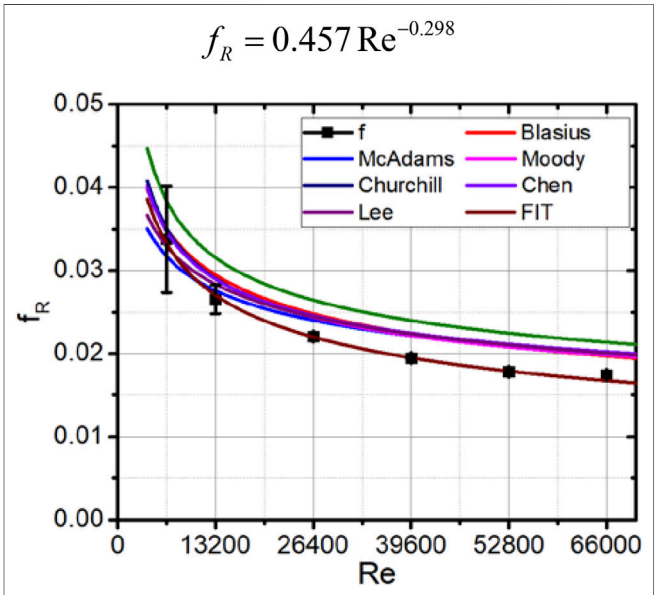

FIGURE 5 | Friction factor in the bared rod bundle.

Measurement System Setup

The pressure loss setup is shown in **Figure 2A**. Three impulse pipes are mounted through the inlet flange, spacer grid, and outlet flange. As shown in **Figure 2B**, the length of the impulse pipes is 1850 and 2000 mm for the two noncenter pipes and the center pipe, respectively. As shown in **Figure 2C**, the three impulse pipes marked blue with an outer diameter of 9.5 mm and an inner diameter of 8 mm pass through the spacer grid from the center rod and two neighboring rods, with three pressure ports of 1 mm diameter on the surface of each impulse pipe. Three pressure taps are used to guide the pressure to the differential pressure transmitters. At the measuring position of $z = -20D_h$, there is still a 279.4 mm length of impulse pipes upstream of the inlet of the rod bundle, which is far enough from the inlet of the rod bundle. The inlet conditions of the rod bundle and the inlet condition at the spacer grid are not influenced by the three impulse pipes. To measure the pressure loss orienting to different angles, an SUS304 angle dial plate of 63.5 mm diameter with scale lines dividing the perimeter into 360° is fixed on the top of the central impulse pipe, as shown in **Figure 2E**. We define the orienting angle on the x axis as equal to 0° and that on the y axis as equal to 90°. Combined with the 3D traverse platform and pressure sensors, the axial and lateral pressure loss of different orienting angles from $z = -20D_h$ to $z = 20D_h$ can be measured by moving the pulse pipes and turning the angle dial plate.

The axial pressure loss at different angles from $z = -20D_h$ to $z = 20D_h$ in sub-channel nos. 6, 7, and 11 is measured using a YOKOGAWA differential pressure transmitter (EJA110A) (range 100 kPa, accuracy 0.065%), and the reference pressure point is set on the top surface of the outlet tank. Only the central impulse pipe is used to measure axial pressure loss at different orienting angles. The lateral pressure loss in sub-channel nos. 7 and 11 was measured using a YOKOGAWA differential pressure transmitter (EJA110E) (range 5 kPa, accuracy 0.065%) for

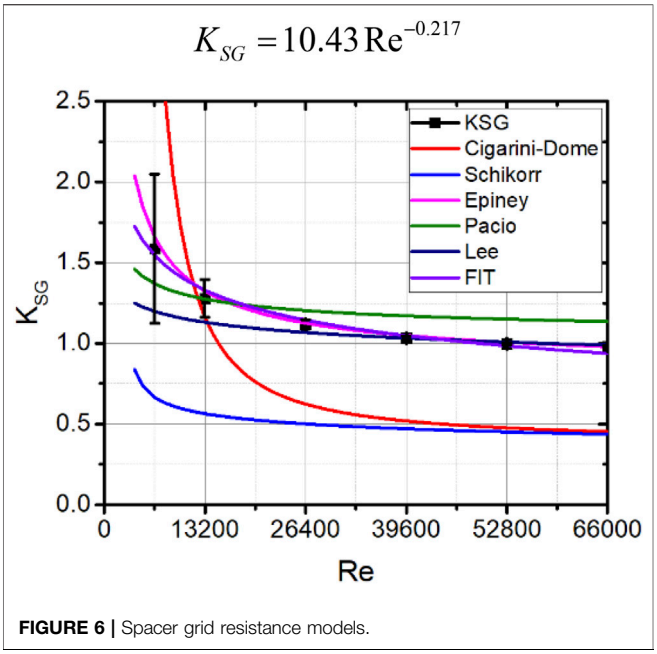

FIGURE 6 | Spacer grid resistance models.

pressure loss from −2500 to 2500 Pa and a YOKOGAWA differential pressure transmitter (EJA110A) (range 100 kPa, accuracy 0.065%) for pressure loss from −50 to 50 kPa. The reference pressure point is set as the lower-right corner pressure port facing the center of sub-channel no. 11, as shown in **Figure 2C**. The central impulse pipe is used to measure lateral pressure loss of different orienting angles from z = $-20D_h$ to z = $20D_h$. During the experimental process, the central impulse pipe can be turned to face a different angle θ ranging from −90° to 90°. By this procedure, the lateral pressure loss around the central impulse pipe at different distances from the spacer grid can be measured. The pressure loss is an averaged pressure loss based on a sample size of 1,000 samples at 10 Hz of sample frequency.

EXPERIMENTAL RESULTS

The pressure loss measurements are conducted at a temperature of 25 ± 0.2°C measured by the calibrated thermal couples, a gauge pressure of 0.12 MPa at the inlet of the test section, and a flow rate of 4.68, 9.35, 18.70, 28.05, 37.4, and 46.75 m^3/h through the test section with an accuracy of 0.05 m^3/h. Equivalently, the corresponding sub-channel Reynolds numbers are 0.66×10^4, 1.32×10^4, 2.64×10^4, 3.96×10^4, 5.28×10^4, and 6.6×10^4, which are calculated by using the bulk velocity and sub-channel hydraulic diameter. The sub-channel hydraulic diameter is calculated by using the inner sub-channel geometry with a pitch of 12.6 mm and a rod diameter of 9.5 mm. The characteristics and models of pressure loss upstream and downstream of the spacer grid are discussed.

Axial Pressure Loss

The axial pressure loss was measured at $\theta = 0°$ and $\theta = 45°$ from z = $-20D_h$ to z = $20D_h$. The axial pressure loss of different sub-channels is almost the same, with an uncertainty of 65Pa, as shown in **Figure 3**. The axial pressure loss is averaged using the data of three sub-channels and subtracted from the averaged axial pressure loss at z = $20D_h$, as shown in **Figure 4**.

The axial pressure loss at different orienting angles is almost the same, so the averaged axial pressure loss of $\theta = 0°$ and 45° is used for the wall friction coefficient model (using data from z = $-20D_h$ to z = $-5D_h$) and the spacer grid resistance model (using data from z = $-5D_h$ to z = $1D_h$). The axial pressure loss contains the wall friction upstream of the spacer grid, the spacer grid resistance, and the wall friction downstream of the spacer grid. The trends of sharp decreasing of axial pressure at the spacer grid region and slight increasing downstream of the spacer grid have also been presented in studies (Caraghiaur et al., 2009; In et al., 2015; Chen et al., 2017; Han et al., 2018; Wu et al., 2017; Xiong et al., 2018; Sibel Tas-Koehler et al., 2020; Wang et al., 2020). As explained (Wu et al., 2017), the rapid decrease in axial pressure in the height of the spacer grid is caused by the local resistance of the spacer grid, especially the form drag on the straps and mixing vanes (Chun and Oh, 1998). Downstream of the spacer grid, the flow cross-sectional area becomes large, so the pressure slightly increases and then decays gradually.

Wall Friction Coefficient Model

The wall friction coefficient is defined as

$$f_R = \frac{\Delta P_R}{0.5\rho W_b^2 (L_R/D_h)}.$$

Here, f is the friction factor in the rod bundle. ΔP_R, ρ, W_b, L_R, and D_h are the pressure loss in the rod bundle, density, bulk velocity measuring length, and sub-channel hydraulic diameter, respectively. The subscript R means the rod bundle. To avoid the inlet effect at the inlet of the rod bundle and the spacer grid effect upstream and downstream on the wall friction pressure loss, we choose the measuring length from z = $-20D_h$ ($23.89D_h$ from the inlet of the rod bundle) to z = $-5D_h$ ($1.60D_h$ upstream of the spacer grid). The experimental data are fitted into a curve as shown in **Figure 5**.

$$f_R = 0.457\mathrm{Re}^{-0.298}.$$

Classical friction factor models listed following Chun and Oh (1998), Yıldırım (2009), and Lee et al. (2012) were compared with the new wall friction model. The rod roughness is equal to 1.5 μm. For the present experimental range, all classical correlations highly predicted the experimental data at higher Reynolds numbers.Blasius correlation

$$f_R = 0.316\mathrm{Re}^{-0.25}, \mathrm{Re} < 3 \times 10^4.$$

McAdams correlation

$$f_R = 0.184\mathrm{Re}^{-0.2}, 3 \times 10^4 < \mathrm{Re} < 1 \times 10^6.$$

Moody correlation

$$f_{SGR} = 0.362\,\mathrm{Re}^{-0.268} - 0.457\,\mathrm{Re}^{-0.298}$$

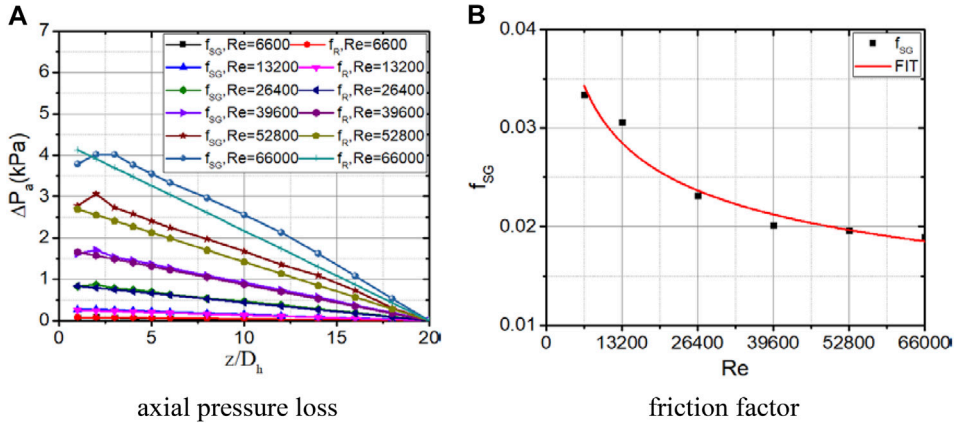

FIGURE 7 | Spacer grid effect on the friction factor downstream of the spacer grid.

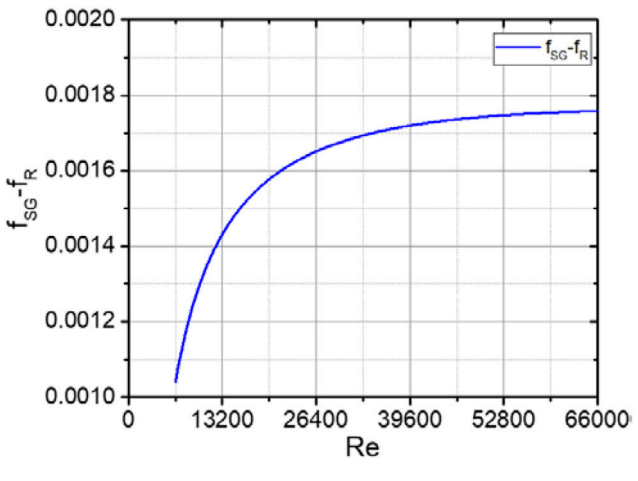

FIGURE 8 | Spacer grid effect on the friction factor downstream of the spacer grid.

$$f_R = 0.0055\left[1 + \left(2\times10^4\frac{\varepsilon}{D_h} + \frac{10^6}{\mathrm{Re}}\right)^{1/3}\right], \Delta\mathrm{Re} < 1\times10^5.$$

Churchill (1973) correlation

$$f_R^{-0.5} = -2\log\left[\frac{\varepsilon}{3.7D_h} + \left(\frac{7}{\mathrm{Re}}\right)^{0.9}\right].$$

Lee (2012) correlation

$$f_R = 0.218\mathrm{Re}^{-0.215}, 3\times10^4 < \mathrm{Re} < 1.3\times10^5.$$

Spacer Grid Resistance Model

The spacer grid resistance coefficient is defined as (Caraghiaur et al., 2009; Deng et al., 2020; In et al., 2015; Lee et al., 2012)

$$K_{SG} = \frac{\Delta P_{SG} - \Delta P_R}{0.5\rho W_b^2}.$$

Here, K_{SG} is the spacer grid resistance, and ΔP_{SG} and ΔP_R are the pressure loss of the spacer grid and the pressure loss of the rod bundle in the height of the spacer grid, respectively. We choose the measuring pressure loss between z = $-5D_h$ and z = $1D_h$ as ΔP_{SG}, and ΔP_R is calculated from the experimental friction factor and the length of $6D_h$ and W_b.

The classical spacer grid models (Rehme, 1973) consider the relative plugging of the flow cross section of the spacer grid to be the main reason for resistance, and the other reason is the Reynolds number corresponding to the friction of the spacer surface. The following is the relationship between the spacer grid resistance coefficient and the relative plugging of the flow cross section:

$$K_{SG} = C_{SG}\alpha^n,$$

where C_{SG} is the modified drag coefficient and α is the blockage ratio of the flow cross section, defined as follows:

$$\alpha = A_p/A_f.$$

Here, A_p is the projected area of the spacer grid, and A_f is the flow area in the bared rod bundle. In this study, $\alpha = 0.243$ based on the geometrical parameters of the spacer grid and the rod bundle. The value of n can be equal to 2 for special types of spacer grids (Cigarini and Donne, 1988; Rehme, 1973; Schikorr et al., 2010), and the modified spacer grid resistance is considered as a function of Re, listed as follows:

$$K_{SG} = C_{SG}\alpha^2.$$

Cigarini–Donne (1988) correlation

$$K_{SG} = \min\left[C_{SG}\alpha^2, 2\right] = \left[\left(3.5 + \frac{73.14}{\mathrm{Re}^{0.264}} + \frac{2.79\times10^{10}}{\mathrm{Re}^{2.79}}\right)\alpha^2, 2\right].$$

Schikorr (2010) correlation

$$K_{SG} = \min\left[C_{SG}\alpha^2, 2.6\right] = \left[\left(3.5 + \frac{73.14}{\mathrm{Re}^{0.264}} + \frac{2.79\times10^{10}}{\mathrm{Re}^{2.79}}\right)\alpha^2, 2.6\right].$$

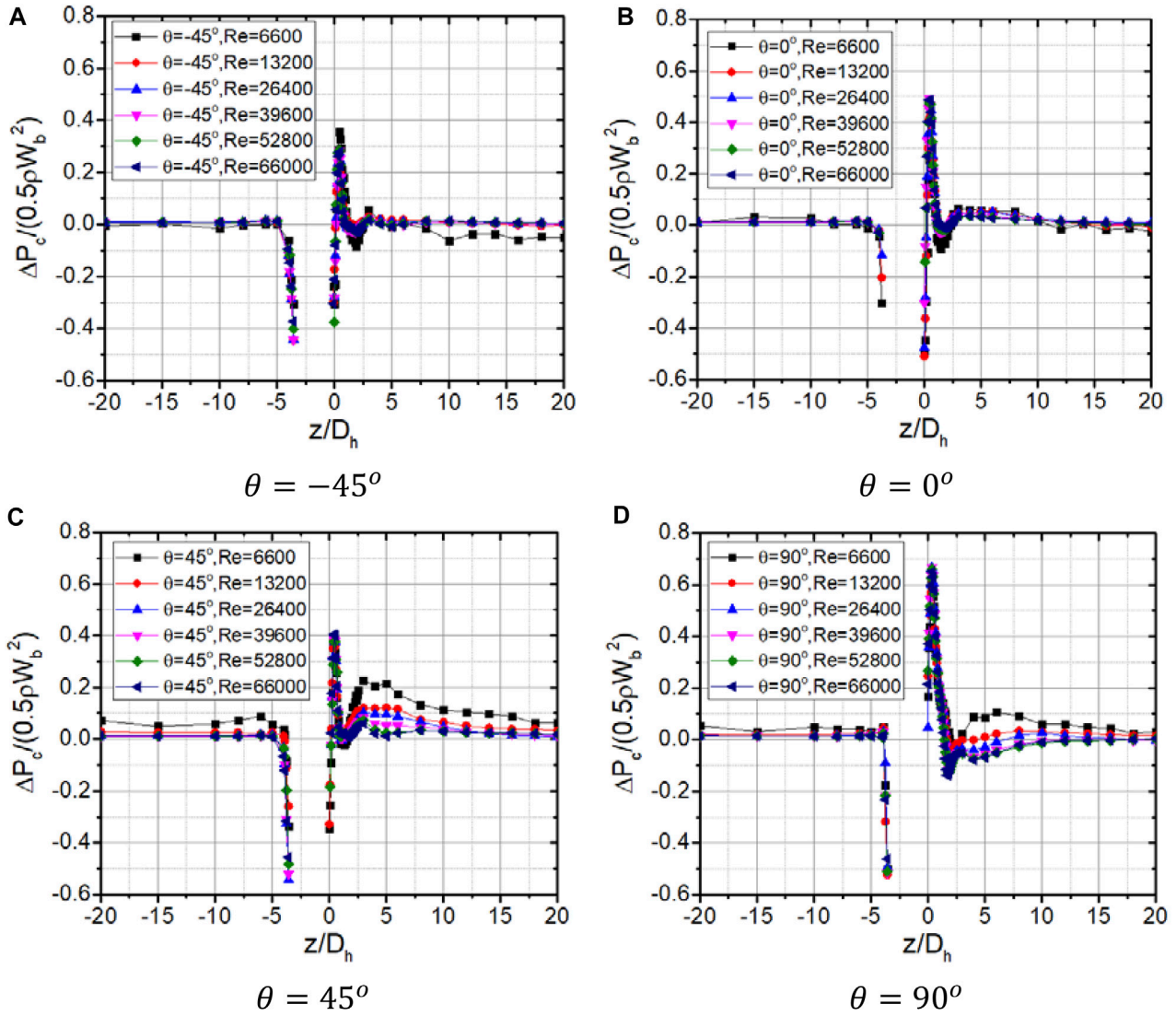

FIGURE 9 | Typical normalized lateral pressure loss from $-20D_h$ to $20D_h$.

Based on experimental data of the spacer grid in the triangular rod bundle (Epiney et al., 2010; Pacio et al., 2014), the spacer grid resistance models are modified as the following correlations, in which n is equal to 0.2.Epiney (2010) correlation

$$K_{SG} = C_{SG}\alpha^{0.2} = \left(1.104 + \frac{791.8}{\mathrm{Re}^{0.748}} + \frac{3.348 \times 10^9}{\mathrm{Re}^{5.652}}\right)\alpha^{0.2}.$$

Pacio (2014) correlation

$$K_{SG} = C_{SG}\alpha^{0.2} = \left(1.315 + \frac{9.455}{\mathrm{Re}^{0.407}} + \frac{10.561}{\mathrm{Re}^{0.43}}\right)\alpha^{0.2}.$$

For each spacer grid, the blockage ratio is constant, so the spacer grid resistance is a function of the Reynolds number. The measured spacer grid resistance is in the form of the power function of Re (Lee et al., 2012).

$$K_{SG} = \mathrm{aRe}^{b}.$$

The spacer grid resistance for the split-type spacer grid and P/D = 1.35 is as follows:

$$K_{SG} = 2.492\mathrm{Re}^{-0.0832}.$$

In this study, the fitting curve of the spacer grid resistance coefficient is a function of Re.

$$K_{SG} = 10.43\mathrm{Re}^{-0.217}.$$

As shown in **Figure 6**, the fitting curve predicts the spacer grid resistance well, while the other correlations, much higher or lower, predict the spacer grid resistance. This is due to the difference between the spacer grids. Downstream of the spacer grid, the axial pressure loss is higher than the pressure loss calculated by the wall friction factor, as shown in **Figure 7A**. Because the strong cross flow generated by the spacer grid introduces extra friction pressure loss in the rod bundle downstream of the spacer grid from z = $3D_h$ to z = $20D_h$, we

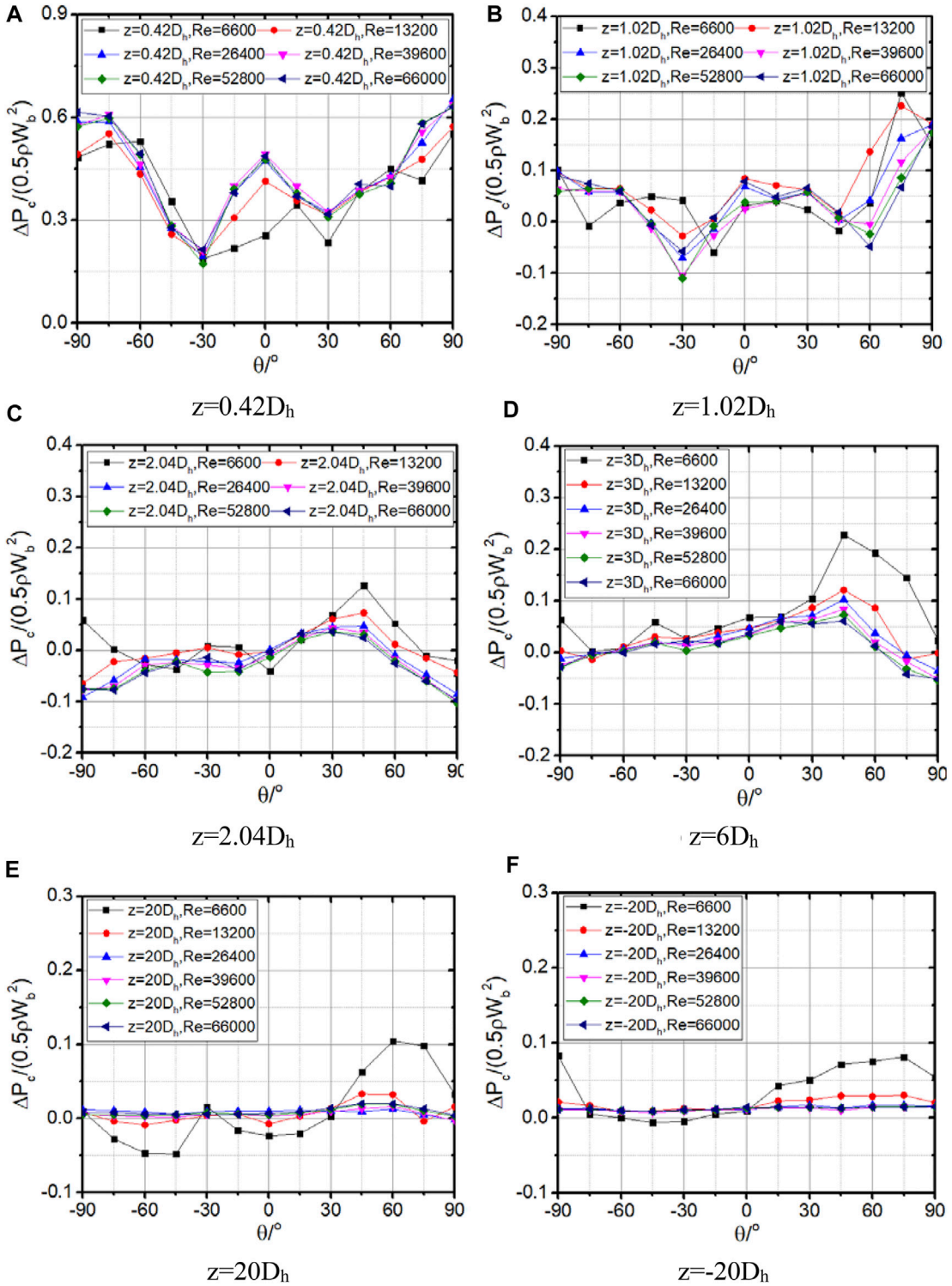

FIGURE 10 | Normalized lateral pressure loss with angles.

consider the axial pressure loss in this range to fit a friction factor curve downstream of the spacer grid, as shown in **Figure 7B**.

$$f_{SG} = 0.362\mathrm{Re}^{-0.268}.$$

To evaluate the spacer grid effect on the friction factor downstream of the spacer grid, we define the parameter f_{SGR}

$$f_{SGR} = f_{SG} - f_R.$$

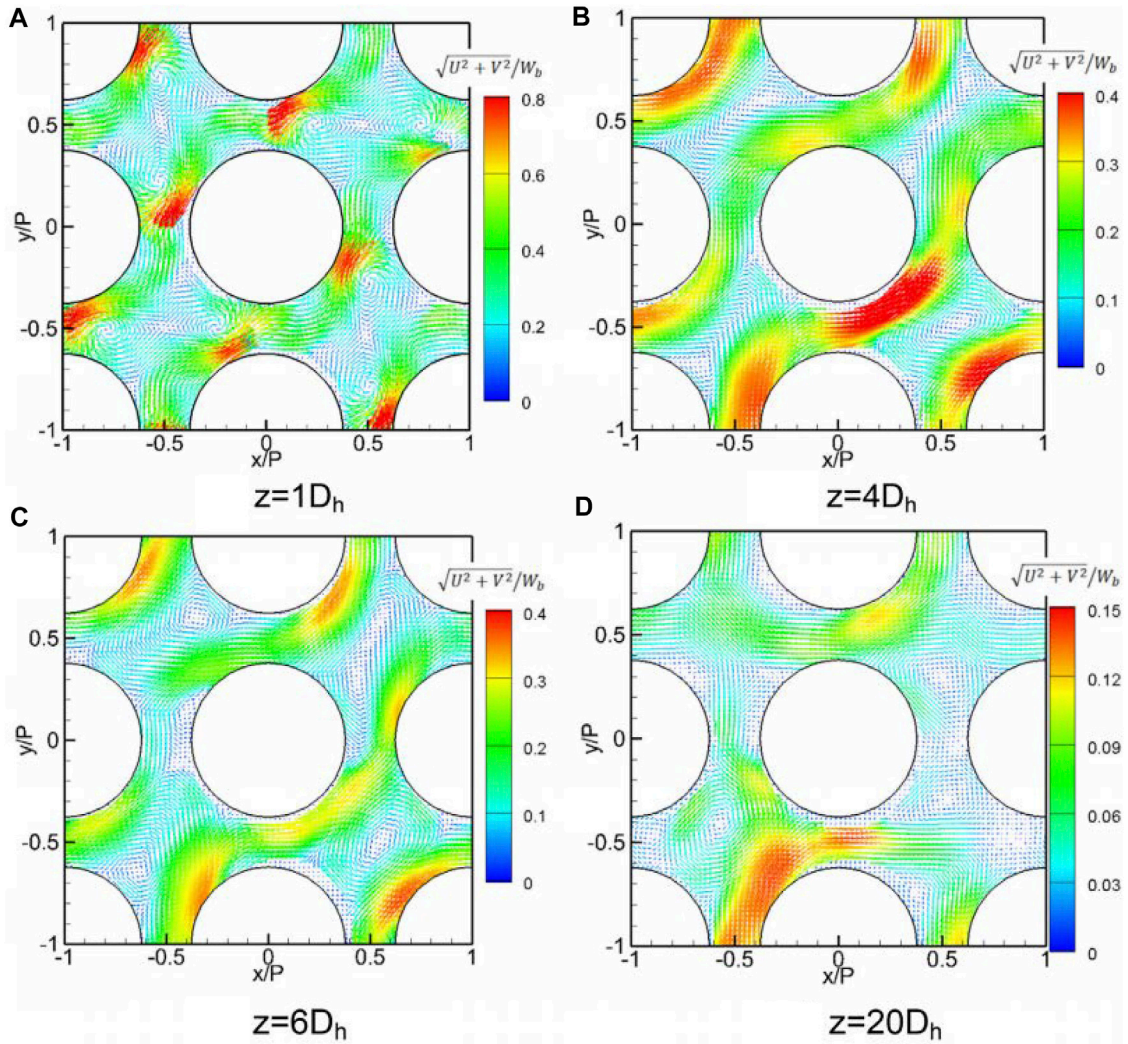

FIGURE 11 | Cross-flow structure from z = 1D_h to z = 20D_h (Xiong et al., 2020).

The curve of f_{SGR} is shown in **Figure 8**. It is clear that the spacer grid effect increases suddenly when the Re increases, and then it reaches a plateau gradually.

$$f_{SGR} = 0.362\mathrm{Re}^{-0.268} - 0.457\mathrm{Re}^{-0.298}.$$

Lateral Pressure Loss

The resistance of the mixing vanes forces lateral pressure distribution following the arrangement of the mixing vanes, generating strong vortex, and cross flow. The lateral pressure loss changes with the orienting angle based on a series of CFD simulations (Li and Gao, 2014; Chang and Tavoularis, 2015; Sibel Tas-Koehler et al., 2020). The lateral pressure loss changes with the distance from the split-type mixing vane spacer grid, and the cross flow develops from two vortices to a single vortex, and then it decays gradually (McClusky et al., 2002; McClusky et al., 2003; Chang et al., 2008; Qu et al., 2019a; Qu et al., 2019b; Xiong et al., 2020). However, lateral pressure measurements were reported in a few studies (Qu et al., 2019a; Turankok et al., 2020; Xiong et al., 2020).

In the experiment, the lateral pressure loss at different angles ranging from z = −20D_h to z = 20D_h was measured, and the typical results are shown in **Figure 9**. The lateral pressure loss is maintained low, close to zero, from z = −20D_h to z = −5D_h because the flow in the rod bundle has been fully developed at z = −20D_h, and the spacer grid blockage effect on the flow upstream is still negligible at z = −5D_h. The lateral pressure loss shows a sharp decrease just upstream of the spacer grid between z = −5D_h and z = −3.4D_h because of the suddenly reduced flow area due to the spacer grid. The root of the mixing vanes locates at z = 0D_h, and the lateral pressure loss increases sharply and reaches its peak value at around half of the height of the mixing vanes (z = 0.40D_h). A similar conclusion can be seen in the work of Chang and Tavoularis (2015). The peak value of lateral pressure loss is strong enough to generate a cross flow comparable to the bulk velocity.

The circumferential distribution of lateral pressure loss can be divided into three regions and two patterns, as shown in **Figure 10**. In the mixing vane region, two lower lateral pressure loss regions and three higher lateral pressure loss regions form the "W" pattern near the spacer grid from z = $0D_h$ to z = $1D_h$, especially in the height of the mixing vanes. This "W" pattern of lateral pressure loss generates two vortices in the sub-channels, as shown in **Figure 11A**. The lateral pressure loss suddenly increases from z = $0D_h$ to z = $0.4D_h$ at the angle $\theta = 15^o$, and the local maximum values of lateral pressure loss is maintained at $\theta = 0^o$ from z = $0.4D_h$ to z = $1.1D_h$. When the flow passes through the mixing vane region, the circumferential pattern of the lateral pressure loss changes quickly from the "W" pattern to the "Λ" pattern from z = $1D_h$ to z = $2D_h$ in the pattern transition region, while the position of the peak lateral pressure loss changes from $\theta = 0^\circ$ to $\theta = 45^\circ$. This pattern transformation will force the vortex pattern change from two vortices to a single vortex further. However, this cross-flow pattern change is almost finished until z = $4D_h$, as shown in **Figure 11B**. This indicates that the cross-flow pattern change lags behind the lateral pressure loss change because of the difference of propagation velocity between the pressure and the flow. In the single peak region, the lateral pressure loss keeps the "Λ" pattern from z = $2D_h$ to z = $20D_h$, while the maximum lateral pressure loss changes its circular position from $\theta = 45^\circ$ to $\theta = 60^\circ$ from z = $2D_h$ to z = $6D_h$. During this region, the lagged vortex pattern changes from two vortices to a single vortex, as shown in **Figure 11C**. Then the single vortex decays gradually, as shown in **Figure 11D**.

CONCLUSION

In this study, axial and lateral pressure loss in the central inner sub-channels of the 5 × 5–rod bundle were measured from z = $-20D_h$ to z = $20D_h$ and from $\theta = -90^\circ$ to $\theta = 90^\circ$ under conditions of the Reynolds number from 6,600 to 66,000.

The axial pressure loss shows a weak correlation with the orienting angles and can be divided into three regions. When the flow is fully developed upstream of the spacer grid, the wall friction is the main reason of axial pressure loss, which is a decreasing power function of the Reynolds number. The spacer grid makes the most contribution to the axial pressure loss, and the spacer grid resistance is also a decreasing power function of the Reynolds number. Downstream of the spacer grid, the mixing vanes generate a strong cross flow circulating the rod surface, resulting in additional wall friction compared with the bared rods. This additional wall friction factor quickly increases with the Reynolds number and is almost kept constant when Re = 66,000.

The lateral pressure loss is caused by the mixing vane blockage to the flow area. The lateral pressure loss increases suddenly just upstream of the spacer grid. In the mixing vane height region, the lateral pressure loss increases sharply from z = $0D_h$ to z = $0.4D_h$ and decreases quickly from z = $0.4D_h$ to z = $0.8D_h$. The lateral pressure loss is obviously huge enough to generate a strong cross flow comparable with the bulk velocity. The "W" pattern of circumferential distribution of lateral pressure loss generates two vortices in the sub-channels. After the flow passes through the mixing vanes, the lateral pressure loss continuously decreases from z = $0.8D_h$ to z = $2D_h$, and the circular distribution pattern of lateral pressure loss becomes the "Λ" pattern. The lateral pressure loss increases slightly from z = $2D_h$ to z = $3D_h$, and then it decreases slowly until it becomes nearly constant at z = $20D_h$. All these deformations of lateral pressure loss will make the cross-flow pattern change later. As the flow develops downstream of the spacer grid, the cross-flow resistance becomes larger and larger until the cross flow disappears.

DATA AVAILABILITY STATEMENT

The raw data supporting the conclusions of this article will be made available by the authors, without undue reservation.

AUTHOR CONTRIBUTIONS

WQ: methodology and writing—original draft, review, and editing. WY: experimental labor and data processing. JX: supervision. XC: supervision.

FUNDING

This work was supported by the China Postdoctoral Science Foundation (2020M681305) and National Key R&D Program of China (2018YFE0116100).

REFERENCES

Agbodemegbe, V. Y., Cheng, X., Akaho, E. H. K., and Allotey, F. K. A. (2015). Correlation for Cross-Flow Resistance Coefficient Using STAR-CCM+ Simulation Data for Flow of Water through Rod Bundle Supported by Spacer Grid with Split-type Mixing Vane. *Nucl. Eng. Des.* 285, 134–149. doi:10.1016/j.nucengdes.2015.01.003

Brkić, D. (2011). Review of Explicit Approximations to the Colebrook Relation for Flow Friction. *J. Pet. Sci. Eng.* 77, 34–48. doi:10.1016/j.petrol.2011.02.006

Caraghiaur, D., Anglart, H., and Frid, W. (2009). Experimental Investigation of Turbulent Flow through Spacer Grids in Fuel Rod Bundles. *Nucl. Eng. Des.* 239, 2013–2021. doi:10.1016/j.nucengdes.2009.05.029

Cevolani, S. (1995). ENEA Themohydraulic Data Base for the Advanced Water-Cooled Reactor Analysis. in 1st Research Co-ordination Meeting of IAEA CRP on Thermohydraulic Relationships for Advanced Water Cooled Reactors, Vienna, Austria.

Chang, D., and Tavoularis, S. (2015). Hybrid Simulations of the Near Field of a Split-Vane Spacer Grid in a Rod Bundle. *Int. J. Heat Fluid Flow* 51, 151–165. doi:10.1016/j.ijheatfluidflow.2014.07.005

Chang, S. K., Moon, S. K., Baek, W. P., and Choi, Y. D. (2008). Phenomenological Investigations on the Turbulent Flow Structures in a Rod Bundle Array with Mixing Devices. *Nucl. Eng. Des.* 238, 600–609. doi:10.1016/j.nucengdes.2007.02.037

Chen, N. H. (1979). An Explicit Equation for Friction Factor in Pipe. *Chem. Eng.* 18 (3), 296–297. doi:10.1021/i160071a019

Chen, X., Du, S., Zhang, Y., Yu, H., Li, S., Peng, H., et al. (2017). Validation of CFD Analysis for Rod Bundle Flow Test with Vaned Spacer Grids. *Ann. Nucl. Energ.* 109, 370–379. doi:10.1016/j.anucene.2017.05.055

Cheng, S.-K., and Todreas, N. E. (1986). Hydrodynamic Models and Correlations for Bare and Wire-Wrapped Hexagonal Rod Bundles - Bundle Friction Factors, Subchannel Friction Factors and Mixing Parameters. *Nucl. Eng. Des.* 92, 227–251. doi:10.1016/0029-5493(86)90249-9

Cheng, S., Chen, H., and Zhang, X. (2017). CFD Analysis of Flow Field in a 5 × 5 Rod Bundle with Multi-Grid. *Ann. Nucl. Energ.* 99, 464–470. doi:10.1016/j.anucene.2016.09.053

Chenu, A., Mikityuk, K., and Chawla, R. (2011). Pressure Drop Modeling and Comparisons with Experiments for Single- and Two-phase Sodium Flow. *Nucl. Eng. Des.* 241, 3898–3909. doi:10.1016/j.nucengdes.2011.07.009

Chun, T.-H., and Oh, D.-S. (1998). A Pressure Drop Model for Spacer Grids with and without Flow Mixing Vanes. Journal of Nuclear Science and Technology Tae-Hyun CHUN, Dong-Seok OH. A Pressure Drop Model for Spacer Grids with and without Flow Mixing Vanes. *J. Nucl. Sci. Tech.* 35 (1998), 7508–7510. doi:10.1080/18811248.1998.9733899

Churchill, S. W. (1973). Empirical Expressions for the Shear Stress in Turbulent Flow in Commercial Pipe. *Aiche J.* 19 (2), 375–376. doi:10.1002/aic.690190228

Churchill, S. W. (1977). Friction Factor Equation Spans All Fluid-Flow Regimes. *Chem. Eng.* 7, 91–92.

Cigarini, M., and Donne, M. D. (1988). Thermohydraulic Optimization of Homogeneous and Heterogeneous Advanced Pressurized Water Reactors. *Nucl. Tech.* 80, 107–132. doi:10.13182/nt88-a35553

Colebrook, C. F. (1939). Turbulent Flow in Pipes with Particular Reference to the Transition Region between the Smooth and Rough Pipe Laws. *Prog. Ind. Civil Eng.* 11. doi:10.1680/ijoti.1939.13150

Deng, J., Lu, Q., Wu, D., Wang, C., Guo, C., Mi, Z., et al. (2020). Sub-channel Code Development of lead-bismuth Eutectic Fast Reactor Available for Multiple Fuel Assembly Structures. *Ann. Nucl. Energ.* 149, 107769. doi:10.1016/j.anucene.2020.107769

Epiney, A., Mikityuk, K., and Chawla, R. (2010). TRACE Qualification via Analysis of the EIR Gas-Loop Experiments with Smooth Rods. *Ann. Nucl. Energ.* 37, 875–887. doi:10.1016/j.anucene.2010.01.020

Fang, X., Xu, Y., and Zhou, Z. (2011). New Correlations of Single-phase Friction Factor for Turbulent Pipe Flow and Evaluation of Existing Single-phase Friction Factor Correlations. *Nucl. Eng. Des.* 241, 897–902. doi:10.1016/j.nucengdes.2010.12.019

Haaland, S. E. (1983). Simple and Explicit Formulas for the Friction Factor in Turbulent Pipe Flow. *J. Fluids Eng.* 105, 89–90. doi:10.1115/1.3240948

Han, B., Yang, B.-W., and Zha, Y. (2018). Numerical Study on the Effect of Grid Mixing Span in 2 × 1 Spacer Grid. *Nucl. Eng. Des.* 339, 11–20. doi:10.1016/j.nucengdes.2018.08.030

Idelchik, I. E. (1986). *Handbook of Hydraulic Resistance*. New York: Hemisphere Publishing Corporation.

In, W. K., Shin, C. H., Kwack, Y. K., and Lee, C. Y. (2015). Measurement and CFD Calculation of Spacer Loss Coefficient for a Tight-Lattice Fuel Bundle. *Nucl. Eng. Des.* 284, 153–161.

Lee, C. Y., Shin, C. H., and In, W. K., (2012). Pressure Drop in Dual-Cooled Annular and Cylindrical Solid Fuel Assemblies for Pressurized Water Reactor. *Nucl. Eng. Des.* 250, 287–293. doi:10.1016/j.nucengdes.2012.05.039

Li, X., Chen, D., and Hu, L. (2019). Numerical Investigation on Mixing Performance in Rod Bundle with Spacer Grid Based on Anisotropic Turbulent Mixing Model. *Int. J. Heat Mass Transfer* 130, 843–856. doi:10.1016/j.ijheatmasstransfer.2018.10.121

Li, X., and Gao, Y. (2014). Methods of Simulating Large-Scale Rod Bundle and Application to a 17×17 Fuel Assembly with Mixing Vane Spacer Grid. *Nucl. Eng. Des.* 267, 10–22. doi:10.1016/j.nucengdes.2013.11.064

Liu, J., and Todreas, N. (1979). *The Comparison of Available Data on PWR Assembly Thermal Hydraulic Behavior with Analytical Predictions*. Cambridge: Energy Laboratory and Department of Nuclear Engineering, 83–86.

Manadilli, G. (1997). Replace Implicit Equations with Signomial Functions. *Chem. Eng.* 104 (8), 129–132.

Maskal, A. B., and Aydogan, F. (2017). Mathematical Spacer Grid Models for Single Phase Flow. *Ann. Nucl. Energ.* 103, 130–146. doi:10.1016/j.anucene.2017.01.019

McClusky, H. L., Holloway, M. V., Beasley, D. E., and Conner, M. E. (2002). Development of Swirling Flow in a Rod Bundle Subchannel. *J. Fluids Eng.* 124, 747–755. doi:10.1115/1.1478066

McClusky, H. L., Holloway, M. V., Conover, T. A., Beasley, D. E., Conner, M. E., and Smith, L. D. (2003). Mapping of the Lateral Flow Field in Typical Subchannels of a Support Grid with Vanes. *J. Fluids Eng.* 125, 987. doi:10.1115/1.1625688

Pacio, J., Daubner, M., Fellmoser, F., Litfin, K., Marocco, L., Stieglitz, R., et al. (2014). Heavy-liquid Metal Heat Transfer experiment in a 19-rod Bundle with Grid Spacers. *Nucl. Eng. Des.* 273, 33–46. doi:10.1016/j.nucengdes.2014.02.020

Qu, W., Wang, Z., Xiong, J., and Cheng, X. (2019a). Experimental Study of Cross Flow and Lateral Pressure Drop in a 5×5 Rod Bundle with Mixing Vane Spacer Grid. *Nucl. Eng. Des.* 353, 110209. doi:10.1016/j.nucengdes.2019.110209

Qu, W., Xiong, J., Chen, S., and Cheng, X. (2019b). High-fidelity PIV Measurement of Cross Flow in 5×5 Rod Bundle with Mixing Vane Grids. *Nucl. Eng. Des.* 344, 131–143. doi:10.1016/j.nucengdes.2019.01.021

Rehme, K. (1973). Pressure Drop Correlations for Fuel Element Spacers. *Nucl. Tech.* 17, 15–23. doi:10.13182/nt73-a31250

Rehme, K. (1970). Widerstandsbeiwerte von Gitterabstandshaltern für Reaktorbrennelemente. *Atomke rnenergie* 15/2, 127–130.

Savatteri, C., Warnsing, R., Loens, J., and Kottowski, H. (1986). Results and Comparison of Dry-Out in Grid and Wire Spaced Bundles at Single- and Two-phase Flow. in Proc.12th Liquid Metal Boiling Working Group (Grenoble, France: LMBWG), 164–190.

Schikorr, M., Bubelis, E., Mansani, L., and Litfin, K. (2010). Proposal for Pressure Drop Prediction for a Fuel Bundle with Grid Spacers Using Rehme Pressure Drop Correlations. *Nucl. Eng. Des.* 240, 1830–1842. doi:10.1016/j.nucengdes.2010.03.039

Sibel Tas-Koehler, G. L., Krepper, Eckhard., Unger, Sebastian., and Hampel, Uwe. (2020). Numerical Investigation on the Effect of Transversal Fluid Field Deformation on Heat Transfer in a Rod Bundle with Mixing Vanes. *Nucl. Eng. Des.* 361, 110575. doi:10.1016/j.nucengdes.2020.110575

Sonnad, J. R., and Goudar, C. T. (2006). Turbulent Flow Friction Factor Calculation Using a Mathematically Exact Alternative to the Colebrook–White Equation. *J. Hydraul Eng. ASCE* 132 (8), 7. doi:10.1061/(asce)0733-9429(2006)132:8(863)

Tapucu, A. (1977). Studies on Diversion Crossflow between Two Parallel Channels Communicating by a Lateral Slot. 1: Transverse Flow Resistance Coefficient. *Nucl. Eng. Des.* 42, 297–306. doi:10.1016/0029-5493(77)90191-1

Toptan, A., Porter, N. W., Salko, R. K., and Avramova, M. N. (2018). Implementation and Assessment of wall Friction Models for LWR Core Analysis. *Ann. Nucl. Energ.* 115, 565–572. doi:10.1016/j.anucene.2018.02.022

Turankok, N., Moreno, F., Bantiche, S., Bazin, F., Biscay, V., Lohez, T., et al. (2020). Unsteady Pressure and Velocity Measurements in 5×5 Rods Bundle Using Grids with and without Mixing Vanes. *Nucl. Eng. Des.* 364, 110687. doi:10.1016/j.nucengdes.2020.110687

Vog, P., Markfort, D., and Ruppert, E., (1971). A thermal-hydraulic Analysis for Fuel Elements with Liquid Metal Cooling, in International Conference of Heat and Mass Transfer, Trogir, Yugoslavia.

Wang, Y., Wang, M., Ju, H., Zhao, M., Zhang, D., Tian, W., et al. (2020). CFD Simulation of Flow and Heat Transfer Characteristics in a 5x5 Fuel Rod Bundles with Spacer Grids of Advanced PWR. *Nucl. Eng. Tech.* 52, 1386–1395. doi:10.1016/j.net.2019.12.012

Wu, J. M., Liang, H. Y., Zhu, F. J., and Lei, J. (2017). CFD Analysis of the Impact of a Novel Spacer Grid with Longitudinal Vortex Generators on the Sub-channel Flow and Heat Transfer of a Rod Bundle. *Nucl. Eng. Des.* 324, 78–92. doi:10.1016/j.nucengdes.2017.08.029

Xiong, J., Cheng, R., Lu, C., Chai, X., Liu, X., and Cheng, X. (2018). CFD Simulation of Swirling Flow Induced by Twist Vanes in a Rod Bundle. *Nucl. Eng. Des.* 338, 52–62. doi:10.1016/j.nucengdes.2018.08.003

Xiong, J., Qu, W., Zhang, T., Chai, X., Liu, X., and Yang, Y. (2020). Experimental Investigation on Split-Mixing-Vane Forced Mixing in Pressurized Water Reactor Fuel Assembly. *Ann. Nucl. Energ.* 143, 107450. doi:10.1016/j.anucene.2020.107450

Yıldırım, G. (2009). Computer-based Analysis of Explicit Approximations to the Implicit Colebrook–White Equation in Turbulent Flow Friction Factor Calculation. *Adv. Eng. Softw.* 40, 1183–1190.

Conflict of Interest: The authors declare that the research was conducted in the absence of any commercial or financial relationships that could be construed as a potential conflict of interest.

frontiers in Energy Research

ORIGINAL RESEARCH
published: 22 June 2021
doi: 10.3389/fenrg.2021.678741

Optimization of a Fuel Assembly for Supercritical Water-Cooled Reactor CSR1000

*Fawen Zhu *, Lele Zheng, Quan-Yao Ren *, Ti Yue, Hua Pang, Linna Feng, Xiang Li, Renjie Ran and Shan Huang*

Science and Technology on Reactor System Design Technology Laboratory, Nuclear Power Institute of China, Chengdu, China

As one of the Generation IV nuclear reactors, the SCWR (supercritical water-cooled reactor) has high economy and safety margin, good mechanical properties for its high thermal efficiency, and simplified structure design. As the key component of nuclear reactor, the fuel assembly has always been the main issue for the design of the SCWR. The design of the fuel assembly for CSR1000 proposed by the Nuclear Power Institute of China (NPIC) has been optimized and presented in this study, which is composed of four subassemblies welded by four filler strips and guide thimbles arranged close together in the cross-shaped passage. Aiming at improving the hydraulic buffer performance of the cruciform control rod, the scram time and terminal velocity of control rod assembly were calculated to assess the scram performance based on the computational fluid dynamics and dynamic mesh method, and the mechanical property and neutronic performance of assemblies were also investigated. It has been demonstrated that the optimized fuel assembly had good feasibility and performance, which was a promising design for CSR1000.

Keywords: supercritical water-cooled reactor (SCWR), fuel assembly, optimization, CSR, control rod property

OPEN ACCESS

Edited by:
Jinbiao Xiong,
Shanghai Jiao Tong University, China

Reviewed by:
Pan Wu,
Xi'an Jiaotong University, China
Wenhai Qu,
Shanghai Jiao Tong University, China

****Correspondence:***
Fawen Zhu
zhufawen1983@126.com
Quan-Yao Ren
renquanyao@foxmail.com

Specialty section:
This article was submitted to Nuclear Energy, a section of the journal Frontiers in Energy Research

Received: *10 March 2021*
Accepted: *01 June 2021*
Published: *22 June 2021*

Citation:
Zhu F, Zheng L, Ren Q-Y, Yue T, Pang H, Feng L, Li X, Ran R and Huang S (2021) Optimization of a Fuel Assembly for Supercritical Water-Cooled Reactor CSR1000. Front. Energy Res. 9:678741. doi: 10.3389/fenrg.2021.678741

INTRODUCTION

The supercritical water-cooled reactor (SCWR) is one of the most promising reactors for Generation IV nuclear reactors due to its higher thermal efficiency and more simplified structure than the state-of-the-art LWRs (light water reactors). In order to achieve a better thermal efficiency, the coolant inlet temperature was 280°C and the outlet temperature was over 500°C in the reactor core, which caused a high heat-up of the coolant within the core by more than 200°C (Squarer et al., 2003). Thus, the fuel assembly had to withstand the high temperature, high temperature difference, and high neutron irradiation in normal operating conditions, making the design of the fuel assembly more complex and difficult.

Although many challenges exist, many countries and research organizations have proposed their fuel assembly concepts since 1990. A two-pass core composed of 121 square fuel assemblies with a single row of fuel rods between water rods was adopted by the Japanese Super LWR (Yamaji et al., 2005), a three-pass core with a square fuel assembly cluster consisting of nine subassemblies was proposed by the European HPLWR (Fischer et al., 2009), and a one-pass core with square assemblies and water rods was developed by the American SCWR (Buongiorno and MacDonald, 2003). In Korea, the assemblies were square-type with a cruciform type U/Zr solid moderator to avoid complicated water flow paths (Bae et al., 2007), while in Canada, the fuel assembly of CANDU-SCWR continued the pressure tube (PT)/Calandria tube (CT) design from CANDU, and the moderator adopted the design of the heavy-water reactor (Leung, 2015). So far, most concept designs of the thermal SCWR fuel assembly were square-type, with

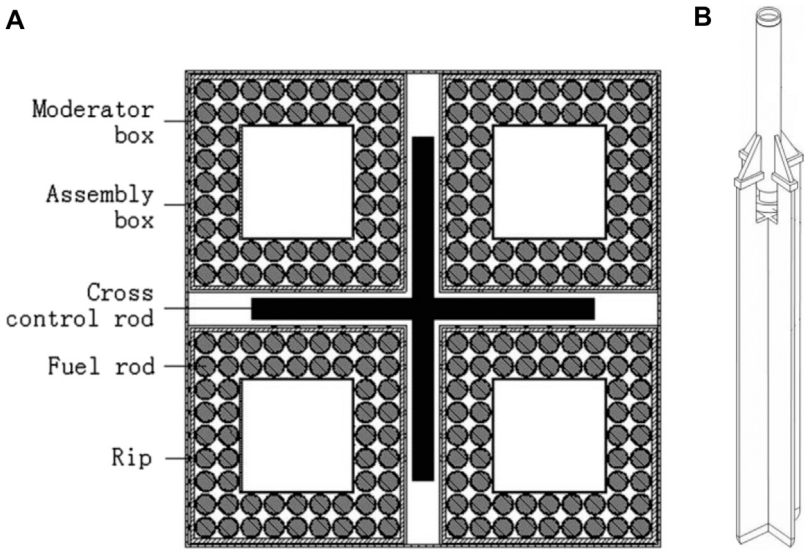

FIGURE 1 | Previous fuel assembly and the cruciform control rod. **(A)** Cross-sectional design and **(B)** the cruciform control rod.

water rods as an extra moderator. The high enthalpy rose in the core enabled the use of two- and three-pass cores, which reduced the maximum cladding temperature (Reiss et al., 2010). Moreover, many studies devoted to the heat transfer performance of supercritical fluid. Xiong et al. (Xiong and Cheng, 2014; Xiong et al., 2015) proposed a four-equation model to predict the mixed convective heat transfer in supercritical pressure fluid and assessed the performance of RANS models in predicting supercritical pressure heat transfer in a 2 × 2 rod bundle. Castro et al. (2020) performed coupled calculations with the CFD code CFX-19.0 and the Monte Carlo neutronic code MCNP6 to analyze the heat transfer in supercritical water flowing through the typical fuel assembly of the high-performance light water reactor (HPLWR).

In China, a thermal spectrum SCWR concept called CSR1000 was proposed by the Nuclear Power Institute of China (NPIC) with a two-pass core arrangement, which increased the core heating length and decreased the temperature difference in the axial direction effectively (Xia et al., 2013). The preliminary safety evaluation (Wu et al., 2014) and LOCA analysis (Chen et al., 2017) for CSR1000 were also conducted. Considering the two-pass core structure of CSR1000 and the separation of moderator water and coolant water, the new design of the 2 × 2 fuel assembly cluster consisting of four subassemblies was developed (Zhu et al., 2013). Furthermore, a kind of configuration design of the fuel assembly with SiC as the cladding material was proposed (Feng and Zhu, 2016). Yang et al. (2012) presented an optimized design of the fuel assembly for the fast zone of a mixed-spectrum supercritical water-cooled reactor (SCWR-M), which had a multilayer structure and was divided into several seed and blanket layers.

However, there still are some issues to be addressed, especially the large drop load of the cruciform control rod on the fuel assembly. In the present study, the design of the fuel assembly for CSR1000 had been optimized, whose scram performance, mechanical properties, and neutron moderation were analyzed and discussed in detail.

THE DESIGN OPTIMIZATION

The Previous Plate-Type Design

CSR1000 was a pressure-vessel SCWR concept with 157 fuel assemblies, and the active core was 4.2 m. In the previous design as shown in **Figure 1**, each fuel assembly consisted of four subassemblies, while each subassembly contained 56 fuel rods and one square moderator box located in the center. In order to strengthen the lateral support and connect subassemblies into a cluster, two grids with the height of 30 mm were designed. The cruciform control rod with the thickness of 8 mm was adopted, which served as the cross channel for the intervention of the cruciform control rod from the top of the assembly (Feng and Zhu, 2016). It should be noted that it contained 60 control rods with the absorber diameter of 5.6 mm.

The numerical simulation was conducted on the dropping and buffering behavior of the cruciform control rod by Xiao et al. (2017), and it was demonstrated that the whole drop time of the cruciform control rod was about 1.018 s, with the drop distance of 4.1 m. However, at the end of the whole drop distance, the velocity of control rod was up to 7.64 m/s, which would result in the too large impact load on the fuel assembly to guarantee the structure integrity of the fuel assembly. The large impact load was attributed to the lack of hydraulic buffer effect when the cruciform control rod was inserted into the fuel assembly, which was a key design for the rod cluster control assemblies (RCCAs) in the pressurized water reactor (PWR). Moreover, considering that the irradiation deformation of the cruciform control rod was much larger than that of the RCCA in the PWR, the gap between the cruciform control rod and the cross channel of the fuel assembly must be set as a reasonable value.

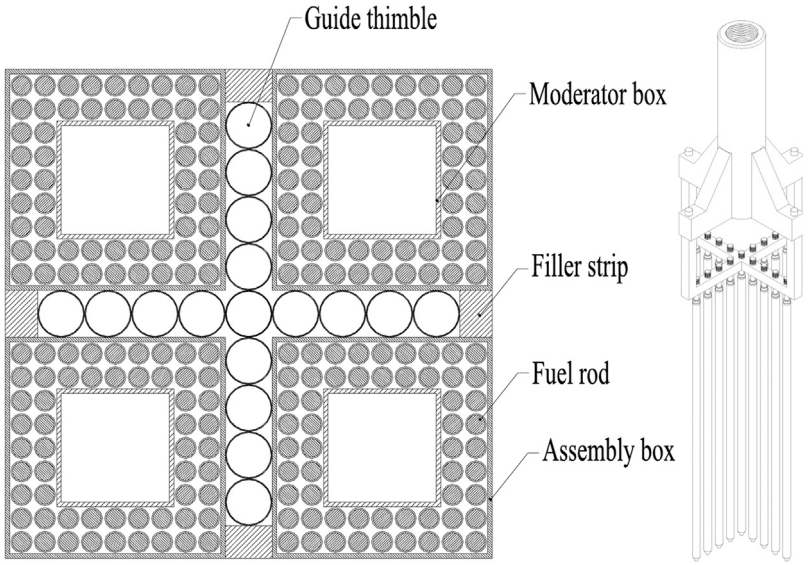

FIGURE 2 | Optimized fuel assembly and the cruciform control rod. **(A)** Cross-sectional design and **(B)** the cruciform control rod.

TABLE 1 | Comparison between the previous design and optimized structure.

Design parameter	Previous design	Optimized design
Subassembly number	4	4
Moderator box number	4	4
Fuel rods number	4 × 56	4 × 56
Fuel assembly sectional dimension (mm × mm)	218 × 218	218 × 218
Width of cross-shaped passage (mm)	21	21
Assembly box outer size/wall thickness (mm)	98.5/2	98.5/2
Moderator box outer size/wall thickness (mm)	52.5/0.8	52.5/2
The number of guide thimbles	—	17
Guide thimble outer/inner diameter (mm)	—	20/19
Inner diameter of dashpot (mm)	—	18
Center distance of guide thimbles	—	20.5
Thickness/diameter of the control plate/rod (mm)	8	17
Diameter of control absorber	5.6	14
Fuel rod diameter/cladding thickness/rod pitch (mm)	9.5/0.57/10.5	9.5/0.57/10.5
The gap between fuel rods and box walls (mm)	0.5	0.5
The gap between the adjacent assemblies (mm)	21	21
Radial fixed position of fuel rod	Rip wrap	Rip wrap
The boxes and cladding materials	310S stainless steel	310S stainless steel

The Optimized Rod-Type Design

In order to strengthen the hydraulic buffer property of the cruciform control rod, an optimized design of the fuel assembly was proposed, as shown in **Figure 2**. The fuel assembly comprised four subassemblies, which were welded together by four filler strips instead of grids along the axial height, so as to minimize thermal deflection of the fuel assembly. The number and dimension of fuel rods among the fuel assembly were the same as those of the previous design. The radial fixed position of the fuel rod was rip wrapped instead of wire wrapped, which can reduce the flow-induced vibration due to the high flow velocity of the coolant. In addition, in order to insulate the heat transfer of inside and outside of moderator box, the thickness of the moderator box was increased to 2 mm, which was the same as that of the assembly box, including the wall thickness of 0.5 mm at both sides and ZrO_2 filling in the middle with the thickness of 1 mm. The comparison of main parameters between the previous plate-type and optimized rod-type fuel assemblies for CSR1000 is listed in **Table 1**.

There were 17 guide thimbles arranged close together in the cross-shaped passage, which was surrounded by the walls of four subassembly boxes. Aiming at reducing the impact load on the fuel assembly, the guide thimbles were designed as shown in **Figure 3**, which consisted of the upper buffer with the inner diameter of 19 mm, the lower buffer with the inner diameter of 18 mm, and the drain hole with the diameter of 3 mm. When the cruciform control rod assembly is inserted into the guide thimbles, the coolant would be ejected out from the drain holes and top gaps between control rods and guide thimbles, which would provide enough and increasing hydraulic buffering force.

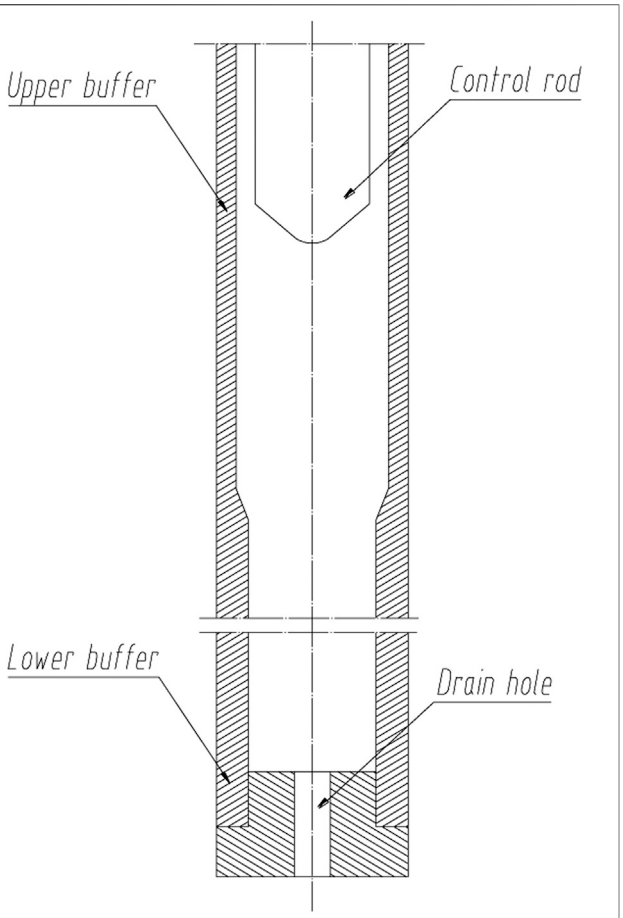

FIGURE 3 | Scheme of guide thimble.

The optimized design of the cruciform control rod is also given in **Figure 2B**. Different from the conventional cruciform control rod design like that in **Figure 1**, the optimized design adopted the cylindrical rods hanging on the cross-shaped beam, which matched the structure of guide thimbles in the optimized fuel assembly in **Figure 2A**. When the optimized cruciform control rod is inserted into the guide thimbles of the fuel assembly, the small annular gap between the control rod and guide thimble increased the hydraulic buffer effect greatly, especially in the lower buffer section. Therefore, the impact force on the fuel assembly might be decreased significantly. Besides, the water gap between the guide thimble and cross-shaped passage could improve the power distribution characteristics and decrease the power peak factor of the fuel assembly in the reactor core.

THE DESIGN ANALYSIS

Scram Analysis

In the SCWR, the control rod drop behavior is the key issues for the reactor safety and the integrity of the fuel assembly. For the optimized cruciform control rod, each control rod corresponded to every single guide thimbles of the fuel assembly. It was expected that the control rods dropped quickly through the upper buffer and dropped slowly in the lower buffer, so as to control the reactivity of the reactor and decrease the impact force on the fuel assembly separately.

TABLE 2 | Physical properties of water.

Parameters	Value
Pressure/MPa	25
Temperature/°C	390
Dynamic viscosity/(Pa•s)	3.17E-5
Density (kg/m^3)	221.0

Computational Fluid Dynamic Numerical Method

In order to evaluate the dropping time and buffering behaviors of the optimized fuel assembly, the dynamic mesh method in computational fluid dynamics (CFD) was utilized to conduct the numerical study on the dropping process of the optimized control rod. Since the whole system was symmetric, the quarter geometrical structure and periodic boundary conditions were used, and all of the boundary conditions for solid in this simulation were set as wall. The gravitational acceleration was set as 0, 0, and −9.81 m/s^2 because the control rod was designed to drop along the *z*-direction. By neglecting that the fluid in the guide thimble was isothermal, only the mass and momentum conservation equations were adopted to analyze the whole process. The RNG k-e turbulence model was recognized to be able to obtain high calculation accuracy in engineering applications; thus, it was applied in the numerical simulation. The mass of the control rod was set as 90 kg, and the physical properties of water are listed in **Table 2**. It should be noted that the water temperature was defined as the average value between the inlet and the outlet temperature.

Aiming at simulating the dropping process of control rod, six degree of freedom (6 DOF, one of the dynamic mesh methods) was used by changing the mesh size to simulate the volume change of fluid domain. Moreover, in order to avoid the appearance of negative volume mesh, structured grid was adopted. And, the layering method was employed to update the mesh, and the height-based layering method with the split factor of 0.4 and collapse factor of 0.2 was used. The total number of grids was approximately 18 million, and the minimum orthogonal quality was 0.23.

Pressure-based solver and SIMPLE scheme were used in this calculation. Because the dropping process of the control rod was dynamic and the whole process was transient, the differential scheme of turbulent kinetic energy and the turbulent dissipation rate were set as the first-order upwind in order to make sure the solution can be converged easily. The transient formulation was also set as the first-order implicit based on the same reason. The differential scheme of the rest of the parameters was set as the second order. To avoid the emergence of negative volume mesh and make sure the solution is converged in every time step, a smaller time step of 0.001 s and maximum 50 iterations per time step were used, respectively.

The Scram Performance

The evolution of dropping distance and velocity of control rod is shown in **Figure 4**, while the pressure force, total drag force, and viscous force

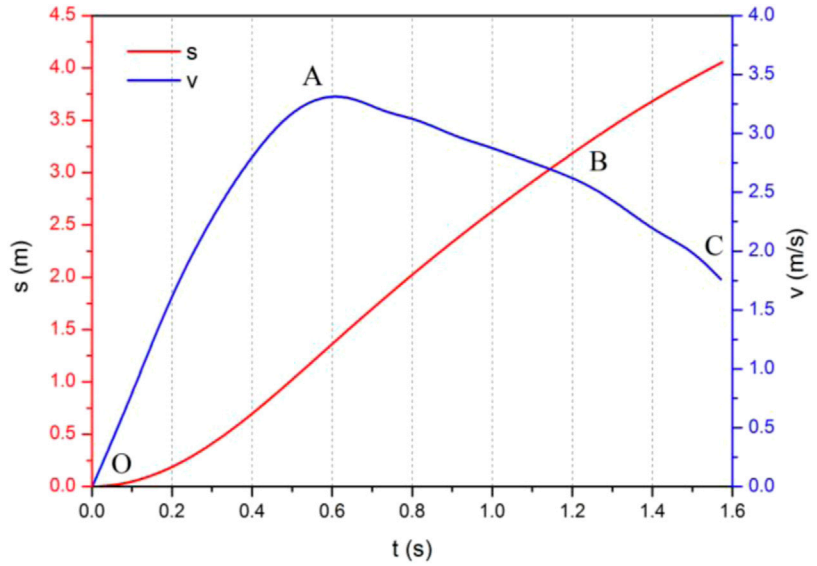

FIGURE 4 | Change of velocity and position over time.

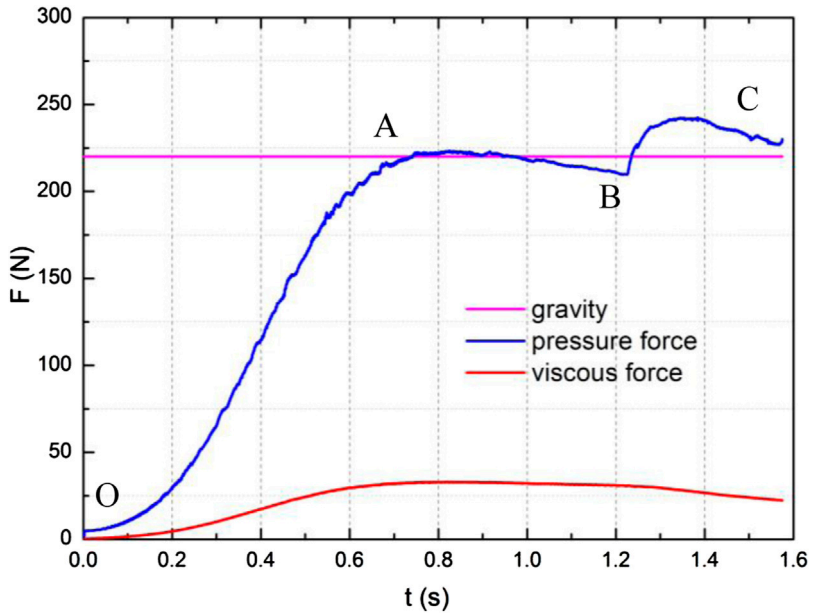

FIGURE 5 | Evolution of forces acting on the control rod.

of control rod assembly are shown in **Figure 5**. As can be seen, the dropping process could be divided into the following three processes:

(1) The acceleration process at the beginning (OA): the dropping velocity of the control rod assembly increased rapidly because of the leading role of gravity, which gave rise to the rapid increment of pressure force as shown in **Figure 5**; at the same time, the pressure in the thimble guide and the water velocity in the drain hole increased rapidly, as shown in **Figure 6**. Meanwhile, the viscous force also increased for the larger velocity difference between the control rod and water. It should be noted that the pressure force represented the force induced by the pressure difference between the top and bottom positions of control rods.

(2) The slow decelerating process in the upper buffer (AB): the dropping velocity of the control rod assembly decreased due to the increasing pressure force and drag force. The pressure in the thimble guide and the water velocity in the drain hole increased further, as shown in **Figure 6**. At the end of the slow decelerating process, the control rod entered into the lower process with a small distance.

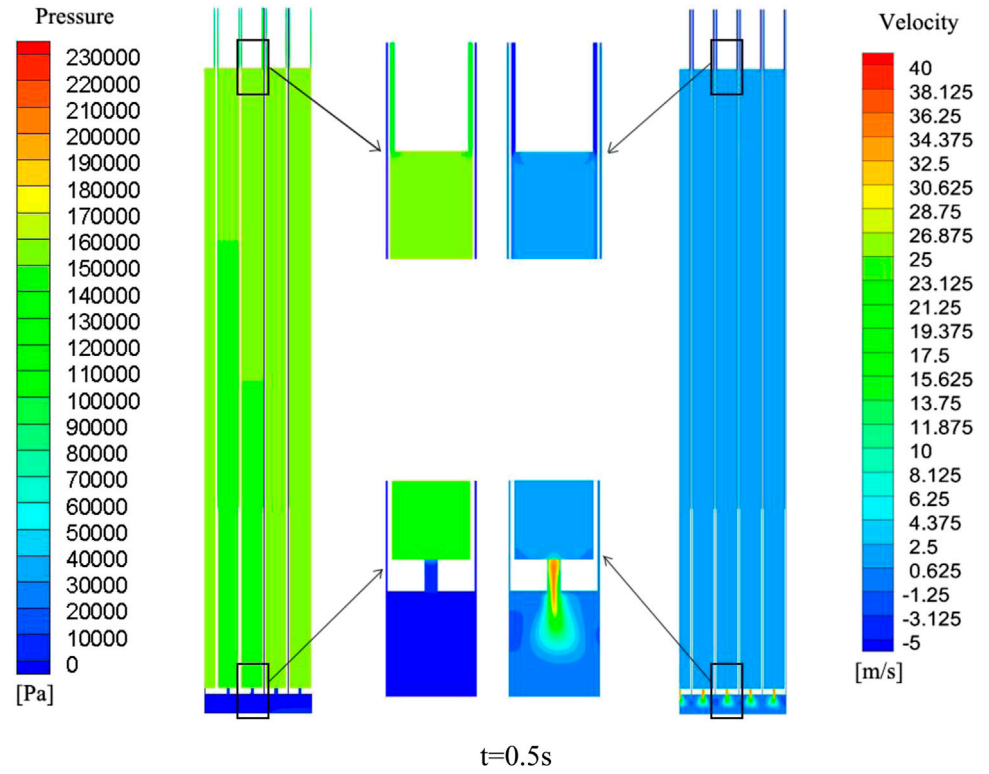

FIGURE 6 | Evolution of pressure and velocity in the guide thimble. **(A)** t=0.5 s. **(B)** t=1.0 s. **(C)** t=1.5 s.

(3) The rapid decelerating process in the lower buffer (BC): the dropping velocity decreased rapidly for the larger pressure force and drag force induced by the larger pressure difference, as shown in **Figure 6**, which resulted from the much lower water draining rate of the water across the gap at the top of guide thimbles for the much larger flow resistance.

On the whole, it took about 1.2 s for the bottom of the control rod to reach the lower buffer region and 1.57 s to insert wholly. Moreover, the terminal velocity of the control rod assembly was about 1.7 m/s, which was much smaller than that of the previous plate-type design. And, the impact load on the fuel assembly would decrease greatly. Therefore, it could be concluded that the design of the optimized fuel assembly and cruciform control rod were feasible for the SCWR in terms of the dropping behavior.

Mechanical Analysis

In order to improve the mechanical performance of the optimized fuel assembly, the outer wall thickness of the moderator box was increased from 0.8 to 2.0 mm. Thus, the mechanical analysis was conducted. For the optimized fuel assembly in **Figure 2**, the average temperature difference of the coolant and moderator inside the fuel assembly was up to 150°C. The pressure difference would exist between the assembly boxes and moderator boxes, which might cause the thermal deflection of assembly boxes and moderator boxes. Based on the study of Hofmeister et al. (2007), assuming the pressure difference of 50 kPa, the maximum deflection of wall thickness should be less than 0.1 mm when the gap between fuel rods and box walls of the optimized fuel assembly was only 0.5 mm as listed in **Table 1**, and the thermal deflection f of the assembly box could be predicted as follows:

$$f = \frac{\Delta p \times l^4}{32 \times E \times s^3}, \tag{1}$$

where Δp is the pressure difference acting on the assembly box, Δp = 0.05MPa; l is the inner side length of the assembly box, l = 94.5 mm; E is Young's modulus of the 310S assembly box, $E = 1.8 \times 10^4$ MPa; and s is the box thickness, s = 2 mm.

Compared with the moderator box, the assembly box had the same wall thickness but longer side length, thus suffering the larger thermal deflection. The calculation result of **Eq. 1** shows that the thermal deflection of the assembly box was about 0.086 mm, not exceeding the maximum deflection of 0.1 mm. Therefore, the mechanical properties of the optimized fuel assembly could meet the requirement of allowed thermal deflection.

Neutron Performance

CSR1000 was a thermal spectrum reactor with UO_2 as the fuel, which was cooled and moderated by light water. Because of high outlet temperature under supercritical water condition, the coolant had a small density, which resulted in the under-moderated issue. In order to improve neutron moderation, moderator boxes were introduced as presented in **Figure 2**. The coolant flowed among the fuel rods

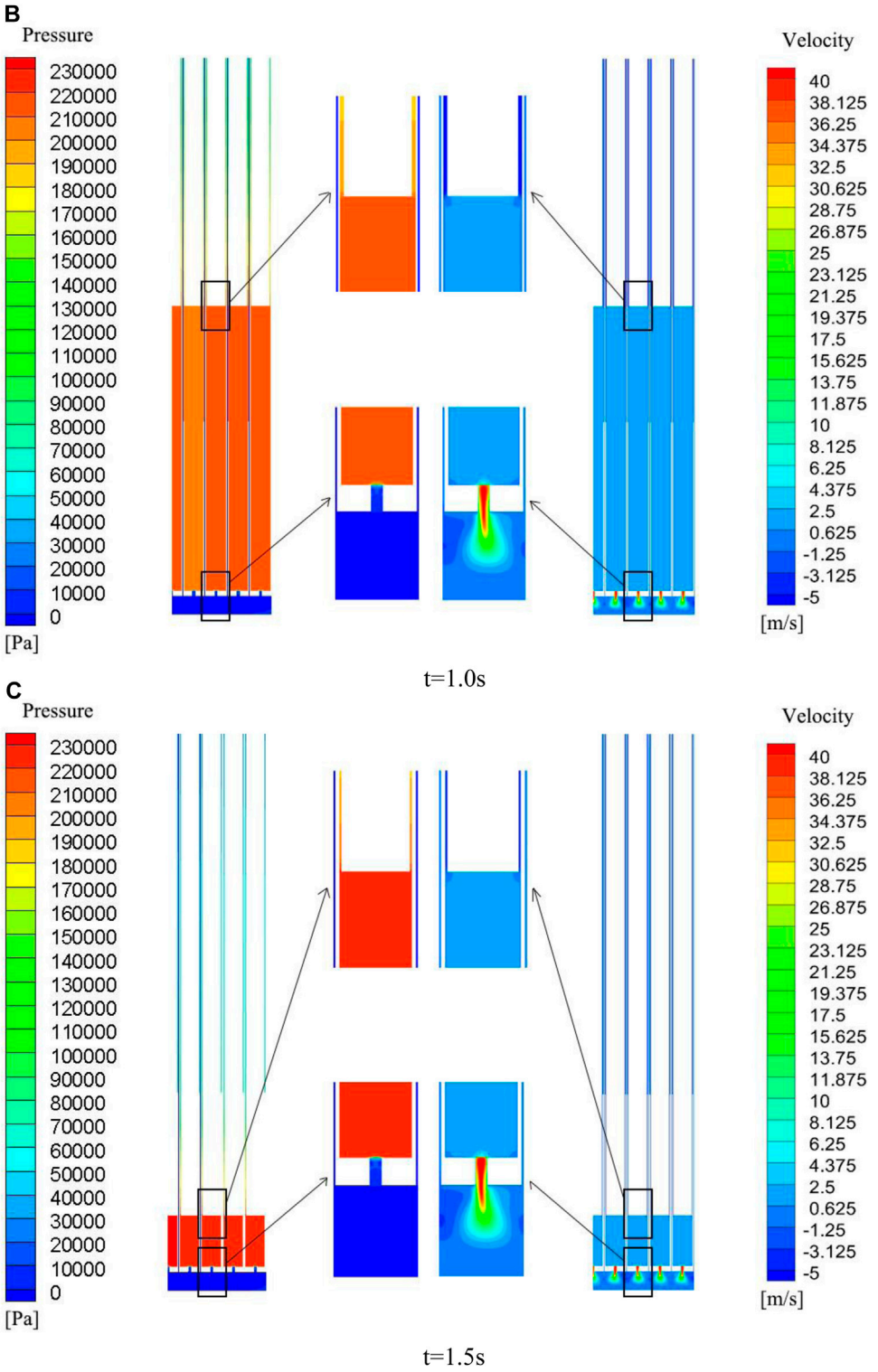

FIGURE 6 | (Continued).

between the assembly box and moderator box, while the water served as the moderator inside the moderator boxes and through the gaps between the adjacent assemblies.

Considering the water density along the height of the active core (Hofmeister et al., 2007), the gap between the adjacent assemblies, and the guide thimbles data (**Table 1**), the water-to-fuel ratio of the optimized fuel assembly was calculated. The average ratio was about 0.08, which was close to that of the typical PWR, with the water-to-fuel ratio of 0.1. Therefore, the optimized fuel assembly had a good neutron-moderating ability.

Moreover, the cross-sectional area of the absorber for the plate-type cruciform control rod is about $60 \times \pi \times 5.6^2/4 = 1{,}477.81\ mm^2$, which was much smaller than that of the absorber for the rod-type cruciform control rod ($17 \times \pi \times 7^2/4 = 2{,}616.95\ mm^2$). Thus, it could be deduced that the control rod worth of the optimized rod-type control rod was larger than that of the previous plate-type design.

CONCLUSION

An optimized design of the SCWR fuel assembly for CSR1000 aiming at solving the hydraulic drop buffering issue of the cruciform control rod had been proposed in this article, which consisted of four subassemblies welded by four filler strips and 17 guide thimbles arranged close together in the cross-shaped passage. The analysis demonstrated that the dropping time and terminal velocity of the control rod met the need of the control rod drop design, and the mechanical property as well as the neutronic performance also met the requirements of the fuel assembly design, which had good feasibility and performance.

DATA AVAILABILITY STATEMENT

The original contributions presented in the study are included in the article/Supplementary Material; further inquiries can be directed to the corresponding authors.

AUTHOR CONTRIBUTIONS

FZ: numerical simulation, data processing, and writing draft paper. LZ: numerical simulation and data processing. Q-YR: data processing and writing—editing. TY: numerical simulation and data processing. HP: writing—reviewing and supervision. LF: investigation and validation, XL: project administration and funding support. RR: project administration and funding support. SH: data processing.

FUNDING

This work was supported by the National Key R&D Program of China (No. 2018YEE0116100).

REFERENCES

Bae, Y.-Y., Jang, J.-S., Kim, H.-Y., Yoon, H.-Y., Kang, H.-O., and Bae, K.-M. (2007). Research Activities on a Supercritical Pressure Water Reactor in Korea. *Nucl. Eng. Tech.* 39, 273–286. doi:10.5516/net.2007.39.4.273

Buongiorno, J., and MacDonald, P. (2003). Study of Solid Moderators for the thermal Spectrum Supercritical Water-Cooled Reactor (Neutronics, Thermo-Mechanicsand Cost). In Proceedings of ICONE-, 11. Tokyo, Japan, 20–23.

Castro, L., Franois, J., and García, C. (2020). Coupled Monte Carlo-CFD Analysis of Heat Transfer Phenomena in a Supercritical Water Reactor Fuel Assembly. *Ann. Nucl. Energ.* 141. doi:10.1016/j.anucene.2020.107312

Chen, J., Zhou, T., Liu, L., and Fang, X. (2017). Analysis on LOCA for CSR1000. *Ann. Nucl. Energ.* 110, 903–908. doi:10.1016/j.anucene.2017.07.026

Feng, L., and Zhu, F. (2016). Fuel Assembly Design for Supercritical Water-Cooled Reactor. *J. Nucl. Eng. Radiat. Sci.* 2, 011014.

Fischer, K., Schulenberg, T., and Laurien, E. (2009). Design of a Supercritical Water-Cooled Reactor with a Three-Pass Core Arrangement. *Nucl. Eng. Des.* 239, 800–812. doi:10.1016/j.nucengdes.2008.12.019

Hofmeister, J., Waata, C., Starflinger, J., Schulenberg, T., and Laurien, E. (2007). Fuel Assembly Design Study for a Reactor with Supercritical Water. *Nucl. Eng. Des.* 237, 1513–1521. doi:10.1016/j.nucengdes.2007.01.008

Leung, L. (2015). *Status of Canadian Generation IV National Program in Supportof SCWR Concept DevelopmentISSCWR-7*. Helsinki: Finland. March 2015.

Reiss, T., Csom, G., Fehér, S., and Czifrus, S. (2010). The Simplified Supercritical Water-Cooled Reactor (SSCWR), a New SCWR Design. *Prog. Nucl. Energ.* 52, 177–189. doi:10.1016/j.pnucene.2009.06.006

Squarer, D., Schulenberg, T., Struwe, D., Oka, Y., Bittermann, D., Aksan, N., et al. (2003). High Performance Light Water Reactor. *Nucl. Eng. Des.* 221, 167–180. doi:10.1016/s0029-5493(02)00331-x

Wu, P., Gou, J., Shan, J., Zhang, B., and Li, X. (2014). Preliminary Safety Evaluation for CSR1000 with Passive Safety System. *Ann. Nucl. Energ.* 65, 390–401. doi:10.1016/j.anucene.2013.11.031

Xia, B., Yang, P., Wang, L., Ma, Y., Li, Q., Li, X., et al. (2013). Core Preliminary Conceptual Design of Supercritical Water-Cooled Reactor CSR1000. *Nucl. Power Eng.* 34 (1).

Xiao, C., Luo, Y., Zhang, H., Liu, X., and Du, H. (2017). Analysis of Control Rod Dropping and Buffering Behavior of Supercritical Water-Cooled Reactor Based on Dynamic Grid Technology. *Nucl. Power Eng.* 38 (S2), 79.

Xiong, J., and Cheng, X. (2014). Turbulence Modelling for Supercritical Pressure Heat Transfer in Upward Tube Flow. *Nucl. Eng. Des.* 270, 249–258. doi:10.1016/j.nucengdes.2014.01.014

Xiong, J., Cheng, X., and Yang, Y. (2015). Numerical Analysis on Supercritical Water Heat Transfer in a 2 × 2 Rod Bundle. *Ann. Nucl. Energ.* 80, 123–134. doi:10.1016/j.anucene.2015.02.005

Yamaji, A., Kamei, K., Oka, Y., and Koshizuka, S. (2005). Improved Core Design of the High Temperature Supercritical-Pressure Light Water Reactor. *Ann. Nucl. Energ.* 32, 651–670. doi:10.1016/j.anucene.2004.12.006

Yang, T., Liu, X., and Cheng, X. (2012). Optimization of Multilayer Fuel Assemblies for Supercritical Water-Cooled Reactors with Mixed Neutron Spectrum. *Nucl. Eng. Des.* 249, 159–165. doi:10.1016/j.nucengdes.2011.07.023

Zhu, F., Lei, T., Cheng, H., Pang, H., Peng, Y., and Ru, J. (2013). Supercritical Fuel Assembly Design Applicable for Cruciform Control Rod. *Nucl. Power Eng.* 34 (1), 35–39.

Conflict of Interest: The authors declare that the research was conducted in the absence of any commercial or financial relationships that could be construed as a potential conflict of interest.

frontiers in Energy Research

ORIGINAL RESEARCH
published: 28 June 2021
doi: 10.3389/fenrg.2021.663341

Experimental Study on the Transition Characteristics and Criterion From Wall-Peak to Core-Peak Phase Distribution in Vertical Rod Bundles

Quan-yao Ren[1], Zengping Pu[1], Ping Chen[1], Liang-ming Pan[2]*, Fawen Zhu[1]*, Meiyin Zheng[1], Haoyu Wang[1], Lie Wei[3] and Hui He[4]**

[1]Science and Technology on Reactor System Design Technology Laboratory, Chengdu, China, [2]Key Laboratory of Low-Grade Energy Utilization Technologies and Systems (Chongqing University), Ministry of Education, Chongqing, China, [3]School of Civil Engineering and Architecture, Southwest Petroleum University, Chengdu, China, [4]Department of Nuclear Science and Engineering, Shanghai Jiao Tong University, Shanghai, China

OPEN ACCESS

Edited by:
Yingwei Wu,
Xi'an Jiaotong University, China

Reviewed by:
Juliana P. Duarte,
Virginia Tech, United States
Boštjan Končar,
Institut Jožef Stefan (IJS), Slovenia

***Correspondence:**
Quan-yao Ren
renquanyao@foxmail.com
Liang-ming Pan
cneng@cqu.edu.cn
Fawen Zhu
zhufawen1983@126.com
Hui He
ME_hehui@sjtu.edu.cn

Specialty section:
This article was submitted to Nuclear Energy, a section of the journal Frontiers in Energy Research

Received: 02 February 2021
Accepted: 03 June 2021
Published: 28 June 2021

Citation:
Ren Q, Pu Z, Chen P, Pan L, Zhu F, Zheng M, Wang H, Wei L and He H (2021) Experimental Study on the Transition Characteristics and Criterion From Wall-Peak to Core-Peak Phase Distribution in Vertical Rod Bundles. Front. Energy Res. 9:663341. doi: 10.3389/fenrg.2021.663341

Aiming at understanding the phase distribution characteristics and developing the transition criterion from wall-peak to core-peak phase distribution in a rod bundle channel, air–water two-phase flow experiments were conducted in 5 × 5 rod bundles in the Interfacial Evolution Research Facility at Chongqing University (IERFC). Based on the experimental data, the influences of gas velocity, liquid velocity, mixing vane spacer grid (MVSG), and geometrical size on phase distribution have been analyzed in detail. With the increasing superficial gas velocity and decreasing liquid velocity, the wall-peak phase distribution turned to core-peak. The wall-peak phase distribution was enhanced by an MVSG, and the transition from the transitional phase distribution to the wall-peak phase distribution appeared when the air–water mixture flowed through the MVSG. The gap size was the key factor for the transition of phase distribution in rod bundles. Moreover, the transition criterion from wall-peak to core-peak phase distribution was developed based on present experimental data and the data in the literature, which was also verified based on the limited data. More experiments were recommended to focus on the detailed phase distribution in the rod bundle channel with different geometrical sizes.

Keywords: phase distribution, wall-peak, core-peak, two-phase flow, rod bundles

HIGHLIGHTS

- The typical wall-peak and core-peak phase distribution characteristics have been analyzed in vertical rod bundles.
- The influences of gas velocity, liquid velocity, spacer grid, and geometrical size on phase distribution have been discussed.
- The mixing vane spacer grid promoted the transitional phase distribution to convert into wall-peak due to the shear force, stronger turbulence, secondary flow, and smaller bubble size.
- The transition criterion from wall-peak to core-peak phase distribution was developed for rod bundle channels with different geometrical sizes.

INTRODUCTION

As the common phenomena in chemical industry, petrochemical industry, nuclear power, and refrigeration, gas–liquid two-phase flows attracted much attention and were intensively investigated numerically and theoretically. As a complex and open geometry, rod bundle channel was widely applied in the nuclear reactor, heat exchanger, and chemical reactor. Thus, it is crucial to make clear the flow resistance, heat transfer characteristics, chemical reaction rate, and critical heat flux in rod bundles, which is of great significance for the safety and efficiency of the equipment. Furthermore, these crucial properties are always affected by the phase distribution characteristics.

Phase Distribution Characteristics in Circular Pipe

A large amount of work focused on phase distribution in conventional channels, especially in the circular pipe. Serizawa et al. (1975a), Serizawa et al. (1975b), and Akimi et al. (1988) studied the local characteristics of air–water two-phase flow in a round pipe with the diameter of 60 mm experimentally. And two typical phase distribution patterns were identified: wall-peak and core-peak phase distributions. For wall-peak phase distribution, bubbles tended to aggregate near the wall and the near-wall-peaks of void fraction profiles appeared. However, the core-peak phase distribution showed the void fraction peaks at the channel center. Ishii et al. (Hibiki and Ishii, 1999; Hibiki et al., 2001) also found the wall-peak and core-peak phase distributions for air–water two-phase flows in 25.4 and 50.8 mm pipes. Based on the wire mesh sensor, Prasser et al. (2007) presented the evolution of the phase distribution structure in the large pipe with the inner diameter of 195 mm, which showed wall-peak and core-peak void fraction profiles for air–water and steam–water (6.5 MPa) two-phase flows.

Some studies were also devoted to making clear the transition characteristics and criteria of phase distribution. Serizawa et al. (1975a), Serizawa et al. (1975b), and Akimi et al. (1988) demonstrated that the phase distribution pattern was determined by bubble size. Moreover, Zun et al. (1988) summarized the phase distribution data in round pipes with the diameter ranging from 20 to 86.4 mm and developed the phase distribution pattern map in the superficial liquid velocity vs. superficial gas velocity diagram. In addition, Mendez-Diaz et al. (2012) developed the transition criterion from wall-peak to core-peak phase distribution in a circular pipe, which was based on the critical bubble Reynolds number [$\mathrm{Re} = (v_g - v_l)D_b\rho/\mu < 1500$] and Weber number [$\mathrm{We} = (v_g - v_l)^2 D_b\rho/\sigma < 8$]. However, it was difficult to adopt the critical bubble Reynolds number and Weber number to predict the phase distribution patterns directly because it was difficult to acquire or calculate the bubble diameter at the working condition, which was determined by many factors, such as the flow regime and gas and liquid velocities.

Phase Distribution Characteristics in Rod Bundles

Compared with those in a round pipe, the experimental and theoretical studies on phase distribution in the complex channel were scarce, especially those in rod bundles. Hosokawa et al. (2014) measured the local void fraction with the double sensor conductivity probe in detail in 4 × 4 rod bundles, which showed the wall-peak and core-peak phase distributions. With the help of the sub-channel void sensor (SCVS), Arai et al. (2012) discovered the small bubbles tended to migrate toward the rod gap. Based on the four-sensor conductivity probe, Paranjape et al. (2010) and Yang et al. (2013) also presented the wall-peak and core-peak phase distributions in 8 × 8 rod bundles. Yun et al. (2008) reported that bubbles gathered near the rod wall in sub-cooled boiling in 3 × 3 rod bundles; and the bubble layer and void fraction peak values were influenced by heat flux and mass flow rate. Ren et al. (2018a) and Ren et al. (2019) presented the detailed wall-peak void fraction profiles for bubbly flow and core-peak phase distribution for cap bubbly flow in 5 × 5 rod bundles. According to Arai et al. (2012) and Lucas et al. (2007), small bubbles were pushed to aggregate near the rod wall by lift force (Tomiyama, 1998; Tomiyama et al., 2002), while large bubbles were kept away from walls by wall lubrication force (Antal et al., 1991). Based on the above introduction, the schematic of typical wall-peak and core-peak phase distributions in rod bundles is presented in **Figure 1**, in which the blue circles represent the rods.

The spacer grid was an important component of rod-type fuel assembly, which improved the flow turbulence, heat transfer efficiency, and critical heat flux for the nuclear reactor. Yang et al. (2013) pointed out that the simplified spacer grids without mixing vanes produced stronger turbulence and made the large bubbles break up. Ren et al. (2018a) demonstrated that, for the wall-peak void fraction profiles, mixing vane space grids (MVSGs) enhanced the wall-peak phenomenon by giving rise to the larger void fraction peak values near the rod wall at the downstream of the MVSG.

Lateral Forces Acting on Bubbles

Essentially, the phase distribution was determined by the lateral forces acting on bubbles, which affected the bubble migrating direction and behaviors. According to Lucas et al. (2007), Liao et al. (2015), and Rzehak and Krepper (2013), the bubble lateral force included lift force, wall lubrication force, and turbulent disperse force. The lift force was induced by the liquid velocity gradient around the bubble, whose direction was vertical to liquid velocity. The lift force coefficient C_L was positive in the co-current upward flow, and the lift force was toward the direction of decreasing liquid velocity. Tomiyama (1998) and Tomiyama et al. (2002) acquired the correlation of the lift force coefficient by analyzing the single bubble motions in the shear flow field of high-viscosity liquid and predicted that the coefficient of lift force would be negative when the bubble size was larger than 5.8 mm (Lucas et al., 2007). The bubbles were pushed back to the main flow by the wall lubrication force when near the wall. In another way, the wall lubrication force prevented bubbles from "passing through" the wall due to the effect of lift force. On the basis of the wall lubrication force correlation developed by Antal et al. (1991) and Hosokawa et al. (2002), the wall lubrication force was determined by the bubble size, bubble Reynolds number, and Eötvös number. The turbulent dispersion force was induced by the liquid turbulence and

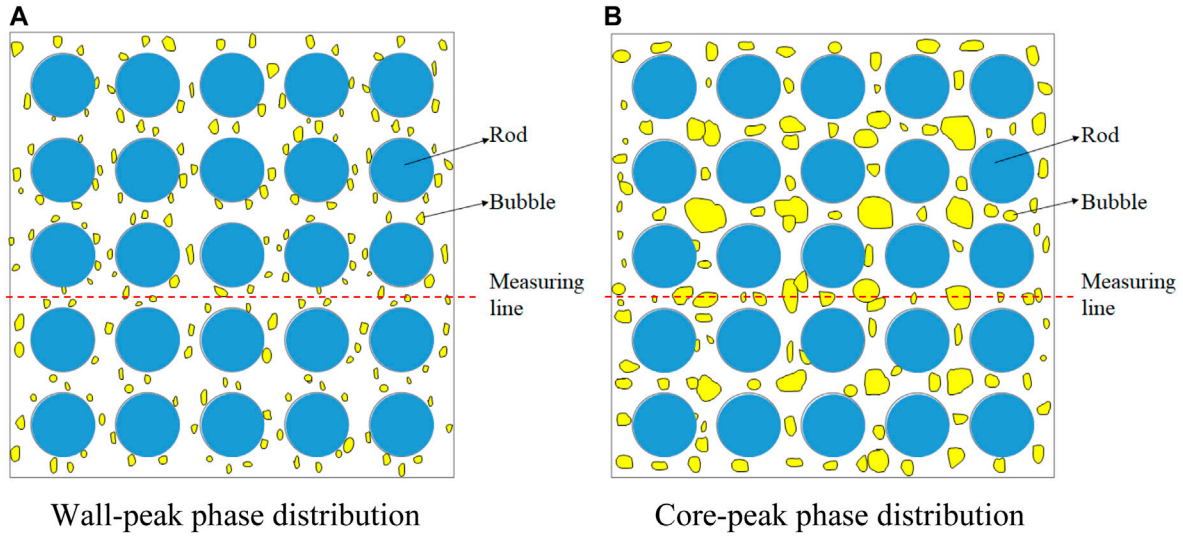

FIGURE 1 | Schematic of the typical phase distribution in rod bundles (top view). **(A)** Wall-peak phase distribution. **(B)** Core-peak phase distribution.

vortexes acting on bubbles (Ishii and Zuber, 1979; Burns et al., 2004), which was associated with the bubble size, void fraction, relative velocity, bubble Reynolds number, and Eötvös number. As discussed above, the total lateral forces acting on bubbles were affected by many factors, such as the bubble size, void fraction, liquid turbulence, bubble Reynolds number, and Eötvös number.

To sum up, although some studies were conducted on the phase distribution characteristics in different rod bundles with the help of different measuring sensors by different researchers, there was no experimental study focusing on the transition mechanisms and criterion from wall-peak to core-peak phase distribution in rod bundles. Compared with that in a circular pipe, two-phase flow in rod bundles was more complex for the limited effect of sub-channel size on large bubbles, the influence of spacer grid, stronger turbulence, and secondary flow. Therefore, it is of great significance to make clear the transition mechanisms and develop the transition criterion from wall-peak to core-peak phase distribution. In this paper, the air–water two-phase flow experiments were performed to acquire the detailed phase distribution characteristics to reveal the influencing mechanisms of different factors acting on the phase distribution. On the basis of the measured data and existing experimental data from the literature, the empirical correlation for the transition from wall-peak to core-peak phase distribution was developed.

EXPERIMENTAL SETUP

Test Loop

The gas–liquid two-phase flow experiments were performed in the Interfacial Evolution Research Facility at Chongqing University (IERFC), as shown in **Figure 2**. The maximum water volumetric flow rate was 30 m^3/h, while the maximum air mass flow rate reached 3,000 SLM (standard liters per minute). In order to produce uniform small bubbles at the inlet of the test section, the air–water mixer was designed, which consisted of four porous metal tubes. Moreover, the phase distribution characteristics at the inlet (Port 0 shown in **Figure 3**) could be referred from Ren et al. 2018a. More information about the experimental setup could be found in the authors' previous research (Ren et al., 2018a; Ren et al., 2018b; Ren et al., 2018c; Ren et al., 2018d; Ren et al., 2018e; Liu et al., 2018; Ren et al., 2019; Ye et al., 2019).

Test Section

The test section was made of transparent PMMA (polymethyl methacrylate). The width and length of the square casing tube were 66.1 and 1,500 mm, respectively, and the rod diameter was 9.5 mm, while the rod gap size was 3.1 mm. It should be noted that the gap size played an important role in confining the bubble motion. Two kinds of spacer grids were adopted in the test section: simplified spacer grid [SSG, different from that in Yang et al. (2013)] and mixing vane spacer grid (MVSG). The structure of the SSG is shown in **Figure 4**, while that of the MVSG can be found in Chen et al. (2017). Detailed description of the test section could be found in Ren et al. (2018a) and Ren et al. (2019).

As shown in **Figure 3A**, six measuring ports (Ports 0–5) were set for a miniaturized four-sensor conductivity probe (MFSCP) at different axial locations (10.7, 50.6, 64.2, 76.8, 90.5, and 115.8 *L*/*D*). It should be noted that, to avoid the disturbance on the flow field, only one MFSCP was installed to measure the local two-phase flow parameters. The moving line of the MFSCP is shown in **Figure 3B** and **Figure 1**, and the distance between two neighboring measuring points was about 1.0 mm. The MFSCP was designed based on the large difference of conductance between gas and liquid, which consisted of a stainless steel tube and four acupuncture needles with different lengths. Moreover, the uncertainty of MFSCP was related to the uncertainty of measured voltage, bubble number, sample

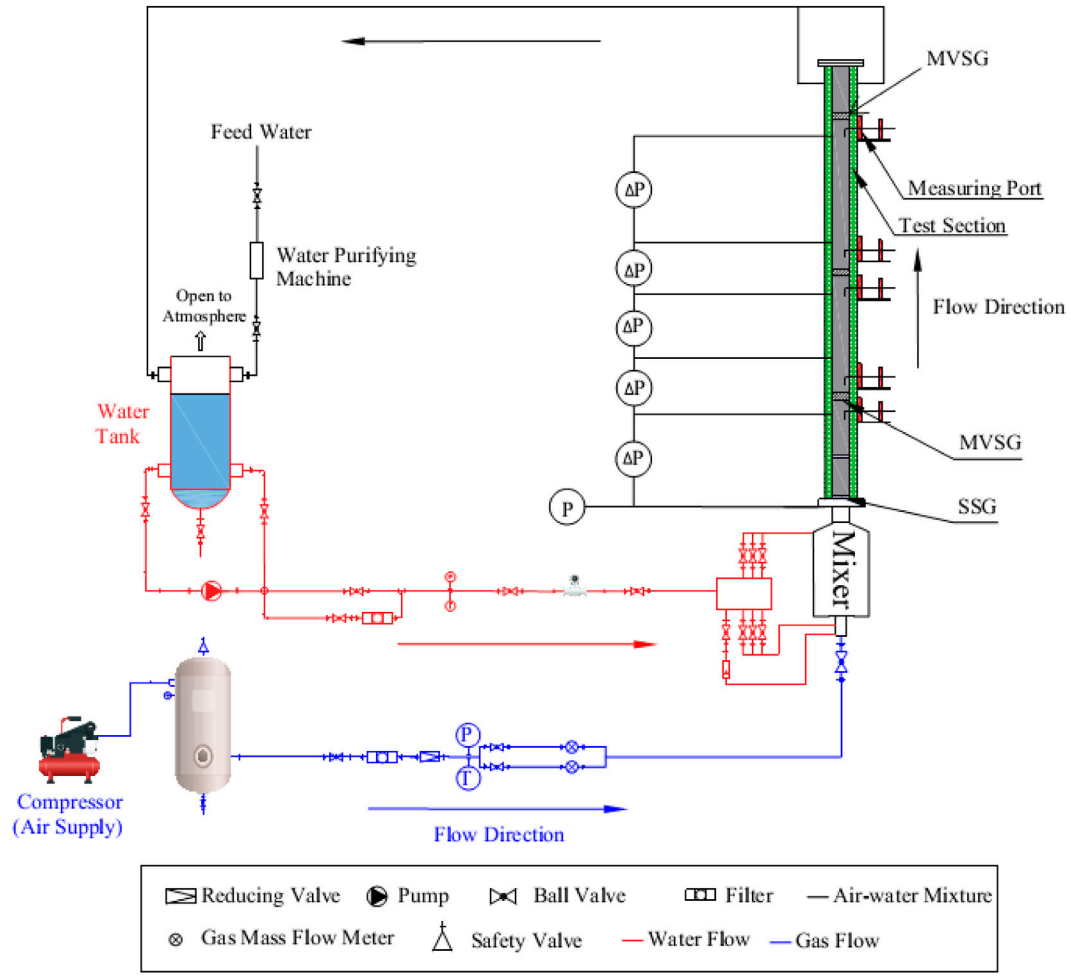

FIGURE 2 | Schematic of the experimental facility.

frequency, and time. Based on the error propagation model, the uncertainty of measured void fraction was about 0.67%. The processing data were demonstrated to be credible with the relative errors of area-averaged void fraction and superficial gas velocity as about 18.5 and 17.8%, respectively. More detailed information on the data processing and verification of the MFSCP could be found in authors' previous researches (Ren et al., 2018a; Ren et al., 2019; Ren et al., 2021).

Test Conditions

The experiments were conducted at the stable flow condition with the preset gas and liquid mass flow rates, which were controlled by the presupposed test conditions shown in **Figure 5**. And the presupposed superficial gas and liquid velocities in the test conditions were determined on the purpose of covering a larger range of flow velocities and flow regimes. The flow regime transition lines for gas-liquid flow in rod bundle channel proposed by different researchers were also shown in **Figure 5**, which includes the global flow regime map proposed by Paranjape et al. (2008) based on a plate-type impedance void meter, the theoretical global flow regime transition criteria developed by Liu and Hibiki (2017), and the inner sub-channel flow regime map acquired by Ren et al. (2018d) based on a sub-channel impedance void meter.

RESULTS AND DISCUSSIONS

Typical Phase Distribution Characteristics in Rod Bundles

Compared with a circular pipe, the rod bundle channel had more rod walls and produced special phase distribution features. The typical wall-peak and core-peak phase distributions in rod bundles are presented in **Figures 6**, **7**. It should be noted j_g denotes the local superficial gas velocity, while j_l is the superficial liquid velocity. As shown in **Figure 1A**, the wall-peak phase distribution meant that the bubbles gathered and flew near the rod walls, which resulted in the peaks of void fraction profiles located near the rod gaps as shown in **Figure 6**. On the contrary, as shown in **Figure 1B**, the core-peak phase distribution indicated that the bubbles were more likely to gather and flow in the center of the sub-channels, which gave rise to the peaks of void fraction

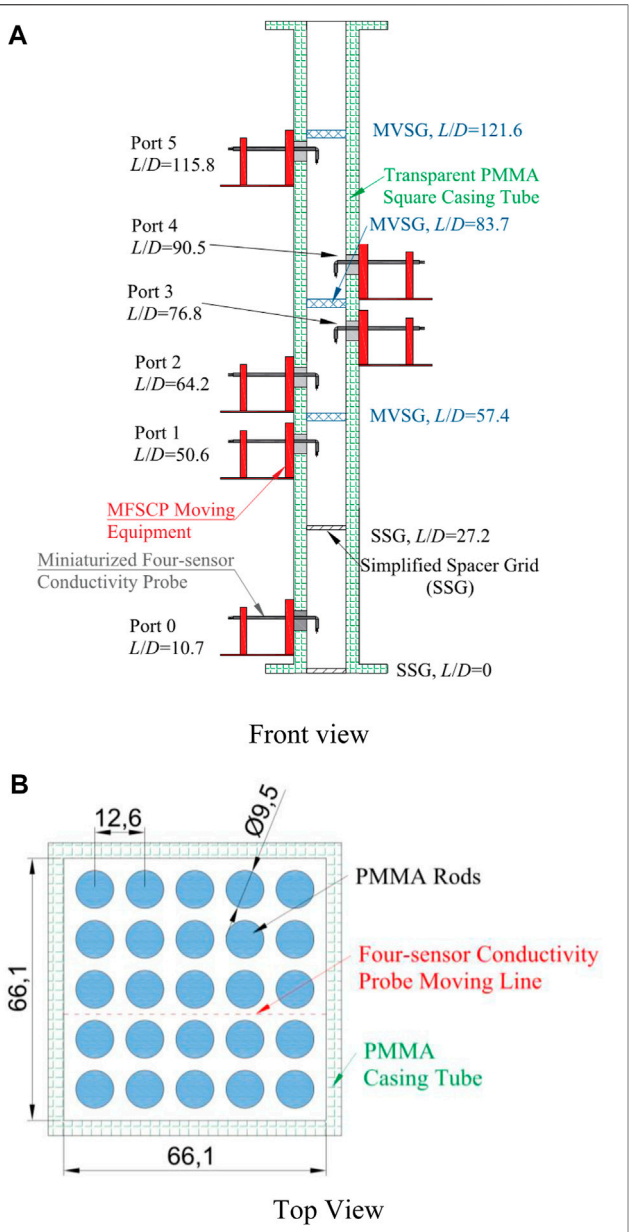

FIGURE 3 | Structure of the test section. **(A)** Front view. **(B)** Top view.

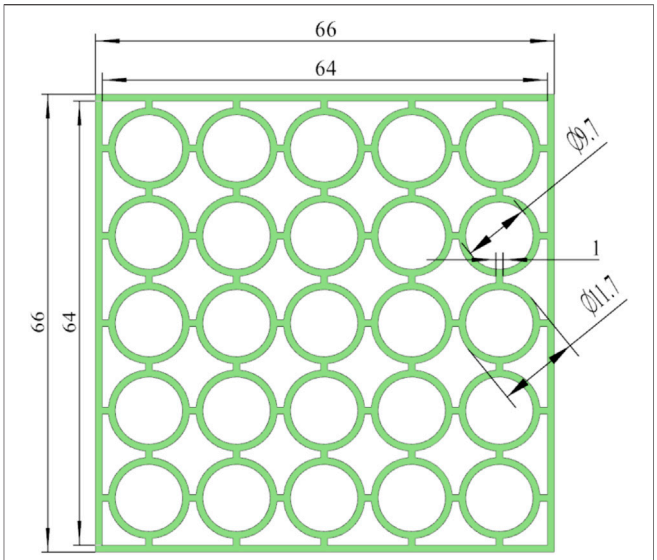

FIGURE 4 | Schematic diagram of the simplified spacer grid (SSG).

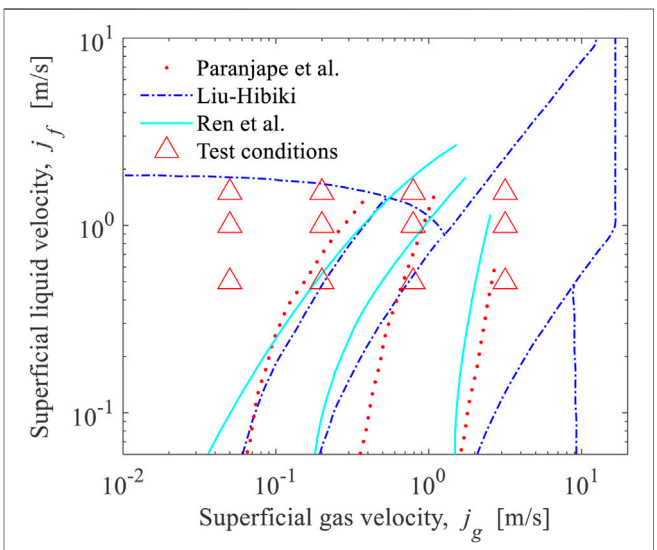

FIGURE 5 | Test conditions.

profiles near the sub-channel center as shown in **Figure 7**. Wall-peak phase distribution was observed at the flow condition with a lower gas velocity and higher liquid velocity as shown in **Figure 6**, while the core-peak pattern appeared at the flow condition with a higher gas velocity and lower liquid velocity as shown in **Figure 7**.

The phase distribution pattern was determined by many factors (Akimi et al., 1988), such as the void fraction, flow regimes, gas velocity, liquid velocity, and bubble size. Serizawa et al. 1975a, Serizawa et al. 1975b, and Mendez-Diaz et al. 2012 reported that phase distribution was mainly affected by bubble size. And the transverse migration of bubbles was determined by the lateral forces in circular pipes (Tomiyama et al., 2002). Furthermore, the bubble lateral forces were affected by bubble size greatly, such as lift force (Tomiyama et al., 2002) and wall lubrication force (Tomiyama, 1998). Therefore, it was necessary to put emphasis on the bubble size when discussing phase distribution characteristics.

As shown in **Figure 6**, the void fraction peak values increased with flow development in the axial direction, while the bubble chord length did not show large change but remained at about 1.3 mm. Therefore, it was concluded that the phase distribution was determined not only by bubble size but also by other factors, which would be analyzed in *The Factors Acting on Phase Distribution*. As can be seen in **Figure 6**, there were some hollows at some peaks of the void fraction profiles at Port 5. It was inferred that some small bubbles coalesced into larger

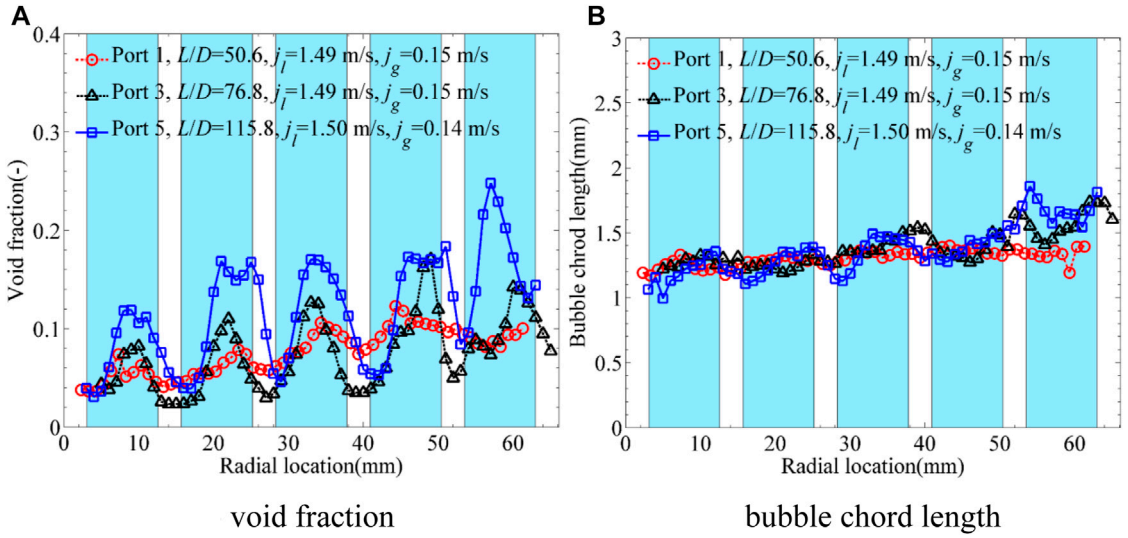

FIGURE 6 | Characteristics of wall-peak phase distribution. **(A)** Void fraction. **(B)** Bubble chord length.

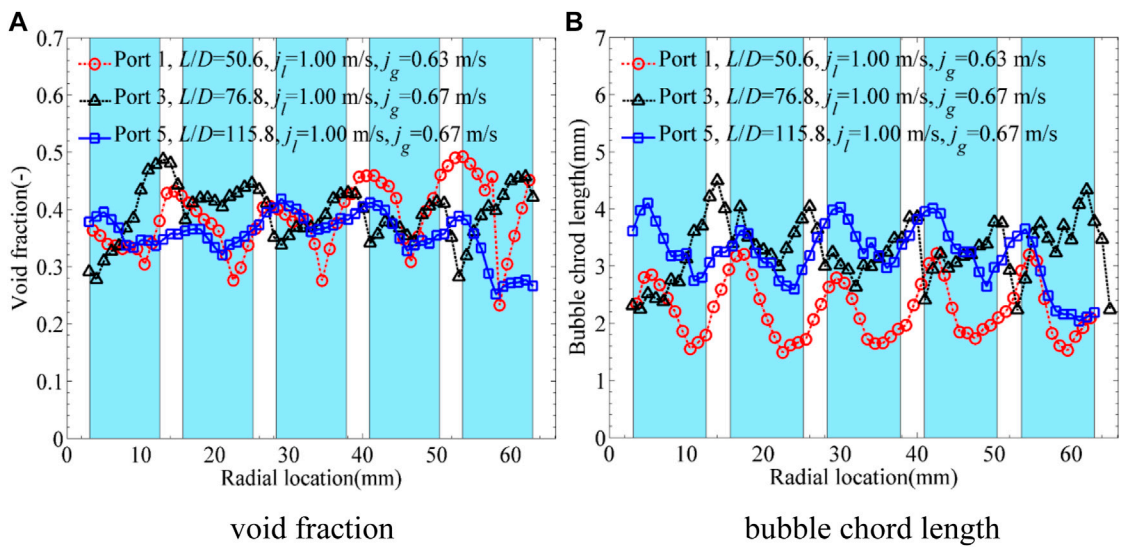

FIGURE 7 | Characteristics of core-peak phase distribution. **(A)** Void fraction. **(B)** Bubble chord length.

bubbles and larger bubbles tended to move to the sub-channel center under the combined effect of lift force and wall lubrication force; then, hollows at some peaks appeared under the complex effects of the wall-peak phase distribution and the limitation of gap size.

The core-peak phase distribution profiles are shown in **Figure 7**. However, due to the strong turbulence and secondary flow, the peaks were not located at the sub-channel center exactly. And the bubble chord length increased from about 2 to 3.5 mm with flow development for bubble coalescence. According to Tomiyama et al. (2002), the lift force value changed from positive to negative when the bubble size was larger than 5.8 mm in air–water two-phase flows. Obviously, it could not be applicable to the present multi-bubble flow system in rod bundles directly. However, when compared to the wall-peak phase distribution in **Figure 6**, it could be deduced that the phase distribution would change from wall-peak to core-peak with the increasing bubble size.

The Factors Acting on Phase Distribution

As discussed above, the phase distribution was related to liquid and gas velocities, flow regimes, and bubble size in the circular pipe (Serizawa et al., 1975a; Serizawa et al., 1975b; Akimi et al., 1988). As regard to the complex geometry of the rod bundle channel, the phase distribution was affected by rod diameter, gap size, spacer grid, bubble size, gas and liquid flow rates. In this

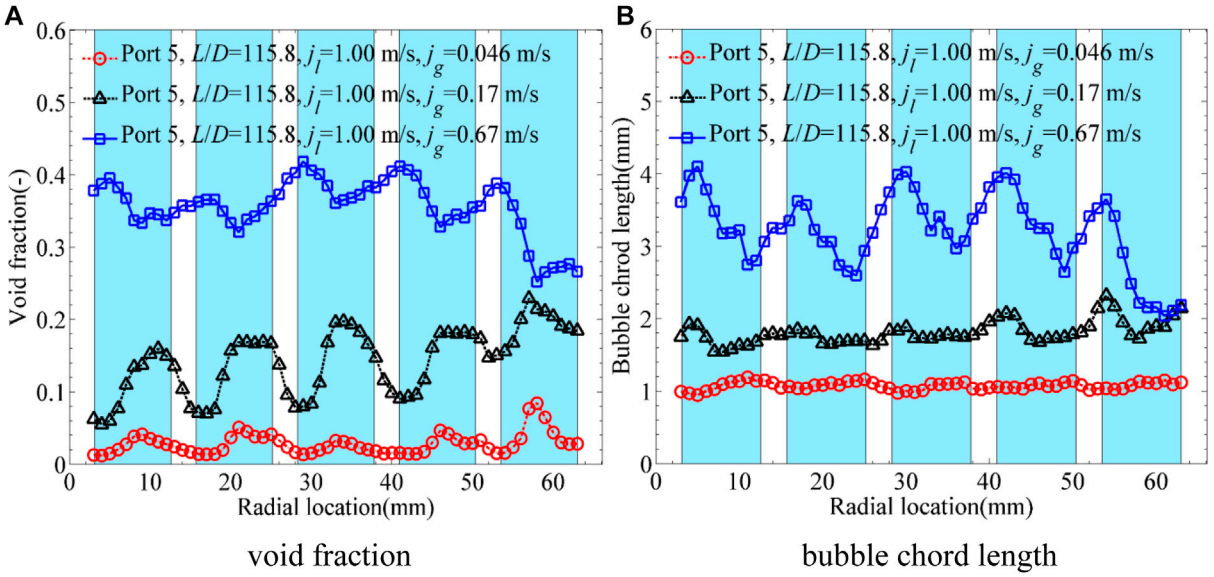

FIGURE 8 | Influence of superficial gas velocity on phase distribution. **(A)** Void fraction. **(B)** Bubble chord length.

section, the influencing factors acting on phase distribution will be analyzed, including superficial gas velocity, superficial liquid velocity, MVSG, and geometrical size.

Superficial Gas Velocity

As shown in **Figure 8**, the wall-peak phase distribution changed to core-peak with the gas velocity increasing at j_l = 1.00 m/s, and the critical superficial gas velocity was in the range from 0.17 to 0.67 m/s. Meanwhile, the void fraction increased from about 0.02 to 0.36, and the bubble chord length increased from about 1 to 3.6 mm. With the increasing gas velocity, void fraction and bubble number increased, which resulted in the larger collision frequency and more coalescences among bubbles. Because of the wall lubrication force and limitation of gap size, the large bubbles migrated toward the sub-channel center, which resulted in the core-peak phase distribution. To sum up, the superficial gas velocity, bubble size, and void fraction played a positive role in the transition from wall-peak to core-peak phase distribution.

Superficial Liquid Velocity

With the increasing superficial liquid velocity, the phase distribution characteristics at $j_{\mathrm{gatm}} \approx 0.20$ m/s are shown in **Figure 9**. It should be noted that j_{gatm} represented the superficial gas velocity at the atmosphere pressure. The local superficial gas velocity j_g was different because of the different local pressures. The core-peak phase distribution was not so apparent at j_l = 0.50 m/s, j_g = 0.19 m/s, which belonged to cap bubbly flow according to the sub-channel flow regime map developed by Ren et al. (2018d). Because the void fraction values at the sub-channel centers were larger than those at the adjacent gaps, it was still deemed as the core-peak phase distribution. The typical wall-peak phase distribution appeared with the increasing liquid velocity as shown in **Figure 9A**, while the bubble chord length decreased from about 2.5 to 1.2 mm as shown in **Figure 9B**. The increment of liquid velocity resulted in the lower void fraction, stronger turbulence, and more vortexes, which gave rise to the bubble breakup and smaller bubble size. The small bubbles tended to migrate toward the walls under the effect of the lift force, which promoted the appearance of wall-peak distribution.

The Mixing Vane Spacer Grid

In the authors' previous study (Ren et al., 2018a; Ren et al., 2019), the effects of the MVSG were summarized as stronger turbulence, stronger secondary flow, bubble breakup, bubble lateral movement, low pressure region downstream of the MVSG, and recirculating flow behind mixing vanes. The influences of MVSG on the wall-peak, transitional, and core-peak phase distributions are shown in **Figures 10–12**, respectively. It should be noted that Ports 3 and 4 were located upstream and downstream of the MVSG, respectively, as shown in **Figure 3**. As shown in **Figure 10**, the MVSG promoted the larger wall-peak values and smaller bubble size for wall-peak phase distribution. However, the larger void fraction peak values near the wall improved the heat transfer resistance between the heated wall and main flow, which needs more attention in the design of a spacer grid. As shown in **Figure 11**, the transitional phase distribution showed large hollows near the rod gaps upstream of the MVSG while presented typical wall-peak features at the downstream of the MVSG. In a similar way, the smaller bubble size was produced by the MVSG for the stronger turbulence and shear force, which promoted the transition from transitional phase distribution to wall-peak phase distribution. With regard to core-peak phase distribution shown in **Figure 12**, the MVSG led to smaller bubble size, but the phase distribution was still maintained as the core-peak phase distribution at the downstream of the MVSG. To sum up, the MVSG enhanced the wall-peak phase distribution and promoted the transition

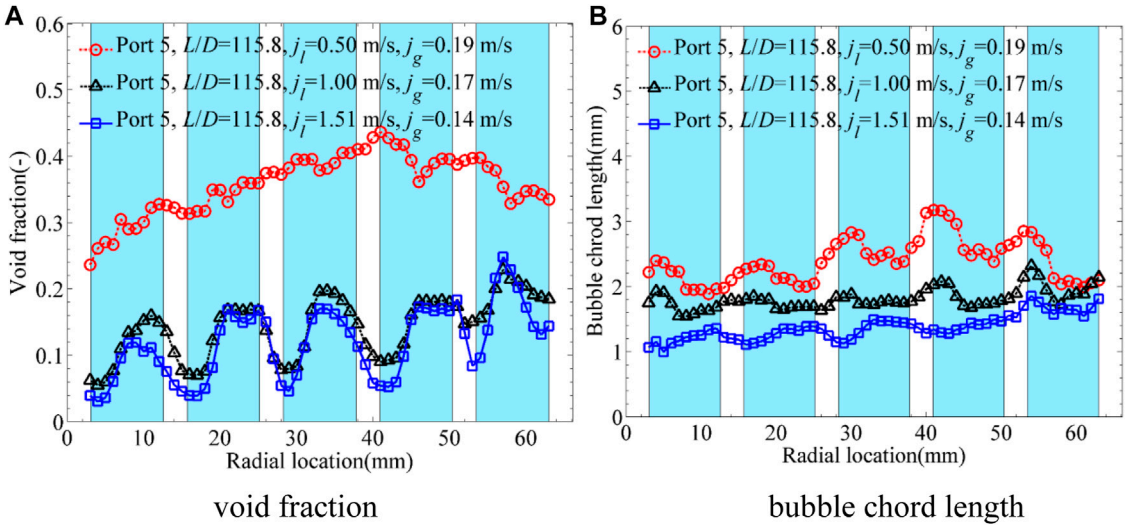

FIGURE 9 | Influence of superficial liquid velocity on phase distribution. **(A)** Void fraction. **(B)** Bubble chord length.

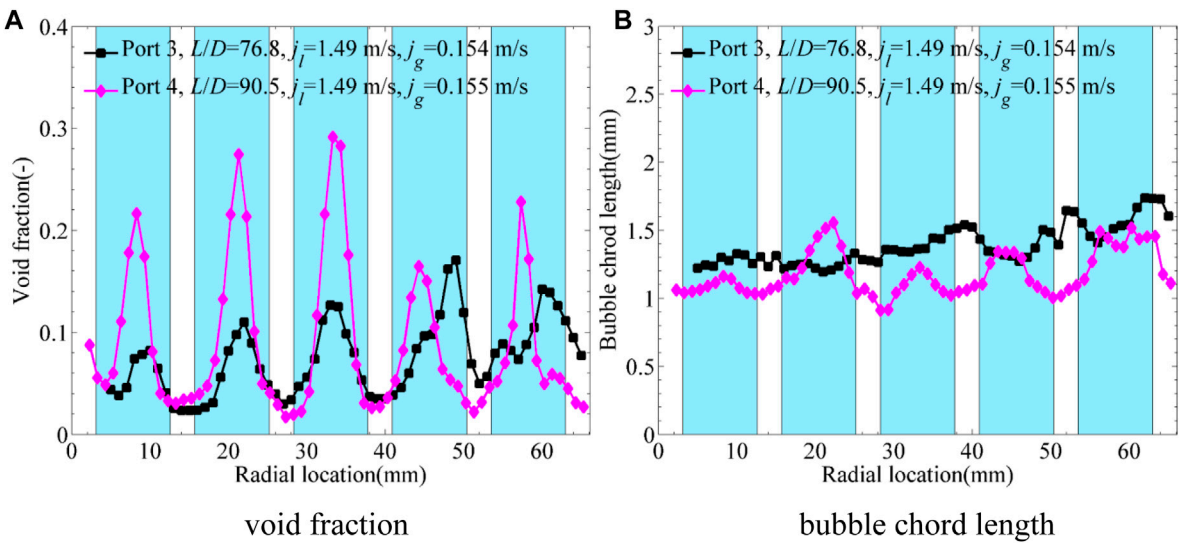

FIGURE 10 | Influence of MVSG on wall-peak phase distribution (Ren et al., 2018a). **(A)** Void fraction. **(B)** Bubble chord length.

from the transitional phase distribution to the wall-peak phase distribution, but it was hard to promote the transition from the typical core-peak phase distribution to the wall-peak phase distribution.

Geometrical Size

As discussed above, the gap size was the main factor limiting the bubble size and affecting the phase distribution. The phase distribution patterns acquired in different rod bundles are presented in **Figure 13**, including present data in 5 × 5 rod bundles with the gap size of 3.1 mm, Yang's data (Yang, 2015; Yang, 2011) in 8 × 8 rod bundles with the gap size of 6.4 mm, Hosokawa's data (Hosokawa et al., 2014) in 4 × 4 rod bundles with the gap size of 2.5 mm, Arai's data (Arai et al., 2012) in 10 × 10 rod bundles with the gap size of 3.0 mm, and Julia's data (Yun et al., 2008) in 3 × 3 rod bundles with the gap size of 8.4 mm. It should be noted that Julia's data was obtained in the sub-cooled boiling flow, while all of the others' data were acquired in air–water two-phase flow. Moreover, Yang's data (Yang, 2015; Yang, 2011) only consisted of the two-phase flow parameters just at the sub-channel centers and rod gaps, which increased the difficulty and uncertainty in recognizing the phase distribution patterns. And the transition lines from wall-peak to transitional and core-peak phase distribution for a circular pipe in **Figure 13** were proposed by Akimi et al. (1988) based on the phase distribution data in

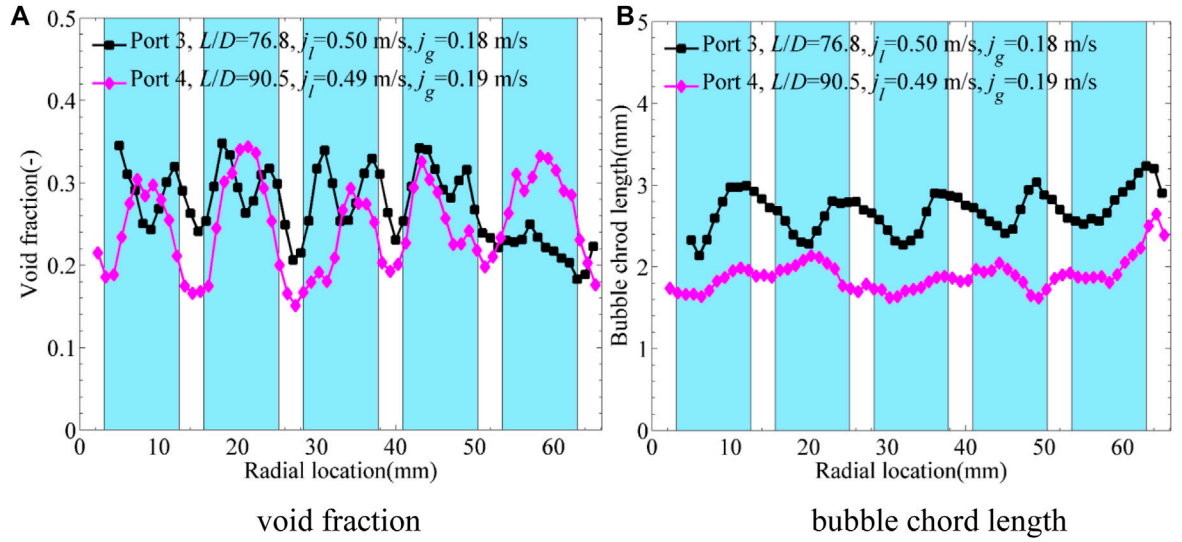

FIGURE 11 | Influence of MVSG on transitional phase distribution. **(A)** Void fraction. **(B)** Bubble chord length.

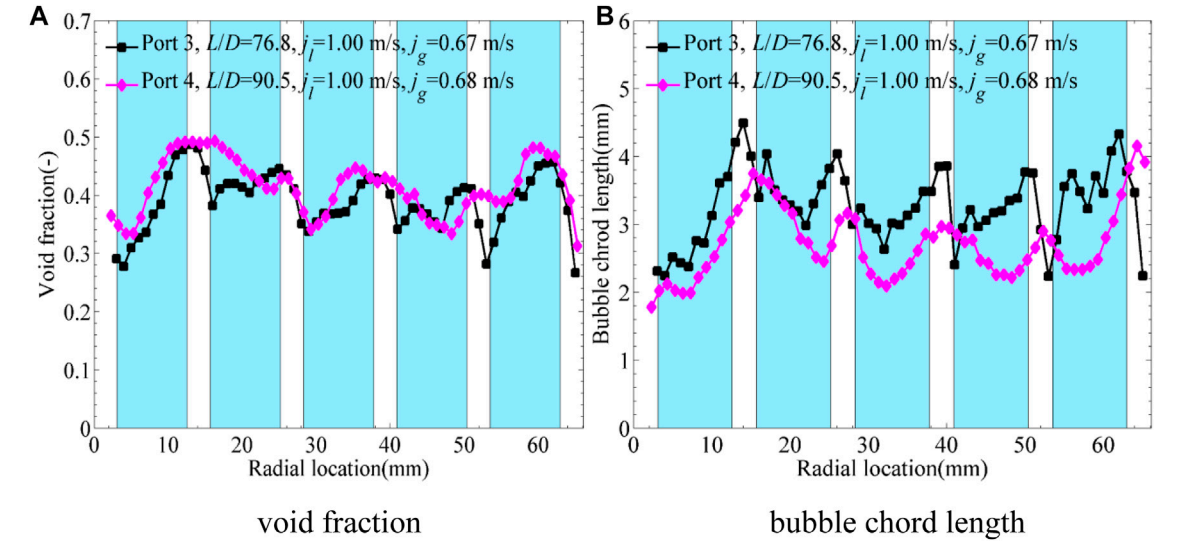

FIGURE 12 | Influence of MVSG on core-peak phase distribution. **(A)** Void fraction. **(B)** Bubble chord length.

different circular pipes. As shown in **Figure 13**, the transition lines in the circular pipe proposed by Akimi et al. (1988) were not fit for the gas–liquid flow in the rod bundle channel.

As shown in **Figure 13B**, the wall-peak phase distribution was hard to appear at low liquid velocity (not larger than 0.23 m/s), which resulted from that the liquid turbulence was not strong enough to produce small bubbles. As for Julia's data (Yun et al., 2008), there were no core-peak flow conditions, which were attributed to the small bubble size in the sub-cooled boiling flow and large gap size (8.4 mm). Based on the comparison among present data, Yang's data (Yang, 2011; Yang, 2015), and Hosokawa's data (Hosokawa et al., 2014) shown in **Figure 13**, the transition from wall-peak to core-peak phase distribution appeared at a lower superficial gas velocity in the rod bundle channel with the smaller gap size.

The Transition Criterion From Wall-Peak to Core-Peak Phase Distribution

Based on the critical bubble Reynolds number and Eötvös number, Mendez-Diaz et al. (2012) proposed the transition criterion from wall-peak to core-peak phase distribution in a circular channel. However, it was difficult to acquire the bubble

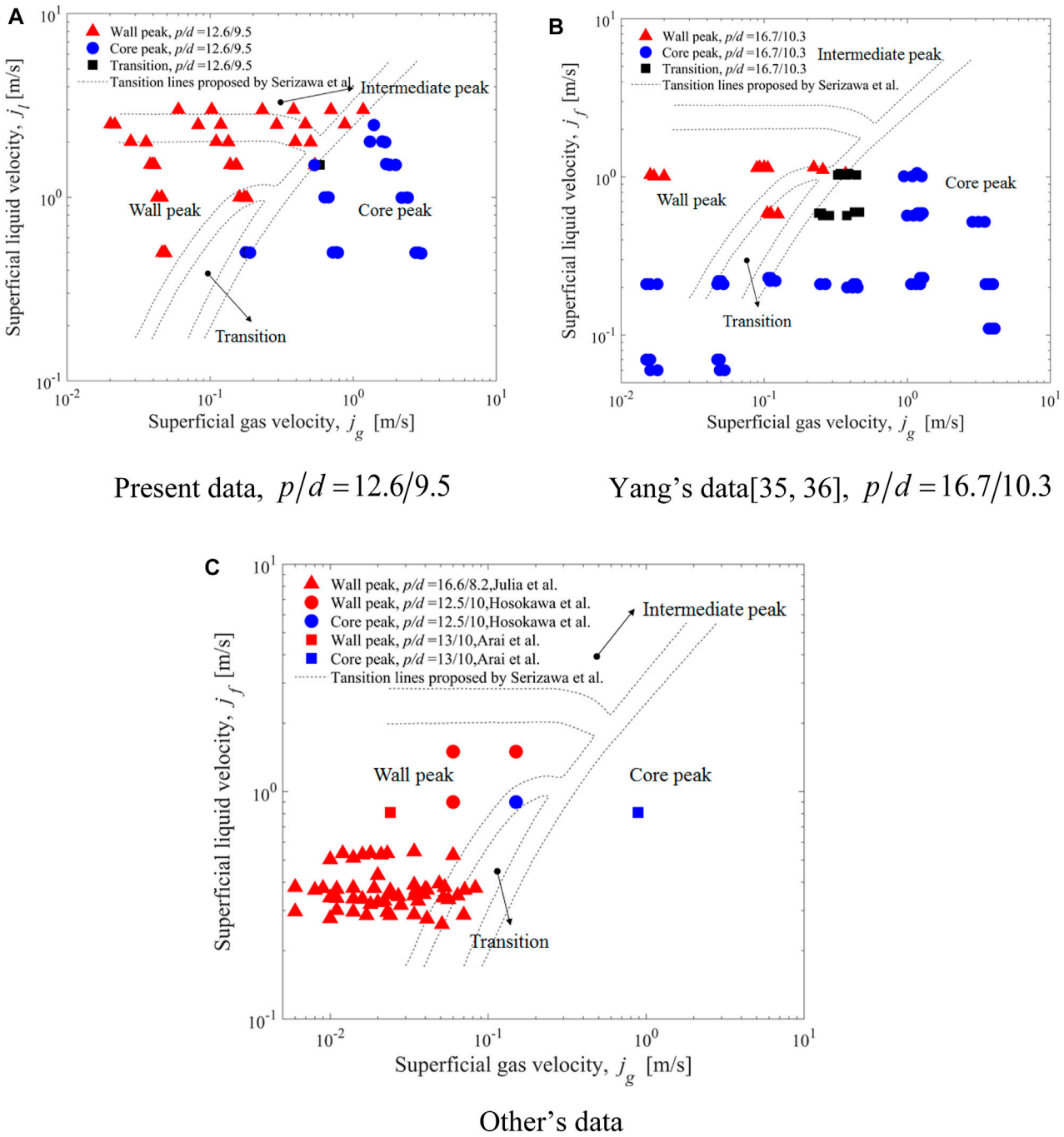

FIGURE 13 | Influence of geometrical size on phase distribution. **(A)** Present data, *p/d* = 12.6/9.5. **(B)** Yang's data (Yang, 2011; Yang, 2015). **(C)** Others' data.

diameter and relative velocity to calculate the bubble Reynolds number and Eötvös number in the actual two-phase flow systems, which limited their application range. Meanwhile, the effect of channel size was not considered in Mendez-Diaz's correlation, which meant it could not be adopted in the complex rod bundle channel. Therefore, it was necessary to develop the transition criterion from wall-peak to core-peak phase distribution in rod bundles, based on which the phase distribution patterns could be identified for the specific working condition. As shown in **Figure 13**, Julia's data (Yun et al., 2008) only included the wall-peak data, while the core-peak data point was far from the wall-peak data point in Arai's data (Arai et al., 2012). Thus, only present data, Yang's data (Yang, 2011; Yang, 2015), and Hosokawa's data (Hosokawa et al., 2014) were adopted to

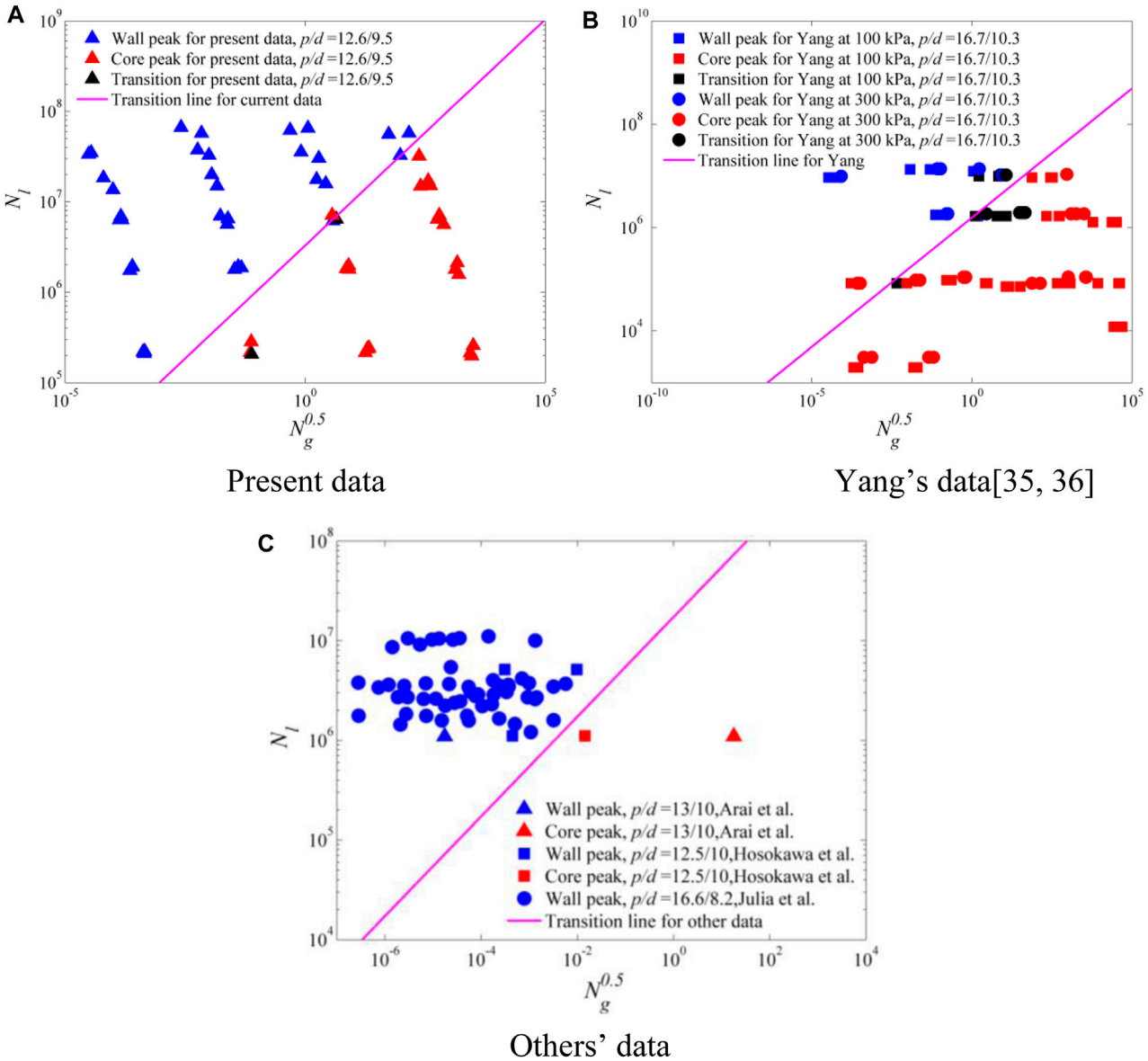

FIGURE 14 | Transition lines for different data. **(A)** Present data. **(B)** Yang's data (Yang, 2011; Yang, 2015). **(C)** Others' data.

develop the empirical correlation for the transition from wall-peak to core-peak phase distribution.

Based on the above discussions, phase distribution was related to many parameters, including bubble size, void fraction, gas and liquid densities, relative velocity, surface tension, distance from the bubble to the wall, liquid turbulence, bubble Reynolds number, and Eötvös number. Aiming at identifying the phase distribution based on the macro and easily acquired two-phase flow parameters, such as superficial gas and liquid velocities, geometrical size, void fraction, and gas and liquid physical properties, the factors acting on the transition from wall-peak to core-peak were divided into two groups: the enhancing factors and the restraint factors. The enhancing factors were summarized as the dimensionless number N_g (expressed as **Eq. 1**), while the restraint factors were considered together as the dimensionless number N_l (expressed as **Eq. 2**). As shown in **Figure 14**, with increasing N_g, the wall-peak phase distribution turned to core-peak; with increasing N_l, the core-peak phase distribution turned to wall-peak. Taking $N_g^{0.5}$ and N_l as X and Y coordinates, respectively, the boundaries between wall-peak and core-peak phase distributions are plotted as magenta lines for present data, Yang's data (Yang, 2015; Yang, 2011), and Hosokawa's data (Hosokawa et al., 2014) as shown in **Figure 14**. The transition line correlations for different geometrical sizes were summarized as **Eq. 3**, which complied with **Eq. 4**. It was deduced that the coefficient C in **Eq. 4** was related to the channel size, especially the gap size. And the phase distribution was determined by the bubble size and bubble shape. Thus, the non-dimensional gap

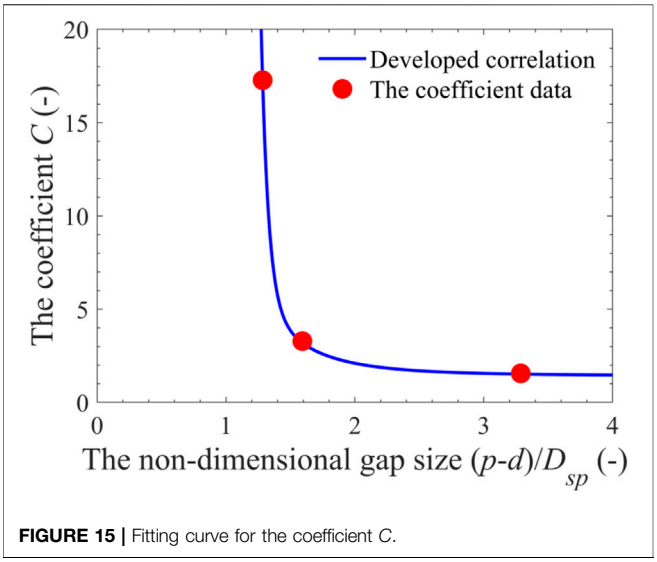

FIGURE 15 | Fitting curve for the coefficient *C*.

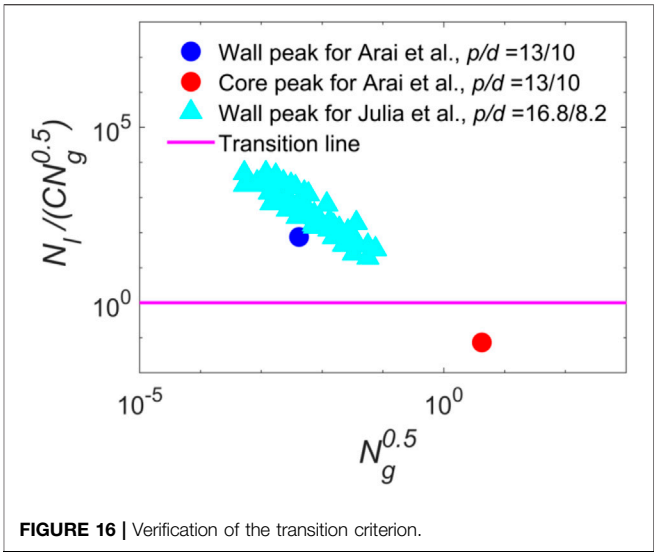

FIGURE 16 | Verification of the transition criterion.

size was developed as **Eq. 5**, in which the maximum spherical bubble size (Kim et al., 2000) was adopted as the standard value.

$$N_g = \alpha Re_g We_g \frac{\sqrt{\sigma/\left[g\left(\rho_l - \rho_g\right)\right]}}{p-d}, \tag{1}$$

$$N_l = Re_l We_l, \tag{2}$$

$$\begin{aligned} N_l &= 3.29 \times 10^6 N_g^{0.5}, \quad p/d = 12.6/9.5, \\ N_l &= 1.56 \times 10^6 N_g^{0.5}, \quad p/d = 16.7/10.3, \\ N_l &= 17.28 \times 10^6 N_g^{0.5}, \quad p/d = 12.5/10, \end{aligned} \tag{3}$$

$$N_l = C N_g^{0.5}, \tag{4}$$

$$L_{gap}^* = \frac{p-d}{D_{sp}}, \tag{5}$$

$$D_{sp} = 4\sqrt{\frac{2\sigma}{g\Delta\rho}} N_{\mu_f}^{1/3}, \tag{6}$$

$$N_{\mu_f} = \frac{\mu_f}{\left(\rho_f \sigma \sqrt{\frac{\sigma}{g\Delta\rho}}\right)^{1/2}}. \tag{7}$$

Aimed at developing the dimensionless transition criterion, the data points are plotted in **Figure 15** by taking the coefficient *C* and dimensionless gap size L_{gap}^* as the coordinates. Because the phase distribution data in different rod bundle channels were scarce in the published literature, there are only three data points in **Figure 15**. As can be seen, with the increasing non-dimensional gap size L_{gap}^*, the coefficient *C* decreased rapidly when the gap size ranged from 2 to 3.1 mm and then decreased slowly when the gap size was larger than 3.1 mm. Although there were only three data points, the correlation between the coefficient *C* and the non-dimensional gap size L_{gap}^* is still developed as

$$C = 1.44 + \frac{11.92}{\left(L_{gap}^*\right)^{4.16}} + 11112.08 e^{-18.44 L_{gap}^* + 16.82}. \tag{8}$$

In order to verify the transition criterion, the data acquired by Yun et al. (2008) and Arai et al. (2012) were adopted. And $N_l/CN_g^{0.5}$ was adopted as the Y coordinate, whose value was larger than 1 for wall-peak phase distribution and smaller than 1 for core-peak phase distribution. As shown in **Figure 16**, the developed correlation was applicable to the data in rod bundle channel with *p*/*d* at 13/10 (Arai et al., 2012) and 16.8/10.2 (Yun et al., 2008), which demonstrated the reliability of the present transition model to some extent. It should be noted that the correlation for the transition from wall-peak to core-peak phase distribution needed more experimental data to amend and verify. More experiments were suggested to focus on the phase distribution patterns in rod bundle channels with different geometrical sizes.

CONCLUSION

In this work, air–water two-phase flow experiments were performed to make clear the phase distribution characteristics and develop the transition criterion from wall-peak to core-peak phase distribution in rod bundles. Based on the analysis on experimental data, the phase distributions in rod bundles were related to many factors, such as the bubble size, void fraction, gas and liquid densities, gas and liquid velocities, surface tension, distance from the bubble to the wall, MVSG, geometrical size, liquid turbulence, and bubble lateral forces. By dividing the influencing factors into the enhancing and restraint factors, the dimensionless correlation for the transition from wall-peak to core-peak phase distribution in rod bundles was developed. Some important conclusions are listed as follows:

- With the increasing superficial gas velocity and decreasing liquid velocity, the wall-peak phase distribution turned to the core-peak pattern.
- For present flow conditions, the MVSG enhanced the wall-peak phase distribution and promoted the transitional phase

distribution to turn to wall-peak, but it was hard to promote the transition from the typical core-peak phase distribution to the wall-peak phase distribution.
- The wall-peak phase distribution was hard to appear at low liquid velocity (not larger than 0.23 m/s) for the weak liquid turbulence according to the experimental data in the literature (Yang, 2011; Yang, 2015).
- The geometrical size of the rod bundle channel had great influence on the transition from wall-peak to core-peak phase distribution in rod bundles, especially the gap size.
- The dimensionless transition criterion from wall-peak to core-peak phase distribution was proposed based on present data, Yang's data (Yang, 2011; Yang, 2015), and Hosokawa's data (Hosokawa et al., 2014) while verified against Julia's data (Yun et al., 2008) and Arai's data (Arai et al., 2012).

It should be noted that the developed transition model needed much more experimental data to amend and verify. More experiments were suggested to focus on the transition from wall-peak to core-peak phase distribution in rod bundle channels with different geometrical sizes.

DATA AVAILABILITY STATEMENT

The original contributions presented in the study are included in the article/Supplementary Material, and further inquiries can be directed to the corresponding authors.

AUTHOR CONTRIBUTIONS

Q-YR: carrying out experiments, data processing and writing draft paper. ZP: paper reviewing. PC: project administration and funding support. L-MP: paper reviewing and supervision. FZ: data processing and writing editing. MZ: project administration and investigation. HW: investigation and carrying out experiments. LW: data processing and paper revising. HH: carring out experiments and data processing.

FUNDING

The authors are grateful for the support of the Natural Science Foundation of China (Grant Nos. 51676020 and 51706026) and National Key R&D Program of China (Grant No. 2018YFE0116100).

REFERENCES

Akimi, S., and Kataoka, I. (1988). "Phase Distribution in Two-phase Flow," in *Transient Phenomena in Multiphase Flow*. Editor N. H. Afgan (New York: Hemisphere Pub. Corp.), 179–223.

Antal, S. P., Lahey, R. T., and Flaherty, J. E. (1991). Analysis of Phase Distribution in Fully Developed Laminar Bubbly Two-phase Flow. *Int. J. Multiphase Flow* 17, 635–652. doi:10.1016/0301-9322(91)90029-3

Arai, T., Furuya, M., Kanai, T., and Shirakawa, K. (2012). Development of a Subchannel Void Sensor and Two-phase Flow Measurement in 10×10 Rod Bundle. *Int. J. Multiphase Flow* 47, 183–192. doi:10.1016/j.ijmultiphaseflow.2012.07.012

Burns, A. D., Frank, T., Hamill, I., and Shi, J. M. (2004). "The Favre Averaged Drag Model for Turbulent Dispersion in Eulerian Multi-phase Flows," in 5th International Conference on Multiphase Flow (Yokohama, Japan).

Chen, X., Du, S., Zhang, Y., Yu, H., Li, S., Peng, H., et al. (2017). Validation of CFD Analysis for Rod Bundle Flow Test with Vaned Spacer Grids. *Ann. Nucl. Energ.* 109, 370–379. doi:10.1016/j.anucene.2017.05.055

Hibiki, T., and Ishii, M. (1999). Experimental Study on Interfacial Area Transport in Bubbly Two-phase Flows. *Int. J. Heat Mass Transfer* 42, 3019–3035. doi:10.1016/s0017-9310(99)00014-9

Hibiki, T., Ishii, M., and Xiao, Z. (2001). Axial Interfacial Area Transport of Vertical Bubbly Flows. *Int. J. Heat Mass Transfer* 44, 1869–1888. doi:10.1016/s0017-9310(00)00232-5

Hosokawa, S., Tomiyama, A., Misaki, S., and Hamada, T. (2002). Lateral Migration of Single Bubbles Due to the Presence of Wall, ASME 2002 Fluids Engineering Division Summer Meeting, Montreal, QC, Canada.

Hosokawa, S., Hayashi, K., and Tomiyama, A. (2014). Void Distribution and Bubble Motion in Bubbly Flows in a 4×4 Rod Bundle. Part I: Experiments. *J. Nucl. Sci. Technol.* 51, 220–230. doi:10.1080/00223131.2013.862189

Ishii, M., and Zuber, N. (1979). Drag Coefficient and Relative Velocity in Bubbly, Droplet or Particulate Flows. *Aiche J.* 25, 843–855. doi:10.1002/aic.690250513

Kim, S., Fu, X. Y., Wang, X., and Ishii, M. (2000). Development of the Miniaturized Four-Sensor Conductivity Probe and the Signal Processing Scheme. *Int. J. Heat Mass Transfer* 43, 4101–4118. doi:10.1016/s0017-9310(00)00046-6

Liao, Y., Rzehak, R., Lucas, D., and Krepper, E. (2015). Baseline Closure Model for Dispersed Bubbly Flow: Bubble Coalescence and Breakup. *Chem. Eng. Sci.* 122, 336–349. doi:10.1016/j.ces.2014.09.042

Liu, H., and Hibiki, T. (2017). Flow Regime Transition Criteria for Upward Two-phase Flow in Vertical Rod Bundles. *Int. J. Heat Mass Transfer* 108, 423–433. doi:10.1016/j.ijheatmasstransfer.2016.12.029

Liu, H., Pan, L.-M., Hibiki, T., Zhou, W.-X., Ren, Q.-Y., and Li, S.-S. (2018). One-dimensional Interfacial Area Transport for Bubbly Two-phase Flow in Vertical 5 × 5 Rod Bundle. *Int. J. Heat Fluid Flow* 72, 257–273. doi:10.1016/j.ijheatfluidflow.2018.06.006

Lucas, D., Krepper, E., and Prasser, H.-M. (2007). Use of Models for Lift, wall and Turbulent Dispersion Forces Acting on Bubbles for Poly-Disperse Flows. *Chem. Eng. Sci.* 62, 4146–4157. doi:10.1016/j.ces.2007.04.035

Mendez-Diaz, S., Zenit, R., Chiva, S., Muñoz-Cobo, J. L., and Martinez-Martinez, S. (2012). A Criterion for the Transition from wall to Core Peak Gas Volume Fraction Distributions in Bubbly Flows. *Int. J. Multiphase Flow* 43, 56–61. doi:10.1016/j.ijmultiphaseflow.2012.02.012

Paranjape, S., Stefanczyk, D., Liang, Y., Hibiki, T., and Ishii, M. (2008). *Global Flow Regime Identification in a Rod Bundle Geometry* in 16th International Conference on Nuclear Engineering Orlando, Florida, USA.

Paranjape, S., Ishii, M., and Hibiki, T. (2010). Modeling and Measurement of Interfacial Area Concentration in Two-phase Flow. *Nucl. Eng. Des.* 240, 2329–2337. doi:10.1016/j.nucengdes.2009.11.009

Prasser, H.-M., Beyer, M., Carl, H., Gregor, S., Lucas, D., Pietruske, H., et al. (2007). Evolution of the Structure of a Gas-Liquid Two-phase Flow in a Large Vertical Pipe. *Nucl. Eng. Des.* 237, 1848–1861. doi:10.1016/j.nucengdes.2007.02.018

Ren, Q.-Y., Pan, L.-M., Zhou, W.-X., Du, S.-J., and Li, Z.-C. (2018a). Phase Distribution Characteristics of Bubbly Flow in 5 × 5 Vertical Rod Bundles with Mixing Vane Spacer Grids. *Exp. Therm. Fluid Sci.* 96, 451–459. doi:10.1016/j.expthermflusci.2018.04.002

Ren, Q-Y., Pan, L-M., Zhou, W-X., Ye, T-P., Liu, H., and Li, S-S. (2018b). "Comparison of Drift-Flux Models for Void Fraction Prediction in Sub-channel of Vertical Rod Bundles," in 26th International Conference on Nuclear Engineering London, England. doi:10.1115/icone26-81435

Ren, Q.-Y., Pan, L.-M., Zhou, W.-X., Liu, H., and Ye, T.-P. (2018c). Drift-flux Model of Sub-channel in Vertical Rod Bundles with Spacer Grids. *Int. J. Heat Mass Transfer* 126, 946–956. doi:10.1016/j.ijheatmasstransfer.2018.05.135

Ren, Q.-Y., Zhou, W.-X., Du, S.-J., Li, Z.-C., and Pan, L.-M. (2018d). Sub-channel Flow Regime Maps in Vertical Rod Bundles with Spacer Grids. *Int. J. Heat Mass Transfer* 122, 1138–1152. doi:10.1016/j.ijheatmasstransfer.2018.01.133

Ren, Q.-Y., Pan, L.-M., Zhou, W.-X., Liu, H., Ye, T.-P., Yu, B., et al. (2018e). Measurement of Subchannel Void Fraction in 5 × 5 Rod Bundles Using an

Impedance Void Meter. *Meas. Sci. Technol.* 29, 104004. doi:10.1088/1361-6501/aad5c3

Ren, Q-Y., Pan, L-M., Zhou, W-X., Pu, Z-P., Zheng, M-Y., Wang, H-Y., and Wei, L. (2019). "Phase Distribution Characteristics of Cap Bubbly Flow in 5 × 5 Vertical Rod Bundles with Mixing Vane Spacer Grids," in 27th International Conference on Nuclear Engineering (Japan: Tsukuba).

Ren, Q-Y., Pan, L-M., Pu, Z-P., Zhu, F-W., and Hui, H. (2021). Two-group Phase Distribution Characteristics for Air-Water Flow in 5 × 5 Vertical Rod Bundle Channel with Mixing Vane Spacer Grids. *Int. J. Heat Mass. Tran* 176, 121444. doi:10.1016/j.ijheatmasstransfer.2021.121444

Rzehak, R., and Krepper, E. (2013). Bubble-induced Turbulence: Comparison of CFD Models. *Nucl. Eng. Des.* 258, 57–65. doi:10.1016/j.nucengdes.2013.02.008

Serizawa, A., Kataoka, I., and Michiyoshi, I. (1975a). Turbulence Structure of Air-Water Bubbly Flow-II. Local Properties. *Int. J. Multiphase Flow* 2, 235–246. doi:10.1016/0301-9322(75)90012-9

Serizawa, A., Kataoka, I., and Michiyoshi, I. (1975b). Turbulence Structure of Air-Water Bubbly Flow-III. Transport Properties. *Int. J. Multiphase Flow* 2, 247–259. doi:10.1016/0301-9322(75)90013-0

Tomiyama, A., Tamai, H., Zun, I., and Hosokawa, S. (2002). Transverse Migration of Single Bubbles in Simple Shear Flows. *Chem. Eng. Sci.* 57, 1849–1858. doi:10.1016/s0009-2509(02)00085-4

Tomiyama, A. (1998). Struggle with Computational Bubble Dynamics. *Multiphase Sci. Technol.* 10, 369–405.

Yang, X., Schlegel, J. P., Liu, Y., Paranjape, S., Hibiki, T., and Ishii, M. (2013). Experimental Study of Interfacial Area Transport in Air-Water Two Phase Flow in a Scaled 8×8 BWR Rod Bundle. *Int. J. Multiphase Flow* 50, 16–32. doi:10.1016/j.ijmultiphaseflow.2012.10.006

Yang, X. (2011). *Experimental Study of Two-phase Flow in Rod Bundle*. West Lafayette, IN, USA: Purdue University.

Yang, X. (2015). *Experimental and Analytical Study of Interfacial Area Transport in Rod Bundle Two-phase Flow*. West Lafayette, IN, USA: Purdue University.

Ye, T.-P., Pan, L.-M., Ren, Q.-y., Zhou, W.-X., and Zhong, T. (2019). Experimental Study on Distribution Parameter Characteristics in Vertical Rod Bundles. *Int. J. Heat Mass Transfer* 132, 593–605. doi:10.1016/j.ijheatmasstransfer.2018.12.008

Yun, B.-J., Park, G.-C., Julia, J. E., and Hibiki, T. (2008). Flow Structure of Subcooled Boiling Water Flow in a Subchannel of 3 × 3 Rod Bundles. *J. Nucl. Sci. Technol.* 45, 402–422. doi:10.1080/18811248.2008.9711450

Zun, I., Kljenak, I., and Serizawa, A. (1988). "Bubble Coalescence and Transition from wall Void Peaking to Core Void Peaking in Turbulent Bubbly Flow," in *Transient Phenomena in Multiphase Flow*. Editor N. H. Afgan (New York: Hemisphere Pub. Corp.), 225–245.

Conflict of Interest: The authors declare that the research was conducted in the absence of any commercial or financial relationships that could be construed as a potential conflict of interest.

frontiers in Energy Research

ORIGINAL RESEARCH
published: 12 July 2021
doi: 10.3389/fenrg.2021.676586

Study on Flow Boiling Characteristics in Rectangle Channel After Formation of Blisters

Huijian Huang[1], Chong Chen[1,2], Luguo Liu[1], Yu Liu[1], Linfeng Li[2], Hao Yu[1,2], Mingjun Wang[2] and Suizheng Qiu[2]*

[1]Nuclear Power Institute of China, Chengdu, China, [2]Department of Nuclear Science and Technology, Xi'an Jiaotong University, Xi'an, China

Plate-type fuel elements is one of the first fuel structure choice for the novel integrated PWR, however, blisters will appear on the cladding induced by irradiation and fission. In this work CFD method was used to investigate the subcooled boiling characteristic of the water in rectangle channel with round and pillow blisters, the modified RPI model was also proposed, we can draw conclusions as follows: In the channel with round blister, as the blisters will increase the local flow resistance and more fluid will flow through center of the channel. Boiling occurred only in the area near the edges, nearly no vapor appeared at the center of the channel. The boiling region in channel with pillow shape blisters is wider and concentrated between two pillow blisters and downstream of the non-blisters side. The dry out area are both in the downstream region of blisters for the two types of channels.

Keywords: plate fuel element, rectangle channel, blister, subcooled boiling, CFD

OPEN ACCESS

Edited by:
Jinbiao Xiong,
Shanghai Jiao Tong University, China

Reviewed by:
Muhammad Saeed,
East China University of Technology, China
Luteng Zhang,
Chongqing University, China

****Correspondence:***
Yu Liu
ly-Liuyu@163.com

Specialty section:
This article was submitted to Nuclear Energy, a section of the journal Frontiers in Energy Research

Received: *05 March 2021*
Accepted: *11 June 2021*
Published: *12 July 2021*

Citation:
Huang H, Chen C, Liu L, Liu Y, Li L, Yu H, Wang M and Qiu S (2021) Study on Flow Boiling Characteristics in Rectangle Channel After Formation of Blisters. Front. Energy Res. 9:676586. doi: 10.3389/fenrg.2021.676586

INTRODUCTION

Plate-type fuel elements is one of the first fuel structure choice for the novel integrated pressurized water reactor. Two kinds of fuel pellets had been used for plate-type fuel elements currently, monolithic fuel and dispersion fuel. The above two plate-type fuel elements do not contain air gaps, the fuel pellet and the cladding are contact directly.

In recent years, many experiments had been conduct to investigate the thermal hydraulic characteristics of plate-type fuel elements, including heat transfer characteristics (Lee and Lee, 2001; Wang et al., 2014a; Chen et al., 2015), subcooled boiling characteristics (Li et al., 2013; Wang et al., 2014b; Al-Yahia and Jo, 2017; Song et al., 2017) and critical heat flux (Debortoli et al., 1958; Sudo et al., 1985).

Li et al. (Li et al., 2013) studied the boiling characteristic of water in narrow rectangular channel at atmospheric pressure. The flow rate is 304.1–760.2 kg m^{-2} s^{-1}, and the inlet temperature is 54.2–86.9°C. They found that the bubble will slide along the wall and two types of sliding bubbles was observed in the experiment. The first type has a short life, and the volume changes rapidly due to rapid evaporation and condensation; the second type of bubble has a long life and slow growth rate. Sudo et al. (Sudo et al., 1985) conducted experiments on 2.25 and 2.80 mm narrow channels for jrr-3 research reactor. The results show that the critical heat flux increases with the mass flow rate, and the inlet subcooling has little effect on CHF when the dimensionless mass flow rate is less than 100.

The behaviors of the plate-type fuel elements in actual operation show that the blisters will be formed on the cladding under irradiation and fission (Dienst et al., 1977; Meyer et al., 2012). On one hand, affected by neutron irradiation, the properties of the cladding material will be changed. On the other hand, fission gas will be released and accumulate in the fuel pellets. The increased gas pressure would cause blistering deformation of the cladding. Li et al. (Li et al., 2019) studied the heat transfer characteristics in single and parallel channels after formation of blisters, the result show that high temperature areas and large temperature gradients will appear, the distribution of heat flux on the surface is not uniform. Under the influence of the blister, vapor will gather at some stagnation areas, which would result in local high void fraction. The high void fraction near the wall affects the heat transfer seriously and the dry out spots will be produced, which may burn out the fuel assembly.

It is difficult to capture the local characteristics of two-phase flow accurately by experimental methods. In recent years, CFD method is widely used in two-phase flow (Chen et al., 2019; Khan et al., 2020; Wang et al., 2021). However, there are no recognized models that can be widely used in various conditions.

Koncar and krepper (Koncar and Krepper, 2008) simulated the subcooled boiling of R-113 in a circular tube, the void fraction, turbulent kinetic energy and liquid temperature on a cross section had been investigate. The simulation results in most working conditions were in good agreement with the experiment. GU et al. (Gu et al., 2017) simulated subcooled boiling characteristic at high pressure (11–15 MPa) using different nucleation site density and bubble departure diameter models, a set of recommendation models are obtained. Lucas (Liao et al., 2018; Liao et al., 2019) proposed a baseline model and establish a set of benchmark model to calculate the two-phase flow.

In present work, CFD method was used to investigate the subcooled boiling characteristic in rectangle channel with round and pillow blisters. The effect of the blisters for mass flow rate, temperature and void fraction in different conditions had also been analyzed.

NUMERICAL MODELS

Governing Equation

In this section, the Euler-Euler multiphase model was used to investigate the boiling process, and the mass, momentum and energy equations of the two phases were shown as follows.

Continuity Equation

1) Vapor Phase

$$\nabla \cdot \left(\alpha_g \rho_g \overrightarrow{v}_g \right) = \Gamma_e - \Gamma_c \tag{1}$$

Where α_g, ρ_g, $\overrightarrow{v}_g$ is the void fraction, density and velocity of vapor respectivity, Γ_e is liquid evaporation rate per unit volume/kg·m^{-3}·s^{-1}, Γ_c is vapor condensation rate per unit volume/kg·m^{-3}·s^{-1}.

2) Liquid Phase

$$\nabla \cdot \left(\alpha_l \rho_l \overrightarrow{v}_l \right) = \Gamma_c - \Gamma_e \tag{2}$$

Where α_l is liquid void fraction, ρ_l is liquid density/kg·m^{-3}, $\overrightarrow{v}_l$ is liquid velocity/m·s^{-1}.

Momentum Conservation Equation

1) Vapor Phase

$$\nabla \cdot \left(\alpha_g \rho_g \overrightarrow{v}_g \overrightarrow{v}_g \right) = -\alpha_g \nabla p + \nabla \cdot \overline{\overline{\tau}}_g + \alpha_g \rho_g \overrightarrow{g} + \overrightarrow{F}_{lg} + \Gamma_e \overrightarrow{v}_l - \Gamma_c \overrightarrow{v}_g \tag{3}$$

Where p is the pressure/Pa, $\overline{\overline{\tau}}_g$ is the corresponding force tensor of vapor/kg·m^{-1}·s^{-2}, $\overrightarrow{g}$ is gravitational acceleration/m·s^{-2}, $\overrightarrow{F}_{lg}$ is the interfacial force of liquid phase acting on vapor per unit volume.

2) Liquid Phase

$$\nabla \cdot \left(\alpha_l \rho_l \overrightarrow{v}_l \overrightarrow{v}_l \right) = -\alpha_l \nabla p + \nabla \cdot \overline{\overline{\tau}}_l + \alpha_l \rho_l \overrightarrow{g} + \overrightarrow{F}_{gl} + \Gamma_c \overrightarrow{v}_g - \Gamma_e \overrightarrow{v}_l \tag{4}$$

Where $\overline{\overline{\tau}}_l$ is the corresponding force tensor of liquid/kg·m^{-1}·s^{-2}, $\overrightarrow{F}_{gl}$ is the interfacial force of vapor phase acting on liquid per unit volume.

Energy Conservation Equation

1) Vapor Phase

$$\nabla \cdot \left(\alpha_g \rho_g \overrightarrow{v}_g h_g \right) = \alpha_g \frac{\partial p_g}{\partial t} + \overline{\overline{\tau}}_g : \nabla \overrightarrow{v}_g - \nabla \cdot \overrightarrow{q}_g + Q_{lg} + \Gamma_e h_l - \Gamma_c h_g \tag{5}$$

Where h_g is vapor specific enthalpy, p_g is vapor pressure, $\overrightarrow{q}_g$ was vapor heat flux, Q_{lg} is heat transfer of liquid to vapor per unit volume, h_l is liquid specific enthalpy.

2) Liquid Phase

$$\nabla \cdot \left(\alpha_l \rho_l \overrightarrow{v}_l h_l \right) = \alpha_l \frac{\partial p_l}{\partial t} + \overline{\overline{\tau}}_l : \nabla \overrightarrow{v}_l - \nabla \cdot \overrightarrow{q}_l + Q_{gl} + \Gamma_c h_g - \Gamma_e h_l \tag{6}$$

Where p_l is liquid pressure, $\overrightarrow{q}_l$ was liquid heat flux, Q_{gl} is heat transfer of vaporto liquid per unit volume.

For the multiphase flow system where only vapor phase and liquid phase exist, the volume fraction of vapor and liquid phase satisfies the following equation:

$$\alpha_g + \alpha_l = 1 \tag{7}$$

Interphase Momentum Transfer

The interphase momentum transfer of bubbles dispersed in the liquid could be expressed as:

$$\vec{F}_{lg} = \vec{F}_D + \vec{F}_L + \vec{F}_{TD} + \vec{F}_W \tag{8}$$

Where $\vec{F}_D$is the drag force on vapor per unit volume, $\vec{F}_L$ is the lift force on vapor per unit volume, $\vec{F}_{TD}$ is the turbulent dispersion force on vapor per unit volume, $\vec{F}_W$ is the wall lubrication force on vapor per unit volume.

Drag Force Model

The drag force exerted by the liquid phase on the vapor phase per unit volume can be expressed as:

$$\vec{F}_D = n_o \vec{D}_g = \frac{3\alpha_g}{4d_b} C_D \rho_l \left|\vec{v}_l - \vec{v}_g\right| \left(\vec{v}_l - \vec{v}_g\right) \tag{9}$$

The drag force coefficient $C_D$was calculated using the Ishii-Zuber model (Ansys, 2013).

Lift Force Model

Due to the non uniformity of flow, the liquid velocity on the direction perpendicular to the bulk flow will exist velocity gradient inevitably, bubbles dispersed in the liquid will be influenced by lift force. The direction of lift force is perpendicular to the relative velocity between vapor and liquid, which can be calculated as **Eq. 10**.

$$\vec{F}_L = -C_L \rho_l \alpha_g \left(\vec{v}_g - \vec{v}_l\right) \times \left(\nabla \times \vec{v}_l\right) \tag{10}$$

Where $C_L$is lift force coefficient.

In present work, Moraga model (Moraga et al., 1999) was selected to calculate the lift force, and the lift coefficient is calculated as follows:

$$C_L = \begin{cases} 0.00767 & \varphi > 6000 \\ -\left(0.12 - 0.2e^{-\frac{\varphi}{3600}}\right) e^{\frac{\varphi}{5} \times 10^{-7}} & 6000 \le \varphi \le 1.9 \times 10^5 \\ -0.002 & \varphi > 1.9 \times 10^5 \end{cases} \tag{11}$$

Where

$$\varphi = Re_g Re_w$$

$$\mathrm{Re}_g = \frac{d_b \rho_l \left|\vec{v}_l - \vec{v}_g\right|}{\mu_l}$$

$$\mathrm{Re}_w = \frac{d_b^2 \rho_l \left(\nabla \times \vec{v}_l\right)}{\mu_l}$$

Turbulent Dispersion Force

The dispersion effect of turbulent flow on the dispersed vapor phase is usually described by the turbulent dispersion force which mainly depends on the volume fraction gradient of vapor. Burns et al. (Burns et al., 2004) consider that turbulent dispersion force was caused by liquid phase vortices which caused by interfacial drag, so the turbulent dispersion force was calculated as:

$$\vec{F}_{TD} = C_{TD} \frac{C_D \mu_l \mu_{t,l} A_i \mathrm{Re}_g}{8 d_g \rho_l \sigma_{lg}} \left(\frac{\nabla \alpha_g}{\alpha_g} - \frac{\nabla \alpha_l}{\alpha_l}\right) \tag{12}$$

Where C_{TD} is turbulent dispersion force coefficient with value of 1.0, σ_{lg} is constant with value of 0.9.

Wall Lubrication Force

The wall lubrication force is calculated as:

$$\vec{F}_W = C_W \rho_l \alpha_g \left|\vec{v}_g - \vec{v}_l\right|^2 \vec{n}_w \tag{13}$$

Where $\vec{n}_w$ is normal wall unit vector, C_W is wall lubrication force coefficient which was calculated by Antal model (Antal et al., 1991):

$$C_W = \max\left(\frac{C_1}{d_b} + \frac{C_2}{y_w}, 0\right) \tag{14}$$

Where C_1 and C_2 are infinite constants, which are −0.01 and 0.05 respectively, y_w is the distance from the wall.

Interphase Energy Transfer

When the bubbles departure from the heating wall and enter the subcooled bulk flow region, the heat transfer between the subcooled fluid and the interface for unit volume can be expressed as:

$$q_{lf} = h_{sl}\left(T_{sat} - T_l\right) \tag{15}$$

Where h_{sl} is equivalent heat transfer coefficient per unit volume/ $\mathrm{W{\cdot}m^{-3}{\cdot}K^{-1}}$.

$$h_{sl} = \frac{k_l}{d_b} A_i Nu_l \tag{16}$$

Where A_i is the interfacial density which represent total area of the interface for per unit volume. The interfacial density is obtained by the algebraic relation between the bubble diameter and the interfacial density:

$$A_i = \frac{6\alpha_g\left(1 - \alpha_g\right)}{d_b} \tag{17}$$

$\mathrm{D_b}$ is the bubble diameter, in this work, the improved model of Anglart and Nylund were adopt. It is considered that when the fluid undercooling is higher thanΔT_0, the bubble diameter in the bulk flow isd_0, and when the fluid undercooling is less than ΔT_1, the bubble diameter isd_1.

$$d_b = \begin{cases} d_0 & \Delta T_{sub} > \Delta T_0 \\ \dfrac{d_1\left(\Delta T_{sub} - \Delta T_0\right) + d_0\left(\Delta T_1 - \Delta T_{sub}\right)}{\Delta T_1 - \Delta T_0} & \Delta T_1 \le \Delta T_{sub} \le \Delta T_0 \\ d_1 & \Delta T_{sub} < \Delta T_1 \end{cases} \tag{18}$$

Where d_0 = 0.0001 m; d_1 = 0.0015 m; ΔT_0= 13.5 K; ΔT_1= 0 K.

Based on the literature (Ansys, 2013), Nu_l can be expressed as:

$$Nu_l = 2 + 0.6\,Re_g^{0.5} Pr_l^{0.33} \tag{19}$$

The heat transfer between the vapor phase and interface for unit volume can be calculated as:

$$q_{gf} = \frac{\alpha_g \rho_g c_{p,g}}{\delta t}\left(T_{sat} - T_g\right) \tag{20}$$

Where δt is time scale, which defaults to 0.05, $c_{p,g}$ is the specific heat capacity of the vapor at constant pressure.

Interphase Mass Transfer

For flow boiling, the interphase mass transfer include two processes: evaporation of liquid phase near the heated wall and mass transfer between vapor and liquid phase in bulk flow. During heating process, the superheated liquid layer near the wall will evaporate and generate bubbles. The evaporation rate of the liquid phase near the wall is calculated as:

$$m_e = \frac{q_e}{h_{fg} + c_{p,l}(T_{sat} - T_l)} \tag{21}$$

Where h_{fg} is latent heat of liquid, $c_{p,\ l}$ is specific heat capacity of the liquid at constant pressure, q_e is heat flux of evaporation.

The mass transfer rate in bulk flow depends on the temperature difference between two phases. When the liquid is subcooled, the vapor phase will condense. And when the liquid temperature is higher than the saturation temperature, the liquid will evaporate.

The mass transfer rate from liquid phase to vapor of per unit volume can be expressed by:

$$m_{lf} = \max\left(\frac{q_{lf}}{h_{fg}}, 0\right) \tag{22}$$

The mass transfer condensation rate from vapor phase to liquid of per unit volume is calculated by:

$$m_{gf} = \max\left(\frac{q_{gf}}{h_{fg}}, 0\right) \tag{23}$$

Wall Boiling Model

Rensselaer Polytechnic Institute (RPI) wall boiling model (Kurul and Podowski, 1990) was a common method to describe near-wall boiling behavior. In this model the total heat flux could be divided into the following three parts:

1) Forced convection heat flux of liquid, q_c;
2) The heat flux of evaporation induced by continuous evaporation of liquid near the wall, q_e;
3) The quenching heat flux carried away by the subcooled liquid after bubble detaching from nucleation point on the wall, q_q.

Therefore, the total heat flux on the wall can be expressed as:

$$q_w = q_c + q_e + q_q \tag{24}$$

In present work, to investigate the dry out phenomenon, a modified model had been proposed. Convective heat flux of vapor was added to the RPI wall boiling model, the total heat flux can be expressed as:

$$q_w = \left(q_c + q_e + q_q\right) f(\alpha_l) + q_v f(\alpha_v) \tag{25}$$

Where q_c, q_e, $q_q$have the same meaning as RPI model, q_v is the convective heat flux of vapor phase.

$f(\alpha)$is a function to determine the wall heat partition which is related to the local volume fraction of each phase. Tentner's form is adopted in this paper:

$$f(\alpha_v) = 1 - f(\alpha_l) = \begin{cases} 0 & , \quad \alpha_v < \alpha_{v,1} \\ \frac{1}{2}\left(1 - \cos\left(\pi \frac{\alpha_v - \alpha_{v,1}}{\alpha_{v,2} - \alpha_{v,1}}\right)\right) & , \quad \alpha_{v,1} < \alpha_v < \alpha_{v,2} \\ 1 & , \quad \alpha_v > \alpha_{v,2} \end{cases} \tag{26}$$

Where $\alpha_{v,1}$, $\alpha_{v,2}$ are the transition break points with values of 0.9 and 0.95, respectively.

Convective Heat Flux of Liquid

The forced convective heat flux of single-phase liquid can be calculated as:

$$q_c = h_l(T_w - T_l)A_c \tag{27}$$

Where h_l is convective heat transfer coefficient of liquid phase, T_w is wall temperature, T_l is liquid temperature in the first layer of mesh near the wall, A_c is the affected area of the liquid phase on the heating wall per unit area. In **Eq. 27**, the liquid phase convective heat transfer coefficient is calculated by the wall function.

The heating area can be divided into two parts: the affected area of nuclear boiling and the area affected by convective heat transfer of liquid. The heating wall is only affected by these two mechanisms and no overlapping area exists. Therefore, these two parts meet the normalization requirements:

$$A_c + A_b = 1 \tag{28}$$

Del Valle and Kenning (Del Valle and Kenning, 1985) assumes that every bubble generated at the nucleation site have the same diameter, which is equal to the bubble departure diameter d_w, and the distance between any two bubbles were greater than the bubble diameter, influence area of nuclear boiling can be written as:

$$A_b = \min\left(1, K\frac{N_w \pi d_w^2}{4}\right) \tag{29}$$

Where N_w is nucleation site density. K represents the ratio between the affected area of the vapor phase and the maximum projected area of the bubble, usually taking a value of four, indicating that the affected area of the bubble is larger than the projected area of the bubble on the heating wall. Considering different degree influence may exist between each

bubble, the K values recommended by various researchers are different, but mostly distributes between 1.8 and 5.0. Del Valle and Kenning et al. conducted a large number of visual experimental studies and obtained the correlation for K:

$$K = 4.8e^{\left(-\frac{\rho_l c p_l \left(T_{sat}-T_l\right)}{80\rho_g h_{fg}}\right)} \tag{30}$$

Evaporative Heat Flux

The heat flux used for evaporation can be expressed as:

$$q_e = m_e h_{fg} = V_d \rho_g N_w h_{fg} f \tag{31}$$

Where m_e is the liquid phase evaporation rate per unit area of heated wall, V_d is the volume of departure bubble, f is the bubble departure frequency.

$$V_d = \frac{1}{6}\pi d_w^3 \tag{32}$$

Where dw is the departure diameter which depends on the force balance in the process of bubble growth. The bubble departure diameter can be obtained by analyzing the bubble force or by the experimental data. In this paper, the bubble departure diameter is calculated by Tolubinsky et al. (Krepper and Rzehak, 2011):

$$d_w = min\left(d_{ref} \cdot e^{\left(-\frac{\Delta T_{sub}}{\Delta T_{ref}}\right)}, d_{max}\right) \tag{33}$$

Where $\Delta T_{sub}$is the subcooling, $d_{ref} = 0.6\ mm$; $\Delta T_{ref} = 45K$; $d_{\max} = 1.4\ mm$

In this paper, the nucleate site density N_w on the heated surface is calculated by Lemmert-Chawla (Kurul and Podowski, 1990):

$$N_w = C^n \Delta T_{\sup}^n \tag{34}$$

Where $C = 210$; $n = 1.805$; $\Delta T_{\sup}$ is wall superheat, $\Delta T_{\sup} = T_w - T_{sat}$

f is the frequency of bubbledeparture, given by Cole (Cole, 1960) correlation:

$$f = \frac{1}{T} = \sqrt{\frac{4g\left(\rho_l - \rho_g\right)}{3C_f d_w \rho_l}} \tag{35}$$

Where C_f is resistance factor of bubble departure, the value is 1.0 in this simulation.

Quenching Heat Flux

Quenching heat flux is the cyclic averaged transient energy transfer related to liquid filling the wall vicinity after bubble detachment, The quenching heat flux is expressed as:

$$q_q = 4\sqrt{\frac{\lambda_l \rho_l c_{p,l}}{5\pi T}} A_b \left(T_W - T\right)_l \tag{36}$$

Convective Heat Flux of Vapor

The convective heat flux of vapor was calculated as follows:

$$q_v = h_v \left(T_w - T_v\right) A_c \tag{37}$$

Where hv is the convective heat transfer coefficient, it determined by the wall function.

NUMERICAL METHODS

Geometry Model

The fuel element and fluid channel studied in present work are choosed according to the general test reactor (Jo et al., 2014), it include two types: 1) the large plate used in the real reactor, its size is 2 mm × 60 mm × 600 mm, the channel gap is 2.5 mm; 2) The small plate used in the RERTR irradiation experiment (Meyer et al., 2012), its size is 1.27 mm × 25.4 mm × 101.47 mm, the channel gap is also 2.5 mm.

Under the guidance of RERTR (Research reactor low concentration Program), Argonne National Laboratory has carried out a series of experimental studies on the performance of plate fuel elements (Meyer et al., 2012). Based the results, the blisters could be classified into two types, the first type occurs at low burnup (low irradiation), the blisters are usually round shape and small (less than 0.17 cm^2). and it usually appears at the edge of the pellet. The second type occurs under high burnup (high irradiation), the blisters are usually pillow shaped which caused by the merging of small blisters. The size of the pillow blisters ranges from 1 to 6 cm^2. The position of pillow blisters also starts from the edge of the pellet and expands to the interface of the pellet and the cladding. The above two types are considered in present work.

Round Blisters

The round blisters were shown in **Figure 1**, its diameter is 5 mm, and the projection diameter is 4 mm, the height is 1 mm. 112 blisters were formed on each side of the channel, which was divided into two columns. There were 56 blisters in each row. The blisters formed on both sides of the channel were assumed to be the same, correspond to each other.

Pillow Blisters

Pillow blisters occur on the small plate which was shown in **Figure 2**. The projection area of pillow blister is 9.5 mm × 25 mm rounded rectangle, and the height is 1 mm. Two pillow-shaped blisters were formed on each side of the channel and arranged side by side along the flow direction, the interval between two blisters were 32 mm. The pillow blisters also formed on both sides of the channel, resulting in the 2 mm blockage in the center of the channel, the gap of flow channel is 0.5 mm.

Mesh Model

As more equations were needed to be solved compared to single phase flow, the unstructured tetrahedral mesh used in single-phase calculation are not suitable for boiling simulation. So in this work, the hexahedral mesh were used for the channel with blisters.

For the channel with round blisters, due to the array nature of geometry, mesh replication array is also used. The mesh was

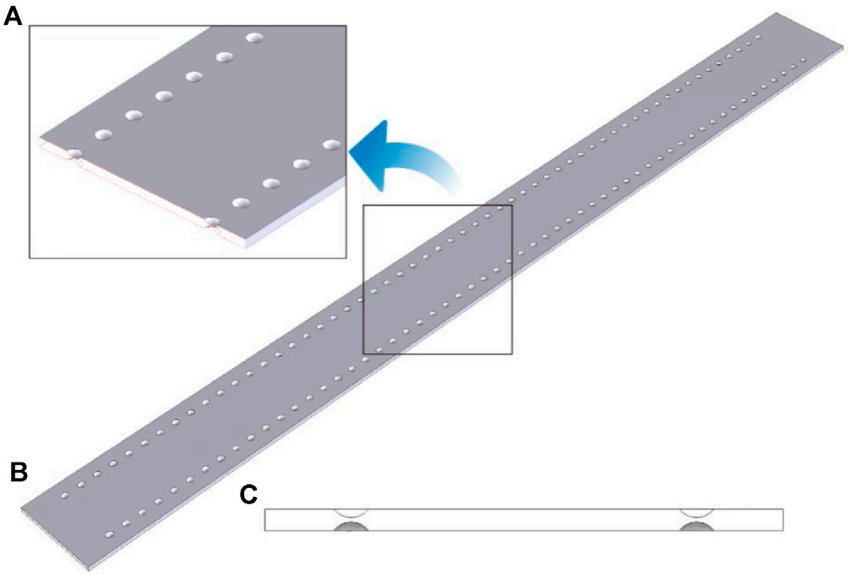

FIGURE 1 | The geometric model of round blisters in a single channel. **(A)** Partial magnification **(B)** Global geometric **(C)** cross section.

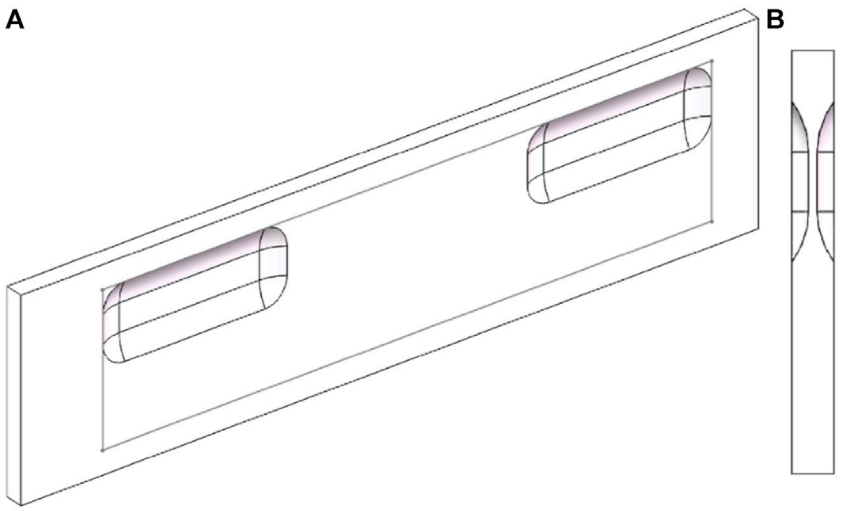

FIGURE 2 | The geometric model of pillow blisters. **(A)** Global geometric **(B)** Cross section.

shown in **Figure 3**, seven layers of mesh are arranged in the gap direction, and the mesh size in the width and length direction is equal to that in the gap direction. Based on mesh sensitivity analysis, the total number of mesh is about two million, the mesh quality is above 0.6 and the maximum aspect ratio is 6.6.

For the channel with pillow blisters, the trimmed mesh was used. As shown in **Figure 4**. Through this method, the mesh on the surface with large curvature could be divided into small meshes, thus it could capture the surface structure better. Like the channel with round blisters, seven layers of mesh were arranged in the gap direction, and the mesh size in the width and length direction is the same as that in the gap direction. Based on mesh sensitivity analysis, the total mesh is about 140,000, the mesh quality is more than 0.3, and the maximum aspect ratio is 14.9.

Boundary Conditions

The boundary conditions are shown in **Table 1**. In present work, the solid region (pellet and cladding) and the gas cavity formed by fission gas are not considered, and the boundary conditions of solid wall are set according to literature (Li et al., 2019). The velocity inlet was used in this work, the water with high subcooling enters the channel and the volume fraction of the vapor is 0, the velocity of the liquid was 1.5 m/s. The pressure

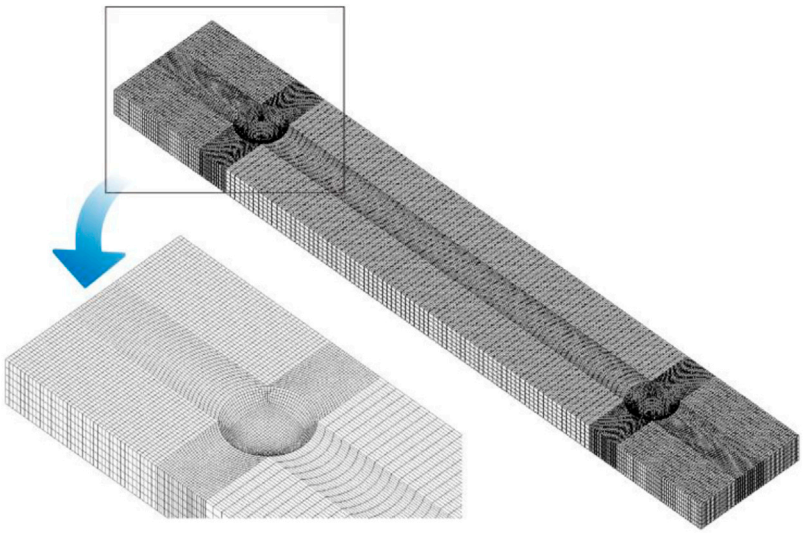

FIGURE 3 | Mesh of channel with round blisters.

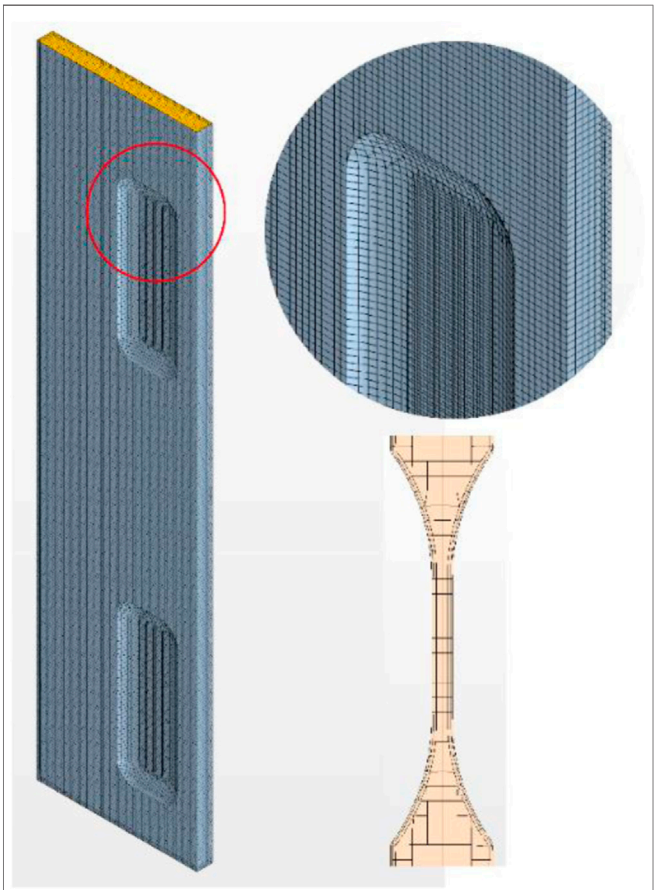

FIGURE 4 | The single-channel pillow bubbling deformation mesh.

TABLE 1 | The boundary conditions for deformation channel.

Boundary	Condition
Operating pressure	1 MPa
Inlet	Velocity inlet
	Subcooling: 80 K
	Velocity: 1.5 m/s
	The volume fraction of liquid is 1
Outlet	Pressure outlet
Cladding wall	Uniform heat flux
Blister wall	1% of the average surface heat flux
Side wall	Adiabatic

outlet was used and the pressure is 1.0 Mpa. The side wall is the adiabatic and non-slip wall.

Uniform heat flux was applied in the wall of cladding and blister. The initial heat flux was calculated according to Jens-Lottes formula. Then the heat flux was increased gradually with 0.5 MW/m^2 as step size.

As the heat flux is greatly reduced by the existence of the gas cavity, so the heat flux at the blasters was assumed to be about 1% of that in other cladding areas.

RESULTS AND DISCUSSION

According to the single-phase calculation results, the flow will be influenced by blisters in the plate-type fuel channels, the scouring action of fluid at the front of blisters may enhance the heat transfer and the flow separation at the trailing edge of blisters may result in a local stagnation area. Vapor will accumulate in the

TABLE 2 | Operating conditions simulated in this study.

Case	Geometric conditions	Pressure/MPa	Inlet velocity/m·s^{-1}	Inlet temperature/K	Inlet subcooling/K	Wall heat flux/MW·m^{-2}
1	Large plate round blisters	1	1.5	350	100	0.9
2		1	1.5	355	95	0.9
3		1	1.5	360	90	0.9
4		1	1.5	365	85	0.9
5		1	1.5	370	80	0.9
6	Small plate pillow blisters	1	1.5	430	23	0.35
7		1	1.5	430	23	0.40
8		1	1.5	430	23	0.45
9		1	1.5	430	23	0.50
10		1	1.5	430	23	0.55
11		1	1.5	430	23	0.60
12		1	1.5	430	23	0.65
13		1	1.5	430	23	0.70
14		1	1.5	430	23	0.75
15		1	1.5	430	23	0.80

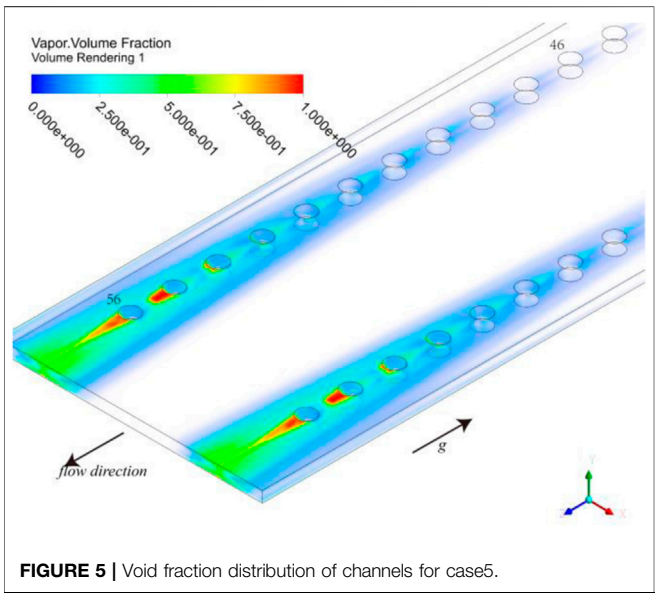

FIGURE 5 | Void fraction distribution of channels for case5.

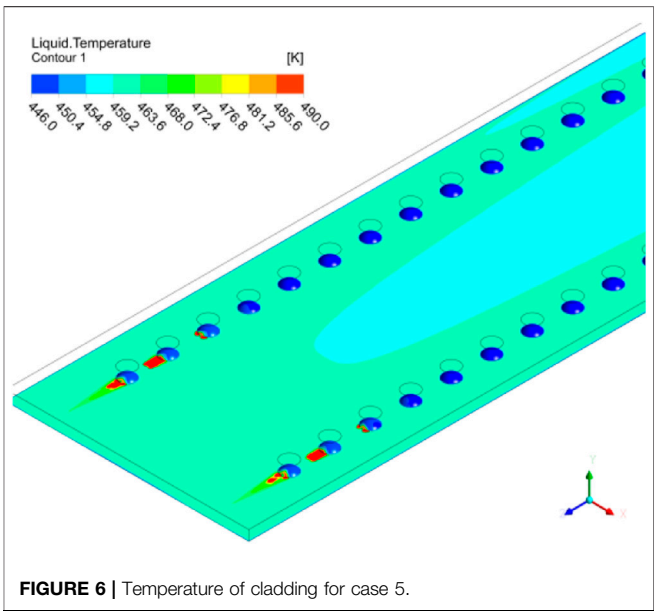

FIGURE 6 | Temperature of cladding for case 5.

stagnation region which could reduce the heat transfer characteristic. In this section, the heat transfer characteristics for two different channels were analyzed firstly, then sensitivity analysis of different parameters was carried out. The operation conditions were shown in **Table2**.

The Round Blisters

The overall boiling phenomenon in the channel depends on evaporation rate and transportation of the vapor phase. In the following, we will first present the void fraction distribution in the channel, which gives the reader an intuitive impression of the boiling region. Then, *Wall Temperature* discusses wall temperature distribution which is directly related to evaporation heat flux (in the RPI model) and to evaporation rate in **Eq. 21**. Following that, *Flow Distribution Across the Channel* analyses the flow distribution in the cross-section of the channel, which explains the uneven distribution of boiling region. Lastly, high-void-fraction region where dryout occurs is closely examined.

Void Fraction Distribution

Firstly case1-case5 were calculated. For these cases, the heat flux was large, subcooled boiling occurred closed to the outlet. The void fraction of the channel was shown in **Figure 5**. We can see that boiling occurred only in the area affected by the blisters, that is, near the edges of the channel. At the onset of nucleate boiling (the 46th row of blisters in **Figure 5**), vapor mainly appeared on the front walls of the blisters. As the increasing of void fraction, the high void fraction regions appeared at the rear edge of the blisters (54th row). The local void fraction almost reached 1.0 near the 55th and 56th rows of blisters. It suggested that dry out may occur more easily at the trailing edge of the blisters, and cladding will be burnout more easily in this region.

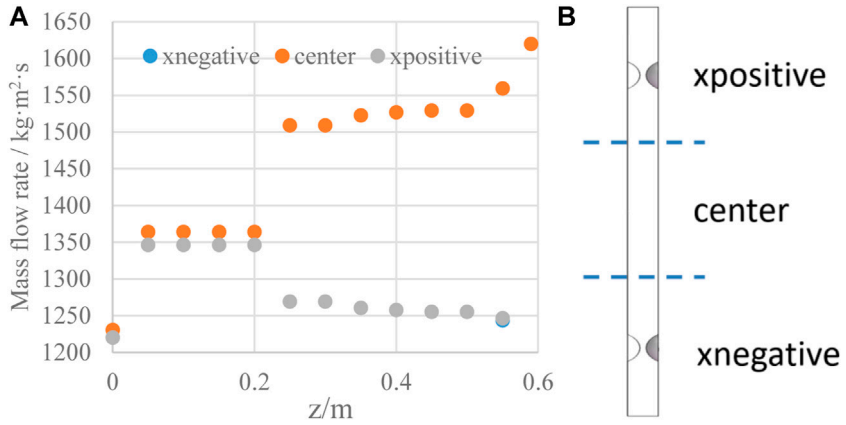

FIGURE 7 | Mass flow rate distribution in the cross section of round blister channel.

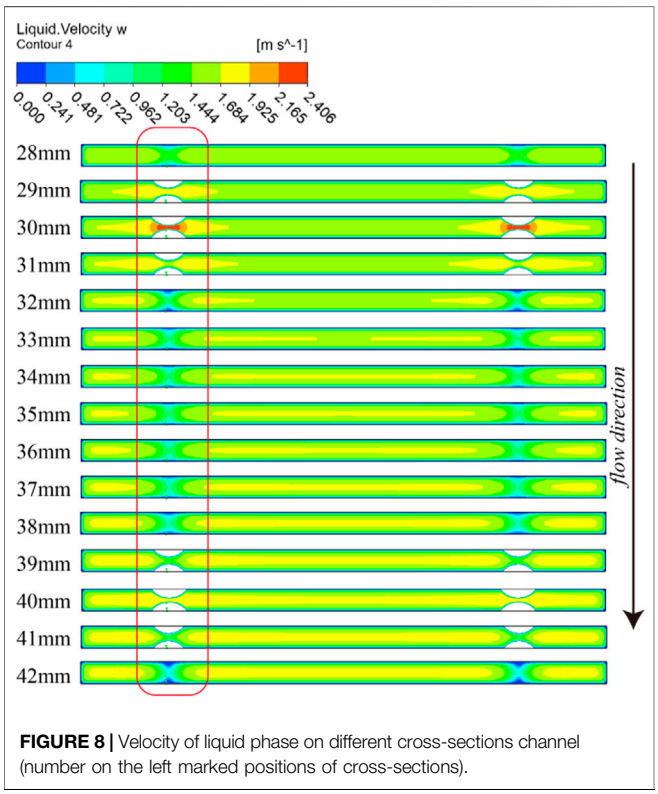

FIGURE 8 | Velocity of liquid phase on different cross-sections channel (number on the left marked positions of cross-sections).

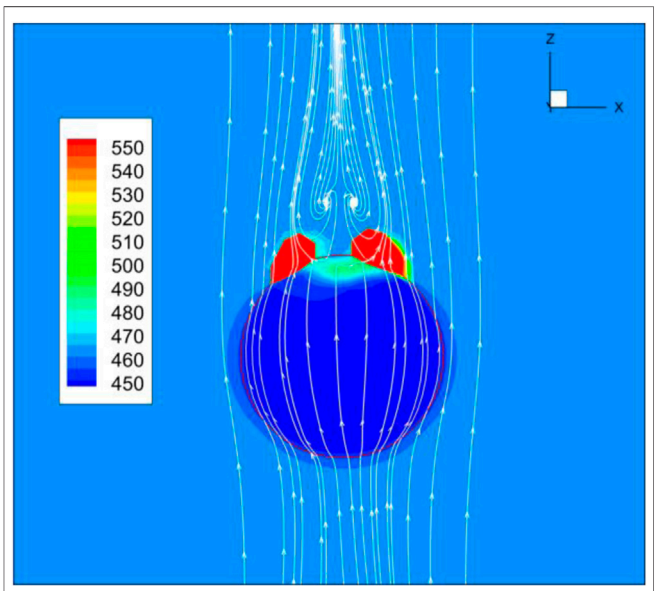

FIGURE 9 | The temperature and wall streamline of the 54th row of blisters for case 5.

We can also see from **Figure 5** that no boiling occurred at the center of the channel. Although uniform heat flux conditions were applied to the entire wall, boiling phenomenon in the center of the channel was different from that on the edge of the channel. This indicates that blisters may have an important influence on the flow rate, so it may affect the initiation and development of boiling.

Wall Temperature

Figure 6 shows the temperature distribution of the cladding surface. We can see that the superheat of the cladding surface was mostly about 15 K, but the temperature in the middle of the fuel plate was lower. Due to the thermal resistance of the internal air, the heat derived from the blisters was less than that from other area, so the temperature was also lower. And the temperature of most blisters surface was lower than the saturation temperature (453 K) at the operating pressure (1 MPa) except for the dry out area.

Flow Distribution Across the Channel

As shown in **Figure 7B**, the cross sections were divided into three parts in the width direction, the mass flow in each part were shown in **Figure 7A**. The blisters in the channel will increase the local flow resistance and reduce the mass flow rate greatly in the blister region, so more fluid will flow through center of the channel. As the decrease of mass flow rate in the blister regions, the heat transfer ability will be weakened, the temperature in these regions was higher.

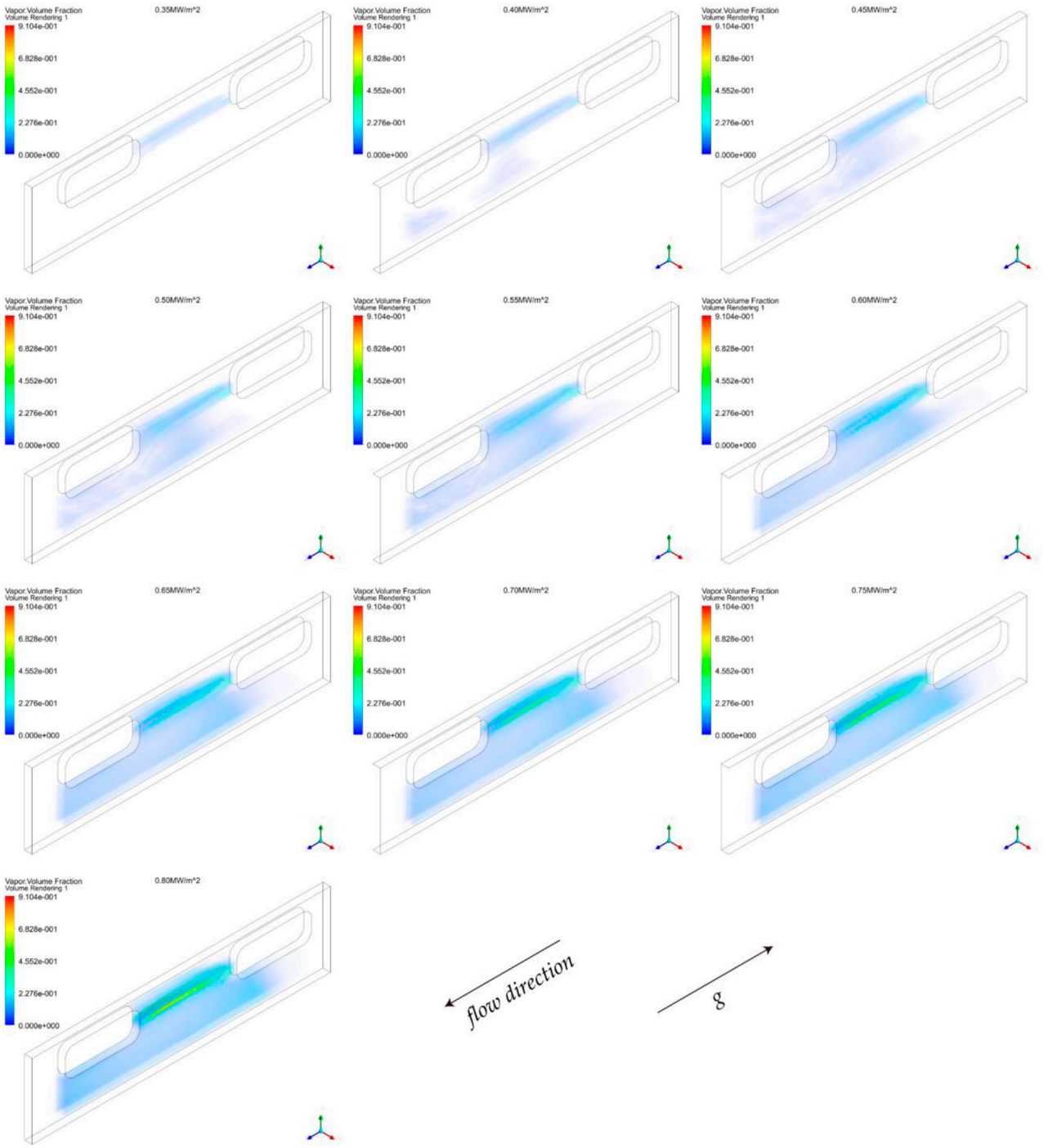

FIGURE 10 | Void fraction in channel with pillow-like blisters.

As water flowing through a row of blisters, the velocity and heat transfer coefficient will change periodically, which may result in different phenomenon for the leading and trailing edges of the blisters.

Figure 8 shows the bulk velocity at different cross sections along the flow direction. After flowing through the first row of blisters, a stagnation area will appear at the trailing edge of the blisters (32 and 42 mm). We can see from the figure of 33–38 mm, there was a low-velocity region near the wall, and the temperature in this region will increase faster along the flow direction. Therefore, boiling is more likely to occur before reaching the next blister (front of blisters). After flowing through the blister, the transverse flow will eliminate the local high temperature of the fluid. So, the onset of nucleate boiling usually occurred at the front of blisters (e.g., 46th row of blisters in **Figure 5**).

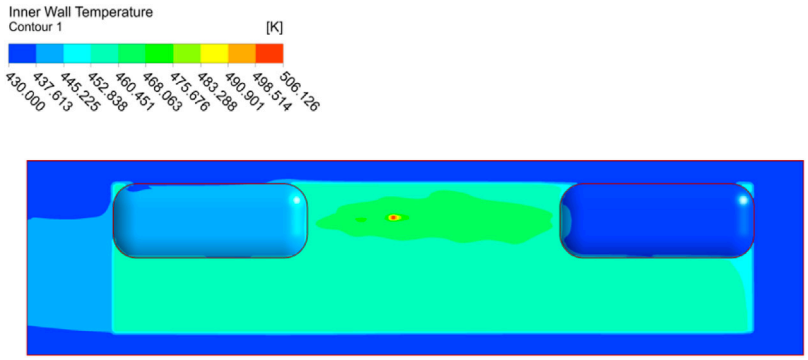

FIGURE 11 | Temperature distribution of cladding with pillow-like blisters.

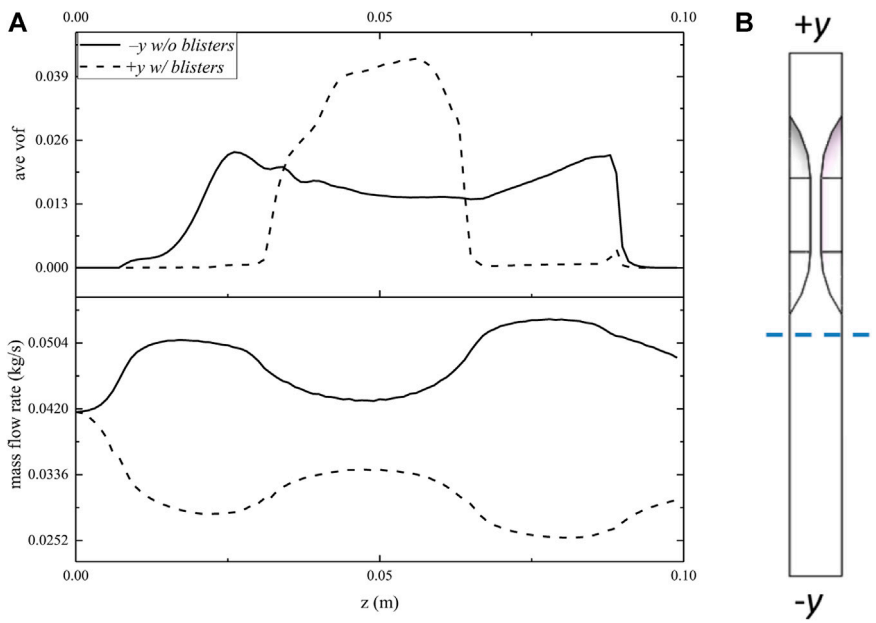

FIGURE 12 | Average void fraction and flow rate in cross section.

Stagnation and Dryout

Figure 9 shows the blisters temperature and the streamline near the 54th row of blisters. We can see that the temperature at the back of blisters is very high and the dry out will also appear in this region. It can be concluded that the backflow and stagnation may be the main reasons for the deterioration of local flow heat transfer, which lead to the local dry out.

Pillow Blisters

The void fraction calculated from case 6–15 were shown in **Figure 10**. In case 6, the heat flux of the wall is 0.35 MW/m^2, and boiling begins to occurring at this condition. Boiling first occurs in regions between two pillow blisters, and then disappears after entering the downstream of blisters. In case 7 (0.40 MW/m^2), vapor will also appear in the downstream of the non-blisters side except regions between two pillow blisters. For the case 8–15 (0.45–0.75 MW/m^2), the regions of boiling are nearly the same. The vapor mostly concentrated in two regions: the region between two pillow blisters and downstream of the channel without blisters. With the increasing of heat flux, the region of boiling will increase gradually. In case 15 (0.80 MW/m^2), the maximum void fraction on the wall is more than 0.9 and local dry out occurs.

The temperature of the cladding surface in case15 was shown in **Figure 11**. It can be seen that the temperature in regions between two pillow blisters is higher. Especially for the region with void fraction higher than 0.9, the local dry out occurs and the temperature is more than 500 K. Due to the accumulation of vapor, convection heat transfer of vapor phase will increase, the overall heat transfer coefficient reduce greatly compared with other regions, so that the temperature will rise sharply.

As shown in **Figure 12B**, the cross sections were divided into two parts in the *Y* direction, in which the +y half of the channel has blisters and the –y half has no blisters. The mass flow rate and average void fraction along the flow direction were shown in **Figure 12A**. Under the influence of pillow-blisters, more fluid will flow through the non-blisters side, the flow rate in the +y half will decrease. And more vapor will be generated in the region with pillow blisters. As the lower velocity and higher heat flux in downstream region of the blisters, there is a higher risk of dryout. This is consistent with the result in **Figure 10**.

Compared with the round blisters, the boiling region of pillow-blisters is wider. However, the dry out area for channel with pillow-blisters and round blisters are consistent, both in the downstream region of blisters.

CONCLUSION

In present work, the subcooled boiling characteristic had been investigated for the rectangle channel with round and pillow blisters, mass flow rate, temperature and void fraction for different conditions had also been analyzed, we can draw conclusions as follows:

1) For round blisters, boiling starts at the front edge of the blisters, however, for pillow blisters, boiling starts at the downstream region;
2) For the channel with round blister, the blisters will increase the local flow resistance and more fluid will flow through center of the channel;
3) For round blister channel, boiling occurred only in the area near the edges, no boiling occurred at the center of the channel;
4) The boiling region of pillow-blisters is wider and concentrated in the region between two pillow blisters and the downstream of the non-blisters side;
5) The dry out area for channel with pillow-blisters and round blisters are both in the downstream region of blisters.

DATA AVAILABILITY STATEMENT

The original contributions presented in the study are included in the article/Supplementary Material, further inquiries can be directed to the corresponding author.

AUTHOR CONTRIBUTIONS

YL and HH contributed to conception and design of the study. CC wrote the first draft of the manuscript. LuL and LiL organized the database. HY performed the statistical analysis. MW and SQ sections of the manuscript. All authors contributed to manuscript revision, read, and approved the submitted version.

REFERENCES

Al-Yahia, O. S., and Jo, D. (2017). Onset of Nucleate Boiling for Subcooled Flow through a One-Side Heated Narrow Rectangular Channel. *Ann. Nucl. Energ.* 109 (1), 30–40. doi:10.1016/j.anucene.2017.05.014

Ansys (2013). *ANSYS Fluent Theory Guide 15.0 [M]*. Cannosburg, PA: ANSYS.

Antal, S. P., Lahey, R. T., and Flaherty, J. E. (1991). Analysis of Phase Distribution in Fully Developed Laminar Bubbly Two-phase Flow. *Int. J. Multiphase Flow* 17 (5), 635–652. doi:10.1016/0301-9322(91)90029-3

Burns, A., Frank, T., Hamill, I., and Shi, J. M. (2004). "The Favre Averaged Drag Model for Turbulent Dispersion in Eulerian Multi-phase Flows," in 5th International Conference on Multiphase Flow. (ICMF'04), 392.

Chen, C., Gao, P.-z., Tan, S.-c., Chen, H.-y., and Chen, X.-b. (2015). Forced Convective Boiling Heat Transfer of Water in Vertical Rectangular Narrow Channel. *Nucl. Eng. Des.* 291 (1), 133–144. doi:10.1016/j.nucengdes.2015.05.012

Chen, C., Wang, M., Zhao, X., Ju, H., Wang, X., Tian, W., et al. (2019). Numerical Study on the Single Bubble Rising Behaviors under Rolling Conditions. *Nucl. Eng. Des.* 349, 183–192. doi:10.1016/j.nucengdes.2019.04.039

Cole, R. (1960). A Photographic Study of Pool Boiling in the Region of the Critical Heat Flux. *Aiche J.* 6 (4), 533–538. doi:10.1002/aic.690060405

Debortoli, R. A., Green, S. J., Letourneau, B. W., Troy, M., and Weiss, A. (1958). *Forced-convection Heat Transfer Burnout Studies for Water in Rectangular Channels and Round Tubes at Pressures above 500 psiaWAPD-188 [R]*. Westinghouse Electric Corporation.

Del Valle, V. H., and Kenning, D. B. R. (1985). Subcooled Flow Boiling at High Heat Flux. *Int. J. Heat Mass Transfer* 28 (10), 1907–1920. doi:10.1016/0017-9310(85)90213-3

Dienst, W., Nazaré, S., and Thümmler, F. (1977). Irradiation Behaviour of UAlx-Al Dispersion Fuels for thermal High Flux Reactors. *J. Nucl. Mater.* 64 (1), 1–13. doi:10.1016/0022-3115(77)90002-2

Gu, J., Wang, Q., Wu, Y., Lyu, J., Li, S., and Yao, W. (2017). Modeling of Subcooled Boiling by Extending the RPI wall Boiling Model to Ultra-high Pressure Conditions. *Appl. Therm. Eng.* 124, 571–584. doi:10.1016/j.applthermaleng.2017.06.017

Jo, D., Park, J., and Chae, H. (2014). Development of thermal Hydraulic and Margin Analysis Code for Steady State Forced and Natural Convective Cooling of Plate Type Fuel Research Reactors. *Prog. Nucl. Energ.* 71, 39–51. doi:10.1016/j.pnucene.2013.11.006

Khan, I., Wang, M., Zhang, Y., Tian, W., Su, G., and Qiu, S. (2020). Two-phase Bubbly Flow Simulation Using CFD Method: A Review of Models for Interfacial Forces. *Prog. Nucl. Energ.* 125, 103360. doi:10.1016/j.pnucene.2020.103360

Koncar, B., and Krepper, E. (2008). CFD Simulation of Convective Flow Boiling of Refrigerant in a Vertical Annulus [J]. *Nucl. Eng. Des.* 238 (3), 693–706. doi:10.1016/j.nucengdes.2007.02.035

Krepper, E., and Rzehak, R. (2011). CFD for Subcooled Flow Boiling: Simulation of DEBORA Experiments. *Nucl. Eng. Des.* 241 (9), 3851–3866. doi:10.1016/j.nucengdes.2011.07.003

Kurul, N., and Podowski, M. Z. (1990). "Multidimensional Effects in Forced Convection Sub Cooled Boiling," in Proceedings of the International Heat Transfer Conference. (Jerusalem, Israel: Begell). doi:10.1615/ihtc9.40

Lee, H. J., and Lee, S. Y. (2001). Heat Transfer Correlation for Boiling Flows in Small Rectangular Horizontal Channels with Low Aspect Ratios. *Int. J. Multiphase Flow* 27 (12), 2043–2062. doi:10.1016/s0301-9322(01)00054-4

Li, L., Fang, D., Zhang, D., Wang, M., Tian, W., Su, G., et al. (2019). Flow and Heat Transfer Characteristics in Plate-type Fuel Channels after Formation of Blisters on Fuel Elements. *Ann. Nucl. Energ.* 134, 284–298. doi:10.1016/j.anucene.2019.06.030

Li, S., Tan, S., Xu, C., Gao, P., and Sun, L. (2013). An Experimental Study of Bubble Sliding Characteristics in Narrow Channel. *Int. J. Heat Mass Transfer* 57 (1), 89–99. doi:10.1016/j.ijheatmasstransfer.2012.10.002

Liao, Y., Krepper, E., and Lucas, D. (2019). A Baseline Closure Concept for Simulating Bubbly Flow with Phase Change: A Mechanistic Model for Interphase Heat Transfer Coefficient. *Nucl. Eng. Des.* 348, 1–13. doi:10.1016/j.nucengdes.2019.04.007

Liao, Y., Ma, T., Liu, L., Ziegenhein, T., Krepper, E., and Lucas, D. (2018). Eulerian Modelling of Turbulent Bubbly Flow Based on a Baseline Closure Concept. *Nucl. Eng. Des.* 337, 450–459. doi:10.1016/j.nucengdes.2018.07.021

Meyer, M. K., Moore, G. A., and Jue, J. F. (2012). *INL/EXT-12-26500; TRN: US1300072 United States 10.2172/1055982 TRN: US1300072 INL English [R]*. Idaho National Laboratory (INL).

Moraga, F. J., Bonetto, F. J., and Lahey, R. T. (1999). Lateral Forces on Spheres in Turbulent Uniform Shear Flow. *Int. J. Multiphase Flow* 25 (6), 1321–1372. doi:10.1016/s0301-9322(99)00045-2

Song, J. H., Lee, J., Chang, S. H., and Jeong, Y. H. (2017). Onset of Nucleate Boiling in Narrow, Rectangular Channel for Downward Flow under Low Pressure. *Ann. Nucl. Energ.* 109 (1), 498–506. doi:10.1016/j.anucene.2017.05.050

Sudo, Y., Miyata, K., Ikawa, H., Kaminaga, M., and Ohkawara, M. (1985). Experimental Study of Differences in DNB Heat Flux between Upflow and Downflow in Vertical Rectangular Channel. *J. Nucl. Sci. Tech.* 22 (8), 604–618. doi:10.1080/18811248.1985.9735705

Wang, C., Wang, H., Li, X., and Gao, P. (2014). Experimental Study of Saturated Boiling Heat Transfer and Pressure Drop in Vertical Rectangular Channel. *Nucl. Eng. Des.* 273 (1), 631–643. doi:10.1016/j.nucengdes.2014.03.053

Wang, C., Wang, H., Wang, S., and Gao, P. (2014). Experimental Study of Boiling Incipience in Vertical Narrow Rectangular Channel. *Ann. Nucl. Energ.* 66 (1), 152–160. doi:10.1016/j.anucene.2013.12.011

Wang, M., Wang, Y., WenxiTian, S. Q., and Su, G. H. (2021). Recent Progress of CFD Applications in PWR thermal Hydraulics Study and Future Directions. *Ann. Nucl. Energ.* 150, 107836. doi:10.1016/j.anucene.2020.107836

Conflict of Interest: HH, CC, LuL, YL, and HY was employed by the company Nuclear Power Institute of China.

The remaining authors declare that the research was conducted in the absence of any commercial or financial relationships that could be construed as a potential conflict of interest.

frontiers in Energy Research

ORIGINAL RESEARCH
published: 22 July 2021
doi: 10.3389/fenrg.2021.667911

Thermodynamic Evaluation of Equilibrium Oxygen Composition of UO_2-Mo Nuclear Fuel Pellet Under High Temperature Steam

*Jae Ho Yang *, Kun Woo Song, Dong Seok Kim, Dong-Joo Kim, Heung Soo Lee, Ji-Hae Yoon and Yang-Hyun Koo*

Korea Atomic Energy Research Institute, Daejeon, South Korea

Micro-plate or microcell UO_2–Mo is considered a promising accident tolerant fuel candidate for water-cooled power reactors. In this work, we evaluated the anticipated oxidation behavior of a UO_2–Mo system under high-temperature steam to understand the impact of Mo oxidation on the fuel degradation mechanism in the event of steam ingress through cracks in the cladding. The equilibrium oxygen compositions of UO_2 and Mo in various steam atmospheres relevant to reactor operating conditions were predicted using thermodynamic calculations and then compared with previous results. The oxidation behavior of UO_2–Mo pellets was discussed through thermodynamic calculations and in terms of kinetic parameters such as oxygen diffusion, fuel temperature profile, and pellet microstructure. Mo oxidation was found to have an insignificant effect on pellet integrity in a cladding leakage scenario under normal reactor operating conditions.

Keywords: accident tolerant fuel, UO_2-Mo pellet, steam oxidation, equilibrium composition, oxygen potential

OPEN ACCESS

Edited by:
Jinbiao Xiong,
Shanghai Jiao Tong University, China

Reviewed by:
Ho Jin Ryu,
Korea Advanced Institute of Science and Technology, South Korea
Di Yun,
Xi'an Jiaotong University, China

****Correspondence:***
Jae Ho Yang
yangjh@kaeri.re.kr

Specialty section:
This article was submitted to Nuclear Energy, a section of the journal Frontiers in Energy Research

Received: *15 February 2021*
Accepted: *08 July 2021*
Published: *22 July 2021*

Citation:
Yang JH, Song KW, Kim DS, Kim D-J, Lee HS, Yoon J-H and Koo Y-H (2021) Thermodynamic Evaluation of Equilibrium Oxygen Composition of UO_2-Mo Nuclear Fuel Pellet Under High Temperature Steam. Front. Energy Res. 9:667911. doi: 10.3389/fenrg.2021.667911

INTRODUCTION

UO_2–Mo micro-plate or microcell pellets, in which small amounts of molybdenum metal particles are arranged in the form of directionally aligned plates or continuous networks, are actively studied worldwide as a promising accident tolerant fuel candidate for light water reactors, because they have improved thermal conductivity (Kim et al., 2017; Kim et al., 2018; Buckley et al., 2019; Cheng et al., 2019; Finkeldei et al., 2019; Cheng et al., 2020; Lee et al., 2020). This fuel design might be easily implemented in nuclear power plants in the near term, as it inherits the superior safety performance of UO_2 nuclear fuel and can leverage existing knowledge and infrastructure.

To successfully implement the micro-plate or microcell concepts in a UO_2 pellet, research is underway on addressing various technical issues. A conventional pressure-less sintering process has been established to produce composite pellets with a specific microstructure (Kim et al., 2017; Kim et al., 2018). From an economic perspective, the fuel cycle length in a UO_2–Mo system is reduced because the addition of Mo reduces U loading, and Mo has a larger neutron absorption cross-section. The neutron penalty is partly mitigated by limiting the Mo addition to less than 3 vol%. The lower fuel operating temperature owing to the improved thermal conductivity is conducive to neutron utilization owing to the MTC feedback effect (Jo et al., 2020). Preliminary calculation showed that UO_2–3vol% Mo fuel with a U235 enrichment of 4.95% can achieve the same fuel cycle length as that in a 4.65% enriched UO_2 fuel.

Phase equilibria serve as a basis for the manufacturing and performance characterization of nuclear fuels. In particular, a comprehensive understanding of phase equilibrium and

thermochemical properties is essential to support licensing by providing data on changes in the thermophysical properties, irradiation damage, and behavior of fission products. Chemical reactions between fuel materials and the atmosphere can result in fuel degradation and is one of the main factors governing nuclear fuel performance. During irradiation in a nuclear reactor, fuel pellets can be in two states where the partial pressure of oxygen in the environmental gas increases. The first state is during normal operation. The oxygen separated from UO_2 by the fission of U increases the oxygen potential of the atmosphere in the fuel rod (Spino and Peerani, 2008). Another state is the ingress of steam through a damaged fuel cladding. The coolant flows into the hot fuel rod and vaporizes, and the steam is decomposed to generate oxygen, which increases the oxygen partial pressure inside the fuel rod. Thermodynamically, Mo has a high oxygen affinity and can undergo oxidization and evaporation when exposed to a high-temperature atmosphere containing oxygen. If UO_2–Mo pellets are oxidized in a leakage scenario (e.g., cladding breach), the oxidation and evaporation of Mo and the resulting volume expansion of the fuel pellets may cause fuel rod failure and exacerbate the accident.

The aim of this study was to evaluate thermodynamically the change in the equilibrium oxygen composition of UO_2–Mo pellets when exposed to high-temperature steam. The impact of Mo oxidation on the degradation behavior of UO_2 pellets in the event of a cladding breach is also discussed. Our preliminary assessments are expected to contribute to the evaluation of this material for use as an accident-tolerant fuel.

CALCULATION OF OXYGEN PARTIAL PRESSURE IN STEAM GAS UNDER VARIOUS CONDITIONS

In fuel rod failure scenarios, UO_2 pellets are exposed to steam at high temperatures and high pressures. In this environment, UO_2 pellets oxidize to a composition that is in equilibrium with the gas phase. To calculate the equilibrium deviation from the stoichiometry of UO_2, it is necessary to know the partial pressure of oxygen in the environment. The oxygen partial pressure of the gas is determined by the temperature, gas composition, and pressure. Under normal operating conditions, the fuel temperature is typically in the range of 400–1,300°C. The internal pressure of the damaged fuel rod is equivalent to a typical reactor operating pressure of 150 atm. Regarding the composition of the gas introduced into the rod, the steam is mixed with hydrogen produced during the oxidation reaction of steam with Zr (Garzarolli and Stehle, 1979; Review of Fu, 2010). Previous studies reported that the highest deviation from the stoichiometry (x in UO_{2+x}) for the pellets in the damaged fuel rods is approximately 0.1 (Une et al., 1995; Kim, 2003; Verrall et al., 2005; Higgs et al., 2007). This deviation implies that some amount of hydrogen is mixed in the introduced steam and that the hydrogen composition varies depending on the location in the fuel rod. Considering the typical operating conditions and anticipated steam compositions, the equilibrium oxygen partial pressure with respect to the temperature was calculated under different hydrogen contents of the mixed steam gas (0, 10, and 1,000 ppm).

Two calculation procedures were applied to obtain the equilibrium oxygen partial pressures in this study: 1) The *Gem* module from HSC Chemistry 9 (HSC Chemistry 9, 2018), which utilizes the built-in Gibbs energy minimization method, and 2) Olander's transcendental equation (Olander, 1986). According to the Olander's transcendental equation, the oxygen partial pressure (p_{O_2} in atm) in the steam and hydrogen mixture can be estimated using the following expression:

$$K_1\left(p_{O_2}\right)^{1/2}\left[\left(\frac{Q}{2}-1\right)+\left(\frac{Q}{2}+1\right)\frac{p_{o_2}}{p_t}\right]=1-(Q+1)\left(\frac{p_{o_2}}{p_t}\right) \quad (1)$$

where,

$$K_1=\exp\left(-\frac{\Delta G^{\circ}}{RT}\right),\ \Delta G^{\circ}=-250800+57.8T\ (J/mol), \quad (2)$$

R is the universal gas constant (8.3145 J/mol·K), and p_t is the total system pressure. The hydrogen-to-oxygen atom ratio (Q) of the environment is given by

$$\mathrm{Q}=2\left(1+\frac{n_{H_2}}{n_{H_2O}}\right) \quad (3)$$

Figure 1 shows the calculated variation in the oxygen partial pressures as a function of temperature for steam and steam–hydrogen mixtures at 1 and 150 atms. For pure steam, the oxygen partial pressure calculated by Olander's formula agrees well with that obtained using the HSC9 program. However, for the steam–hydrogen mixture, the oxygen partial pressures obtained from Olander's solution were slightly lower. Many previous studies have used Olander's equation to evaluate the equilibrium oxygen partial pressure of steam–hydrogen mixed gases. In this study, Olander's solution was used to estimate the equilibrium oxygen composition to ensure consistency with previous results.

Figure 2 shows the equilibrium oxygen partial pressures of the mixed steam as a function of temperature at pressures of 1 and 150 atm obtained by Olander's solution. The mixing of a small amount of hydrogen significantly reduces the equilibrium oxygen partial pressure of the steam. However, as the temperature increases, the oxygen partial pressure difference between the pure steam and the mixture gradually narrows because of the decomposition reaction of the steam. Evidently, in pure steam, the oxygen partial pressure increases with increasing pressure in the calculated temperature range. In the case of the mixed gas, the pressure has little effect in the low-temperature region. Above a certain temperature, however, the oxygen concentration increases because of the

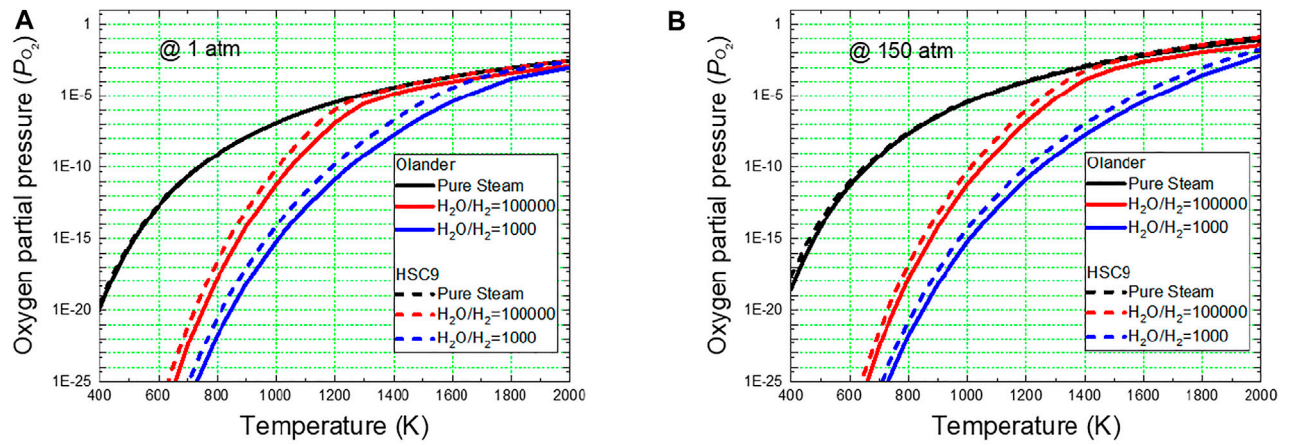

FIGURE 1 | Comparison of equilibrium oxygen partial pressures of steam and steam–hydrogen mixed gases as a function of temperature for total pressures of **(A)** 1 atm and **(B)** 150 atm, calculated through the HSC9 program (HSC Chemistry 9, 2018) and Olander's equation (Olander, 1986).

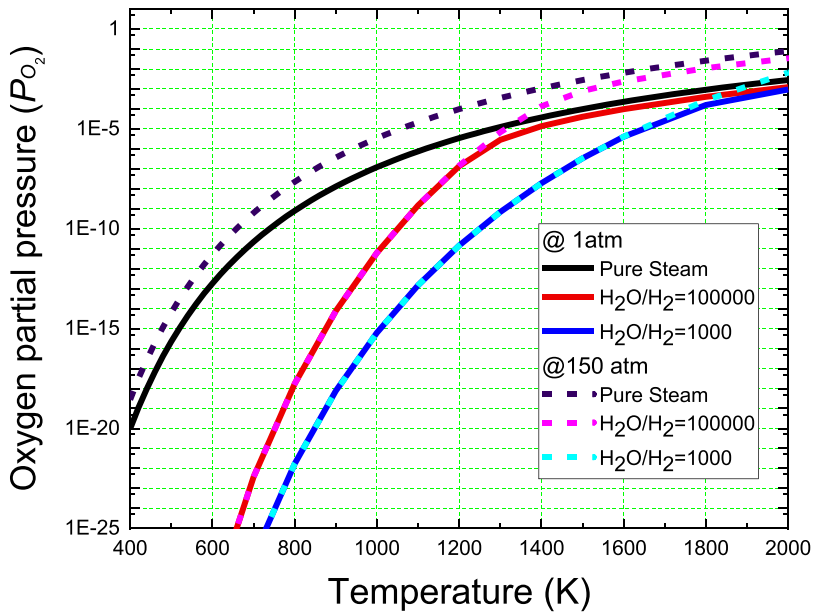

FIGURE 2 | Effects of H_2 mixing and pressure on the equilibrium oxygen partial pressures of steam calculated by Olander's equation (Olander, 1986).

decomposition reaction of the steam, thereby increasing the oxygen partial pressure at high pressures.

EVALUATION OF EQUILIBRIUM OXYGEN COMPOSITIONS OF UO_2 AND Mo AT HIGH TEMPERATURE STEAM AND STEAM-HYDROGEN MIXTURES

The equilibrium oxygen composition of U–O and Mo–O systems can be estimated using the oxygen partial pressures of the environment and *p-C-T* (p_{O_2}-*composition-temperature*) diagram. **Figure 3** shows the phase diagram of the U–O system with oxygen pressure isoatms, presented by Kim (Kim, 2000). **Figure 2** indicates that the equilibrium oxygen partial pressure of pure steam at 1000 K and 1 atm is approximately 1×10^{-7}. At this oxygen partial pressure, U_3O_{8-x} is in a stable oxide phase, as denoted by point B (red dot) in **Figure 3**. On the other hand, at 1500 K, the equilibrium oxygen partial pressure increases to approximately 1.2×10^{-4}, and the corresponding equilibrium phase should be UO_{2+x}, as marked by point A (blue dot) in **Figure 3**.

Figures 4A,B show the phase stability diagrams of the U–O system constructed using thermodynamic equations established

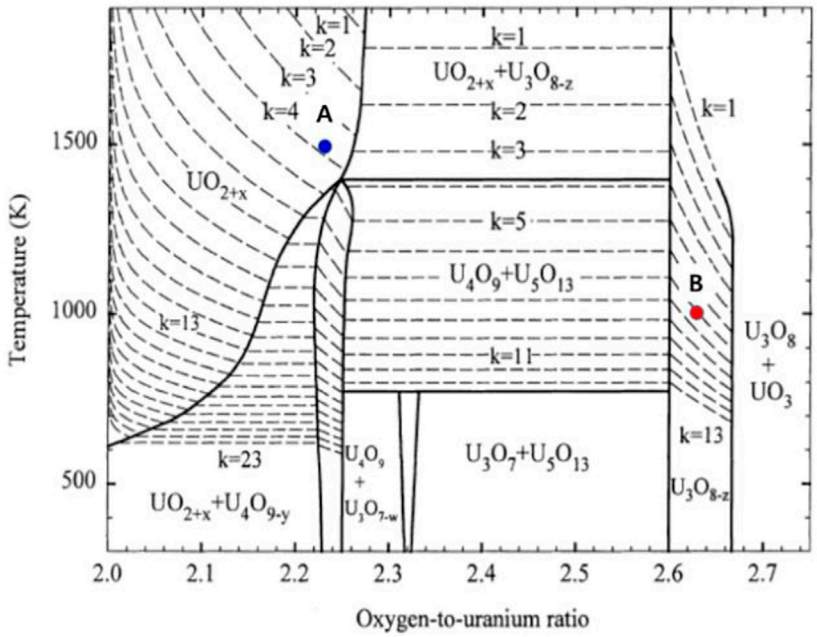

FIGURE 3 | Variation in the equilibrium oxygen stoichiometry with temperature of the U–O system in pure steam atmosphere. The points A (blue dot) and B (red dot) indicate the equilibrium oxygen partial pressures of pure steam at 1500 and 1000 K, respectively. The U–O phase diagram is from Ref. (Kim, 2000).

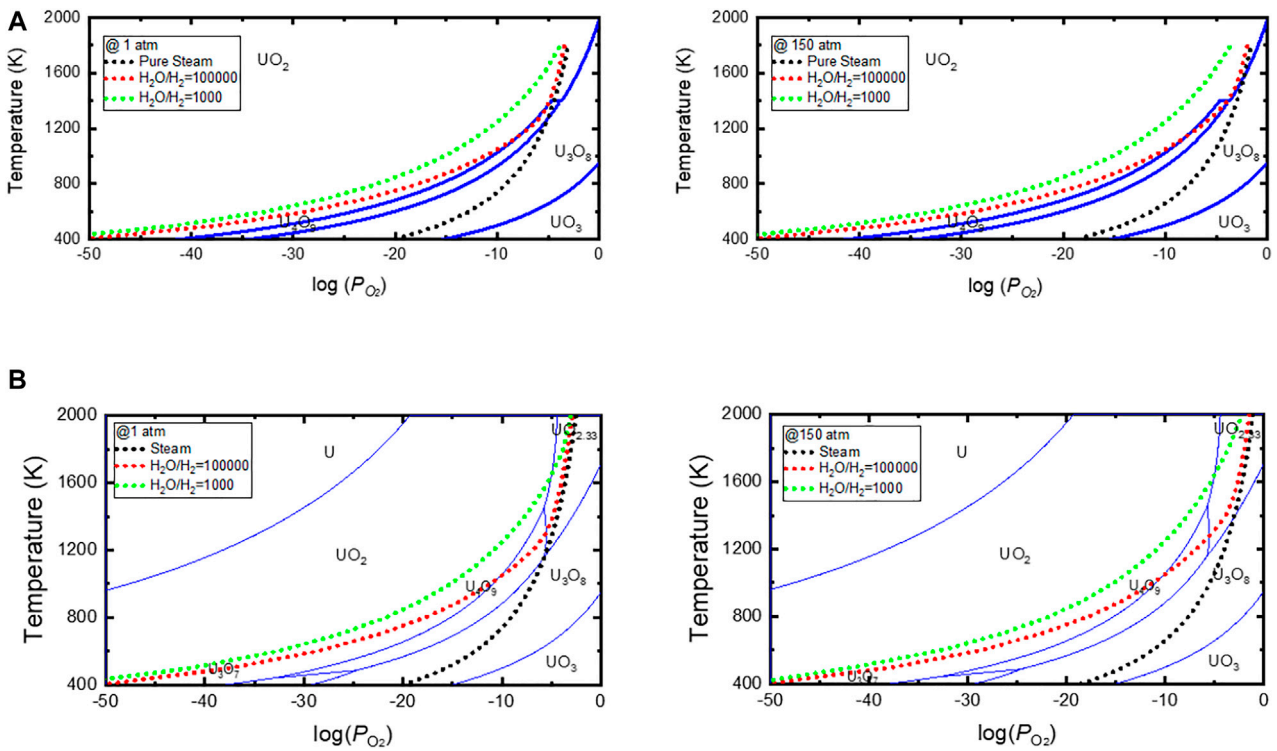

FIGURE 4 | U–O stability diagram and equilibrium oxygen potentials of steam and steam–hydrogen mixed gas. U–O stability boundary is constructed using **(A)** thermodynamic equations in Ref. (Kim, 2000), and **(A)** *Tpp* module in HSC9 Chemistry (HSC Chemistry 9, 2018).

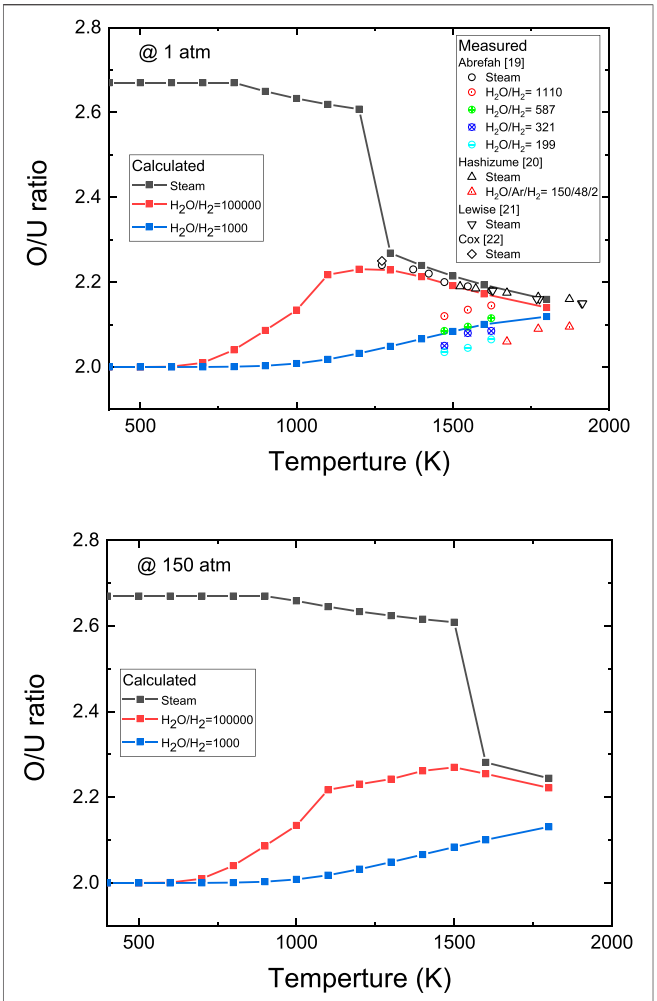

FIGURE 5 | Calculated equilibrium O/U ratio of the U–O system using the equations in Ref (Kim, 2000). and comparison with experimental data.

by Kim and *Tpp* module in HSC9 Chemistry, respectively. The equilibrium oxygen potential curves for the pure steam and steam–hydrogen mixtures in this study are also shown. From **Figure 4**, we can predict the oxidation behavior of UO_2 with temperature changes when UO_2 is exposed to high-temperature steam. As shown in **Figure 4A**, when UO_2 pellets are exposed to pure steam at a pressure of 150 atm and a temperature above 1573 K, there is no significant change in the pellet shape owing to the stable cubic phase of UO_{2+x}. However, when the temperature decreases below 1573 K, the orthorhombic phase of U_3O_8 becomes stable, and UO_2 pellets pulverize to U_3O_{8-x} powder. **Figure 4A** also reveals that reducing the pressure or mixing a small amount of hydrogen in the steam can help significantly extend the temperature range in which the cubic phases of UO_{2+x} or U_4O_{9-y} are stable. For example, mixing more than 10 ppm of hydrogen in the steam can help prevent UO_2 pellets from being oxidized to U_3O_8. The two stability diagrams shown in **Figures 4A,B** are similar but not entirely consistent. As shown in the stability diagram of **Figure 4B** obtained using HSC9, the UO_2 pellets pulverize to U_3O_8 when exposed to steam at a pressure of 150 atm and a temperature below 1373 K. This temperature limit is ~200 K lower than that shown in **Figure 4A**.

Figure 5 shows detailed variations in the calculated equilibrium O/U ratio of the U–O system with the steam composition, pressure, and temperature. The equilibrium O/U ratio was calculated using the equations presenting the best *p-C-T* relationship proposed by Kim (Kim, 2000). As expected, in **Figure 4A**, the O/U ratio of pure steam abruptly changes at the stability boundary temperature between the cubic phases (UO_{2+x}, U_4O_{9-y}), and U_3O_8. When the steam-to-hydrogen ratio (H_2O/H_2) is 100,000, the cubic phase is stable over the calculated temperature range, and no U_3O_8 phase is expected. Since the oxygen potential curve of this gas is closest to the stability boundary at approximately 1273 K, the equilibrium O/U ratio shows a parabolic shape with a peak value located in the temperature range of approximately 1,273–1373 K. When the hydrogen content is increased further (H_2O/H_2 = 1,000), the oxygen potential of the atmosphere is largely reduced, and consequently, the equilibrium O/U ratio decreases. Published experimental data (Abrefah et al., 1994; Hashizume et al., 1999; Lewis et al., 1990; Cox et al., 1986) on O/U ratio variations following UO_2 oxidation in steam and steam–hydrogen mixture are compared in **Figure 5A**. The experimental data measured above 1273 K are in good agreement with the calculated values. While several experimental datasets on the equilibrium O/U ratio exist for steam oxidation of UO_2 pellets above 1273 K, few data are available for steam oxidation below 1273 K owing to the slow oxidation of UO_2 at low temperatures and the challenges related to controlling the steam–hydrogen composition. Kuhlman (Kuhlman, 1948) found no significant weight change in UO_2 after exposure to oxygen-free steam at 873 K for 6 h. Bittel et al. (Bittel et al., 1969) reported that the final average O/U ratio of pellets annealed at 1158 K for 290 min in steam was 2.039, which is far below the calculated value. On the contrary, Dumitrescu et al. (Dumitrescu et al., 2015) reported that UO_2 pellets pulverize to U_3O_8 after annealing in 873 K steam for 10 h. Recently, Jung et al. (Jung et al., 2020) have also shown the formation of U_3O_8 particles on the UO_2 pellet annealed for 1,000 min in steam maintained at a temperature range of 673–733 K. This discrepancy between the experimental results appears to be due to the very slow oxidation reaction in low-temperature steam and the strong influence of the oxygen and hydrogen contents on the equilibrium oxygen potential of the steam.

The melting point of pure molybdenum is 2896 K. However, the formation of low-melting-temperature oxides is the drawback of this refractory metal. The Mo–O temperature–concentration diagram shows various molybdenum oxides, where the principal stable oxide phases in the Mo-O system are MoO_3 ($T_m = 1073 \pm 5\ K$) and MoO_2 ($T_m = 2600 \pm 100\ K$) (Brewer and Lamoreaux, 1980).

The phase stability diagrams for the Mo–O system with the variations in the temperature and oxygen partial pressure have been presented by several researchers (Chen et al., 2018; Lee et al., 2019a; Zhang et al., 2014). **Figure 6** shows the stability diagrams applied in this study, plotted using the *Tpp* module in HSC9 program (HSC Chemistry 9, 2018). The stability diagram is similar to that prepared by Chen (Chen et al., 2018) using

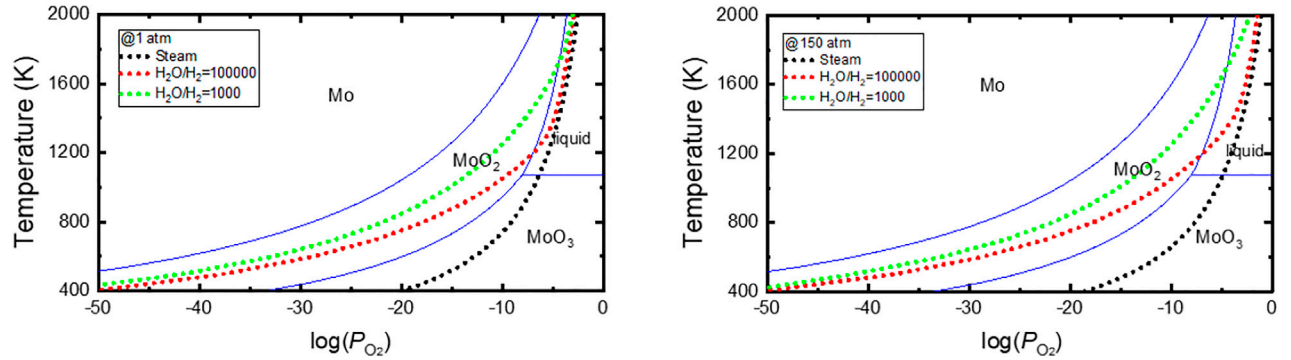

FIGURE 6 | Mo–O stability diagram and equilibrium oxygen potentials of steam and steam–hydrogen mixed gas, constructed using the HSC9 program.

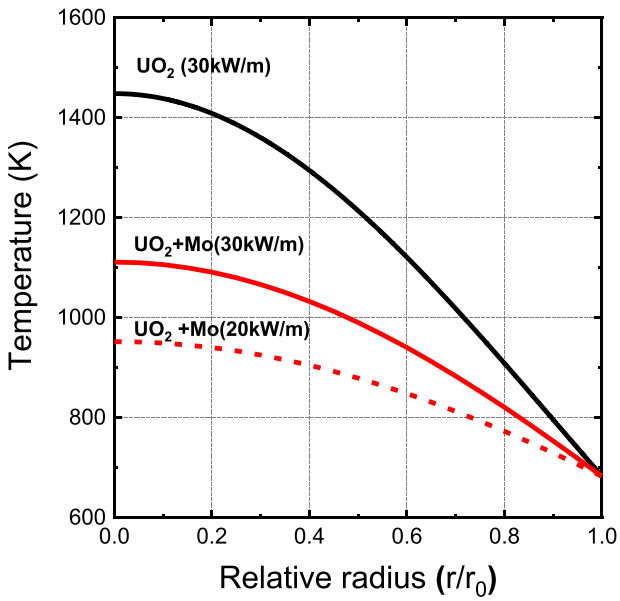

FIGURE 7 | Comparison of radial temperature profile between UO_2 and UO_2–Mo pellets.

FactSage 6.2 (GTT Technologies, Germany) and that calculated by Lee (Lee et al., 2019a) using meta-generalized-gradient approximation and hybrid density functional theory calculations. Zhang et al. constructed a Mo–O stability diagram using the CALPHAD method (Zhang et al., 2014). However, the stability diagram differs considerably from that shown in **Figure 6**, characterized by a narrower area of stability for solid oxides.

The oxygen partial pressure or equilibrium oxygen potential curves were superimposed on these figures to assess the anticipated equilibrium oxygen composition of the Mo–O system when exposed to atmospheres as those shown in **Figure 2**. **Figure 6** indicates that MoO_3 is a stable oxide in pure steam. Therefore, when Mo is exposed to steam, it will oxidize to MoO_3, becoming a liquid above 1073 K and vaporizing above 1428 K. Indeed, the oxidation test of Mo in 100% steam showed a rapid weight loss above 1073 K (Nelson et al., 2014). The oxidation behavior of Mo changes significantly even when very small amounts of hydrogen is added to the steam. As shown in **Figure 6**, in 150 atm steam mixed with 1,000 ppm of hydrogen, the equilibrium oxide composition is MoO_2, and a liquid phase is formed at approximately 1673 K, which is approximately 600 K higher than that in the case of pure steam. The effect of hydrogen content in steam on the oxidation of Mo has been determined at 1273 K. The test result shows that the material loss rate can be meaningfully reduced by adding hydrogen to the steam, consistent with the effect of hydrogen predicted and shown in **Figure 6** (Nelson et al., 2014).

PREDICTION OF THE OXIDATION BEHAVIOR OF UO_2-Mo PELLETS IN THE EVENT OF CLADDING BREAKAGE DURING THE NORMAL OPERATION

The oxidation behavior of UO_2 and Mo in various steam atmospheres relevant to reactor operating condition was studied independently. In this section, the oxidation behavior of UO_2–Mo pellets is predicted when steam is introduced into the fuel rod through cladding leaks under reactor operating conditions.

Figure 7 shows a comparison of the calculated temperature profile along the radial direction between conventional UO_2 and micro-plate UO_2–3vol% Mo pellets operating at a linear heat generation rate of 30 kW/m. The temperature gradient of the UO_2 pellets was calculated using the thermal conductivity model from the MATPRO handbook (Hagrman and Reymann, 1979). The temperature profile of UO_2- 3vol% Mo pellets was calculated using the measured thermal conductivity of the pellet in which Mo plates with an average diameter of ~45 μm and an average thickness of ~1.5 μm were dispersed in UO_2 (Kim et al., 2020). The thermal conductivity of both pellets was corrected to 95% of the theoretical density for temperature calculation.

Since the thermal conductivity is more than 80% higher than that of UO_2 pellets, the operating temperature is significantly reduced in the case of the UO_2–3vol% Mo pellet. The centerline

temperature of UO_2–3vol% Mo is calculated to be 1093 K, approximately 300 K lower than that of UO_2.

As shown in **Figure 5**, the high-pressure steam ingress into the fuel rod pulverizes the UO_2 pellets, and consequently, the fuel rods are severely damaged because of the volume expansion and fission gas release. However, the fuel failure mechanism due to the oxidation of UO_2 pellets has not been reported thus far. In fact, the secondary failure mechanisms observed in defective fuel rods were mostly due to the formation of ZrO_2 or ZrH_2 ((2010). Review of Fu, 2010). As mentioned in *Calculation of Oxygen Partial Pressure in Steam Gas Under Various Conditions*, this fact reveals that the steam introduced to the fuel rod is mixed with hydrogen and consequently has a much lower oxygen partial pressure than pure steam.

Assuming a constant thermal conductivity of the fuel pellets during the oxidation reaction, the oxidation behavior of UO_2–3vol % Mo pellets operating at a 30 kW/m when exposed to 150 atm steam mixed with hydrogen can be predicted as follows. **Figures 4**, **5** indicate that the equilibrium oxygen composition deviation from stoichiometric UO_2 (x in UO_{2+x}) is ~0.22 and decreases toward the pellet periphery, when the hydrogen content in the steam is 10 ppm. The equilibrium phase of Mo under this condition is MoO_2, which has a melting temperature of ~1193 K, as shown in **Figure 6**. When the hydrogen content in the steam increases to 1,000 ppm, the maximum deviation of x in UO_{2+x} decreases to less than 0.02, and the melting temperature of MoO_2 increases to ~1673 K. The theoretical densities of Mo, MoO_2 and MoO_3 are 10.28, 6.47, and 4.69 g/cm^3, respectively. The lattice parameters of UO_{2+x} are known to contract linearly with an increase in x, and the contraction factor (line slope) is in the range of −0.132 and −0.07 Å, depending on temperature and x (Perio, 1955; Rachev et al., 1965; Belbeoch et al., 1967; Touzelin and Dode, 1969; Teske et al., 1983; Yakub et al., 2009). Considering the specific situation where only Mo is oxidized to MoO_3 in UO_2-3vol% Mo pellet, the pellet will show a volume increase of up to 3.6%. However, in that situation, UO_2 is also oxidized to UO_{2+x}, so the volume expansion due to MoO_3 formation is offset by the volume reduction due to oxidation of UO_2. If we assume the oxidation reaction terminated with the formation of solid MoO_3 and $UO_{2.15}$, and the contraction factor is −0.07 Å, the volume of the pellet will be increased by about 3%. When the oxidation reaction with the steam-hydrogen mixture is completed and the pellet reaches an equilibrium state, the pellet volume is expected to increase to less than 3%, considering the volume expansion due to MoO_2 formation and volume reduction due to UO_2 oxidation. Moreover, no liquid phase is expected in the equilibrium state because the maximum pellet temperature is much lower than the melting temperature of MoO_2.

The diffusion mobility of oxygen as well as the kinetic parameters should also be considered in the prediction of the oxidation behavior. Higgs et al. have developed a theoretical model to evaluate the UO_2 pellet oxidation behavior in operating defective fuel elements, taking into account multi-phase transport including oxygen diffusion by both chemical and thermal gradients and steam-hydrogen transport along gap and in fuel cracks (Higgs et al., 2007).

Thermoelastic fracture owing to the temperature gradient dominates the formation of primary radial cracks in UO_2 pellets under irradiation (Oguma, 1983; Lee et al., 2019b; Li and Shirvan, 2021). The number of cracks measured under various out-of-pile conditions in the UO_2 pellet is roughly proportional to linear power of the fuel rod (Oguma, 1983). Multiphysics phase-field modeling of quasi-static cracking in UO_2 pellet showed typically eight primary radial cracks are developed and interconnected during the reactor startup and cooling (Li and Shirvan, 2021). In the case of UO_2-Mo composite pellet, lower temperature gradient would reduce the thermal hoop stress, thereby decreasing pellet region where the thermal hoop stress is higher than fracture stress of UO_2 (Lee et al., 2019b), suggesting the UO_2-Mo could be more resistant to cracking than the UO_2 pellet even for the same linear power, as was observed in U_3Si_2 fuel (Cappia and Harp, 2019). However, the composite structure would probably have insignificant effect on cracking behavior because the volume fraction of Mo plates or Mo wall is just 3% and its thickness is only several micrometers. Therefore, the linear power will be a dominant factor in the cracking behavior and, if the temperature gradients between the UO_2 and UO_2-Mo pellets are the same, the crack patterns observed in both pellets are expected to be similar to each other.

Two assumptions have been made. First, the UO_2-3 vol% Mo pellet are fragmented into eight parts by eight primary radial cracks that penetrate the center. Second, considering the average diameter of Mo plates (~45 μm), the Mo particles located within 50 μm of the fragments surface will be exposed to environment directly. Under the circumstance, it is calculated that about 0.45 vol% of Mo among the 3 vol% of Mo will directly contact with steam transported along the gap and fuel cracks, and the remaining 2.55 vol% of Mo will be embedded in the UO_2 matrix.

The oxidation reaction of the Mo plates embedded in the UO_2 matrix will be governed by oxygen diffused through UO_2 lattice or grain boundaries. Therefore, oxygen diffusion inside the UO_2 matrix is an important parameter that needs to be considered to better understand the influence of Mo on oxidation behavior. Considering the diffusion distance for oxygen to reach the Mo surface via the dense UO_2 and the low lattice diffusion rate owing to the low pellet temperature of less than 1093 K (Bittel et al., 1969), relatively long incubation time seems to be required for the Mo inside the pellet fragment to meet with oxygen and start the oxidation reaction. The MoO_2 layer is known to adhere to the Mo surface and act as an anti-corrosion layer, so the formation of a MoO_2 surface layer is expected to further delay the oxidation rate. Therefore, the oxidation reaction rate of Mo by oxygen diffusion is expected to be low, particularly in the outer region of the pellet with low temperature. In contrast to the Mo plate inside the pellet fragment, the Mo plate located near the pellet periphery or fragment surface would be rather quickly oxidized even at low temperature by direct contact with the steam introduced through the cladding defects, gas gaps and fuel cracks. In particular, the volume expansion due to preferential oxidation of Mo possibly develops secondary cracks on the surface, and steam can penetrate through the cracks to accelerate oxidation. However, the rapid oxidation of exposed Mo is expected to be confined to a small number of pellets located around the defect. The experimental and computational results showed that O/U ratio of pellet located at opposite side of or far from the defect is much lower than that of pellet near the defect (Une et al., 1995; Kim, 2003; Verrall et al., 2005; Higgs et al., 2007). The steam-hydrogen transport rate,

another important parameter controlling the rate of reaction, is probably limited in the opposite area of the pellet to defect or at a location away from the defect. In particular, the hydrogen concentration increases where the gas transports is stagnant, and then, the local oxidation rate is further delayed.

There was a concern about the accelerated degradation of UO_2–Mo fuel rods due to the oxidation of Mo in a cladding leakage scenario. However, a thermodynamic evaluation showed that the equilibrium composition of Mo is the solid phase of MoO_2, and the maximum volume expansion of a pellet due to the complete oxidation of Mo to MoO_2 is estimated to be less than 3%. Given the low fuel temperature and the microstructure of the pellets, where most of Mo is imbedded in UO_2 matrix, and considering UO_2 pellet oxidation behavior in operating defective fuel element (Garzarolli and Stehle., 1979; Review of Fu, 2010; Une et al., 1995; Kim, 2003; Verrall et al., 2005; Higgs et al., 2007), it will take a long time for Mo to reach the equilibrium composition of MoO_2, and the volume expansion of the pellet will also proceed gradually. Therefore, the effect of Mo oxidation on the pellet integrity in a cladding leakage scenario is expected to be insignificant.

The thermodynamic prediction of the oxidation behavior was evaluated under the assumption that the thermal conductivity of the pellet remains constant and that there are no reactions at the UO_2/MoO_2 interface. However, the thermal conductivity may decrease depending on the degree of oxidation of UO_2 and Mo, and the formation of new compounds has an additional effect on the volume change. Subsequently, the pellet temperature will increase, and the oxidation behavior of the fuel rod may vary. U-Mo-O ternary compounds, which are possibly formed at the UO_2/Mo interface, would influence the oxygen transport and thus the oxidation behavior of the pellets. When the thermal conductivity decreased and fuel temperature increased, Mo oxides in the central region of pellet might form liquid or vapor phases. Those phases can negatively affect the integrity of the fuel rods by increasing the fuel internal pressure and reacting with pellet and cladding. Therefore, to accurately assess the fuel behavior, further experimental studies are required to obtain data on the diffusion mobility of oxygen near the phase boundary between UO_2 and Mo, reactions at the UO_2/Mo and UO_{2+x}/MoO_2 interfaces (Bharadwaj et al., 1984; Sarrasin et al., 2019), phase equilibria in U-Mo-O ternary system and the change in the thermal conductivity with the degree of oxidation. Multiple and complex chemical reactions, including cladding and fission products, as well as interactions between UO_2-Mo and steam are expected to occur under accidents such as loss of coolant or station black out. Although the volume fraction of Mo in UO_2 is small (3%), which is expected to have a limited impact on accident progress, integral test of fuel rod is required to understand the behavior of UO_2-Mo pellets and their interactions with cladding in the event of accidents.

CONCLUSION

The oxidation behavior of a UO_2–Mo system in a steam atmosphere relevant to reactor operating conditions was evaluated through thermodynamic calculations for a preliminary assessment of the impact of Mo oxidation on the fuel behavior of UO_2–Mo pellets in the event of steam ingress through cracks in the cladding. In the thermodynamic equilibrium state, the oxidation reaction is terminated with the formation of solid MoO_2 and hyper-stoichiometric UO_{2+x}, and the volume expansion after the termination of the reaction is estimated to be less than 3%. In terms of the kinetic parameters, such as the steam-hydrogen flow, fuel temperature, and cracked-pellet microstructure, the impact of Mo oxidation on the fuel integrity in a cladding leakage scenario is expected to be insignificant. Limitations of the current preliminary thermodynamic assessment include the thermal conductivity degradation due to the formation of U-Mo-O compounds, steam/hydrogen transports along the fuel cracks and gap, and simplified thermo-mechanical cracking behavior. Future experimental study would include the oxidation behavior of Mo located near fuel crack and inside UO_2 under the anticipated oxygen potential, the microstructure change after the mechanical cracks or during the oxidation, and the variation of effective thermal conductivity owing to the formation of Mo-oxides and U-Mo-O compounds. Integral test using fuel and cladding assembly would also be necessary to estimate the effect of steam/hydrogen mixed gas transport in the defective fuel rod and its local composition on the overall oxidation behavior of UO_2-Mo-Zr fuel system. Combining the thermodynamic evaluation in this study with experimental data in the future, it will be possible to simulate the behavior of fuel rods in the event of a cladding breach.

DATA AVAILABILITY STATEMENT

The original contributions presented in the study are included in the article/Supplementary Material, further inquiries can be directed to the corresponding author.

AUTHOR CONTRIBUTIONS

JHY: Conceptualization, Methodology, Calculation, Visulaization, Writing-Original draft, Review and; Editing. KWS: Methodology, Data collection, Review and; Editing. DSK: Methodology, Data collection, Review and; Editing. D-JK: Methodology, Data collection, Review and; Editing. HSL: Methodology, Data collection, Review and; Editing. J-HY: Methodology, Data collection, Review and; Editing. Y-HK: Methodology, Review and; Editing.

FUNDING

This work was supported by the National Research Foundation funded by Ministry of Science and ICT of Korea (grant number 2017M2A8A5015056).

REFERENCES

Abrefah, J., Aguiar Braid, A. D., Wang, W., Khalil, Y., and Olander, D. R. (1994). High Temperature Oxidation of UO2 in Steam-Hydrogen Mixtures. *J. Nucl. Mater.* 208, 98–110. doi:10.1016/0022-3115(94)90201-1

Belbeoch, B., Boivineau, J. C., and Perio, P. (1967). Changements de structure de l'oxyde U4O9. *J. Phys. Chem. Sol.* 28, 1267–1275. doi:10.1016/0022-3697(67)90070-4

Bharadwaj, S. R., Chandrasekharaiah, M. S., and Dharwadkar, S. R. (1984). On the Solid State Synthesis of $UMoO_6$. *J. Mater. Sci. Lett.* 3, 840–842. doi:10.1007/BF00727990

Bittel, J. T., Sjodahl, L. H., and White, J. F. (1969). Steam Oxidation Kinetics and Oxygen Diffusion in UOz at High Temperatures. *J. Am. Ceram. Soc.* 52, 446–451. doi:10.1111/j.1151-2916.1969.tb11976.x

Brewer, L., and Lamoreaux, R. H. (1980). The Mo-O System (Molybdenum-Oxygen). *Bull. Alloy Phase Diagrams* 1, 85–89. doi:10.1007/bf02881199

Buckley, J., Turner, J. D., and Abram, T. J. (2019). Uranium Dioxide - Molybdenum Composite Fuel Pellets with Enhanced thermal Conductivity Manufactured via Spark Plasma Sintering. *J. Nucl. Mater.* 523, 360–368. doi:10.1016/j.jnucmat.2019.05.059

Cappia, F., and Harp, J. M. (2019). Postirradiation Examinations of Low Burnup U3Si2 Fuel for Light Water Reactor Applications. *J. Nucl. Mater.* 518, 62–79. doi:10.1016/j.jnucmat.2019.02.047

Chen, W.-F., Chen, H., Koshy, P., Nakaruk, A., and Sorrell, C. C. (2018). Effect of Doping on the Properties and Photocatalytic Performance of Titania Thin Films on Glass Substrates: Single-Ion Doping with Cobalt or Molybdenum. *Mater. Chem. Phys.* 205, 334–346. doi:10.1016/j.matchemphys.2017.11.021

Cheng, L., Gao, R., Xu, Q., Yang, Z., Li, F., Li, B., et al. (2020). UO_2-Mo-Be Composites for Accident Tolerant Fuel: SPS Fabrication, Microcracks-free in As-Fabricated State and superior thermal Conductivity. *Ceramics Int.* 46, 28939–28948. doi:10.1016/j.ceramint.2020.08.064

Cheng, L., Yan, B., Gao, R., Liu, X., Yang, Z., Li, B., et al. (2019). Densification Behaviour of UO_2/Mo Core-Shell Composite Pellets with a Reduced Coefficient of thermal Expansion. *Ceram. Int.* 46, 4730–4736. doi:10.1016/j.ceramint.2019.10

Cox, D. S., Iglesias C, F. C., Atmrand, R. D., In Hunt, J. R., Mitchell, N. A., and O'Connor Proc, R. F.E. L (1986). "Oxidation of UO_2 in Air and Steam with Relevance to Fission Product Releases Keller," in Symposium Chemical Phenomena Associated with Radioactivity Releases During Severe Nuclear Plant Accidents. Anaheim, CA: NUREG/CP-0078, 35–49.

Dumitrescu, I. M., Mihalache, M., Abrudeanu, M., Dumitru, O., and Dinu, A. (2015). Isothermal Oxidation of UO_2 Fuel Pellets in Steam. *Rev. Chim. (Bucharest)* 66, 290–293.

Finkeldei, S. C., Kiggans, J. O., Hunt, R. D., Nelson, A. T., and Terrani, K. A. (2019). Fabrication of UO_2-Mo Composite Fuel with Enhanced thermal Conductivity from Sol-Gel Feedstock. *J. Nucl. Mater.* 520, 56–64. doi:10.1016/j.jnucmat.2019.04.011

Garzarolli, R. H., and Stehle, V. Y. (1979). The Main Causes of Fuel Element Failure in Water-Cooled Power Reactors. *At. Energ. Rev.* 17, 31–128.

Hagrman, D. L., and Reymann, G. A. (1979). *MATPRO, A Handbook of Materials Properties for Use in the Analysis of Light Water Reactor Fuel Rod Behavior*. Idaho Falls: NUREG/CR-0497. doi:10.2172/6442256

Hashizume, K., Wang, W.-E., and Olander, D. R. (1999). Volatilization of Urania in Steam at Elevated Temperatures. *J. Nucl. Mater.* 275, 277–286. doi:10.1016/S0022-3115(99)00123-3

Higgs, J. D., Lewis, B. J., Thompson, W. T., and He, Z. (2007). A Conceptual Model for the Fuel Oxidation of Defective Fuel. *J. Nucl. Mater.* 366, 99–128. doi:10.1016/j.jnucmat.2006.12.050

HSC Chemistry 9 (2018). Outotec. URLAvailable at: http://www.outotec.com/hsc.

IAEA Nuclear Energy Series (2010). *Review of Fuel Failures in Water Cooled Reactor*. Vienna: IAEA Nuclear Energy Series No. NF-T-2.1.

Jo, Y., Jeong, E., Cherezov, A., and Lee, D. (2020). *Preliminary Neutronic Analysis Results of Accident Tolerant Fuel Loaded OPR-1000 with Stream/RAST-K 2.0 Code*. Transactions of the Virtual meeting, KNS.

Jung, T.-S., Soo, N., Min-, J. J., Na, Y.-S., Joo, M.-J., Lim, K.-Y., et al. (2020). Thermodynamic and Experimental Analyses of the Oxidation Behavior of UO2 Pellets in Damaged Fuel Rods of Pressurized Water Reactors. *Nucl. Eng. Techn.* 52, 2880–2886. doi:10.1016/j.net.2020.05.007

Kim, D. S., Kim, K. S., Kim, J. J., Kim, D.-J., Yang, Oh, J.-S., Koo, Y.-H., et al. (2017). *Aligning Mo Metal Strips in UO_2 Fuel Pellets for Enhancing Radial Thermal Conductivity*. Jeju, Korea: Water Reactor Fuel Performance Meeting at Korean Nuclear Society (KNS).

Kim, D. S., Kim, D.-J., Yang, J. H., Yoon, J. H., Lee, H.-S., and Kim, H.-G. (2020). *Development of Mo Microplate Aligned UO_2 Pellets for Accident Tolerant Fuel*. Transactions of the Korean Nuclear Society Virtual Autumn Meeting.

Kim, D.-J., Kim, K. S., Kim, D. S., Oh, J. S., Kim, J. H., Yang, J. H., et al. (2018). Development Status of Microcell UO2 Pellet for Accident-Tolerant Fuel. *Nucl. Eng. Techn.* 50, 253–258. doi:10.1016/j.net.2017.12.008

Kim, Y. S. (2000). A Thermodynamic Evaluation of the U-O System from UO_2 to U_3O_8. *J. Nucl. Mater.* 279, 173–180. doi:10.1016/s0022-3115(00)00019-2

Kim, Y. S. (2003). *PWR Fuel Failure Analysis Due to Hydriding Based on PIE Data in Fuel Failure in Water Reactor; Cause and Mitigation*. Vienna, Austria: IAEA-TECDOC-1245.

Kuhlman, W. C. (1948). *Treatment of Uranium Dioxide with Water Vapor at High Temperature*. Oak Ridge: Mallinckrodt Chemical Works. MCW-103. doi:10.2172/4309589

Lee, H. S., Kim, D. J., Yang, J. H., and Kim, D. R. (2019). Numerical and Experimental Investigation on thermal Expansion of UO2-5vol% Mo Microcell Pellet for Qualitative Comparison to UO2 Pellet. *J. Nucl. Mater.* 518, 342–349. doi:10.1016/j.jnucmat.2019.03.003

Lee, Y.-J., Lee, T., and Soon, A. (2019). Phase Stability Diagrams of Group 6 Magnéli Oxides and Their Implications for Photon-Assisted Applications. *Chem. Mater.* 31, 4282–4290. doi:10.1021/acs.chemmater.9b01430

Lewis, B. J., Iglesias, F. C., Cox, D. S., and Gheorghiu, E. (1990). A Model for Fission Gas Release and Fuel Oxidation Behavior for Defected UO2Fuel Elements. *Nucl. Techn.* 92, 353–362. doi:10.13182/nt90-a16236

Li, W., and Shirvan, K. (2021). Multiphysics Phase-Field Modeling of Quasi-Static Cracking in Urania Ceramic Nuclear Fuel. *Ceramics Int.* 47, 793–810. doi:10.1016/j.ceramint.2020.08.191

Nelson, A. T., Sooby, E. S., Kim, Y.-J., Cheng, B., and Maloy, S. A. (2014). High Temperature Oxidation of Molybdenum in Water Vapor Environments. *J. Nucl. Mater.* 448, 441–447. doi:10.1016/j.jnucmat.2013.10.043

Oguma, M. (1983). Cracking and Relocation Behavior of Nuclear Fuel Pellets during Rise to Power. *Nucl. Eng. Des.* 76, 35–45. doi:10.1016/0029-5493(83)90045-6

Olander, D. R. (1986). Oxidation of UO2by High-Pressure Steam. *Nucl. Techn.* 74, 215–217. doi:10.13182/nt86-a33806

Perio, P. (1955). *Contribution to the Crystallography of the Uranium–Oxygen System*. Paris: Doctoral Dissertation, University of Paris. CEA-363.

Sarrasin, L., Gaillard, C., Panetier, C., Pipon, Y., Moncoffre, N., Mangin, D., et al. (2019). Effect of the Oxygen Potential on the Mo Migration and Speciation in UO2 and UO2+x. *Inorg. Chem.* 58, 4761–4773. doi:10.1021/acs.inorgchem.8b03076

Lee, H. S., Kim, D.-J., Kim, D. S., and Kim, D. R. (2020). Evaluation of Thermomechanical Behaviors of UO_2–5 Vol% Mo Nuclear Fuel Pellets with Sandwiched Configuration. *J. Nucl. Mater.* 539. , 2020 Available at: http://www.ncbi.nlm.nih.gov/pubmed/152295. doi:10.1016/j.jnucmat.2020.152295

Spino, J., and Peerani, P. (2008). Oxygen Stoichiometry Shift of Irradiated LWR-Fuels at High Burn-Ups: Review of Data and Alternative Interpretation of Recently Published Results. *J. Nucl. Mater.* 375, 8–25. doi:10.1016/j.jnucmat.2007.10.007

Teske, K., Ullmann, H., and Rettig, D. (1983). Investigation of the Oxygen Activity of Oxide Fuels and Fuel-Fission Product Systems by Solid Electrolyte Techniques. Part I: Qualification and Limitations of the Method. *J. Nucl. Mater.* 116, 260–266. doi:10.1016/0022-3115(83)90110-1

Touzelin, B., and Dode, M. (1969). *Rev. Int. Hautes. Temper. Refract.* 6, 267.

Une, K., Imamura, M., Amaya, M., Korei, Y., and Yagnik, S. K. (1995). Fuel Oxidation and Irradiation Behaviors of Defective BWR Fuel Rods. *J. Nucl. Mater.* 223, 40–50. doi:10.1016/0022-3115(94)00693-8

Verrall, R. A., He, Z., and Mouris, J. F. (2005). Characterization of Fuel Oxidation in Rods with Clad-Holes. *J. Nucl. Mater.* 344, 240–245. doi:10.1016/j.jnucmat.2005.04.049

Rachev, V. V., Kobva, L. M., Ippolitova, E. A., and Khim, Z. N.(1965). 10, 573.

Yakub, E., Ronchi, C., and Staicu, D. (2009). Computer Simulation of Defects Formation and Equilibrium in Non-stoichiometric Uranium Dioxide. *J. Nucl. Mater.* 389, 119–126. doi:10.1016/j.jnucmat.2009.01.029

Zhang, C., Gao, M. C., Yang, Y., and Zhang, F. (2014). Thermodynamic Modeling and First-Principles Calculations of the Mo-O System. *Calphad* 45, 178–187. doi:10.1016/j.calphad.2013.12.006

Conflict of Interest: The authors declare that the research was conducted in the absence of any commercial or financial relationships that could be construed as a potential conflict of interest.

frontiers in Energy Research

ORIGINAL RESEARCH
published: 21 September 2021
doi: 10.3389/fenrg.2021.663533

Numerical Investigation of Conjugated Heat Transfer of the Plate-Type Fuel Assembly in the Research Reactor

Quan Li, Qiang Ma, Yuanming Li, Ping Chen*, Chao Ma, Bo Zhao and Hao Chen*

Science and Technology on Reactor System Design Technology Laboratory, Nuclear Power Institute of China, Chengdu, China

In nuclear reactors, the research of conjugated heat transfer between the fuel and coolant in the fuel assembly is fundamental for improving the safety, reliability and economy. The numerical approach based on Computational Fluid Dynamics (CFD) can be used to realize the rapid analysis of the conjugated heat transfer. Besides, the numerical simulation can provide detailed physical fields that are useful for the designing and optimizing of the fuel assembly. The plate-type fuels are generally used to enhance heat transfer in research reactors with high power density. In this study, a standard plate-type fuel assembly in the research reactor was taken into consideration. The solid-fluid conjugated heat transfer of the fuel assembly and coolant was numerically investigated. In the fluid region, the subcooled flow boiling simulation model was established by implementing the Rensselaer Polytechnic Institute model into the Euler multi-phase flow method. The results show that the conjugated heat transfer of the fuel assembly and coolant can be simulated using the model established in this work. The influence of fluid velocity, power density and the width of the flow channel on the temperature distribution and the conjugated heat transfer was investigated and discussed.

Keywords: conjugated heat transfer, numerical simulation, plate-type fuel assembly, subcooled flow boiling, multi-phase flow

OPEN ACCESS

Edited by:
Yingwei Wu,
Xi'an Jiaotong University, China

Reviewed by:
Boštjan Končar,
Institut Jožef Stefan (IJS), Slovenia
Marco Colombo,
University of Leeds, United Kingdom
Deqi Chen,
Chongqing University, China

****Correspondence:***
Yuanming Li
lym_npic@126.com
Ping Chen
chenping_npic@163.com

Specialty section:
This article was submitted to Nuclear Energy, a section of the journal Frontiers in Energy Research

Received: *03 February 2021*
Accepted: *23 August 2021*
Published: *21 September 2021*

Citation:
Li Q, Ma Q, Li Y, Chen P, Ma C, Zhao B and Chen H (2021) Numerical Investigation of Conjugated Heat Transfer of the Plate-Type Fuel Assembly in the Research Reactor. Front. Energy Res. 9:663533. doi: 10.3389/fenrg.2021.663533

INTRODUCTION

Research reactors are widely used to produce high neutron flux for research, training, education, and irradiation test (Gong et al., 2015; Guo et al., 2018). The fuel assembly used in the research reactors is generally the plate-type fuel assembly, including several fuel plates, two side plates and narrow rectangular channels formed between the fuel plates. The research of heat transfer of the fuel assembly is fundamental for improving the safety, reliability and economy. However, the coolant flow and heat transfer characteristics in the narrow rectangular channels are significantly different from those of conventional channels and tubes (Sun et al., 2020). Therefore, investigation of coolant flow and heat transfer characteristics in the plate-type fuel assembly is important for research reactors designing.

In the last few years, 1-dimensional codes, 1.5-dimensional codes and 2-dimensional codes, such as the RELAP5/MOD3 (Lu et al., 2009; Son et al., 2015), FRAPCON (Phillippe et al., 2012), FEMAX (Yoo et al., 2006) and FROBA (Deng et al., 2016) were used for the thermo-mechanical coupling analysis and safety analyses of the fuels. In order to improve the accuracy of the calculation, 3-dimensional simulations based on MOOSE (He et al., 2018) and COMSOL (Liu and Zhou, 2017) were used. However, the fluid was considered as 1-dimensional flow in the calculations and the detailed flow and heat transfer characteristics cannot be obtained.

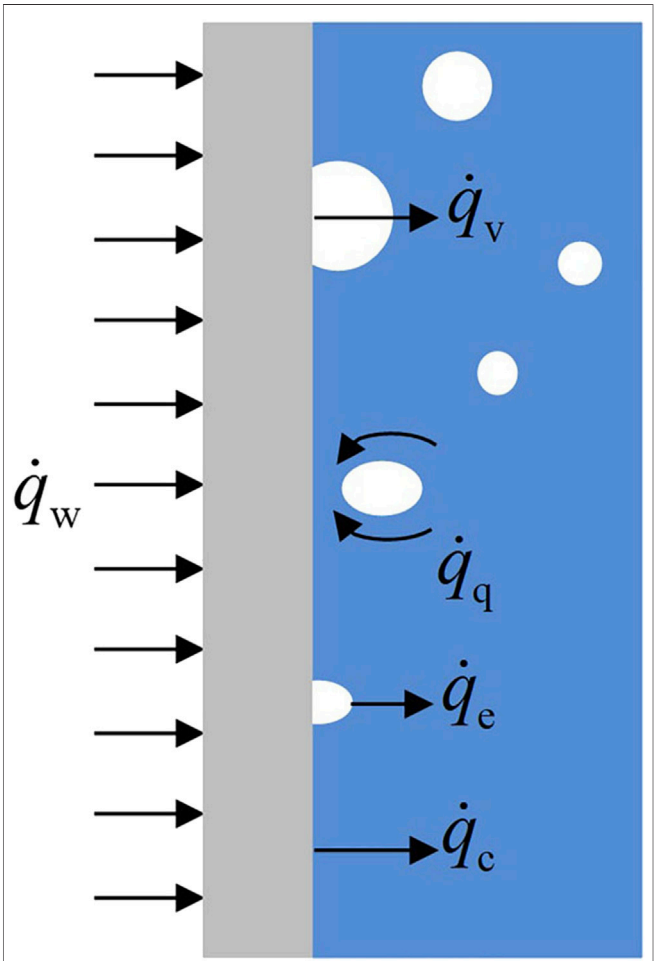

FIGURE 1 | Schematic of wall boiling heat flux partitioning.

The numerical investigation based on Computational Fluid Dynamics (CFD) can provide 3-dimensional detailed physical fields that are useful for the designing and optimizing of the fuel assembly. Recently, with the help of CFD, some researchers investigated the thermal-hydraulic characteristics of the fuel assembly. Li et al. (2020) numerically investigated the flow fields and phase distributions in the subchannel of a pressurized water reactor fuel assembly based on the CFD model of subcooled flow boiling. Kumar et al. (2018) and Zhang and Liu (2020) carried out CFD simulations to predict the void and temperature distribution inside the rod bundle. The influence of the spacer grid on the flow and heat transfer characteristics of subcooled flow boiling was studied by Zhang and Liu (2020). Shirvan (2016) numerically investigated the boiling crisis for helical cruciform-shaped rods using commercial software Star CCM+.

As for the plate-type fuel assembly, some researchers focused on the single-phase flow in the channels (Gong et al., 2015; González Mantecón and Mattar Neto, 2018; Liao et al., 2020). Gong et al. (2015) investigated the heat transfer characteristics of the plate-type fuel assembly. The single-phase turbulence flow was calculated using the commercial software FLUENT. The temperature distribution of the fuel assembly was obtained with different coolant inlet velocity and the assembly with a hot spot was specially studied. Liao et al. (2020) conducted the fluid-solid coupling simulation with the consideration of irradiation effects for plate-type fuel assembly. The thermo-hydraulic model in the fluid domain was established based on FLUENT. González Mantecón and Mattar Neto (2018) numerically investigated fluid-structure interaction of the plate-type fuel assemblies using the commercial software ANSYS CFX for modeling fluid flow and ANSYS Mechanical for modeling the plates. The maximum deflection of the plates was detected at the leading edge. An extra deflection peak was observed near the trailing edge of the plates for fluid velocities greater than the Miller's velocity.

The research of subcooled flow boiling heat transfer in the fuel assembly is fundamental for improving the safety, reliability and economy. However, fewer thermal-hydraulic investigations of the plate-type fuel assembly have taken the subcooled flow boiling into consideration. Guo et al. (2018) conducted the thermal-hydraulic analysis of flow blockage in the fuel assembly in the JRR-3M research reactor. The 3-dimensional model of the fuel assembly was built and the flow and heat transfer characteristics were simulated using FLUENT. Guo et al. (2018) found when the blockage ratio of the fuel assembly is 70%, the departure from nucleate boiling will occur. Park et al. (2021) investigated the thermal-hydraulic behaviors of flow channels of the plate-type fuel assembly by the CFD simulation with a multi-phase flow model. The wall boiling model proposed by Kurul and Podowski (1991) was used and the influence of the flow channel blockage on the flow instability and heat transfer was studied.

In this work, a standard plate-type fuel assembly in a research reactor was taken into consideration. The solid-fluid conjugated heat transfer of the fuel assembly and the coolant was numerically investigated. In the simulation, the Euler multi-phase flow method was used with the Rensselaer Polytechnic Institute (RPI) wall boiling model implemented. The temperature distribution and the flow field of the fuel assembly were obtained. The influence of power density, fluid inlet velocity and subchannel width on the conjugated heat transfer was investigated.

MATHEMATIC MODEL AND NUMERICAL METHOD

The simulation of conjugated heat transfer considering the phase change process is complicated. In this work, the conjugated heat transfer model was established. The simulation domain was divided into the solid region and the fluid region. The heat transfer of each region was calculated using different models and the heat transfer between the two regions was calculated.

Solid Region

In the solid region, heat is transferred by conduction. Since the thermal conductivity of the solid was assumed as constant, the heat transfer of the solid region was calculated by

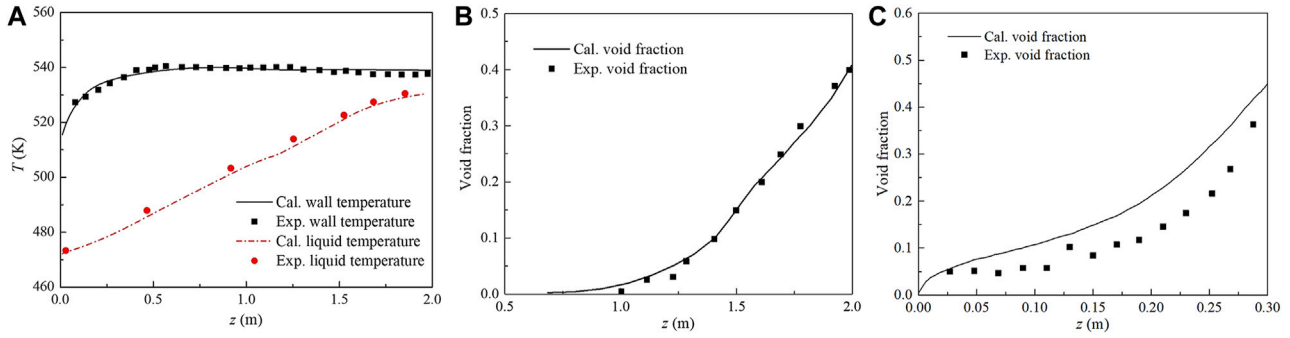

FIGURE 2 | Model validation of axial distribution of **(A)** wall temperature, coolant temperture and **(B)** void fraction in tube and **(C)** void fraction in annulus channel.

$$\rho_s c_s \frac{\partial T}{\partial t} = k_s \nabla^2 T + \dot{q}_s \tag{1}$$

where ρ_s is the density of the solid, c_s is the specific heat of the solid, T is the temperature, t is time, k_s is thermal conductivity of the solid, $\dot{q}_s$ is the volume heat source.

Fluid Region

In the fluid region, the subcooled flow boiling was numerically simulated based on the Euler multi-phase flow method with liquid water being the primary phase and water vapor being the second phase. The volume fraction was used to represent the content of each phase and only two phases were set in the fluid region.

$$\alpha_l + \alpha_v = 1 \tag{2}$$

where α_l is the liquid phase volume fraction, α_v is the vapor phase volume fraction i.e., the void fraction.

The governing equations included the mass conservation equations, the momentum conservation equations and the energy conservation equations for each phase. In order to simplified the description of the governing equations, the subscripts p and q were used denote the two phases.

TABLE 1 | Parameters of the research reactor fuel assembly.

Parameter	Value	Unit
Number of fuel plate	20	—
Length of fuel plate	770	mm
Width of fuel plate	66.6	mm
Thickness of fuel plate	1.52	mm
Length of fuel	750	mm
Width of fuel	61.6	mm
Thickness of fuel	0.76	mm
Thickness of cladding	0.38	mm
Coolant	Light water	—
Width of coolant channel	2.28	mm
Fuel	U_3Si_2-Al	—
Fuel density	6,030	kg/m^3
Fuel thermal conductivity	50.03	W/(m K)
Fuel specific heat	338.4	J/(kg K)
Cladding	Al (6,061)	—
Cladding density	2,700	kg/m^3
Cladding thermal conductivity	176.01	W/(m K)
Cladding specific heat	998.56	J/(kg K)
Coolant inlet temperature	35	°C
Core inlet pressure	152	kPa

1) Mass conservation equations

The mass conservation equation for phase q in the Euler multi-phase flow method was

$$\frac{\partial}{\partial t}\left(\alpha_q \rho_q\right) + \nabla \cdot \left(\alpha_q \rho_q \mathbf{u}_q\right) = \dot{m}_{pq} - \dot{m}_{qp} \tag{3}$$

where ρ_q and $\mathbf{u}_q$ are the density and the velocity of phase q respectively, $\dot{m}_{pq}$ and $\dot{m}_{qp}$ are the mass transfer from phase p to phase q and the mass transfer from phase q to phase p.

2) Momentum conservation equations

The momentum conservation equation for phase q in the Euler multi-phase flow method was

$$\frac{\partial}{\partial t}\left(\alpha_q \rho_q \mathbf{u}_q\right) + \nabla \cdot \left(\alpha_q \rho_q \mathbf{u}_q \mathbf{u}_q\right) = -\alpha_q \nabla p + \alpha_q \rho_q \mathbf{g} + \nabla \cdot \bar{\bar{\tau}}_q + \left(\dot{m}_{pq}\mathbf{u}_p - \dot{m}_{qp}\mathbf{u}_q\right) + \mathbf{M}_q \tag{4}$$

where $\bar{\bar{\tau}}_q$ is the stress-strain tensor for phase q

$$\bar{\bar{\tau}}_q = \alpha_q \mu_q \left(\nabla \mathbf{u}_q + \nabla \mathbf{u}_q^T\right) + \alpha_q \left(\lambda_q - \frac{2}{3}\mu_q\right) \nabla \cdot \mathbf{u}_q \bar{\bar{I}} \tag{5}$$

where μ_q and λ_q are the shear and bulk viscosity of phase q, p is pressure, $\mathbf{g}$ is gravity, $\dot{m}_{pq}\mathbf{u}_p - \dot{m}_{qp}\mathbf{u}_q$ is the momentum transfer caused by phase change mass transfer and $\mathbf{M}_q$ is the momentum transfer due to the interfacial forces.

The standard k-ε turbulence model was chosen to calculate the effect of turbulent flow and the two-layer model with all y+ wall function was employed. Generally, the interfacial momentum transfer between liquid and vapor should be the sum of the drag force, turbulent dispersion force, lift force, wall lubrication force and virtual mass force.

The sensitivity analysis of the forces on the simulation result of subcooled flow boiling was conducted. The simulation object and

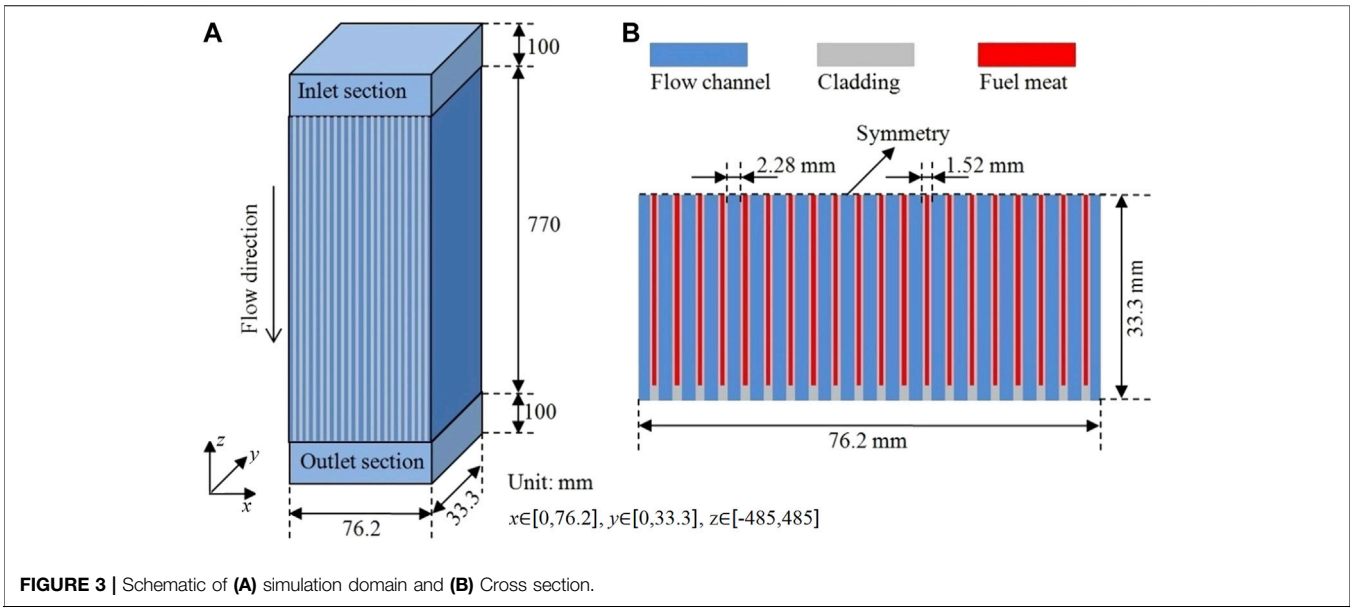

FIGURE 3 | Schematic of **(A)** simulation domain and **(B)** Cross section.

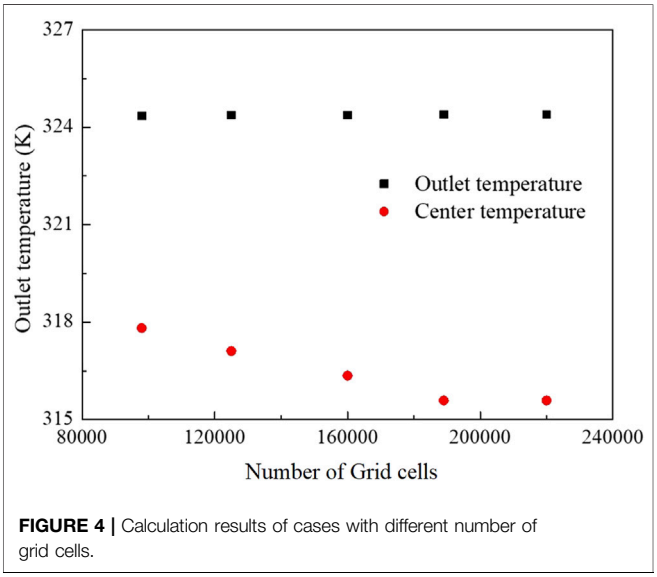

FIGURE 4 | Calculation results of cases with different number of grid cells.

conditions were the same as those in the experiment conducted by Zeitoun and Shoukri (1996). The channel geometry was an annulus with a 306 mm length. The outer wall diameter was 25.4 mm and the heated inner wall diameter was 12.7 mm. The heat flux of the inner wall of the channel was 508 kW/m^2, the mass flux of the coolant was 264.3 kg/(m^2 s), the coolant inlet temperature was 94.6°C and the system pressure was 150 kPa. The result shows that the influence of the lift force, wall lubrication force and virtual mass force on the calculated wall temperature was less than 1 K. Similar to the results of the sensitivity analysis we finished in our previous work (Li et al., 2018), the effects of the three forces are to move the vapor bubbles radially away from or towards the heated surface. While the forces have little influence on the void fraction distribution along the coolant flow direction.

Since the lift force, wall lubrication force and virtual mass force have little effect on the simulation results and the inclusion of the three forces takes more time to obtain convergence, only the drag force and turbulent dispersion force were taken into consideration in this work.

$$\mathbf{M}_q = \mathbf{F}_{D,q} + \mathbf{F}_{TD,q} \tag{6}$$

where $\mathbf{F}_{D,k}$ is the drag force and $\mathbf{F}_{TD,k}$ is the turbulent dispersion force.The drag force can by calculated using

$$\mathbf{F}_D = \frac{3}{4}\frac{\alpha_v \rho_l}{d_B} C_D |\mathbf{u}_r| \mathbf{u}_r \tag{7}$$

where $\mathbf{u}_r = \mathbf{u}_l - \mathbf{u}_v$ is the relative velocity between the two phases, d_B is the bubble diameter and C_D is the drag force coefficient. In this work, the bubble diameter was calculated using the Anglart's method (Anglart and Nylund, 1996) and the drag force coefficient was calculated using the Tomiyama's method (Tomiyama, 2004).

The turbulent dispersion force plays an important role in taking the vapor bubbles from the near wall region to the bulk liquid region. The turbulent dispersion force was calculated using the method proposed by Lopez de Bertodano (1991).

$$\mathbf{F}_{TD} = C_{TD} \rho_l k_l \nabla \alpha_v \tag{8}$$

where C_{TD} is the turbulent dispersion coefficient and k_l is the turbulent kinetic energy of the liquid phase.

3) Energy conservation equations

The energy conservation equation for phase q in the Euler multi-phase flow method was

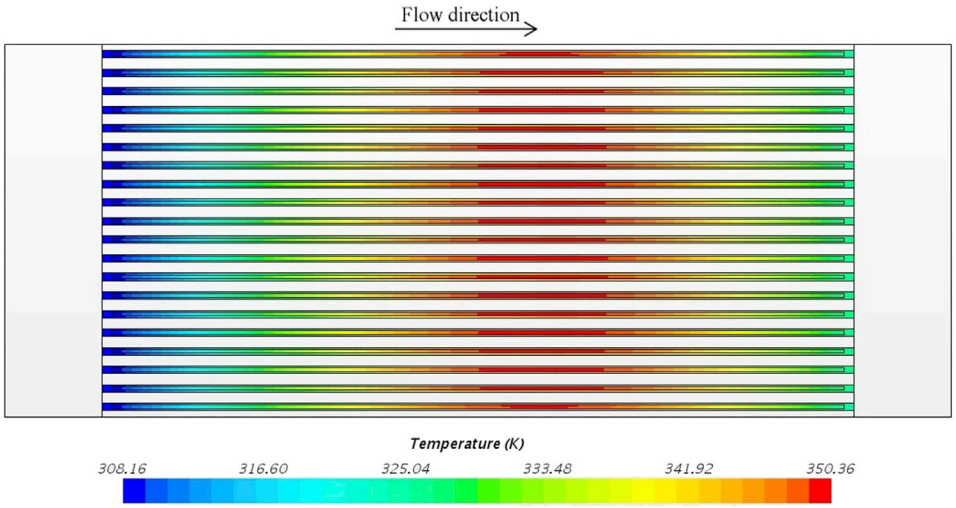

FIGURE 5 | Temperature distribution of the fuel plates (scale: *x*:*z* = 1:5).

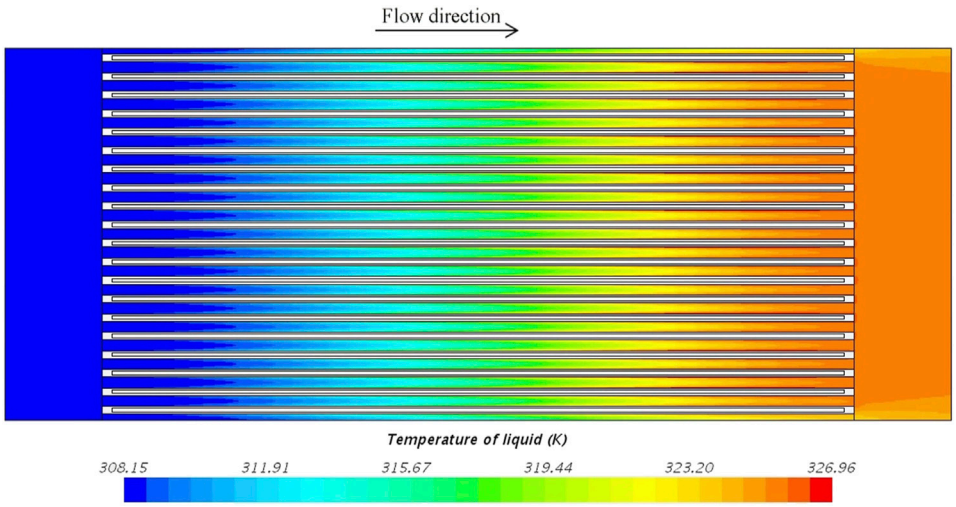

FIGURE 6 | Temperature distribution of the coolant (scale: *x*:*z* = 1:5).

$$\frac{\partial}{\partial t}\left(\alpha_q \rho_q h_q\right) + \nabla \cdot \left(\alpha_q \rho_q \mathbf{u}_q h_q\right) = \alpha_q \frac{\partial p}{\partial t} + \bar{\bar{\tau}}_q : \nabla \mathbf{u}_q - \nabla \mathbf{q}_q + \dot{m}_{pq} h_{pq} - \dot{m}_{qp} h_{qp} \tag{9}$$

where h_q is the specific enthalpy of phase q, $\mathbf{q}_q$ is the heat flux, h_{qp} and h_{pq} are the interphase enthalpy.

Solid-Fluid Boundary

At the solid-fluid boundary, heat transferred from the solid region to the fluid region.

$$\dot{q}_w|_{fluid} = -\dot{q}_w|_{solid} = \dot{q}_w \tag{10}$$

where $\dot{q}_w|_{fluid}$ is the heat flux of the fluid region and $\dot{q}_w|_{solid}$ is the heat flux of the solid region at the solid-fluid boundary.

Wall Boiling Model

Figure 1 shows the schematic of wall boiling heat flux partitioning. The Rensselaer Polytechnic Institute (RPI) wall boiling model (Kurul and Podowski, 1991) divided the total heat flux from the hot wall to the fluid region $\dot{q}_w$to the liquid convection heat flux $\dot{q}_c$, the quenching heat flux $\dot{q}_q$and the evaporation heat flux $\dot{q}_e$. Lavieville et al. (2005) modified the RPI model by considering the heat flux directly from the hot wall to the vapor $\dot{q}_v$. Thus, the total heat flux can be calculated by

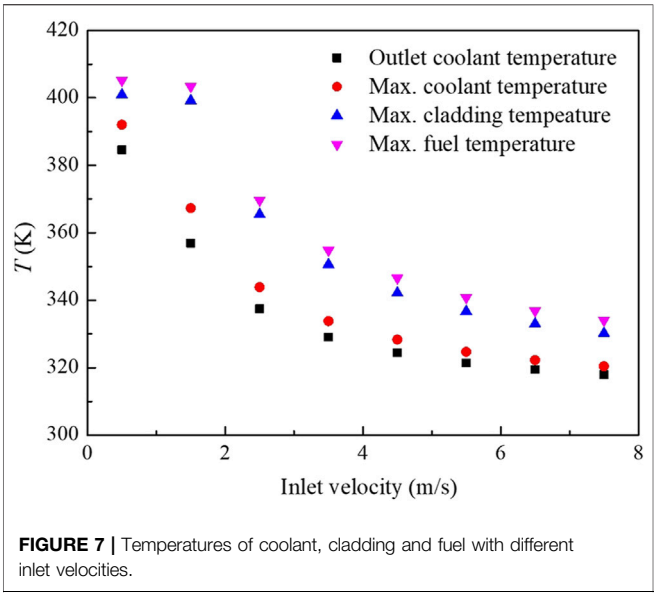

FIGURE 7 | Temperatures of coolant, cladding and fuel with different inlet velocities.

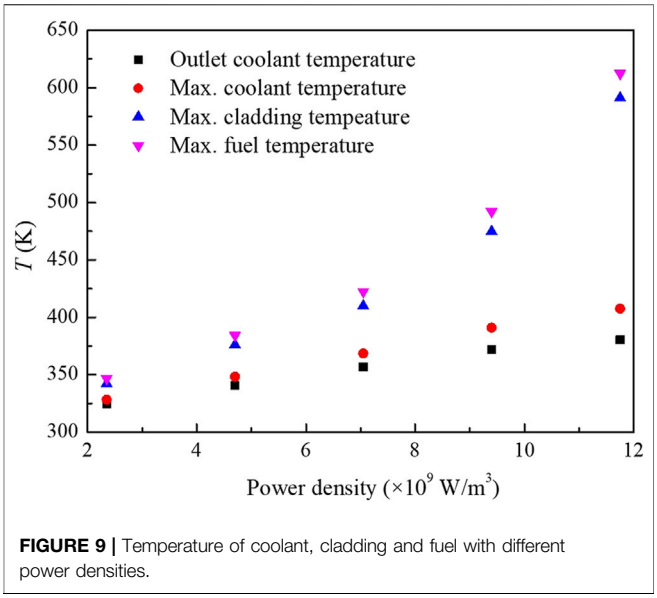

FIGURE 9 | Temperature of coolant, cladding and fuel with different power densities.

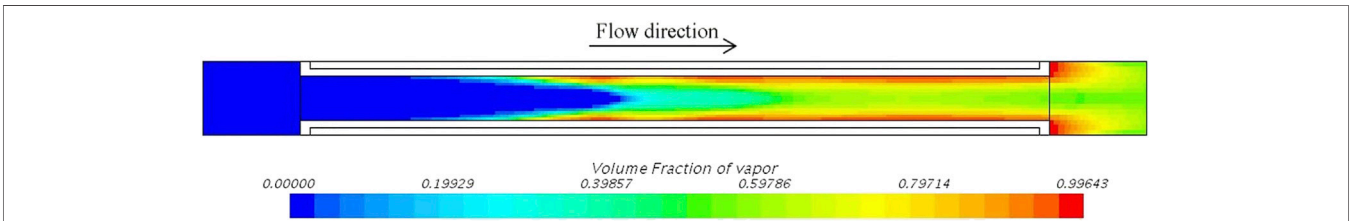

FIGURE 8 | Void fraction distribution with 0.5 m/s inlet velocity (scale: *x*:*z* = 1:20).

$$\dot{q}_w = \left(\dot{q}_c + \dot{q}_q + \dot{q}_e\right)\left(1 - K_{dry}\right) + K_{dry}\dot{q}_v \tag{11}$$

where K_{dry} is the wall contact area fraction for vapor. K_{dry}can be calculated by

$$K_{dry} = \begin{cases} 0, & \alpha_\delta < \alpha_{dry} \\ \beta^2(3-2\beta), & \alpha_\delta \geq \alpha_{dry} \end{cases} \tag{12}$$

$$\beta = \frac{\alpha_\delta - \alpha_{dry}}{1 - \alpha_{dry}} \tag{13}$$

where α_δ is the average void fraction in the mesh near the hot wall, α_{dry} is the critical void fraction.The four parts heat flux can be calculated by

$$\dot{q}_c = \frac{\rho_l c_{pl} u_l^+}{T_l^+}\left(T_w - T_l\right) \tag{14}$$

$$\dot{q}_q = 2K_{quench} f_d \sqrt{\frac{\rho_l c_{pl} k_l t_w}{\pi}}\left(T_w - T_{l,quench}\right) \tag{15}$$

$$\dot{q}_e = \frac{\pi}{6} D_d^3 f_d N_w \rho_v h_{lv} \tag{16}$$

$$\dot{q}_v = \frac{\rho_v c_{pv} u_v^+}{T_v^+}\left(T_w - T_v\right) \tag{17}$$

where u_l^+ and u_v^+ are the frictional velocities of liquid and vapor near the hot wall, T_l^+ and T_v^+ are the non-dimensional parameters for liquid and vapor, K_{quench} is the bubble influence wall area fraction and was calculated using the model proposed by Kurul and Podowski (1991), t_w is the bubble waiting time, D_d and f_d are the bubble departure diameter and bubble departure frequency, N_w is the active nucleation site density.

In this work, the widely used active nucleation site density model proposed by Lemmert and Chawla (1977), the bubble departure diameter model proposed by Tolubinsky and Kostanchuk (1970) and the bubble departure frequency model proposed by Cole (1960) were used. In Tolubinsky's model, D_0 was 0.6 mm.

$$N_w = C^n\left(T_w - T_{sat}\right)^n, C = 210, n = 1.805 \tag{18}$$

$$D_d = D_0 e^{\frac{-\Delta T_w}{45}} \tag{19}$$

$$f_d = \sqrt{\frac{4g\Delta\rho}{3D_d\rho_l}} \tag{20}$$

Model Validation

Due to the lack of experimental results of subcooled flow boiling in the plate-type fuel assembly, the conjugated heat transfer model was validated using the experimental results of subcooled flow boiling in a tube conducted by Bartolemei and Chanturiya (1967) and the experimental results of subcooled flow boiling in an annulus channel conducted by Zeitoun and Shoukri (1996). In Bartolemei's

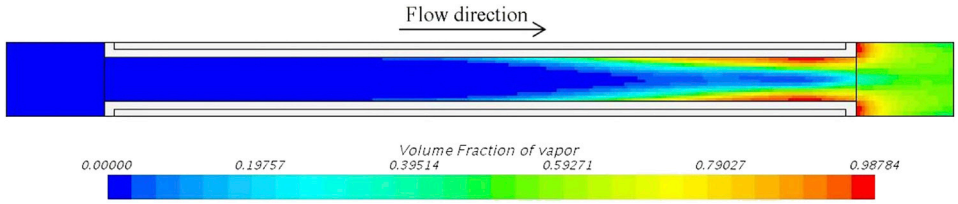

FIGURE 10 | Void fraction distribution with 11.75 × 10^9 W/m^3 power density (scale: *x*:*z* = 1:20).

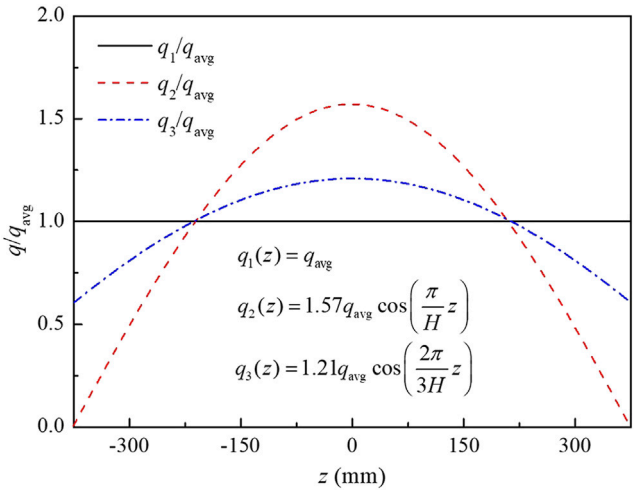

FIGURE 11 | Power density distribution along the height direction.

work, the tube diameter was 15.4 mm, the heat flux of the tube wall was 0.57 MW/m^2, the mass flux of the coolant was 900 kg/(m^2 s), the subcooled temperature of the coolant was 60 K and the system pressure was 4.5 MPa. The coolant temperature, wall temperature and void fraction were measured by Bartolemei and Chanturiya (1967). Since the system pressure in Bartolemei's work was larger than that in our simulation for plate-type fuel assembly, the experimental results at lower system pressure obtained by Zeitoun and Shoukri (1996) were also used to validate the model. **Figures 2A,B** show the comparison of the numerical results of the coolant temperature, wall temperature and void fraction along the coolant flow direction with the experimental results obtained by Bartolemei and Chanturiya (1967). **Figure 2C** shows the comparison of the numerical results of void fraction along the coolant flow direction with the experimental results obtained by Zeitoun and Shoukri (1996). It can be seen that the calculated results agree well with the measured data and the calculated void fraction is slightly larger than the measured data at lower system pressure.

PHYSICAL MODEL

In this work, a standard plate-type fuel assembly of the research reactor was chosen as the simulation object. The structure, material and thermal-hydraulic parameters of the fuel assembly were the same as those used in Gong's work (Gong et al., 2015). **Table 1** shows the structure, material and thermal-hydraulic parameters of the standard plate-type fuel assembly.

A three-dimensional model of the standard plate-type fuel assembly was built on the Star CCM+ platform. **Figure 3** shows the simulation domain of the conjugated heat transfer of the plate-type fuel assembly. The simulation domain included the inlet section, the test section and the outlet section. In the test section, there were 20 fuel plates with 1.52 mm thickness and 19 subchannels with 2.28 mm width and two by-pass subchannels with 1.24 mm width. The fuel, cladding and coolant parts were considered in the simulation domain. As shown in **Figure 3B**, half of the fuel assembly was included in the simulation domain due to the symmetry of the geometry and the fluid field.

The hexahedral mesh was used for the physical model. In the mesh independence analysis, a single calculation unit of the assembly was used. A flow channel with two half of the fuel plates was included in the unit. The power distribution of the fuel was assumed to be uniform with 2.35 × 10^9 W/m^3. The coolant inlet temperature, inlet velocity and the system pressure were 35°C, 4.5 m/s and 152 kPa, respectively. **Figure 4** shows the calculation results of coolant outlet temperature and the coolant temperature at the center of the calculation region with different number of grid cells. The calculation results of the coolant outlet temperature change a little with the number of grid cells due to the energy conservation. The coolant temperature at the center of the calculation region changes a little when the number of grid cells exceeds 180,000. Thus, the mesh with a 189,000 grid cells was used in this work and the same meshing method was used for the whole fuel assembly. The cell size was chosen as $\Delta x \approx 0.23$ mm, $\Delta y \approx 1.1$ mm, $\Delta z \approx 2$ mm in the fluid domain and $\Delta x \approx 0.19$ mm, $\Delta y \approx 2.4$ mm, $\Delta z \approx 3$ mm in the solid domain.

RESULTS AND DISCUSSION

Conjugated Heat Transfer of the Assembly

The conjugated heat transfer of the plate-type fuel assembly was carried out. The power distribution of each plate along height direction was assumed to be a cosine distribution as

$$q(z) = q_{\max} \cdot \cos\left(\frac{\pi}{H} \cdot z\right) \tag{21}$$

where $q_{\max}$ is the maximum power density and was set as 3.654 × 10^9 W/m^3, H is the height of the fuel.

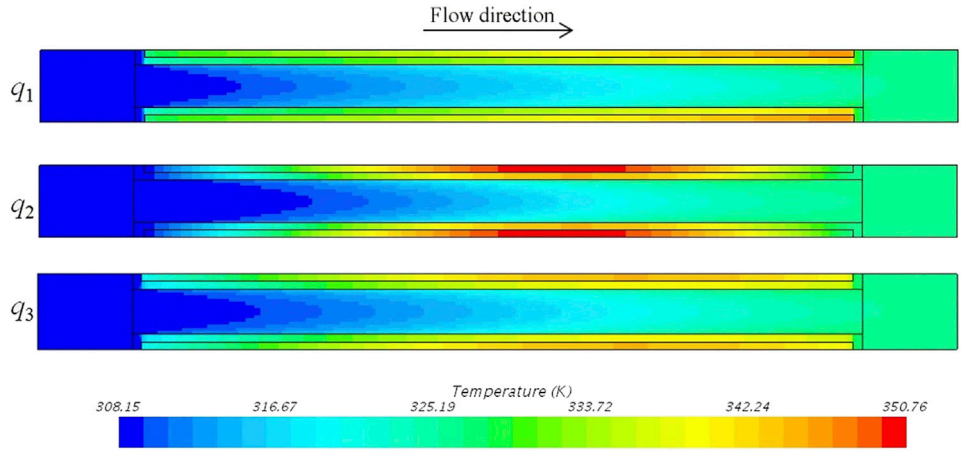

FIGURE 12 | Temperature distribution with different power density distributions (scale: *x*:*z* = 1:20).

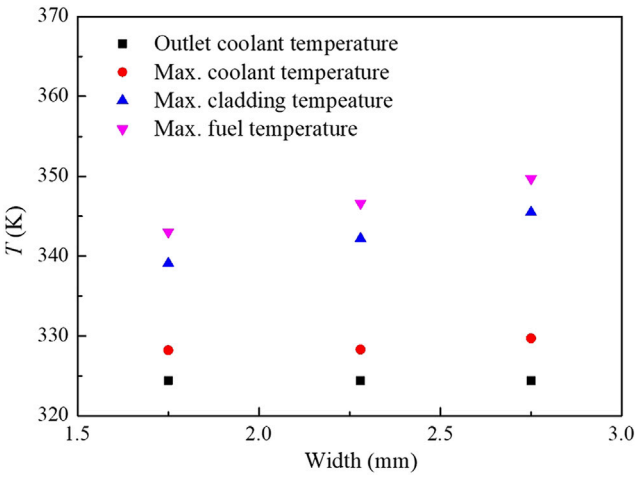

FIGURE 13 | Temperature of coolant, cladding and fuel with different channel widths.

Figure 5 shows the temperature distribution of the fuel plates and **Figure 6** shows the temperature distribution of the coolant. The maximum temperature appears near the center of the fuel plate due to the non-uniform power density distribution of the fuel. Since the power density is zero, the temperature near the ends of the fuel plate equals to the coolant temperature approximately.

Conjugated Heat Transfer of a Single Unit

In order to reduce the time consuming of the simulation, the conjugated heat transfer of a single unit was investigated in this section. The influence of power density, inlet velocity and channel width on the conjugated heat transfer was investigated.

Influence of Inlet Velocity

Figure 7 shows the coolant outlet temperature, maximum coolant temperature, maximum cladding temperature and maximum fuel temperature with different inlet velocities. The uniform power density of the fuel was 2.35×10^9 W/m^3 and the coolant inlet temperature was 35°C. As shown in **Figure 7**, the temperatures of the coolant, cladding and fuel decrease with the increase of the inlet velocity due to the increase of the coolant mass flux. Within the inlet velocity range of 1.5–7.5 m/s, the maximum coolant temperature was lower than the saturation temperature of the coolant. The fuel plate can keep safe since no local nucleate boiling occurs. The difference between the coolant temperature and the cladding temperature is the smallest with 7.5 m/s inlet velocity due to the enhancement of single phase convective heat transfer at the highest inlet velocity.

With 0.5 m/s inlet velocity, the maximum coolant temperature exceeds the saturation temperature of the coolant, which means the boiling phase change occurs in the flow channel. As shown in **Figure 7**, the difference between the coolant temperature and the cladding temperature is small with 0.5 m/s inlet velocity. This is because the nucleate boiling occurs and the heat transfer between the coolant and the cladding was enhanced by nucleate boiling. **Figure 8** shows the void fraction distribution in the flow channel with 0.5 m/s inlet velocity. As shown in **Figure 8**, vapor appears near the hot fuel plate. The vapor fraction increases along the flow direction due to the increase of the coolant temperature. The maximum void fraction appears at the leeward of the plate due to the small velocity.

Influence of Power Density

Figure 9 shows the coolant outlet temperature, maximum coolant temperature, maximum cladding temperature and maximum fuel temperature with the different uniform power density of the fuel. The inlet velocity was 4.5 m/s and the coolant inlet temperature was 35°C. The coolant temperature, the cladding temperature and the fuel temperature increase with the power density as shown in **Figure 9**. Since the maximum coolant temperature reaches above the saturation temperature with 9.40×10^9 and 11.75×10^9 W/m^3 power density, the boiling phase change occurs. As shown in **Figure 10**, due to the high power density, the void fraction near the fuel plate at the rear of the flow channel was very large, which

weaken the heat transfer and lead to higher maximum fuel temperature and higher maximum cladding temperature.

The influence of power density distribution on the conjugated heat transfer was numerically investigated. Three kinds of power density distributions along the height direction were used with the total power of the fuel plate maintained, as shown in **Figure 11**. **Figure 12** shows the simulation results of the temperature distribution of the calculation region with $q_{avg} = 2.35 \times 10^9$ W/m^3. As shown in **Figure 12**, the coolant outlet temperatures were equal for these three cases due to the conservation of energy. The maximum temperature of the cladding and the fuel is the largest for q_2 due to the concentrate distribution of the power density. The maximum cladding temperature and the maximum fuel temperature were lower for the uniform distribution of the power density. With the uniform power density distribution, the maximum temperature of the fuel plate appears at the rear due to the increase of the coolant temperature along the flow direction.

Influence of Channel Width

The conjugated heat transfer with different channel widths was simulated. In the simulations, the coolant inlet mass flux was maintained. **Figure 13** shows the coolant outlet temperature, maximum coolant temperature, maximum cladding temperature and maximum fuel temperature with different channel widths, 1.75, 2.28 and 2.75 mm. Since the coolant inlet mass flux was maintained, the inlet velocities were 5.23, 4.50, and 4.00 m/s for these three cases, respectively. As shown in **Figure 13**, the coolant outlet temperature does not change with the channel width due to the conservation of energy. The maximum cladding temperature and maximum fuel temperature increase with the channel width. This is because, with the channel width increase, the coolant velocity decreases and the convective heat transfer weakens.

CONCLUSION

The conjugated heat transfer model between the plate-type fuel assembly and the coolant was established in this paper. With the RPI wall boiling model added into the Euler multi-phase flow method, the heat transfer and boiling phase change process in the whole fuel assembly and a single unit of the assembly of the research reactor were simulated. In the model validation, the simulated wall temperature variation, coolant temperature variation and void fraction variation were in good agreement with the experimental results in the literature.

The influence of the coolant inlet velocity, power density and flow channel width on the conjugated heat transfer was numerically investigated. According to the simulation results, the coolant outlet temperature, maximum coolant temperature, maximum cladding temperature and maximum fuel temperature increase with the decrease of the inlet velocity and increase with the increase of the fuel power density. Three kinds of power density along the axial direction were considered in this work. The maximum cladding temperature and the maximum fuel temperature were lower for the uniform distribution of the power density. As for the investigation of the influence of channel width on the conjugated heat transfer, the coolant inlet mass flux was maintained. The maximum cladding temperature and maximum fuel temperature increase with the increase of channel width.

Among the simulation conditions in this work, the boiling phase change occurs with 0.5 m/s inlet velocity under 2.35×10^9 W/m^3 power density, 4.5 m/s inlet velocity under 9.4×10^9 W/m^3 power density and 4.5 m/s inlet velocity under 11.75×10^9 W/m^3 power density. The maximum void fraction appears at the leeward of the plate and the rear of the flow channel near the plate.

DATA AVAILABILITY STATEMENT

The raw data supporting the conclusions of this article will be made available by the authors, without undue reservation.

AUTHOR CONTRIBUTIONS

QL: Conceptualization, Methodology, Investigation, Resources, Writing – Review & Editing; QM: Conceptualization, Methodology, Data curation, Writing – Original Draft, Writing – Review & Editing; YL: Conceptualization, Supervision; PC: Conceptualization, Supervision; CM: Data curation, Resources; BZ: Methodology, Data curation; HC: Methodology, Writing – Review & Editing.

FUNDING

This work was supported by the Youth Program of National Natural Science Foundation of China (No. 11805195).

REFERENCES

Anglart, H., and Nylund, O. (1996). CFD Application to Prediction of Void Distribution in Two-phase Bubbly Flows in Rod Bundles. *Nucl. Eng. Des.* 163 (1-2), 81–98. doi:10.1016/0029-5493(95)01160-9

Bartolemei, G. G., and Chanturiya, V. M. (1967). Experimental Study of True Void Fraction when Boiling Subcooled Water in Vertical Tubes. *Therm. Eng.* 14 (2), 123–128.

Cole, R. (1960). A Photographic Study of Pool Boiling in the Region of the Critical Heat Flux. *Aiche J.* 6, 533–538. doi:10.1002/aic.690060405

Deng, Y., Wu, Y., Zhang, D., Tian, W., Qiu, S., and Su, G. H. (2016). Development of a thermal-mechanical Behavior Coupling Analysis Code for a Dual-Cooled Annular Fuel Element in PWRs. *Nucl. Eng. Des.* 301, 353–365. doi:10.1016/j.nucengdes.2016.03.021

Gong, D., Huang, S., Wang, G., and Wang, K. (2015). *Heat Transfer Calculation on Plate-type Fuel Assembly of High Flux Research Reactor*. Science and Technology of Nuclear Installations, 198654. doi:10.1155/2015/198654

González Mantecón, J., and Mattar Neto, M. (2018). Numerical Methodology for Fluid-Structure Interaction Analysis of Nuclear Fuel Plates under Axial

Flow Conditions. *Nucl. Eng. Des.* 333, 76–86. doi:10.1016/j.nucengdes.2018.04.009

Guo, Y., Wang, G., Qian, D., Yu, H., Hu, B., Guo, S., et al. (2018). Accident Safety Analysis of Flow Blockage in an Assembly in the JRR-3M Research Reactor Using System Code RELAP5 and CFD Code FLUENT. *Ann. Nucl. Energ.* 122, 125–136. doi:10.1016/j.anucene.2018.08.031

He, Y., Chen, P., Wu, Y., Su, G. H., Tian, W., and Qiu, S. (2018). Preliminary Evaluation of U 3 Si 2 -FeCrAl Fuel Performance in Light Water Reactors through a Multi-Physics Coupled Way. *Nucl. Eng. Des.* 328, 27–35. doi:10.1016/j.nucengdes.2017.12.019

Kumar, M., Moharana, A., Nayak, A. K., and Joshi, J. B. (2018). CFD Simulation of Boiling Flows inside Fuel Rod Bundle of a Natural Circulation BWR during SBO. *Nucl. Eng. Des.* 338, 300–329. doi:10.1016/j.nucengdes.2018.08.011

Kurul, N., and Podowski, M. (1991). "On the Modeling of Multidimensional Effects in Boiling Channels," in Proceedings of the 27th National Heat Transfer Conference, Minneapolis, Minnesota, USA.

Lavieville, J., Quemerais, E., Mimouni, S., Méchitoua, N., and Boucker, M. (2005). *Neptune CFD V1.0, Theory Manual*. France: Electricite De France.

Lemmert, M., and Chawla, J. (1977). Influence of Flow Velocity on Surface Boiling Heat Transfer Coefficient. *Heat Transfer Boiling*, 237–247.

Li, Q., Avramova, M., Jiao, Y., Chen, P., Yu, J., Pu, Z., et al. (2018). CFD Prediction of Critical Heat Flux in Vertical Heated Tubes with Uniform and Non-uniform Heat Flux. *Nucl. Eng. Des.* 326, 403–412. doi:10.1016/j.nucengdes.2017.11.009

Li, Y., Li, W., Wan, L., Xi, Y., and Wang, N. (2020). Numerical Simulation of Boiling Two-phase Flow in the Subchannel under Static State and Rolling Motion. *Int. J. Heat Mass Transfer* 163, 120416. doi:10.1016/j.ijheatmasstransfer.2020.120416

Liao, H., Wang, Y., Li, Y., Wu, Y., Deng, Y., Su, M., et al. (2020). 3D Fluid-Solid Coupling Simulation for Plate-type Nuclear Fuel Assemblies under the Irradiation Condition. *Prog. Nucl. Energ.* 126, 203428. doi:10.1016/j.pnucene.2020.103428

Liu, R., and Zhou, W. (2017). Multiphysics Modeling of Novel UO2-BeO sandwich Fuel Performance in a Light Water Reactor. *Ann. Nucl. Energ.* 109, 298–309. doi:10.1016/j.anucene.2017.05.037

Lopez de Bertodano, M. (1991). "Turbulent Bubbly Flow in a Triangular Duct,". Ph.D. Thesis (Troy, New York: Rensselaer Polytechnic Institute).

Lu, Q., Qiu, S., and Su, G. H. (2009). Flow Blockage Analysis of a Channel in a Typical Material Test Reactor Core. *Nucl. Eng. Des.* 239, 45–50. doi:10.1016/j.nucengdes.2008.06.016

Park, J.-P., Park, C., and Park, S. (2021). A Numerical Analysis for a Damage Propagation in a Plate-type Fuel Assembly of a Research Reactor. *Ann. Nucl. Energ.* 153, 108071. doi:10.1016/j.anucene.2020.108071

Phillippe, A. M., Ott, L., Clarno, K., and Banfield, J. (2012). *Analysis of the IFA-432, IFA-597, and IFA-597 MOX Fuel Performance Experiments by FRAPCON-3.4*. America: Oak Ridge National Laboratory.

Shirvan, K. (2016). Numerical Investigation of the Boiling Crisis for Helical Cruciform-Shaped Rods at High Pressures. *Int. J. Multiphase Flow* 83, 51–61. doi:10.1016/j.ijmultiphaseflow.2016.03.014

Son, H. M., Yang, S. H., Park, C., and Lee, B. C. (2015). Transient thermal-hydraulic Analysis of Complete Single Channel Blockage Accident of Generic 10 MW Research Reactor. *Ann. Nucl. Energ.* 75, 44–53. doi:10.1016/j.anucene.2014.08.002

Sun, R., Song, G., Zhang, D., Deng, J., Su, G. H., Kulacki, F. A., et al. (2020). Experimental Study of Single-phase Flow and Heat Transfer in Rectangular Channels under Uniform and Non-uniform Heating. *Exp. Therm. Fluid Sci.* 114, 110055. doi:10.1016/j.expthermflusci.2020.110055

Tolubinsky, V., and Kostanchuk, D. (1970). "Vapour Bubbles Growth Rate and Heat Transfer Intensity at Subcooled Water Boiling," in Proceedings of the 4th International Heat Transfer Conference, Paris-Versailles, France, 31 August - 5 September. doi:10.1615/ihtc4.250

Tomiyama, A. (2004). "Drag Lift and Virtual Mass Forces Acting on a Single Bubble," in Third International Symposium on Two- Phase Flow Modeling and Experimentation, Pisa, Italy, September 22-24.

Yoo, J., Oka, Y., Ishiwatari, Y., and Liu, J. (2006). Thermo-mechanical Analysis of Supercritical Pressure Light Water-Cooled Fast Reactor Fuel Rod by FEMAXI-6 Code. *Ann. Nucl. Energ.* 33, 1379–1390. doi:10.1016/j.anucene.2006.10.004

Zeitoun, O., and Shoukri, M. (1996). Bubble Behavior and Mean Diameter in Subcooled Flow Boiling. *J. Heat Transfer* 118, 110–116. doi:10.1115/1.2824023

Zhang, T., and Liu, Y. (2020). Numerical Investigation of Flow and Heat Transfer Characteristics of Subcooled Boiling in a Single Rod Channel With/without Spacer Grid. *Case Stud. Therm. Eng.* 20, 100644. doi:10.1016/j.csite.2020.100644

Conflict of Interest: The authors declare that the research was conducted in the absence of any commercial or financial relationships that could be construed as a potential conflict of interest.

Publisher's Note: All claims expressed in this article are solely those of the authors and do not necessarily represent those of their affiliated organizations, or those of the publisher, the editors and the reviewers. Any product that may be evaluated in this article, or claim that may be made by its manufacturer, is not guaranteed or endorsed by the publisher.

frontiers in Energy Research

ORIGINAL RESEARCH
published: 22 September 2021
doi: 10.3389/fenrg.2021.663937

Research on Detection Technology of ^{235}U Enrichment and Loading Uniformity for Nuclear Fuel Rods

Mingfei Gu[1], Dagui Huang[1], Dongbao Yu[2], Hui Tang[2] and Yongli Zhu[2]*

[1]School of Mechanical and Electrical Engineering, University of Electronic Science and Technology of China, Chengdu, China, [2]China North Nuclear Fuel Co., Ltd., Baotou, China

To ensure that fuel rods operate in nuclear reactors safely and reliably, UO_2 pellets with different enrichment levels of ^{235}U in the same production line are manufactured in batches and divisionally managed to avoid confusion or the potential misloading of UO_2 pellets with different enrichment levels. At the same time, nondestructive tests for their enrichment levels and loading uniformity and all UO_2 pellets must be nondestructively tested during production. By studying the enrichment detection mechanism of the UO_2 pellets of ^{235}U, the design of an integral standard rod was carried out, and a single integral standard rod was used to achieve the calibration of the enrichment measurement curve, as well as the detection and calibration of abnormal pellets. This study undertook a comparison test of ^{235}U enrichment between the neutron activation method and the array multi-probe passive method. The test results showed that the array multi-probe passive method had higher detection efficiency and equal accuracy.

Keywords: nuclear fuel rods, UO2 pellets, enrichment, neutron activation method, passive method

OPEN ACCESS

Edited by:
Yingwei Wu,
Xi'an Jiaotong University, China

Reviewed by:
Tengfei Zhang,
Shanghai Jiao Tong University, China
Zeyun Wu,
Virginia Commonwealth University, United States

****Correspondence:***
Dagui Huang
dg_huang@vip.163.com

Specialty section:
This article was submitted to Nuclear Energy, a section of the journal Frontiers in Energy Research

Received: *04 February 2021*
Accepted: *29 June 2021*
Published: *22 September 2021*

Citation:
Gu M, Huang D, Yu D, Tang H and Zhu Y (2021) Research on Detection Technology of ^{235}U Enrichment and Loading Uniformity for Nuclear Fuel Rods. Front. Energy Res. 9:663937. doi: 10.3389/fenrg.2021.663937

INTRODUCTION

Nuclear fuel rods (hereinafter referred to as fuel rods) are the energy source and core of nuclear power plant reactors. The main function of fuel rods is to release heat and contain nuclear fission products. Since the nuclear power plants have different reactor types and different refueling batches, the ^{235}U enrichment of the UO_2 pellets in the fuel rods may vary. To ensure the safe and reliable operation of nuclear fuel rods in nuclear power plant reactors, the ^{235}U enrichment and charging uniformity of the UO_2 pellets inside the fuel rods must conform to relevant design and production requirements. On the production line of a nuclear fuel element production plant, fuel rods with different enrichments are manufactured in batches and undergo very strict differentiated management. It is forbidden to accidentally load UO_2 pellets with different enrichments into fuel rods. If the UO_2 pellets with different enrichment are misloaded in fuel rods, the axial power distribution of the fuel rods will be uneven, and local hot spots may be generated. In severe cases, the fuel rods may rupture, cause radioactive material leakage, contaminate the coolant, and affect the safety of the reactor operation (Zhang et al., 2013). Therefore, to prevent the potential misloading of UO_2 pellets with different enrichment (hereinafter referred to as abnormal pellets) during the fuel rod manufacturing process, and to ensure the safe and reliable operation of fuel rods in nuclear power plant reactors, the UO_2 pellets in the fuel rods must be subject to 100% non-destructive inspection of ^{235}U enrichment and charging uniformity (hereinafter referred to as enrichment inspection). Generally, fuel rod enrichment detection methods include the neutron activation method and the passive method. The current fuel element production line mainly uses the

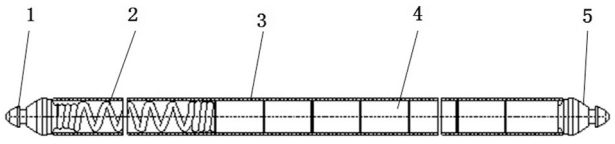

FIGURE 1 | Schematic diagram of fuel rods.

neutron activation method. In the 1970s, the first ^{252}Cf thermal neutron detection system, which was designed by the American Alamos Laboratory H.O. Menlove, was used to measure the total content of fissile material in the fuel rods of the light water power reactor. At the end of the 1990s, Chinese researchers also developed a fuel rod neutron activation detection device by using a^{252}Cf neutron source, the source was surrounded by neutron moderators, and utilized a neutron protective material as the outer layer and lead as the gamma-ray shielding material. The transmission device allows the fuel rod to pass through the irradiator at a constant speed. The exit of the irradiator is equipped with a NaI(TI) gamma-ray detector. The gamma rays induced by the fuel rod after neutron irradiation are ten times higher than the spontaneous decay of ^{235}U, which is convenient for checking ^{235}U enrichment (Chen and Liu, 2007). Although the neutron activation method has high detection efficiency, it has disadvantages such as needing to replace neutron sources regularly, and the high cost of detection, maintenance, and management. Although the detection cost of the traditional single-probe passive method is low, the poor detection efficiency leads to difficulty in satisfying the needs of the fuel rod production line. In recent years, with the advancement of sensor technology, fuel rod enrichment inspection based on the array multi-probe passive method has been rapidly developed and attracted widespread attention. The United States NDA and the Zhengzhou branch of China Nuclear Power Engineering Co. Ltd., the Institute of High Energy Physics, the Chinese Academy of Sciences (Liu et al., 2019), and other units have carried out related research.

In this paper, through the analysis and research on the detection mechanism of UO_2 pellet ^{235}U enrichment, a comparative experiment of neutron activation method and array multi-probe passive method is carried out. The test results show that the array multi-probe passive method has higher detection accuracy. The high detection efficiency and recognition rate of abnormal pellets can replace the traditional method for fuel rod neutron activation enrichment detection and loading uniformity detection.

THE TEST REQUIREMENTS OF FUEL ROD STRUCTURE AND ENRICHMENT

Fuel Rod Structure

The fuel rod is composed of a cladding tube, UO_2 pellets, spring, upper end plug, and lower end plug, as shown in **Figure 1**. The fuel rod has an outer diameter of 9.5 mm and a length of about 4 m. Each type of fuel rod generally only contains UO_2 pellets with the same enrichment. During the fuel rod production process, UO_2 pellets have various types of enrichment, such as 1.8, 2.4, 3.1, 4.45, 4.95%, etc. The incident of loading different enrichment UO_2 pellets into fuel rods is prohibited during the production process. All fuel rods must be tested 100% for enrichment.

Enrichment Test Requirements

1) It can detect the average enrichment value of UO_2 pellet ^{235}U in fuel rods.
2) Abnormal pellets in fuel rods can be detected. For fuel rods mixed with UO_2 pellets with a relative enrichment of ± 15.6%, detection confidence can be 95%. For fuel rods mixed with UO_2 pellets with relative enrichment of ± 8%, the detection confidence can be 2.5%.
3) The efficiency of enrichment detection should meet the needs of the fuel rod production line.

Enrichment Deviation

The enrichment deviation refers to the percentage difference between the matrix pellets and the abnormal pellets, which is defined as follows:

$$\ln(C_t/C_0) = -kt \tag{1}$$

where:

ΔE-Relative enrichment deviation, %,
E_0-Nominal enrichment value of matrix pellets, %,
E_i-Abnormal pellet enrichment, %,
M_0-Matrix pellet enrichment, %,
M_i-Abnormal pellet mass, g.

In general, considering that the diameter of matrix pellets and abnormal pellets are the same, and their density difference is small, the above formula can be rewritten as:

$$\Delta E = \frac{(E_i - E_0)L_i}{E_0 L_0} \times 100\% \tag{2}$$

where L_0 and L_i are the height of matrix pellets and abnormal pellets, respectively. That is, when calculating the deviation of abnormal pellets, the height of pellets should be considered.

PRINCIPLE OF FUEL ROD ENRICHMENT DETECTION

The spontaneous alpha decay of the ^{235}U nuclide in the UO_2 pellet is accompanied by 98 and 185.7 keV gamma-ray radiations. gamma rays of 185.7 keV are generally selected as fuel rod enrichment inspection signals. When the fuel rod passes through the γ probe at a constant speed, the signal is collected and processed by measuring the circuit to obtain the distribution γ spectrum of ^{235}U enrichment in the direction of the horizontal axis of the fuel rod. The γ spectrum is analyzed and processed through data analysis and processing. By comparing calibration data of standard rods, the average enrichment value of fuel rods can be obtained and it can be

judged whether there are abnormal fuel pellets with different enrichment levels in fuel rods.

EQUIPMENT CALIBRATION OF STANDARD ROD DESIGN AND INSPECTION

Enrichment inspection of the standard rod design is one of the key technologies for checking fuel rods. Usually, a set of reference fuel rods with the same structure and same geometric dimensions but different UO_2 pellet enrichment are used to calibrate inspection equipment and make a ^{235}U relationship curve between enrichment and γ-ray intensity. Then calibration curve, rejection limit, supervision limit, and control limit are established to realize the detection of fuel rod enrichment and abnormal pellets.

A standard rod is equipped with a series of UO_2 pellets with different enrichments arranged along the axial length. The remaining structure and dimensions are the same as the fuel rod. That is, a certain enrichment (E_0) is used as matrix pellets, and the pellets are placed in appropriate positions. Individual pellets are loaded with different enrichment (called abnormal pellets) and then assembled, welded, and the pellet gap is measured according to the fuel rod manufacturing process. Finally, through scanning inspection, the isolated abnormal pellets in these rods are obtained. The γ-ray intensity difference $\Delta\gamma$ between abnormal and the matrix pellets is used to obtain the relationship between the relative deviation of pellet enrichment ΔE and γ-ray intensity difference $\Delta\gamma$ through one-variable linear regression α. If the curve passes through the origin, the linear relationship between the two variables can be expressed as:

$$\Delta y = A\delta e \tag{3}$$

Design requirements are when the deviation of enrichment of abnormal pellets mixed in a fuel rod is ≥ 15.6%, inspection method and inspection equipment should be able to detect these abnormal pellets with a detection efficiency of 95% confidence. The rejection limit Rj exceeding this design requirement is:

$$R_j = a\Delta E + k\sigma \tag{4}$$

where.

R_j-Abolishment limit, Count;
A-The slope of curve;
ΔE-Enrichment deviation allowed by the technical specification, %;
k-95% 95% confidence factor. When calculating positive deviation, k is -1.96. When calculating negative deviation, k is +1.96; σ-Standard deviation of the measured value.

Any measurement signal that exceeds the rejection limit may indicate that there is an abnormal pellet. In practice, it is allowed to be checked again. If a signal exceeding the rejection limit R_j is repeated, the fuel rod will be judged as a disqualified product (Mou et al., 2010) (He et al., 2008).

Two methods of enrichment standard rods can be used in fuel rod production, multiple standard rods and one-piece standard rods.

Multiple Standard Rods

Multiple standard rods include enrichment measurement standard rods (the same kind of ^{235}U enriched UO_2 pellets are packed into a fuel rod to manufacture fuel rods) and abnormal pellet standard rods (the other UO_2 pellets with 235U enrichment different from matrix pellets). According to the technical conditions, the fuel rods are made of a mixture of these pellets and matrix pellets, which are used to calibrate the inspection equipment. Taking an ^{235}U enrichment standard 4.45% rod as an example, there are two standard rods, of which one is an enrichment calibration standard rod, and the other one is an abnormal pellet calibration standard rod.

Integral Standard Rod

Integrated standard rod combines the measurement functions of the enrichment calibration standard rod and the abnormal pellet calibration standard rod into one standard rod. Integrated standard rod includes enrichment measurement section and abnormal pellet measurement section. The enrichment measurement section is used to fit and calibrate the enrichment measurement curve. Generally, it should not be less than three calibration points. The abnormal pellet measurement section is used to identify misloaded UO_2 pellets. Generally, it should include possible production for pellets with different enrichment, take ^{235}U enrichment 4.45% standard rod as an example, see **Figure 2**.

SINGLE PROBE PASSIVE METHOD FUEL ROD ENRICHMENT INSPECTION

The single-probe passive method fuel rod enrichment inspection equipment is relatively simple and low cost. A set of gamma-ray intensity measurement systems only needs an NaI probe, amplifier, single-channel analyzer, and calibrator. First, the standard rod is used to calibrate the γ-ray intensity measurement system. After determining fuel rod enrichment and abnormal pellet rejection limit, fuel rod product enrichment can be checked.

The disadvantage of this equipment is that the inspection efficiency is relatively low and the fuel rod transmission speed is slow. So multi-channel measurement methods are often used, such as an eight-channel single-probe passive fuel rod enrichment inspection system, as shown in **Figure 3**. However, the inspection efficiency is still relatively low, and it is difficult to satisfy the demand for mass production of fuel rod products in general.

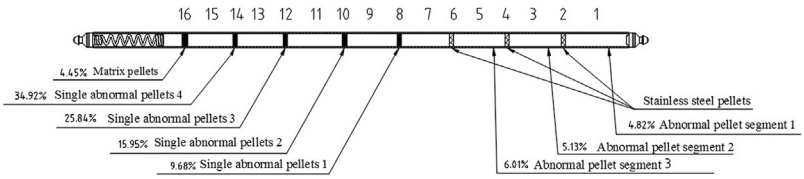

FIGURE 2 | Integral enrichment standard rod.

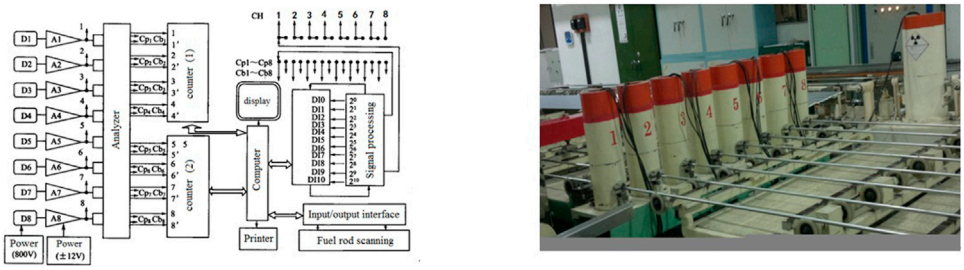

FIGURE 3 | single probe inspection equipment.

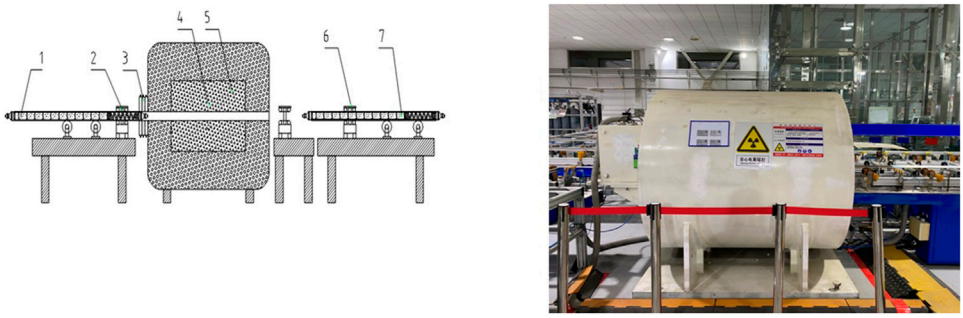

FIGURE 4 | Schematic diagram of neutron activation equipment.

THE ENRICHMENT DETECTION OF FUEL RODS BY NEUTRON ACTIVATION METHOD

Basic Principles of Neutron Activation Method

The neutron activation method by using the characteristic of ^{235}U has a large neutron capture cross section for thermal neutrons. ^{252}Cf neutron source irradiation device is attached to the inspection device. The half-life of ^{252}Cf is 2.638 years. The most important nuclear property of ^{252}Cf is that it can release a large number of neutrons in spontaneous fission, and the yield is 2.35×10^{12}n/(s.g). Moreover, the average neutron energy of the neutrons is 2.348 MeV. The ^{235}U in UO_2 pellet induces nuclear fission reaction under activation of neutron irradiation, the produced fission products are accompanied by a series of beta decays, releasing a large amount of delayed gamma rays, which are ten times higher than gamma rays of ^{235}U spontaneous decay. Several times, by measuring fissile prompt gamma rays and delayed gamma rays, the content of fissionable material in tested material can be determined. ^{252}Cf neutron activation method is currently a commonly used method in fuel rod production lines.

Neutron Activation Inspection System

The fuel rod is irradiated by thermal neutrons to induce strong gamma rays. Delayed gamma intensity is recorded by NaI detector, and the ^{235}U content of each pellet in the fuel rod can be distinguished. The maximum speed of fuel rod inspection can reach 9 m/min. The structure of the device is shown in **Figure 4**. It is not affected by the age of UO_2 pellets. The resolution of abnormal pellets is equivalent to that of passive methods.

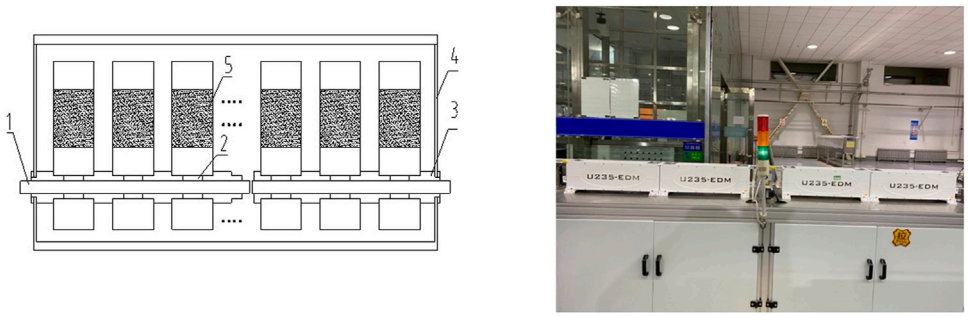

FIGURE 5 | Array of multi-probe passive devices.

Advantages and Disadvantages of Neutron Activation

The advantages of neutron activation detection fuel rod enrichment are fast speed, good resolution, and suitability for pellets of any age. However, it is necessary to select measurement parameters reasonably to optimize detection efficiency. The intensity of the slow emission line released by activated pellets decreases exponentially with time (because the half-life of most fission products is very short). Therefore, the distance between detector and neutron source should be as small as possible. Inevitably, the distance will be limited by the irradiation shielding shell of the device. To obtain the best resolution, the window of the detector collimation hole is set in a range of 15–20 mm. The scanning speed of the fuel rod is closely related to the intensity of the neutron source. Generally, after a half-life (2.638 years), neutron yield decreases significantly. At this time, it is necessary to appropriately reduce the scanning speed of the fuel rod to achieve the detection resolution of abnormal fuel pellets. The main disadvantage of neutron activation is the high cost of equipment, and the need to replace the ^{252}Cf neutron source regularly, high operating costs, and strict radiation protection requirements. Fuel rods that have undergone neutron activation inspections need to be stored for about 50 min before they can be manually transported.

ARRAY MULTI-PROBE PASSIVE ENRICHMENT INSPECTION OF FUEL ROD

The principle of the array multi-probe passive method for fuel rod enrichment inspection is the same as that of the single-probe passive method. It directly collects 185.7 keV gamma rays from the spontaneous alpha decay of ^{235}U nuclide. The difference is that the array multi-probe passive method uses dozens or even hundreds of gamma probes arranged in the horizontal axis. When each UO_2 pellet passes through these gamma probes, in turn, the gamma rays released by it will be affected by these gamma probes. The probe accepts, so it can get more γ-rays than single-probe passive method. Therefore, combining the corresponding data analysis algorithm, the array multi-probe passive method can obtain a higher inspection efficiency and recognition rate, as shown in **Figure 5**.

CONTRAST TEST OF ARRAY MULTI-PROBE PASSIVE METHOD AND NEUTRON ACTIVATION METHOD

The 4.45 and 4.95% enrichment standard rods commonly used in production are selected for the test. Test parameters include standard rod transmission speed, collection interval, recognition rate, and other parameters, which are shown in **Table 1**.

4.45% Enrichment Fuel Rod Inspection

4.45% Enrichment Standard Rod

The 4.45% enrichment standard bar information is shown in **Table 2**, and the structure diagram is shown in **Figure 2**.

4.45% Enrichment Standard Rod Calibration Data

The array multi-probe passive fuel rod enrichment inspection system uses pellets with different enrichments in standard rods and corresponding average gamma counts to calibrate the inspection system.

The Calibration Curve of 4.45% Standard Pellet

The calibration curve of 4.45% standard pellet is shown in **Figure 6**

Comparison of 4.45% Standard Rod Passive Enrichment Detection System and Active Enrichment Detection System

A comparison of 4.45% standard rod passive enrichment detection system and active enrichment detection system, the results are shown in **Table 3**.

4.95% Enrichment Fuel Rod Inspection

4.95% Enrichment Standard Rod

The 4.95% enrichment standard bar information is shown in **Table 4**.

Calibration Data of 4.95% Enrichment Standard Rod

The 4.95% standard rods were verified at speeds of 6.6 and 7.5 m/min, of which 7.5 m/min was used to verify the maximum detection speed of the passive enrichment detection system.

4.95% Standard Rod Calibration Curve

The calibration curve of 4.95% standard bar is shown in **Figure 7**.

TABLE 1 | Comparative test parameters.

Serial number	Enrichment (%)	Array multi-probe passive method		Neutron activation method		Remarks
		Speed (m/min)	Collection interval (mm)	Speed (m/min)	Collection interval(mm)	
1	4.45%	6.0	7	5.0	17.2	
2	4.95%	6.0	7	5.2	17.2	
3	4.95%	7.5	7	5.2	17.2	Verify the maximum speed

TABLE 2 | 4.45% Enrichment standard rod information.

Serial number	Enrichment (%)	Abnormal pellet and matrix pellet enrichment (%)				Relative deviation of single abnormal pellet enrichment (%)			
		1	2	3	4	1	2	3	4
1	4.45	4.45	4.82	5.13	5.56	9.68	15.60	25.80	34.90
2	4.95	4.95	5.36	5.73	6.71	7.88	15.01	24.68	34.24

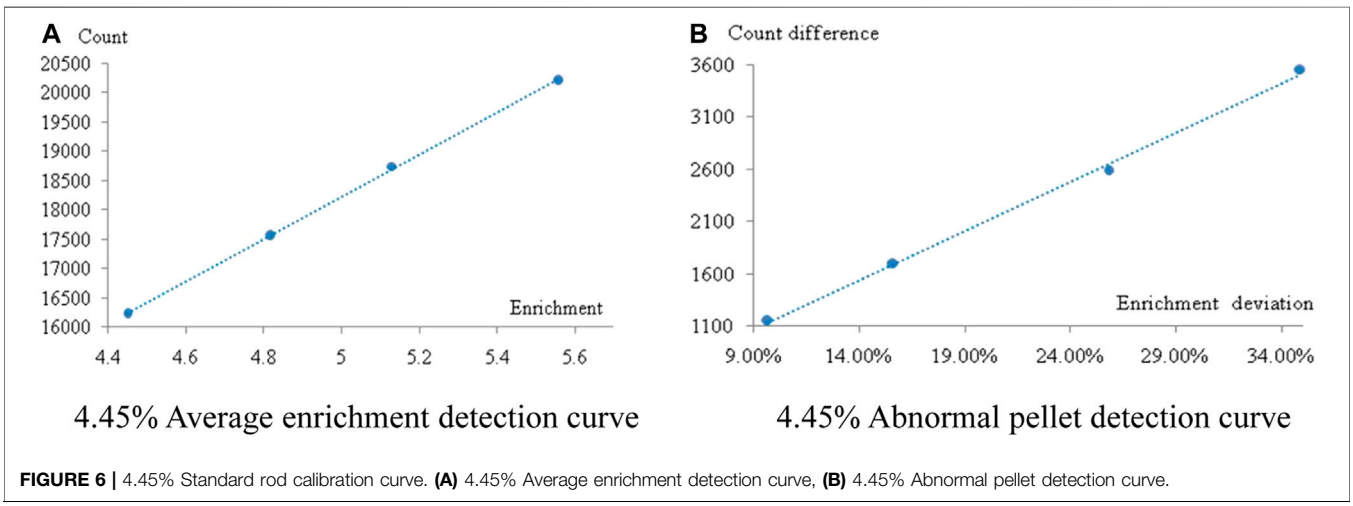

FIGURE 6 | 4.45% Standard rod calibration curve. **(A)** 4.45% Average enrichment detection curve, **(B)** 4.45% Abnormal pellet detection curve.

TABLE 3 | 4.45% Standard rod calibration comparison.

Comparison items	Passive system	Active system	Technical specification	Comparison conclusion
Average enrichment curve correlation coefficient	0.9997	0.9910 (Best)	≥0.99	Passive is better
Correlation coefficient of abnormal pellet curve	0.9989	0.9985 (Best)	≥0.99	Passive is better
8% Abnormal pellet detection rate	95%	40%	≥2.5%	Passive is better
15.6% Abnormal pellet detection rate	100%	100%	≥95%	Same

TABLE 4 | 4.95% Standard rod calibration comparison.

Comparison items	Passive system		Active system	Technical specification	Comparison conclusion
	6.6 m/min	7.5 m/min			
Average enrichment curve correlation coefficient	0.9990	0.9994	0.9910 (Best)	≥0.99	Passive is better
Correlation coefficient of abnormal pellet curve	0.9999	0.9977	0.9985 (Best)	≥0.99	Passive is better
8% Abnormal pellet detection rate	30%	2.5%	25%	≥2.5%	Passive is better
15.6% Abnormal pellet detection rate	100%	100%	100%	≥95%	Same

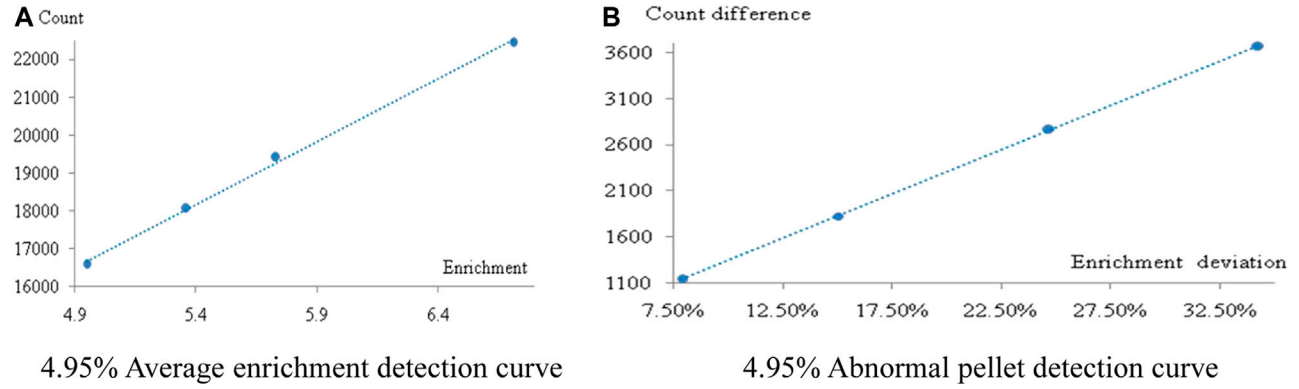

FIGURE 7 | 4.95%Standard rod calibration curve. **(A)** 4.95% Average enrichment detection curve, **(B)** 4.95% Abnormal pellet detection curve.

TABLE 5 | System repeatability index.

Items	Technical specification	Calculation method	Remarks
Matrix pellet RSD	RSD≤0.5%	$RSD_1 = \frac{S_0}{\overline{X_0}} * 100\%$	S_0: Standard deviation of matrix pellet count $\overline{X_0}$ Average difference of matrix pellet count
Abnormal pellet RSD for deviation 15.6%	RSD≤10%	$RSD_2 = \frac{S_1}{\overline{X_1}} * 100\%$	S_1: Standard deviation of count difference between abnormal pellet and matrix pellet for deviation 15.6% $\overline{X_1}$ Average count difference between abnormal pellets and matrix pellets for deviation 15.6%

To fully verify the repeatability of the passive enrichment detection equipment, 20 times and 50 times tests were used to calculate repeatability on site.

Comparison of 4.95% Standard Rod Passive Enrichment Detection System and Active Enrichment Detection System

Comparison of 4.95% standard rod passive enrichment detection system and active enrichment detection system. The comparison results are shown in **Table 4**.

Conclusion of Calibration Data Comparison

From the comparison of passive and active calibration data in the above *4.45% Enrichment Fuel Rod Inspection to 4.95% Enrichment Fuel Rod Inspection* sections, we can conclude:

1) The correlation coefficient of the average enrichment calibration curve and correlation coefficient of abnormal pellet calibration curve of the passive enrichment detection system are better than those of the active enrichment detection system, indicating that the data linearity of the passive enrichment detection system is better;
2) The detection rate of 8% abnormal pellets is the most critical sensitivity index of this detection system, which characterizes the most precise detection requirements. The passive enrichment detection system, no matter what enrichment standard bar, is 8%. The detection rate of abnormal pellets is far better than the active enrichment detection system, which shows that the passive enrichment detection system is more sensitive to the detection of abnormal pellets.
3) The collection interval of the passive enrichment detection system in **Table 1** is 7 mm. The collection interval of the active enrichment detection system is 17 mm. It further proves the high sensitivity of the passive enrichment detection system for abnormal pellet detection.

SYSTEM REPEATABILITY VERIFICATION

The repeatability of the system characterizes the consistency of multiple measurement results of the detection system, and can also be regarded as the stability index of the detection system. Therefore, it is necessary to further verify the project. The repeatability of the system requires repeated measurement of a standard rod 20 times, and the following indicators are calculated for evaluation, shown in **Table 5**.

Repeatability Verification (20 times Inspections)

The results of the count value of the standard rod (20 times) detected by the passive enrichment detection system are shown in **Table 6**.

According to the above table, checking the repeatability of the detection system:

$$RSD_1 = \frac{33.2}{31724} \times 100\,\% = 0.1050\,\% \quad (5)$$

TABLE 6 | 20 Times of repeatable validation data.

Items	Count									
	1	2	3	4	5	6	7	8	9	10
Matrix pellet count	0.692	0.696	0.703	0.688	0.686	0.700	0.714	0.680	0.710	0.714
	−0.718	−0.696	−0.703	−0.750	−0.714	−0.700	−0.714	−0.720	−0.710	−0.714
8% Abnormal pellet count	0.714	0.703	−0.708	−0.722	−0.709	−0.709	−0.706	−0.704	0.722	0.706
	−0.714	−0.708	0.708	0.667	0.709	0.709	0.706	0.704	−0.722	−0.706
15.6% Abnormal pellet count	−0.722	0.704	−0.707	−0.706	−0.711	−0.708	−0.707	−0.714	−0.692	0.706
	0.667	−0.710	0.707	0.706	0.700	0.708	0.707	0.705	0.692	−0.706

TABLE 7 | Repeatable validation data of 50 times.

Items	Count									
	1	2	3	4	5	6	7	8	9	10
Matrix pellet count	0.920	0.351	1.556	1.000	1.036	0.148	1.000	−0.125	−0.097	−0.640
	−1.280	−0.514	−0.815	0.115	−0.714	−0.889	−0.600	−1.000	−1.516	−1.440
	−0.760	1.081	−0.796	−0.308	0.143	−0.815	−0.320	−0.800	0.484	0.920
	0.240	−1.459	0.444	−1.500	−1.321	−0.074	−1.120	0.500	1.194	0.720
	0.880	0.595	−0.370	0.769	0.821	1.630	1.080	1.425	−0.097	0.360
8% Abnormal pellet count	0.238	0.993	−0.945	0.431	−1.452	−1.460	−0.531	−1.461	0.382	0.244
	−0.119	−0.871	0.506	0.604	0.405	0.476	1.269	−0.470	0.000	−1.209
	−0.750	0.879	−1.213	0.139	−0.500	−0.111	0.869	0.130	1.441	0.797
	1.560	−1.193	0.884	−1.757	1.167	−0.175	−0.944	0.957	−1.059	1.041
	−0.952	0.207	0.774	0.576	0.429	1.286	−0.675	0.843	−0.779	−0.884
15.6% Abnormal pellet count	−0.036	1.178	−1.306	0.306	−1.379	−1.661	−0.645	−1.663	0.372	0.369
	0.262	−0.963	0.694	0.702	0.545	0.881	1.296	−0.143	0.603	−1.096
	−0.524	0.776	−0.852	0.240	−0.394	0.220	0.876	0.480	1.064	0.732
	1.488	−1.056	0.661	−1.760	1.288	−0.186	−0.722	0.918	−1.397	1.025
	−1.214	0.065	0.803	0.529	−0.091	0.593	−0.793	0.408	−0.641	−1.025

TABLE 8 | Comparison of repeatability verification.

Item	Passive enrichment detection system		Active enrichment detection system (Optimal condition)	Technical specification	Conclusion
	Verification 20 times	Verification 50 times			
Matrix pellet RSD	0.1050%	0.1003%	0.21%	RSD ≤ 0.5%	Passive is better
Abnormal pellet RSD with deviation 15.6%	7.54%	7.13%	8.88%	RSD ≤ 10%	Passive is better

$$\mathrm{RSD}_2 = \frac{135.17}{1793} \times 100\% = 7.54\% \quad (6)$$

The verification results meet technical requirements.

Repeatability Verification (50 times Inspections)

The count result of the standard rod (50 times) detected by the passive enrichment detection system is shown in **Table7**.

According to the above table, checking the repeatability of the detection system:

$$\mathrm{RSD}_1 = \frac{31.4}{31704} \times 100\,\% = 0.1003\,\% \quad (7)$$

$$\mathrm{RSD}_2 = \frac{128.3}{1800} \times 100\,\% = 7.13\,\% \quad (8)$$

The verification results meet technical requirements.

Comparison of Repeatability Results

The repeatability of the passive enrichment detection system was compared with the active one, and the results are shown in **Table 8**.

CONCLUSION

The comparison between array-type multi-probe passive enrichment detection system and the active enrichment detection system resulted in the following conclusions:

1) The detection speed of array type multi-probe passive enrichment detection system is not lower than that of the active enrichment detection system.

2) The linear correlation coefficient of the average enrichment detection curve meets technical specifications, and the linear correlation coefficient of the abnormal pellet detection curve meets technical specifications and is better than an active enrichment detection system.
3) The detection rate of 8% abnormal pellets meets technical specifications, and the detection rate of 15.6% abnormal pellets meets technical specifications and is not lower than the detection capability of the active enrichment detection system.
4) The repeatability of the system meets technical specifications and is better than an active enrichment detection system.
5) The array multi-probe passive method has high detection accuracy, detection efficiency, and recognition rate of abnormal pellets, which can replace traditional fuel rod neutron activation methods for enrichment and loading uniformity detection methods.

DATA AVAILABILITY STATEMENT

The raw data supporting the conclusion of this article will be made available by the authors, without undue reservation.

AUTHOR CONTRIBUTIONS

MG: writing, calculation, modeling DH: writing, review, guide DY: calculation.

REFERENCES

Chen, B., and Liu, C. (2007). *Light Water Reactor Fuel Element[M]*. Beijing, China: Chemical Industry Press, 198–204.

He, L., Meng, Y., Shao, J., and Gao, Q. (2008). Application of Gamma Spectroscopy in the Verification and Measurement of 235U Enrichment of Fast Reactor New Fuel[J]. *Isotope* Vol. 21, 61–64.

Liu, Y., Liu, S., and Wang, Y. (2019). *Nuclear Fuel Rod Enrichment Passive Detection System[P]*. China: Utility Model Patent.

Mou, W., Li, Y., Wang, X., and Liu, G. (2010). ^{235}U Enrichment Detection[J]. *At. Energ. Sci. Technol.* 44 (No. 7), 782–784.

Zhang, L., Liu, M., and Ma, J. (2013). Software Design of ^{235}U Enrichment Detection Equipment for ^{252}Cf Neutron Activated Nuclear Fuel Rods[J]. *Nucl. Electron. Detect. Technol.* 33 (4), 467–471.

Conflict of Interest: DY, HT, and YZ were employed by the China North Nuclear Fuel Co., Ltd.

The remaining authors declare that the research was conducted in the absence of any commercial or financial relationships that could be construed as a potential conflict of interest.

Publisher's Note: All claims expressed in this article are solely those of the authors and do not necessarily represent those of their affiliated organizations, or those of the publisher, the editors and the reviewers. Any product that may be evaluated in this article, or claim that may be made by its manufacturer, is not guaranteed or endorsed by the publisher.

Advantages of publishing in Frontiers

OPEN ACCESS
Articles are free to read for greatest visibility and readership

FAST PUBLICATION
Around 90 days from submission to decision

HIGH QUALITY PEER-REVIEW
Rigorous, collaborative, and constructive peer-review

TRANSPARENT PEER-REVIEW
Editors and reviewers acknowledged by name on published articles

Frontiers
Avenue du Tribunal-Fédéral 34
1005 Lausanne | Switzerland

Visit us: www.frontiersin.org
Contact us: frontiersin.org/about/contact

REPRODUCIBILITY OF RESEARCH
Support open data and methods to enhance research reproducibility

DIGITAL PUBLISHING
Articles designed for optimal readership across devices

FOLLOW US
@frontiersin

IMPACT METRICS
Advanced article metrics track visibility across digital media

EXTENSIVE PROMOTION
Marketing and promotion of impactful research

LOOP RESEARCH NETWORK
Our network increases your article's readership